UCL CHEMICAL ENGINEERING: DOCTORAL THESIS

Development of Novel Alloy Electrocatalysts for the Hydrogen Oxidation Reaction in Alkaline Media and their Application to Low Temperature Fuel Cells

Rhodri Jervis

2015

A thesis submitted for the partial fulfilment of the requirements for the degree of Doctor of Philosophy at University College London

Department of Chemical Engineering,
University College London,
Torrington Place,
London,
WC1E 7JE

Declaration

I, Rhodri Jervis, confirm that the work presented in this thesis is my own. Where information has been derived from other sources, I confirm that this has been indicated in the thesis.

.....

Signature

.....

Date

Acknowledgments

I would first like to thank Dan Brett for the opportunity to study such an interesting area of research and for all his help and guidance throughout the project. It has been a thoroughly exciting and enjoyable time, and I am very pleased to remain in the group for my post-doctoral work. I would also like to thank Chris Gibbs for his expert help in the lab, imparting of wisdom and infectious enthusiasm for fuel cells. My secondary supervisor, Paul Shearing for casting a valued second opinion over my work and proving many a useful contact, specifically for synchrotron experiments. Also, Simon Jones for the improvement of the catalyst to the high surface area version and expert guidance on XPS, amongst other techniques.

Many experiments were conducted with the supervision and assistance of others, specifically: Chiu Tang and Claire Murray at Diamond for the synchrotron X-ray powder diffraction, Andy Dent and Stephen Price, also at diamond, for the EXAFS experiments – in particular Stephen who helped immensely with my understanding of the theory behind the fitting of the data, Ana Belén Jorge Sobrido for TEM, HR-TEM and XPS among many other things, Amal Mansor for general help and discussion on the electrochemical testing including much co-work on the same catalyst, Sarah Fearn at Imperial College for the LEIS work, Carsten Kuenzel, also at Imperial, for conduction of the TGA and ICP-AES experiments, Toby Neville for SEM and general lab wisdom, Tom Mason for the AAEM resistivity measurements, Vidal Bharath for carrying out the QCM investigations into carbonate formation in the membranes, Quentin Meyer and Toby for useful discussion on EIS and fitting, Jason Millichamp for his considerable help with experimental construction and design and all other members of the EIL for their general guidance and scientific and social stimulation. Also thanks to Matthias Arenz at the University of Copenhagen for producing the PTFE cell used in this work.

Thanks to my office neighbours Philip Reardon, David Martin, Mayowa Obeisun, Aliya Toleuova, Lawrence Edomwonyi-Otu, Quentin and Amal for making being cooped up in a basement bearable. To Rema Abdulaziz and Ana Belén for coffee mornings and memorable late nights, and many more to come. Paddy Cullen, for all the as-yet-unrealised Nobel prize winning ideas generated in the pub and sticking around through undergrad, PhD

and post-doctoral studies. Thanks to Vidal for putting a roof over my head when I needed it and being so generous. Ishanka Dedigama for being far less innocent than her face would suggest and making me feel so welcome when I started in the group, as did Mithila Manage, Toby, Jay, Flora Daniels and Tom.

I have been lucky enough to be involved in many synchrotron experiments outside the work contained in this thesis and so thank the following people for inviting me to be part of it and providing an excellent diversity of experience as well as top entertainment on the late night shifts: Paul Shearing, Leon Brown, James Robinson, Donal Finegan, Dami Taiwo, Vidal, Rema and Quentin.

My public engagement work with UCell has afforded me the opportunity to discuss my research, and renewable energy in general, outside of the lab, which I've found a rewarding and complimentary experience during my PhD. It would not be possible, or enjoyable, without all the people involved: Vidal Bharath and Erik Engebretsen (The Generals), Leon, Paul, Ralph Clauge, Mithila, Tom Heenan, James, Dami, Anna Ploszajski, Donal, Bernhard Tjaden and, more recently, Josh Bailey, Chloe Knox, Dina Ibrahim and Rema.

The EIL is a very sociable place to study and thanks go to all the members for providing well needed relief from the work, but in particular Ana Belén, Vidal, Erik and James for always being up for 'just a quick drink'. Thanks go to all my friends outside of the PhD for being *genuinely* interested in my research and always being there for me during the good and the bad for the last ten years or more; in particular Saz for her unwavering pastoral care from whichever corner of the globe she happened to be in, and at whatever hour of the night. My biggest thanks go to my main distraction for making the last year the best of my life – diolch.

Finally, I would like to thank my Parents for their support of my endeavours throughout my life, without which I would not be where I am today.

Abstract

Fuel cells represent a promising technology for alternative electricity generation in both automotive and stationary applications. However, at present, cost and durability of the materials employed in fuel cells are barriers to commercial ubiquity. One of the main sources of cost in fuel cells is the platinum or platinum based catalysts used in the electrodes, particularly at the cathode where the sluggish oxygen reduction reaction (ORR) kinetics require high loading of precious metals.

An alternative to the more widely studied polymer electrolyte membrane (PEM) acidic fuel cell is the alkaline anion exchange membrane (AAEM) fuel cell. Though the alkaline membranes are less developed than the acidic membranes used in PEM fuel cells, AAEMs are seen as a promising route to cost reduction due to the more facile ORR kinetics in alkaline media. This allows the employment of non-noble metals at the cathode, significantly reducing the amount of precious metals required in the fuel cell. However, the hydrogen oxidation reaction (HOR) kinetics (an often neglected area of study in acidic PEM fuel cells due to the negligible activation losses on the anode) in alkaline are an order of magnitude slower and thus, in order to unlock the potential of cheaper cathode catalysts, more active anode catalysts must be developed before AAEMs can be seen as a true alternative to the more established PEM technology.

This thesis describes the synthesis, characterisation and electrochemical activity of a novel carbon-supported PdIr catalyst for the HOR in alkaline media. Initial synthesis methods showed the catalyst to have comparable activity with platinum through electrochemical testing, and on increasing the surface area with improved synthesis a two-fold increase in exchange current density was achieved The catalyst has been characterised with a variety of methods including SEM, HR-TEM, XRD, EXAFS and LEIS, and initial in-situ fuel cell polarisation curves are also presented.

Publications

Primary Publications

- R. Jervis, N. Mansor, C. Gibbs, C. Murray, C. Tang, D. Brett. **Hydrogen Oxidation on PdIr/C Catalysts in Alkaline Media**, J. Electrochem. Soc., 2014, 161, 4, F458-F463
- R. Jervis, N. Mansor, C. Gibbs, C. A. Murray, C. C. Tang, and D. J. L. Brett, **Novel PdIr/C Catalysts for the Hydrogen Oxidation Reaction in Alkaline Media**, ECS Transactions, vol. 58, pp. 637-650, August 31, 2013 2013

Patents

- D. Brett, C. Gibbs, R. Jervis, N. Mansor. Fuel Cell, **WO 2013093449 (A2)**
- R. Jervis, N. Mansor, D. Brett, C. Gibbs. Electrolysis electrocatalyst, **WO 2014045049 (A1)**
- D. Brett, C. Gibbs, R. Jervis, N. Mansor. Fuel Cell, **US 20140342262 (A1)**

Secondary Publications

- N. Mansor, A. Jorge, F. Cora, C. Gibbs, R. Jervis, P. McMillan, X. Wang, D. Brett. **Development of Graphitic-Carbon Nitride Materials as Catalyst Supports for Polymer Electrolyte Fuel Cells**, J. Electrochem. Soc. Trans. 2013, 58, 1767-1778
- N. Mansor, A. B. Jorge, F. Cora, C. Gibbs, R. Jervis, P. F. McMillan, et al., **Graphitic Carbon Nitride Supported Catalysts for Polymer Electrolyte Fuel Cells**, The Journal of Physical Chemistry C, vol. 118, pp. 6831-6838, 2014/04/03 2014.
- J. B. Robinson, L. D. Brown, R. Jervis, O. O. Taiwo, J. Millichamp, T. J. Mason, et al., **A novel high-temperature furnace for combined in situ synchrotron X-ray diffraction and infrared thermal imaging to investigate the effects of thermal gradients upon the structure of ceramic materials**, Synchrotron Radiation, vol. 21, 2014.
- J. B. Robinson, L. D. Brown, R. Jervis, O. O. Taiwo, T. M. Heenan, J. Millichamp, et al., **Investigating the effect of thermal**

gradients on stress in solid oxide fuel cell anodes using combined synchrotron radiation and thermal imaging, Journal of Power Sources, vol. 288, pp. 473-481, 2015.

- J. Millichamp, T. J. Mason, T. P. Neville, N. Rajalakshmi, R. Jervis, P. R. Shearing, et al., **Mechanisms and effects of mechanical compression and dimensional change in polymer electrolyte fuel cells – A review**, Journal of Power Sources, vol. 284, pp. 305-320, 6/15/ 2015
- A. B. J. Sobrido, I. Dedigama, N. Mansor, R. Jervis, T. Miller, F. Cora, et al., **Graphitic Carbon Nitride Materials for Energy Applications**, ECS Transactions, vol. 64, pp. 13-30, 2015
- L. Brown, R. Abdulaziz, R. Jervis, V. Bharath, R. Attwood, C. Reinhard, et al., **Following the electroreduction of uranium dioxide to uranium in LiCl–KCl eutectic in situ using synchrotron radiation**, Journal of Nuclear Materials, vol. 464, pp. 256-262, 2015
- Q. Meyer; S. Ashton; R. Jervis; D. Finegan; P. Boillat; M. Cochet; O. Curnick; T. Reisch; P. Adcock; P. Shearing; D. Brett, **The Hydro-electro-thermal Performance of Air-cooled, Open-cathode Polymer Electrolyte Fuel Cells: Combined Localised Current Density, Temperature and Water Mapping**, Electrochimica Acta, Submitted May 2015

Book Chapters

- R. Jervis and D. J. L. Brett, **Alkaline Anion Exchange Membrane Fuel Cells**, in Materials for Low-Temperature Fuel Cells, ed: Wiley-VCH Verlag GmbH & Co. KGaA, 2014, pp. 3-32.
- R. Jervis, Thomas J. Mason, Jason Millichamp, Paul R. Shearing and Dan J.L. Brett, **Proton Exchange Membrane Fuel Cells**, in Advanced Materials for a Sustainable Energy Future; Wiley, in press

Conferences Attended

- STFC Early Career Researchers Conference 2015, Abingdon. **Presentation**: Novel PdIr/C Catalysts for the Hydrogen Oxidation Reaction in Alkaline Media

- ECS 224th Meeting 2013, San Francisco. **Presentation**: Novel PdIr/C Catalysts for the Hydrogen Oxidation Reaction in Alkaline Media
- Electrochem 2013, University of Southampton. **Presentation**: Novel PdIr/C Catalysts for the Hydrogen Oxidation Reaction in Alkaline Media
- Anion-Exchange Membranes for Energy Generation Technologies 2013, University of Surrey. **Poster**: Catalyst Development for the Alkaline Fuel Cell
- Catalysis Winter School Dec 2012, Oxford University. **Poster**: Catalyst Development for the Alkaline Fuel Cell
- UCL-ICL Catalyst Initiative, Jan 2012, Imperial College London. **Presentation**: Catalysis at the EIL
- iChemE Catalysis for Energy University of Birmingham 2012. **Poster**: Anode Catalyst Development for the Alkaline Flexible Fuel Cell
- Enterprising Electrochemistry, SCI, London 2012. **Presentation**: Spin in and Spin out: a student perspective
- Zing Conference 2011, Mexico. **Presentation**: Catalyst Development for the Alkaline Flexible Fuel Cell
- Electrochemical Horizons 2011, Bath. **Poster**: Catalyst Development for the Alkaline Flexible Fuel Cell

List of Abbreviations

AAEM	Alkaline Anion Exchange Membrane
ADEFC	Alkaline Direct Ethanol Fuel Cell
ADMFC	Alkaline Direct Methanol Fuel Cell
AFC	Alkaline Fuel Cell
B-V	Butler-Volmer
C_{DL}	Double-Layer Capacitance
CV	Cyclic Voltammetry/Voltammogram
CO CV	Carbon Monoxide Stripping CV
COD	Crystallographic Open Database
CPE	Constant Phase Element
DFT	Density Functional Theory
ECSA	Electrochemical Surface Area
EDX	Energy Dispersive X-Ray Spectroscopy
EIS	Electrochemical Impedance Spectroscopy
GDE	Gas Diffusion Electrode
GDL	Gas Diffusion Layer
GDM	Gas Diffusion Medium
HER	Hydrogen Evolution Reaction
HOR	Hydrogen Oxidation Reaction
ICP-AES	Inductively Coupled Plasma Atomic Emission Spectroscopy
IPA	Isopropyl Alcohol, $CH_3CH(OH)CH_3$
LEIS	Low Energy Ion Scattering
MEA	Membrane Electrode Assembly
OCV	Open Circuit Potential
ORR	Oxygen Reduction Reaction
PTFE	Polytetrafluoroethylene
QCM	Quartz Crystal Microbalance
RDE	Rotating Disk Electrode
RRDE	Rotating Ring Disk Electrode
RHE	Reversible Hydrogen Electrode
R_{CT}	Charge Transfer Resistance
R_{EL}	Electrolyte Resistance

$\mathbf{R_D}$	Diffusion/Mass Transport Resistance
SEM	Scanning Electron Microscopy
SIMS	Secondary Ion Mass Spectrometry
SHE	Standard Hydrogen Electrode
STP	Standard Temperature and Pressure
TEM	Transmission Electron Microscopy
TGA	Thermogravimetric Analysis
HR-TEM	High Resolution TEM
XAFS	X-Ray Absorption Fine-Structure
EXAFS	Extended X-Ray Absorption Fine-Structure Spectroscopy
XANES	X-Ray Absorption Near-Edge Spectroscopy
XPS	X-Ray Photoelectron Spectroscopy
XRD	X-ray Diffraction
SXPD	Synchrotron X-Ray Powder Diffraction

Contents

List of Tables

List of Figures

1 Introduction

1.1 Motivation

In an increasingly power hungry world, fossil fuels remain the major source of energy generation, with 83% of global energy consumption coming from coal, oil and natural gas in 2012 [1]. As well as the threat of global warming from the greenhouse gas emissions associated with fossil fuels, supplies are ever dwindling or becoming more costly, difficult and controversial to extract. There is a clear need for an increase in installed renewable energy generation to mitigate against the threat of climate change and volatile fossil fuel markets. However, a large percentage of electricity generation from intermittent sources such as solar or wind can be problematic for electricity grids and can lead to unreliable supply. As such, it is difficult to move away from fossil fuel base loads without new energy storage solutions or significant demand shaping.

Furthermore, the sector with the fastest projected growth is transportation [2], where use of renewables requires a fundamental shift away from the combustion engine to the use of electric vehicles. New technologies will be required in order to facilitate the reduction in use of fossil fuels and increase in renewable, clean energy generation.

1.2 Fuel Cells

Fuel cells represent a potentially integral technology in a greener electricity-based energy economy. Converting chemical energy directly into electricity with no moving parts and no particulate or greenhouse gas emissions at point of operation, they can offer higher efficiencies than combustion and greater energy storage and reduced 'charge' times compared to batteries. While they retain few of the disadvantages of existing electricity generation technologies a major barrier to commercialisation and widespread use at present is cost [3]. The key working part of a fuel cell, the membrane electrode assembly (MEA) comprises a catalyst, usually containing platinum, and an ionic polymer membrane, both of which contribute significantly to the overall cost of a fuel cell [4]. This thesis will concentrate on catalyst de-

velopment as a way to reduce costs and help realise commercial ubiquity of fuel cells in various energy sectors.

1.2.1 What is a Fuel Cell?

The fundamental concept behind a fuel cell is the direct conversion of chemical energy to electrical energy. In this respect it is similar to a battery, but it differs in having a constant supply of fuel and oxidant as opposed to the closed system of a battery. The essence of a fuel cell is an anode, where fuel is oxidised, and a cathode, where oxidant is reduced, separated by an electrolyte. This basic idea of the fuel cell goes back as far as 1839 when Swansea-born physicist Sir William Grove realised that reverse electrolysis of water was possible [3]. However, development from this concept was slow and it was not until the 1960s and the Apollo Space Programme that fuel cells became practicable, in the form of aqueous alkaline electrolyte fuel cells. Aqueous electrolyte-based fuel cells have many disadvantages for portability (see Section 2.1.3) causing recent focus to shift towards solid electrolytes, in particular towards Polymer Electrolyte Membrane (PEM) fuel cells. These employ an ionomer, which is a polymer containing an ionic functional group in the monomer, as the electrolyte in order to allow ion transport through a non-aqueous medium. Recent improvements in membrane technology, and in particular the performance of the industry standard Nafion membranes, have made PEM fuel cells a major focus of research [5].

1.2.2 Fuel Cell Principles

The main elemental principle of a fuel cell is the direct electrochemical redox reaction that produces the electrical current. In the hydrogen/oxygen fuel cell the redox reaction is composed of two electrochemical half equations; the hydrogen oxidation reaction (HOR) at the anode:

$$H_2 \rightleftharpoons 2H^+ + 2e^- \qquad \text{Equation 1.1}$$

and the oxygen reduction reaction (ORR) at the cathode:

$$\tfrac{1}{2}O_2 + 2H^+ + 2e^- \rightleftharpoons H_2O \qquad \text{Equation 1.2}$$

These combine to give the overall redox reaction:

$$H_2 + \frac{1}{2}O_2 \rightleftharpoons H_2O \qquad \text{Equation 1.3}$$

A schematic of the PEM fuel cell can be seen in Figure 1.1. Hydrogen is fed into the anode and air/oxygen to the cathode through flow-fields and diffuses through a gas diffusion layer (GDL) to the catalyst layer where the gas, catalyst and electrolyte meet in what is called a triple phase boundary (Figure 1.2). It is here where the HOR and ORR occur on the anode and cathode respectively, separated by the polymer membrane electrolyte. The protons generated by the HOR diffuse through the electrolyte to react at the cathode and the electrons generated, impeded by the insulating polymer, travel through the external circuit creating a current.

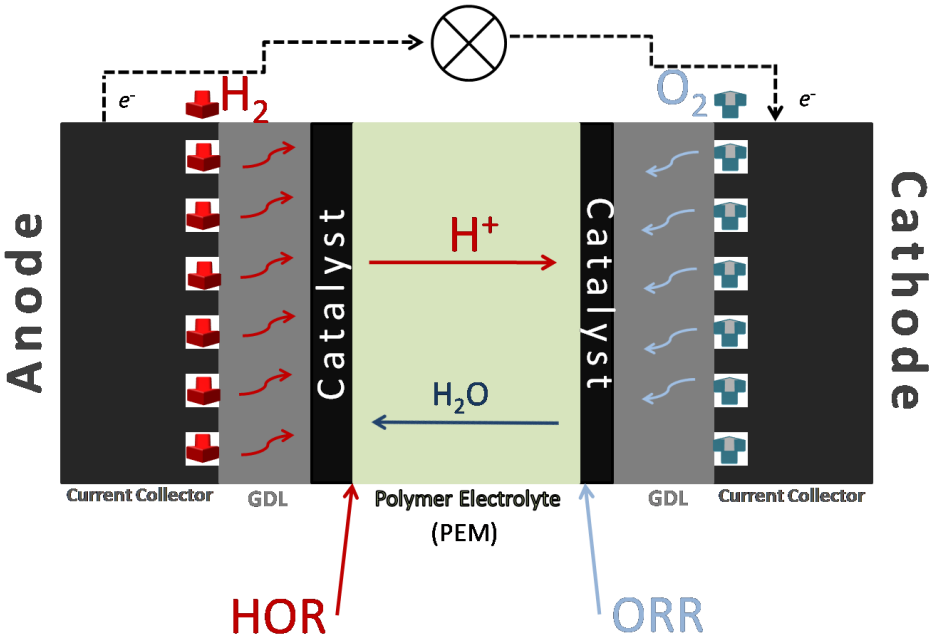

Figure 1.1 Schematic of an acidic PEM fuel cell.

1.2.3 Fuel Cell Components

Though the chemistry behind the working of a fuel cell occurs at the triple phase boundary in the catalyst layer, there are multiple components that are vital to the good operation of the cell.

Bipolar plates: Usually made from a carbon composite or metal, bipolar plates have two main functions: as flow channels to deliver fuel and oxidant and remove water, and as current collectors to provide electrical connection to the external circuit and between indi-

vidual cells in a stack. The flow-fields are machined from the graphite and shape and size can have a direct impact on the performance of the cell [6]. They also contribute a significant amount to the cost and weight of cells so are an active focus of cost reduction efforts.

Gas diffusion layer: The GDL is a carbon-based macro-porous material, usually in the form of a fibrous paper or a cloth, which facilitates the even diffusion of the gases from the flow-fields into the catalyst layer. Often coated in hydrophobic PTFE-based carbon ink they help to reduce flooding issues by repelling any water that builds up in the catalyst layer, allowing it to be swept away in the gas stream. GDLs form an important electrical connection between the catalyst layer and the bipolar plate and so, though an often overlooked component of the fuel cell, play a vital role in the performance of the cell [7, 8].

Catalyst layer: this is where the HOR and ORR occur. The most widely used catalyst for both the anode and the cathode is Pt in the form of nanoparticles of metal supported on larger particles of carbon. The small size and distribution of the nanoparticles help to increase the surface area to mass ratio (specific surface area) and thus the utilization of the platinum. The catalyst is made into an ink along with an ionomer solution of the same type as the membrane electrolyte, acting as both a binder and as a pathway for protons to travel from the membrane to the triple phase boundary [9] (Figure 1.2). This helps to give good ionic and physical contact with the membrane and maximise the amount of catalyst particles that are available for reaction [10]. The catalyst ink is usually painted, sprayed or printed onto either the GDL or the membrane, in the case of the former producing an electrode.

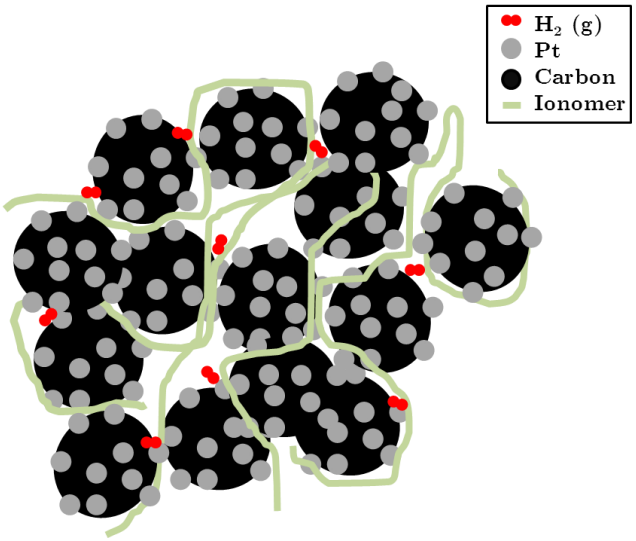

Figure 1.2 The triple phase boundary at the anode, consisting of the catalyst (Pt nanoparticles supported on carbon particles), ionomer binder and hydrogen molecules.

Membrane: The polymer membrane is the electrolyte in PEM fuel cells. It serves to conduct protons from the anode to the cathode, as an electrical insulating layer isolating the anode from the cathode and as an impermeable layer stopping the two gases mixing. The most widely used membrane is Nafion and is based on a polytetrafluoroethylene (PTFE) backbone with a side chain containing a sulphonic acid group (see Figure 1.3). It is this hydrophilic group that allows the transfer of protons. As the membrane absorbs water, proton conduction channels form, giving increased conductivity with increasing water content, up until a point where the concentration of the protons is diluted [11]. For this reason, both the gas streams are usually humidified to maintain the water content of the membrane and thus the ionic conductivity [12-14]. Nafion has become an industry standard thanks to its thermal and chemical stability and excellent conduction properties. Thicker membranes can give higher ionic resistivity, but offer better mechanical strength and reduced fuel crossover (see Section 1.4.4).

The GDL, catalyst layer and membrane are all hotpressed, together under pressure and heat, to form the membrane electrode assembly (MEA) which can be considered as the essence of the fuel cell. Other peripherals such as pumps, humidifiers, fans, heaters and flow regulators also play their role in a functioning fuel cell system, but this thesis will be concerned main-

ly with the MEA, and specifically the catalyst layer as a method of cost reduction and/or performance improvement of fuel cells.

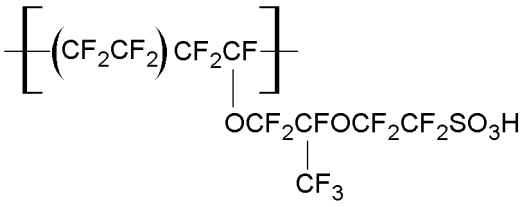

Figure 1.3 The structure of Nafion polymer membrane [15].

1.3 Fuel Cell Thermodynamics

The capacity of a fuel cell to do work is governed by the thermodynamics of the overall reaction of the fuel cell (Equation 1.3). The enthalpy change (ΔH) of this reaction is given by the difference in the heat of formation of the products and the reactants and represents the maximum amount of thermal energy that it is possible to extract from hydrogen, by reaction with oxygen. At standard temperature and pressure (STP, 298 K and 1 atm) the value for hydrogen is 286 kJmol^{-1} [16].

In reality it is not possible to extract all this energy in a useful manner such as that of the direct electrochemical reaction in a fuel cell. Due to entropy changes during a reaction (ΔS), the maximum electrical energy extractable is given by the Gibbs free energy of the reaction:

$$\Delta G = \Delta H - T\Delta S \qquad \text{Equation 1.4}$$

At STP the Gibbs free energy change for the reaction of hydrogen and oxygen is 237.34 kJmol^{-1}. This represents the maximum amount of the enthalpy that can be converted into electrical energy, with the difference being 'wasted' heat.

1.3.1 Theoretical Fuel Cell Potential

The electrical work can be thought of as the work required to move a charge q through a potential E:

$$W = qE \qquad \text{Equation 1.5}$$

The charge created when one mole of H_2 reacts in a fuel cell is given by:

$$q = nF \qquad \text{Equation 1.6}$$

Where n is the number of electrons produced per mole of H_2 (two) and F is Faraday's constant. As the maximum electrical work is equivalent to the Gibbs free energy change of the reaction, we get:

$$E = \frac{-\Delta G}{nF} \qquad \text{Equation 1.7}$$

Equation 1.7 at STP yields a maximum theoretical voltage of +1.229 V for the H_2/O_2 fuel cell (if all the enthalpy were available for electrical work the voltage would be 1.482 V). From this we can calculate a maximum theoretical efficiency of a fuel cell as the ratio of the Gibbs free energy change and the enthalpy change of the reaction, $\Delta G/\Delta H$, giving a value of 83%.

1.3.2 Effect of Temperature

Substituting Equation 1.4 into Equation 1.7 we can see that the cell potential will decrease with increasing temperature (at the low temperatures experienced in PEM fuel cells the change in ΔH and ΔS with temperature is negligible). This reduction in theoretical cell potential will obviously manifest itself as a reduction in efficiency of the fuel cell.

1.3.3 Effect of Pressure

From fundamental thermodynamics the change in Gibbs free energy is:

$$\mathrm{d}G = -S\mathrm{d}T + V\mathrm{d}P \qquad \text{Equation 1.8}$$

For an isothermal process ($\mathrm{d}T = 0$) and an ideal gas ($PV = nRT$), Equation 1.8 after integration becomes:

$$G = G_0 + RTln\left(\frac{P}{P_0}\right) \qquad \text{Equation 1.9}$$

Where G_0 is the Gibbs free energy at STP, R is the molar gas constant and P_0 is the standard pressure of 1 atm. For a general chemical equation of the form $a\mathrm{A}+b\mathrm{B}\rightarrow c\mathrm{C}+d\mathrm{D}$ Equation 1.9 becomes:

$$\Delta G = \Delta G_0 + RTln\left[\frac{\left(\frac{P_C}{P_0}\right)^c\left(\frac{P_D}{P_0}\right)^d}{\left(\frac{P_A}{P_0}\right)^a\left(\frac{P_B}{P_0}\right)^b}\right] \qquad \text{Equation 1.10}$$

Recognising that $\frac{P_X}{P_0}$ is the partial pressure of substance x, substituting in Equation 1.7 and applying to the reaction of hydrogen and oxygen in a fuel cell (Equation 1.3) we get the equation:

$$E = E_0 - \frac{RT}{nF} \ln \left[\frac{P_{H_2} P_{O_2}^{0.5}}{P_{H_2O}} \right] \qquad \text{Equation 1.11}$$

Equation 1.11 is known as the Nernst equation and is one of the most important equations in electrochemistry. It shows an increase in operating pressure of the cell will increase the cell potential, and for this reason back-pressure is sometimes used in fuel cell operation [17].

1.4 Fuel Cell Polarisation Losses

The ideal thermodynamics discussed above apply only at equilibrium, i.e. when the fuel cell is producing zero net current. Naturally, this is not a useful state for the fuel cell to be in as it produces zero power. As more current is drawn from the fuel cell its potential deviates from its ideal thermodynamic open circuit voltage (OCV) due to irreversible voltage losses incurred in operation. As discussed in section 1.3.1, a decrease in potential will give a reduction in efficiency but it is a price that must be paid to operate the device at a useful current density. Minimising these voltage losses, or overpotentials (η), is vital for a high performance fuel cell and is the crux of most fuel cell optimization work. The losses can be categorized into 4 main types:

1. Activation Losses
2. Ohmic Losses
3. Concentration Losses
4. Open Circuit Losses

1.4.1 Activation Losses

The activation or kinetic overpotential stems from the energy barrier that must be surmounted in order for reaction to occur at the electrode, i.e. the activation energy (E_A). All electrochemical reactions involve charged species whose free energy is related to voltage and thus can be manipulated by changing the cell voltage, in turn changing the energy of the reaction barrier. In this way the potential of the cathode and anode can be sacrificed to overcome the activation energy and produce current from the fuel cell.

The cathode polarisation is negative, reducing from the reversible voltage of 1.229 V *vs* the standard hydrogen electrode (SHE) and promoting reduction, and the anode polarisation is positive, increasing from 0.000 vs SHE to promote oxidation, with the overall result of reducing the cell potential as an increasing function of current. Taken to the extreme, there is eventually a current reached where the difference between the cathode and anode potentials is zero and no more current can be drawn. This is known as the limiting current, i_{limit}.

1.4.1.1. Influence of the Charge Double Layer

Electrochemical reactions must occur at the electrode interface for the reason that, in the case of the HOR, $H_{2(g)}$ and H^+ ions cannot exist within the electrode and electrons cannot exist in the electrolyte. Thus, there must be a region (the triple phase boundary) where the electrode, electrolyte and reactant meet, allowing the products to form and exist in their respective media. Again taking the HOR as an example, the free energy of the reactant state (hydrogen atoms adsorbed to the catalyst, M---H) is higher than that of the products (an electron and H^+). This has the effect of giving unequal reaction barriers for the forward and reverse reactions of the HOR, meaning the forward reaction proceeds faster than the reverse, resulting in a build-up of charge – negative electrons accumulating in the metal catalyst and positive protons accumulating in the electrolyte. This is called the charge double layer and results in a potential difference at the interface. The charge will continue to accumulate until this potential difference exactly counters the difference in free energies of the products and reactants, resulting in electrochemical equilibrium (Figure 1.4) [18]. An alternative view is to imagine the interface potential as equalising the free energy potential of the products to that of the reactants and giving a symmetrical activation barrier and thus equally fast forward and reverse reactions.

At this dynamic equilibrium there is no net current flowing, so in order to generate a useful current (or charge transfer rate) the forward, electron producing reaction must once again be more favoured than the reverse reaction. To do this the situation must be forced from the equalised potential created by the charge double layer to a state where the potential of the products is lower than that of the reactants. This is achieved by sacrificing some of the electrode potential to drive a potential difference between the reactants and products, and hence a current. This is the source of the acti-

vation overpotential (η_{act}); the voltage sacrificed to overcome the equalising effect of the charge double layer and induce net charge transfer from a state of dynamic equilibrium [19].

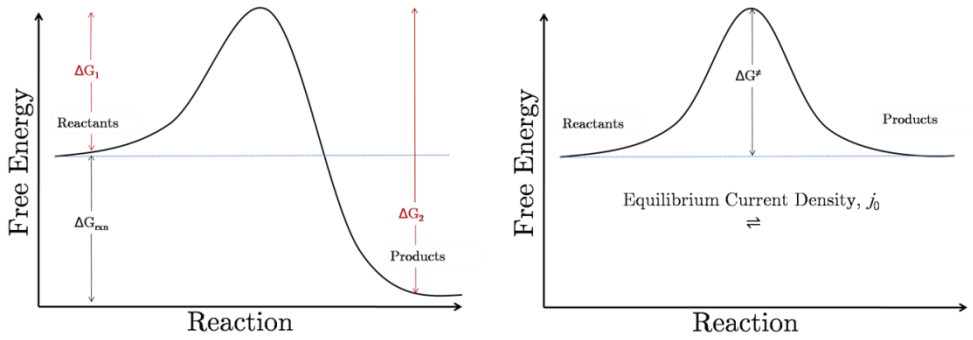

Figure 1.4 Activation energies for reaction. Left: the products have lower free energy than the reactants and the forward reaction is favoured. Right: on the build-up of the charge double layer the potential is equalised and results in electrochemical equilibrium.

1.4.1.2. Equilibrium Kinetics

The HOR and ORR reactions occurring at the electrodes of fuel cells are linked only through the conservation of charge; the electrons and protons produced at the anode must be consumed at the cathode. Though the current is therefore identical at both electrodes, the activation polarisation required to generate this current for each reaction is not. As current is a rate of charge, and electrons are produced and consumed in electrochemical half reactions, the current is a direct measure of the rate of an electrochemical reaction. If reaction of one mole of reactant yields n moles of electrons, the current, i, is given by:

$$i = nF\frac{\mathrm{d}N}{\mathrm{d}t} \qquad \text{Equation 1.12}$$

Where $\frac{\mathrm{d}N}{\mathrm{d}t}$ is the rate of reaction in mol s^{-1}. As these reactions occur at interfaces, the current is generally normalised to area (A) such that $j = \frac{i}{A}$ and the reaction rate per unit area is v, where j is called the current density (this also helps in comparison between different fuel cells of different geometric areas). Rearranging Equation 1.12 for rate we get:

$$v = \frac{j}{nF} \qquad \text{Equation 1.13}$$

Reaction rate is a product of the surface concentration and a reaction rate constant, such that:

$$\nu_1 = C_\mathrm{r} k_1 \qquad \text{Equation 1.14}$$

From statistical mechanics it can also be shown that the rate constant is a function of the Gibbs free energy of the transition state because the reactants must be in the transition state in order to have a probability of reacting. This rate constant is given by the Eyring equation [20]:

$$k_1 = \frac{k_\mathrm{B} T}{h} e^{-\left(\frac{\Delta G_1}{RT}\right)} \qquad \text{Equation 1.15}$$

Where, k_B is Boltzman's constant, T is temperature (in Kelvin), h is Plank's constant, R is the molar gas constant and ΔG_1 is the activation energy for the forward reaction given by the difference in free energy between the reactants' free energy and the transition state free energy, as in Figure 1.4.

However, ν_1 is just the rate of the forward reaction of the electrochemical half reaction. The rate of the reverse reaction, ν_2, is given by substituting ΔG_1 for ΔG_2, the difference in free energy between the products and the activation energy. Then, the overall reaction rate ν is given by $\nu_1 - \nu_2$ and therefore the net current is:

$$j = nF(\nu_1 - \nu_2) \qquad \text{Equation 1.16}$$

At equilibrium, the rate of the forward reaction and reverse reaction are equal and j, the overall current density is 0. However, j is composed of the forward current density, $j_1 = nF\nu_1$, and the reverse current density, $j_2 = nF\nu_2$, which at equilibrium are both equal to what is known as the exchange current density, j_0. From Figure 1.4 right, at equilibrium both the forward and reverse reactions have the same activation energy, $\Delta G^{\neq}$. Thus the exchange current density is given by:

$$j_0 = nFC_r f e^{-\left(\frac{\Delta G^{\neq}}{\mathrm{RT}}\right)} \qquad \text{Equation 1.17}$$

Where the pre-exponential term of Equation 1.15 has been compressed to f. The forward and reverse activation energies, $\Delta G^{\neq}$, are the same in this example by virtue of the transition state being symmetrical. This is not always the case however and so a symmetry factor, β, is used for the general case. β is a measure of the asymmetry of a transition state in that it measures the fraction of a change in potential of the electrode that pro-

motes the forward reaction. β takes a value between 0 and 1 and the fraction of the potential that would promote the reverse reaction is given by $(1-\beta)$. If, as in Figure 1.4, the transition state is symmetrical, then β is 0.5 and the forward and reverse reactions are promoted equally by an increase in electrode potential. This is the case with most catalysts as they promote the oxidation and reduction directions of a half reaction equally by lowering the activation energy (due to a lowering of the transition state). So it is a reasonably safe assumption that β is 0.5, except that this applies to only a single electron transfer reaction. If there are multiple and sequential electron transfer reactions in a mechanism, β may still be 0.5 if one step is significantly slower and thus the rate determining step; however, this is not always the case. Because of this, β is often replaced by an experimental parameter called the charge transfer coefficient, α, which does not necessarily sum to 1 for the forward and reverse coefficients, unlike for the symmetry factor β. For this reason, the experimental value αn is often quoted instead of α [21].

Substituting Equation 1.7 and the charge transfer coefficient into the exchange current density we get:

$$j_0 = nFC_r f_1 e^{\left(\frac{\alpha_1 nFE_0}{RT}\right)} = nFC_p f_2 e^{\left(\frac{-\alpha_2 nFE_0}{RT}\right)} \qquad \text{Equation 1.18}$$

Where α_1 and α_2 are the charge transfer coefficients for the forward and reverse reactions respectively and E_0 is the reversible equilibrium potential for the given half reaction. By rearranging Equation 1.18 and taking the natural logarithm it is shown that:

$$E_0 = \frac{RT}{nF}\ln\left(\frac{f_1}{f_2}\right) - \frac{RT}{nF}\ln\left(\frac{C_\mathrm{r}}{C_\mathrm{p}}\right) \qquad \text{Equation 1.19}$$

Which is the Nernst equation. This is expected as any kinetic theory should reduce to a thermodynamic one when at equilibrium [16, 22, 23].

1.4.1.3. Butler-Volmer Kinetics

As shown in Section 1.4.1.1, the activation overpotential can be used to control the direction and rate of reaction away from equilibrium. If we con-

sider applying an overpotential of η to an electrochemical half reaction such that the resulting potential is:

$$E = \eta + E_0 \qquad \text{Equation 1.20}$$

And the overall net current density is:

$$j = j_1 - j_2 = nFC_r f_1 e^{\left(\frac{\alpha_1 nF(\eta+E_0)}{RT}\right)} - nFC_p f_2 e^{\left(\frac{-\alpha_2 nF(\eta+E_0)}{RT}\right)} \qquad \text{Equation 1.21}$$

And from Equation 1.18 we can see our two definitions of exchange current density occur in Equation 1.21, meaning it simplifies to yield:

$$j = j_0 \left[e^{\left(\frac{\alpha_1 nF\eta}{RT}\right)} - e^{\left(\frac{-\alpha_2 nF\eta}{RT}\right)} \right] \qquad \text{Equation 1.22}$$

This is the Butler-Volmer (B-V) equation and is widely used to model fuel cell reactions. It should be noted that all of the above derivations refer to just one half reaction at just one of the electrodes and the B-V equation should be applied to each electrode individually. The HOR at the anode and the ORR at the cathode will have different exchange current densities, charge transfer coefficients and activation overpotentials, but are linked through the conservation of charge meaning that the total cell current is the same as the cathode current and the same as the anode current; $i_{cell} = i_c = i_a$. Because of this we can equate the two B-V equations at each electrode:

$$j_{0,a} \left[e^{\left(\frac{\alpha_{1,a} nF\eta_a}{RT}\right)} - e^{\left(\frac{-\alpha_{2,a} nF\eta_a}{RT}\right)} \right] = j_{0,c} \left[e^{\left(\frac{\alpha_{1,c} nF\eta_c}{RT}\right)} - e^{\left(\frac{-\alpha_{2,c} nF\eta_c}{RT}\right)} \right] \qquad \text{Equation 1.23}$$

In this way the overpotential of the cathode and anode will adjust to drive the desired current density from the fuel cell, with the negative polarisation of the cathode and the positive polarisation of the anode sacrificing more and more of the reversible potential of the cell until no more is left and the limiting current is reached.

1.4.1.4. Exchange Current Density

The exchange current density is an extremely important parameter that has a dominating influence on the kinetics of electrochemical reactions (see Fig-

ure 1.9). It reflects the rate of charge transfer, and thus a high j_0 is desired for facile electrode kinetics and therefore minimised activation potential losses. The definition of exchange current density given in Equation 1.18 is a rather simplistic one given that it doest not account for changes in the reactant and product concentrations during reaction, and doest not explicitly show the effect of temperature on j_0. The surface area and loading of the catalyst can also be accounted for to give a definition of j_0 as follows [18]:

$$j_o = j_0^0 a \left(\frac{C_\mathrm{r}}{C_\mathrm{r}^0}\right) e^{\left[-\frac{E_0}{RT}\left(1-\frac{T}{T_0}\right)\right]} \qquad \text{Equation 1.24}$$

Where j_0^0 is a reference exchange current density measured at a reference temperature, T_0, and a reference concentration, C_r^0. The parameter a is a roughness factor given as the ratio between the actual electrochemical surface area of the catalyst and the geometric surface area of the electrode. From Equation 1.24 we can see that the exchange current density is an exponentially increasing function of temperature, and though the B-V Equation 1.22 suggests ostensibly that there should be higher activation losses with higher temperature, in fact the effect of increasing temperature is to greatly increase j_0 and so significantly decrease kinetic losses, in a highly non-linear way. Thus, fuel cells operating at higher temperatures will tend to have greatly reduced activation losses.

Though the exchange current density is not an intrinsic property of the catalyst, it is strongly related to the catalyst type. Increasing the j_0 of a catalyst/reaction is highly desirable for good fuel cell performance and can be achieved in the following ways:

Increase the reactant concentration

Decrease the activation energy, E_0

Increase the temperature

Increase the roughness factor, a

Increasing the reactant concentration has a minor effect on the thermodynamics of the reaction (due to the logarithmic form of the Nernst equation) but can have a significant benefit on the rate of a reaction (linear). For this reason, fuel cells are often operated on pure oxygen as the partial pressure of oxygen in air is only 0.2, and so the exchange current density is reduced when operating with air.

Decreasing the activation energy represents the catalyst's influence on j_0. The catalyst can do this by offering a favourable surface for reaction and stabilising the transition state, giving a lower activation barrier. The strength of bonds between the catalyst and the adsorbed species is an important consideration when looking for a suitable catalyst. The bond strength needs to be 'just right', in that it has enough strength to hold the reactant species to the catalyst in the first place, giving greater chance of reaction, but not so strong that it is difficult to break and form products, which would mean lots of immovable adsorbed reactant and a reduction in the number of available sites for reaction. This concept, known as the Sabatier principle, is often illustrated by a so called volcano plot, with platinum group metals generally having the optimum intermediate strength bonds (Figure 1.5).

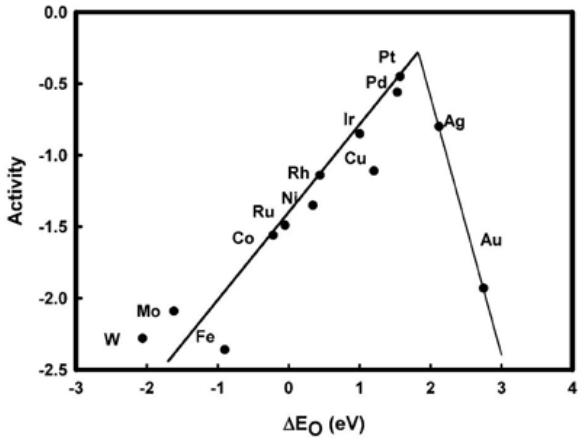

Figure 1.5 Volcano plot of activity of various transition metals for the ORR as a function of binding energy of the O atom to the catalyst. From [24].

A more sophisticated treatment of the Sabatier principle comes from d-band theory. As already outlined, the binding energy of an absorbed species is highly dependent on the electronic structure of the surface itself [25]. In the case of hydrogen and platinum, the interaction can be considered in two stages; first, the coupling of the H 1s state with the Pt 6s state creates a low-energy filled bonding orbital and a high-energy empty antibonding orbital. The coupling of these s-states is essentially invariable across the transition metals, giving roughly the same degree of attractive interaction for Pt as, say, Fe. However, this bonding orbital then interacts with the d-states of the metal, stabilising the bonding orbital further (d-σ) but also creating

an additional antibonding orbital just above the d-states (d-σ)* [26, 27] (see Figure 1.6).

The extent of the filling of the antibonding state depends on the surface density of states of the metal, which can vary from metal to metal and also be affected by alloying of metals or metal-substrate interactions (see Section 2.2.1). The metal-adsorbate interaction can be destabilised by increasing the filling of the antibonding state, and vice versa, and the filling of this state is inversely correlated with the position of the d-band centre relative to the Fermi level. That is, a higher d-band centre gives an increase in energy, relative to the Fermi level, and thus a decrease in filling of the (d-σ)* state and so a stronger bond [28]. For the example of Pt catalysing the ORR, Pt has a too-strong interaction with oxygen and so lowering the d-band centre (filling the antibonding state to a greater extent) by, for example, alloying can help to weaken the interaction and thus improve the activity of the catalyst towards the ORR [29]. Advances in density functional theory have led to the pre-screening and theoretical design of potential catalysts and good agreement between theory and experiment is regularly achieved [30].

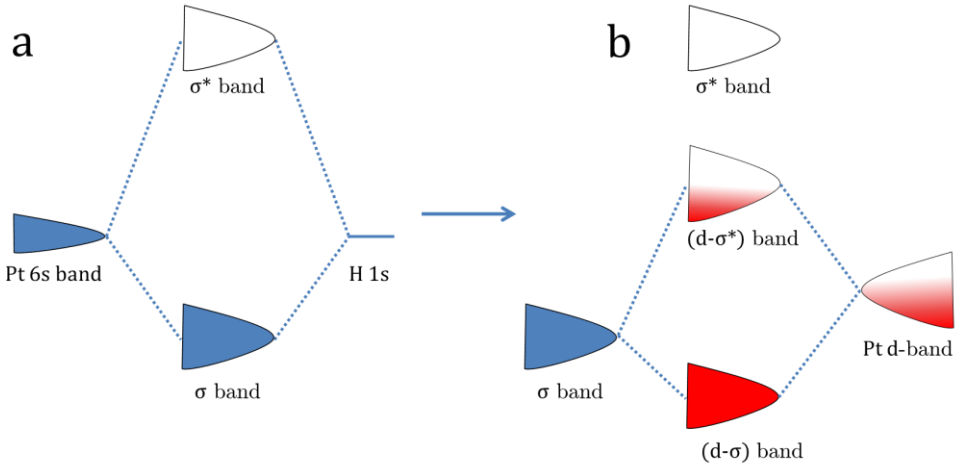

Figure 1.6 Simplified schematic of the d-band theory applied to a hydrogen adsorbate on a metallic platinum surface. In which (a) the Pt 6s band couples with the H 1s orbital, forming broadened bonding and antibonding bands, and (b) subsequent coupling of the bonding band to the Pt d-band forms a more stabilised bonding band (d-σ) and a partially filled antibonding band (d-σ)*.

In general, the activation energy is also affected by the complexity of the reaction, with more complex mechanisms incurring much greater activation losses than for more simplistic ones. For this reason the ORR is much

slower than the very facile HOR and usually contributes the majority of the activation losses in an acidic PEM fuel cell (Figure 1.7).

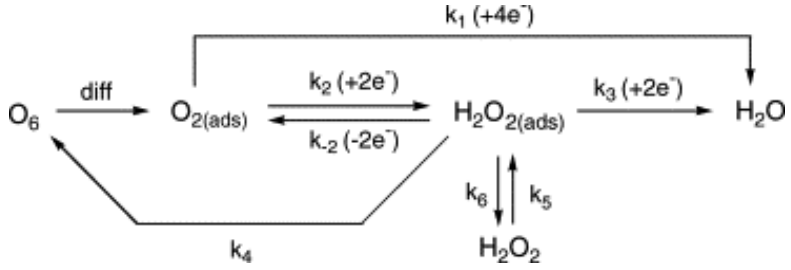

Figure 1.7 The possible reaction mechanistic pathways for oxygen reduction. The direct 4 electron pathway (k_1) is desired as it is more efficient and does not generate the potentially damaging peroxide intermediate. Reproduced from [31]

The HOR in acid solution is considered to proceed through either the Tafel-Volmer or Heyrovsky-Volmer mechanisms, depending on the nature of the adsorption step. If it is a purely chemical process the mechanism is Tafel-Volmer and if it is a combined chemical and electrochemical process it is Heyrovsky-Volmer [32].

$$H_2 + M_{cat} \rightleftharpoons 2M_{cat}H_{chem} \text{ (Tafel)} \qquad \text{Equation 1.25}$$

$$M_{cat}H_{chem} \rightleftharpoons M_{cat} + H^+ + e^- \text{ (Volmer)} \qquad \text{Equation 1.26}$$

$$H_2 + M_{cat} \rightleftharpoons M_{cat}H_{chem} + H^+ + e^- \text{ (Heyrovsky)} \qquad \text{Equation 1.27}$$

As already discussed, increasing the temperature will increase the exchange current density. The physical reason for this is that a higher proportion of the reactant molecules will have sufficient energy to react to give products.

Increasing the roughness factor, a, is the equivalent of increasing the electrochemical surface area of the catalyst, i.e. increasing the number of surface sites available for reaction. This will obviously increase the exchange current density as more reactions can take place per second. Roughness factors for carbon supported platinum electrodes (a widely used fuel cell catalyst) vary between 600 and 2000 [33].

1.4.1.5. Butler-Volmer Simplifications: Linear

The B-V equation, though a very good model for electrode kinetics, is not explicit for the overpotential, η. Solving the equation for overpotential is useful as it models the activation voltage loss one might expect for a given current density of a fuel cell. In order to express the B-V in terms of η, some simplifications and assumptions need to be made. The first such simplification can be made in the low polarisation region for facile kinetics.

This occurs when the exchange current density is very high and there is little current being drawn. Substituting $x = \frac{\alpha_i nF\eta}{RT}$ into the B-V Equation 1.22 and expanding e^x as a power series, excluding the higher order terms we can approximate e^x as $1 + x$, giving:

$$j = j_o \left[\left(\frac{\alpha_1 nF\eta}{RT} + 1 \right) - \left(\frac{-\alpha_2 nF\eta}{RT} + 1 \right) \right] \qquad \text{Equation 1.28}$$

Rearranging for η gives:

$$\eta = \frac{j}{j_0} \frac{RT}{(\alpha_1 + \alpha_2)nF} \qquad \text{Equation 1.29}$$

This is known as the low field approximation and is only applicable at low polarisation and with high j_o such as in the case of high temperature and/or very facile kinetics. Mench estimates that the linear approximation is only valid for $x = \frac{\alpha_i nF\eta}{RT} < 0.15$ [19].

1.4.1.6. Butler-Volmer Simplifications: Tafel

At higher polarisation or smaller j_0 the Tafel approximation of the B-V equation can be made. For high η, one of the two exponential terms in the B-V will be diminishingly small and can be ignored, leaving the Tafel model for electrode kinetics:

$$\eta = \pm \frac{RT}{\alpha_i nF} \ln\left(\frac{j}{j_0}\right) \qquad \text{Equation 1.30}$$

Which branch of the B-V diminishes depends on the sign of the polarisation, with the polarisation at the anode being positive and the cathode being negative. Equation 1.30 is known as the high field approximation. Tafel kinetics are applicable to practically all situations in fuel cells, except for very facile HOR at high temperature. There is an underestimation of the activation losses with low polarisation when using the Tafel approximation, but Mench estimates that it is applicable once $x = \frac{\alpha_i nF\eta}{RT} > 1.2$ [19]. Tafel initially proposed this relationship due to experimental results where he ob-

served the following relationship between overpotential and current density [34]:

$$\eta = a + b \ln j \qquad \text{Equation 1.31}$$

Where $a = \frac{RT}{\alpha_i nF} \ln j_0$ and $b = -\frac{RT}{\alpha_i nF}$. By plotting overpotential *vs* the log of the current density, a straight line known as a Tafel Plot is obtained with a Tafel slope of b and an intercept of a. Thus, from the slope and the intercept of this plot the charge transfer coefficient and the exchange current density can be determined. This is a vital tool for assessing the electrochemical activity of catalysts (see section 5.1.3.3).

1.4.1.7. Butler-Volmer Simplifications: Sinh Approximation

If the forward and reverse transfer coefficients are equivalent ($\alpha_1 = \alpha_2$) the B-V equation can be expressed in terms of η with no approximation needed due to the mathematical relationship:

$$\sinh(x) = \frac{1}{2}(e^x - e^{-x}) \qquad \text{Equation 1.32}$$

Where $x = \frac{\alpha nF}{RT}\eta$. The B-V equation therefore becomes:

$$j = 2j_0 \sinh\left(\frac{\alpha nF}{RT}\eta\right) \qquad \text{Equation 1.33}$$

And expressed for η:

$$\eta = \frac{RT}{\alpha nF} \sinh^{-1}\left(\frac{j}{2j_0}\right) \qquad \text{Equation 1.34}$$

This applies across the whole polarisation range and for any value of j_0, provided the charge transfer coefficients of the forward and reverse reactions are equal. Using the sinh approximation the effect of the activation overpotential on the cell voltage can be modelled as in Figure 1.8, showing that the activation potential has a dramatic effect on cell voltage at low current densities with the influence tailing off at higher current densities. Though the kinetic losses are present across the whole range of the fuel

cell's operating current, they are dominant at low current density and so this region is known as the kinetic or activation region. The strong effect that j_0 has on the overpotential is shown in Figure 1.9. It should be noted that j_0 is entered as a constant value in this model and not as described in Equation 1.24. It is obvious that achieving as high a j_0 as possible is paramount to good fuel cell performance, as it is the major contributor to the initial losses at low current density and so sets the starting point for the best possible performance expected at operating current densities (around 1 Acm^{-2}).

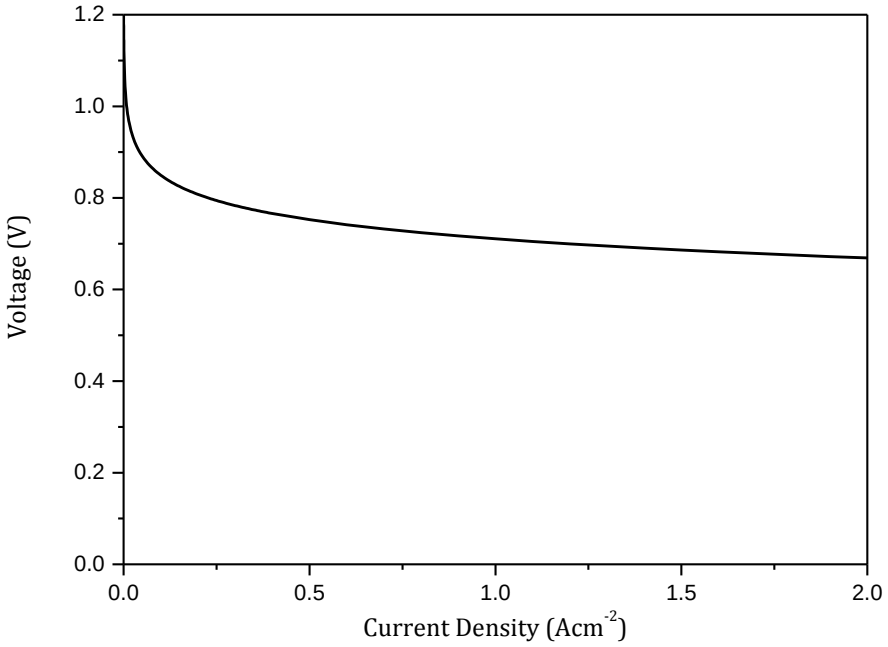

Figure 1.8 The effect of activation overpotential on the cell voltage with current density. Modelled using Equation 1.34 and subtracting the resulting overpotential from an initial voltage of 1.2 V, a current density j_0 of 3×10^{-4} A cm^{-2}, α=0.5 and a temperature of 350 K.

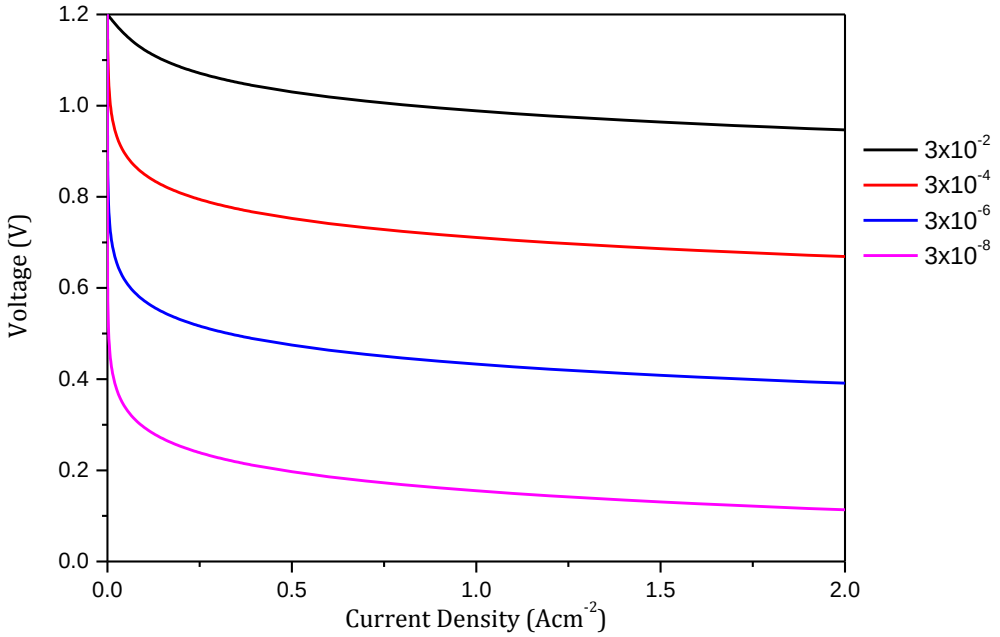

Figure 1.9 The effect of j_0 on activation overpotential. Modelled using the same parameters as in Figure 1.8 with j_0 values of 3×10^{-2} (black), 3×10^{-4} (red), 3×10^{-6} (blue) and 3×10^{-8} (pink) A cm^{-2}.

1.4.2 Ohmic Losses

Ohmic losses are incurred due to the electronic and ionic resistance of the fuel cell.

$$\eta_{\text{ohm}} = jR_i \qquad \text{Equation 1.35}$$

Where R_i is the total internal area-specific resistance of the cell, made up from the ionic resistance of the membrane, the electronic resistances and contact resistances. Of these the membrane resistance contributes the most to these losses and so a well-hydrated and conductive membrane is vital in minimising the ohmic overpotential [12]. Thinner membranes also produce lower resistances, as might be expected, though Slade et al. found that the situation is slightly more complicated when corrected for membrane thickness, with thinner Nafion membranes showing relatively higher resistance, probably due to the difference between the skin and bulk properties of the membranes [35].

1.4.3 Concentration Losses

Concentration losses occur when there is a lack of reactant to provide the current density required. As the reaction occurs in the catalyst layer, at the surface of the catalyst, we can differentiate the surface concentration of reactants from that of the bulk and use the Nernst equation to predict the overpotential incurred from this concentration gradient:

$$\eta = \frac{RT}{nF}\ln\left(\frac{C_{\mathrm{r,b}}}{C_{\mathrm{r,s}}}\right) \qquad \text{Equation 1.36}$$

Where $C_{\mathrm{r,b}}$ and $C_{\mathrm{r,s}}$ are the concentration of the reactants in the bulk and at the catalyst surface, respectively. The steady state diffusion current density is given by:

$$j = -\frac{nFD\left(C_{\mathrm{r,b}} - C_{\mathrm{r,s}}\right)}{\delta} \qquad \text{Equation 1.37}$$

Where D is the diffusion coefficient of the reactant and δ is the diffusion distance (electrode thickness) [36]. When the operating current of the fuel cell is such that the reactant is being consumed as soon as it reaches the catalyst layer, the current is said to be mass transport limited. The current is limited by the rate that the reactant diffuses from the bulk to the electrode layer, which effectively means that the concentration at the catalyst surface is 0 ($C_{\mathrm{r,s}} = 0$). Thus we obtain an expression for the mass transport or diffusion limiting current value of:

$$j_L = -\frac{nFDC_{\mathrm{r,b}}}{\delta} \qquad \text{Equation 1.38}$$

Combining Equation 1.36, Equation 1.37 and Equation 1.38 we get an expression for the concentration overpotential in terms of the limiting current value:

$$\eta = \frac{RT}{nF}\ln\left(\frac{j_{\mathrm{L}}}{j_{\mathrm{L}} - j}\right) \qquad \text{Equation 1.39}$$

The concentration overpotential has little effect on the fuel cell performance until high current densities are reached and $j_{\mathrm{cell}} \to j_{\mathrm{L}}$. Because the catalyst is mainly influential in the activation losses of a fuel cell, this high current

density is generally not of interest to catalyst development researchers (though the diffusion properties of the catalyst layer play a large role in the limiting current value) and so the relative performance of various catalysts in fuel cells tends to be judged at lower operating currents, safely away from the mass transport limiting regime. A more detailed account of concentration overpotential can be found here [37].

1.4.4 Open Circuit Losses

The voltage losses described so far have been functions of the operating current of the fuel cell, but there are also losses incurred from the theoretical maximum OCV expected at zero current density. As shown in section 1.3.1, due to entropic effects we already lose operating voltage from the full enthalpy of formation value of hydrogen, and the OCV is further reduced by operating at a higher temperature than that of STP. However, these losses still do not account for the experimentally observed OCVs of most fuel cells. There are two further effects that serve to deprive the fuel cell of open circuit voltage, and thus reduce the starting maximum point for the operation of the cell; the mixed potential and fuel crossover currents.

1.4.4.1. Mixed Potential

As well as the HOR and ORR, there is the possibility of corrosion half reactions occurring at the electrodes of the fuel cell. The oxidation of the carbon support ($E^0 = 0.21$ V) and the Pt catalyst ($E^0 = 0.88$ V) counter the reduction potential of the ORR at the cathode and affect a reduction in the E^0 value of 1.229 V (the magnitude depending on the extent of oxidation) to give a mixed potential of a lower value than that of the thermodynamically predicted one [38-40]. This effect is not fully understood in the literature.

1.4.4.2. H_2 Crossover

Although the membrane electrolyte acts as an impermeable gas separator in theory, in practice they often allow some crossover of fuel to the cathode where it can react with oxygen as in Equation 1.3. In a similar way to the mixed potential, this has the effect of reducing the OCV and can be modelled as a Tafel approximation of the B-V equation as follows:

$$\eta_{C.O.} = \frac{RT}{\alpha n F} \ln\left(\frac{j_{\text{C.O.}}}{j_0}\right) \qquad \text{Equation 1.40}$$

Where $j_{\text{C.O.}}$ is the H_2 crossover exchange current density. One can imagine a smaller side electrochemical reaction formed of the H_2/O_2 couple occurring (just as it does in the operating fuel cell) on just one electrode, creating an internal shorting current of $j_{\text{C.O.}}$ on that electrode, even though there is no net current flowing through the cell *between* electrodes.

It should be noted that the terms α, n and j_0 refer to the ORR, as the overpotential due to the HOR is much smaller (especially as at the cathode the HOR is experiencing an effective polarisation of around 1.2 V due to the cathode potential, driving the HOR very hard) and can be neglected. There is also an O_2 crossover to the anode, though the flux through the membrane is lower than that of H_2. The overpotential due to this is low, however, as the ORR at the anode (0.00 V E^0) is again experiencing a high polarisation compared to its E^0 of 1.229 V and thus is being driven hard with minimal activation loss, and the HOR in acid has such facile kinetics that its activation loss is minimal. Vilekar and Datta modelled this crossover effect in detail and showed that the experimentally observed drop from expected OCV can be wholly attributed to the H_2 crossover overpotential at the cathode [41]. The losses due to crossover currents can cause the OCV to drop to as low as 0.9 V (with 0.95-1.05 V being typical [40]) and are exacerbated by membrane degradation that occurs over long-term fuel cell use.

In addition to internal crossover currents, electrical shorting of the system can occur through protrusion of the GDL fibres through the membrane or improper setup of the test cell, and for this reason the OCV of the system is often a very useful first indication of the health of an MEA.

1.4.5 The Fuel Cell Polarisation Curve

With all the various overpotentials and voltage losses accounted for, a description of how a fuel cell's voltage changes with current density can be formulated, resulting in a fuel cell polarisation (or 'polar') curve. The total cell voltage is given by:

$$E_{\text{cell}} = E_{\text{thermo}} - \eta_{\text{act}} - \eta_{\text{ohm}} - \eta_{\text{conc}} - \eta_{\text{OCV}} \qquad \text{Equation 1.41}$$

Where E_{thermo} is the thermodynamically predicted potential at given temperature and pressure and η_{act}, η_{ohm}, η_{conc} and η_{OCV} refer to the losses due to activation, ohmic resistance, mass transport and internal currents, respectively, as described in the previous sections. A typical polar curve is shown in Figure 1.10. It should be noted that although the curve can be roughly segregated into domains where each of the losses are most influential, losses that are a function of operating current (η_{act}, η_{ohm} and η_{conc}) have an influence across the full range of the polar curve.

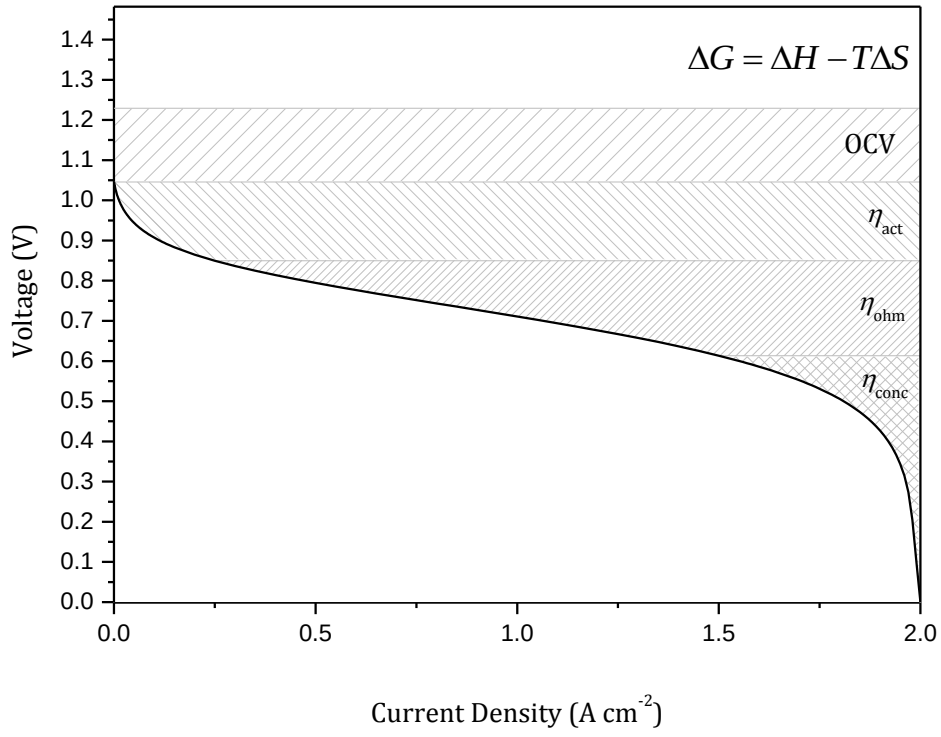

Figure 1.10 An example polar curve modelled from the preceding treatment of fuel cell behaviour. Showing regions where the decrease in voltage from the value given by the enthalpy of formation of H_2 have most influence; entropy, internal currents, kinetic losses, resistive losses and mass transport losses, respectively.

2 Alkaline Fuel Cells

Most of the discussion so far has pertained to acidic PEM fuel cells as they have been the main focus of low temperature fuel cell research for the last 20 years or so [5]. They have many advantages warranting this focus but also some disadvantages; one major one being the sluggish kinetics of the ORR in acid media. As the kinetics of the ORR are more facile in alkaline media [42-47], the alkaline fuel cell (AFC) is seen as a potential way to utilise cheaper, non-precious metal cathode catalysts such as Ag [48, 49], Au (both unstable in highly acidic media) [50] or Ni [51, 52], or to simply allow lower cathode loading of Pt.

2.1.1 The ORR Mechanism

The key step in reduction of oxygen at a catalytic surface is the breaking of the O-O bond which requires 4 coupled proton and electron transfers, opening up a possibility of many side reactions and products [43] (see Figure 1.7). The complexity of the ORR and its numerous potential side products means that it is still relatively poorly understood, though the consensus is that it proceeds either via a direct 4-electron reduction pathway, or via a peroxide intermediate in a 2+2 'serial' 4-electron pathway [53-55].

The direct 4-electron pathway (Equation 2.1) requires breaking of the O-O bond before the first electron transfer can occur (considered the rate determining step [49, 56]), and as the dissociation energy of O_2 is large, this is only energetically favourable with a strong Cat-O bond to repay the energy required to break the initial bond (and incurring a significant overpotential). The energetically favoured pathway is therefore the so-called serial 4-electron pathway (Equation 2.2 and Equation 2.3); a 2-electron reduction to peroxide, then a further 2-electron reduction of the peroxide to water (as the dislocation energies of the O_2^- and O_2^{2-} anions are lower than that of O_2) [48].

Studies by Markovic et al. suggested that the ORR on Pt surfaces in acid proceeds via the series pathway but that presence of adsorbed anions and underpotentially deposited hydrogen can prevent the second two electron reduction of peroxide from occurring properly, meaning a certain percentage of the reaction stops at the peroxide intermediate [57-59]. The effect of

strongly adsorbed anions is to reduce the number of adjacent Pt sites available for O_2 adsorption and O-O bond breaking [55] and manifests its self in the analysis as n being less than 4 (i.e., some percentage of reactant does not proceed fully to 4-electron reduction into water). These multiple steps and the possibility of desorption of peroxide intermediates mean that the ORR has poor kinetics, with only Pt and certain Pt alloys offering reasonable catalysis.

It is often stated in the literature that it is well known that the ORR kinetics are more facile in alkaline media [47, 60-63], but it is not fully explained why this might be the case and is often attributed to anion adsorption effects stemming from electrolyte choice and experiments in aqueous electrolytes [48, 64, 65]. As the polymer electrolytes employed in fuel cells do not have mobile anions, these sorts of fundamental ORR studies may not be so applicable to a working fuel cell environment [65], though Srinivasan suggests that the kinetics in AFCs are still faster than in acidic PEM fuel cells [66]. The morphology and type of Pt catalyst (single crystal, polycrystalline or Pt/C) can also have a large effect on the kinetics and reported exchange current densities for the ORR, [65, 67-70] with Pt bulk surfaces showing higher activity for ORR than Pt nanoparticles [71, 72]. Nevertheless, although some studies show a similar activity for Pt in acid and alkaline [73] and suggest that Pt or Pt/C are still the best catalysts for ORR in alkaline [74], there is potential for utilisation of cheaper cathode catalysts in alkaline fuel cells [42-46].

Blizanac et al. [48, 49] studied the pH effect of ORR on silver single crystals with a rotating ring disk electrode (RRDE – allowing the detection of intermediate species) and found that in alkaline electrolyte the ORR proceeds almost entirely through a 4-electron pathway, with very little peroxide intermediate detected. In contrast, acidic electrolyte required high overpotentials to prevent the 2-electron pathway (producing peroxide) from dominating, and the onset potential for the ORR was also higher than in alkaline. ORR on gold is also known to be significantly better in alkaline solution than acid, with the Au_{100} surface showing selectivity for the 4-electron pathway [75]. In alkaline the direct pathway is given by:

$$O_2 + 2H_2O + 4e^- \rightarrow 4OH^- \qquad \text{Equation 2.1}$$

And the serial pathway by:

$$O_2 + H_2O + 2e^- \rightarrow HO_2^- + OH^- \qquad \text{Equation 2.2}$$

Followed by:

$$HO_2^- + H_2O + 2e^- \rightarrow 3OH^- \qquad \text{Equation 2.3}$$

Carbon-supported catalysts (such as those employed in fuel cell electrodes) can show potentially very different behaviour for the ORR than that of the bulk metal. Yang et al. [76] showed that Pd/C catalysts in alkaline had high activity for ORR, and that the carbon support itself is active for the two electron reduction of O_2 to peroxide (which can then migrate to the Pd particles for subsequent 2-electron reduction to water). It is shown that all carbon materials have some ORR activity in alkaline solution (but none in acid), normally for the 2-electron reduction to peroxide, though some oxidised carbon surfaces can complete the serial reduction to water at higher overpotentials [62, 77-79].

Thus, the alkaline fuel cell is seen as a way to utilise much cheaper cathode catalysts and therefore reduce the cost of fuel cells for commercialisation.

2.1.2 The HOR in Alkaline

The kinetics of the hydrogen oxidation reaction in acidic PEM fuel cells above room temperature are often so fast that they contribute a negligible voltage to the overall activation overpotential, which is therefore often assumed to be wholly attributable to the ORR [80]. This allows catalyst loadings on the anode to be as low as 0.05 $mg_{Pt}cm^{-2}$ without affecting overall fuel cell performance significantly [81] and means catalyst development is mainly focused on the cathode. However, in alkaline media the HOR on polycrystalline Pt has been suggested to have an exchange current density two orders of magnitude lower than that in acid [82], and so the activation polarisation at the anode in alkaline fuel cells cannot be negated so easily [66]. In fact, in order to take advantage of the ability to use cheaper cathode catalysts in AFCs, anode HOR catalysis is a vitally important and oft-neglected area of required improvement [73, 83].

The mechanism of HOR is thought to follow a similar Tafel-Volmer or Heyrovsky-Volmer mechanism, as discussed in section 1.4.1.4, except with OH^- mediated reactions:

$$H_2 + M_{cat} \rightleftharpoons 2M_{cat}H_{chem} \text{ (Tafel)} \qquad \text{Equation 2.4}$$

$$M_{cat}H_{chem} + OH^- \rightleftharpoons M_{cat} + H_2O + e^- \text{ (Volmer)} \qquad \text{Equation 2.5}$$

$$H_2 + M_{cat} + OH^- \rightleftharpoons M_{cat}H_{chem} + H_2O + e^- \text{ (Heyrovsky)} \qquad \text{Equation 2.6}$$

Single crystal Pt studies of HOR in alkaline have suggested that the Tafel or Heyrovsky steps are rate-determining [84, 85]. There are said to be two states of adsorbed H atoms on electrode surfaces; a strongly bound underpotentially-deposited hydrogen, H_{UPD}, and the weakly adsorbed reactive intermediate, overpotentially adsorbed hydrogen H_{OPD} [86]. The reason for the slower HOR in alkaline has been attributed to the adsorption of OH species, which serves to block H_2 adsorption sites and hinder reaction [55, 84] and is even suggested to alter the energetics of the H_{OPD} layer [85].

Sheng et al. [73] recently compared the rotating disk electrode (RDE) studies of the HOR in acid and alkaline, and for carbon supported Pt (Pt/C) for the first time. RDE studies are used to separate the current into its kinetic and diffusion based constituents, as shown by the Koutecky-Levich equation:

$$\frac{1}{i} = \frac{1}{i_k} + \frac{1}{i_d} = \frac{1}{i_k} + \frac{1}{Bc_0\omega^{\frac{1}{2}}} \qquad \text{Equation 2.7}$$

Where B is a constant given by $0.62nFD^{2/3}\nu^{-1/6}$ in which D is the diffusion coefficient and ν is the kinematic viscosity of the electrolyte, c_0 is the bulk concentration of the reactant and ω is the rotation rate of the disk electrode rads^{-1}. In this way, varying the rotation rate of the electrode and plotting the inverse of the current vs $\omega^{-1/2}$ can give an intercept of the inverse of the kinetically controlled current, and therefore deconvolute the diffusion controlled and kinetically controlled currents from the overall current, giving valuable information about the kinetics of reaction (see section 5.1.4).

Sheng et al. [73] showed that for the HOR in acid, RDE experiments follow the diffusion current very closely (meaning essentially infinitely fast kinetics) even with high rotation rates (giving high diffusion limiting currents), meaning that the HOR in acid is too fast to study accurately with RDE and can lead to underestimation of the exchange current densities in literature [32]. On the other hand, the HOR in alkaline deviated significantly from the diffusion-only behaviour meaning that the kinetic currents can be elucidated properly in RDE experiments. These slower kinetics in alkaline were predicted to contribute significant anode overpotentials of around 130 mV if the ultra-low loading of Pt used on PEM anodes [81] is employed in AFCs, underlining the need for anode catalyst development in order to take advantage of potentially cheaper cathode catalysts in AFCs.

The only other studies of non-bulk metal HOR in alkaline come from Cabot et al. [63, 83] who used a Pt-containing gas diffusion electrode (GDE) to closely represent the electrodes of a fuel cell in their RDE experiments. They concluded that at low overpotentials (near the OCV) the Tafel reaction is the rate determining step in a Tafel-Volmer mechanism, with the diffusion of H_2 becoming rate determining at higher overpotentials. These studies also showed that the exchange current density for HOR is lower in alkaline media for GDE.

In conclusion, the kinetics of the ORR in alkaline give the advantage of cheaper cathode catalysts, but the significant overpotential for HOR requires anode catalyst development in order to fully utilise the potential of the alkaline fuel cell.

2.1.3 The Aqueous Electrolyte AFC

The superior ORR kinetics of the AFC meant that in the early days of fuel cell development it was the dominant technology, with the pioneering work of Bacon [87] and the use of AFCs in the Apollo space missions. The AFC employs an aqueous KOH electrolyte, usually around a $30\%_{wt}$ solution, often contained in a matrix (Figure 2.1). As with other H_2/O_2 fuel cells, the HOR occurs at the anode and the ORR at the cathode, though the half reactions are slightly different in alkaline media as they are mediated by the OH^- anion, and not protons [88]:

$$H_2 + 2OH^- \rightleftharpoons 2H_2O + 2e^- \text{ (HOR)} \qquad \text{Equation 2.8}$$

$$\tfrac{1}{2}O_2 + H_2O + 2e^- \rightleftharpoons 2OH^- \text{ (ORR)} \qquad \text{Equation 2.9}$$

Giving the same overall redox reaction:

$$H_2 + \tfrac{1}{2}O_2 \rightleftharpoons H_2O \qquad \text{Equation 2.10}$$

Note that 2 moles of water are generated at the anode and one consumed at the cathode, as opposed to one mole of water being produced at the cathode in acid systems. This can cause potential flooding and water management issues at the anode. The aqueous, highly caustic, electrolyte presents obvious hazards and is also susceptible to the following carbonation reaction in the presence of CO_2:

$$CO_2 + 2OH^- \rightarrow (CO_3)^{2-} + H_2O \qquad \text{Equation 2.11}$$

The carbonate anion can precipitate out of solution in combination with a metal cation and cause blockages in the electrodes and reduction in conductivity of the electrolyte, severely hampering performance [89] and so only pure, CO_2-free oxygen and hydrogen could be used in these systems. Due to these disadvantages and the improvements in proton conducting membrane technology, the AFC was overtaken by the PEM fuel cell as the main focus of low temperature fuel cell research. Though there have been recent improvements in AFC technology [90], this thesis concerns the recent developments in solid polymer electrolyte alkaline technology, and so further detail on AFC progress can be found in the reviews of McLean et al [47] and Bidault et al [61].

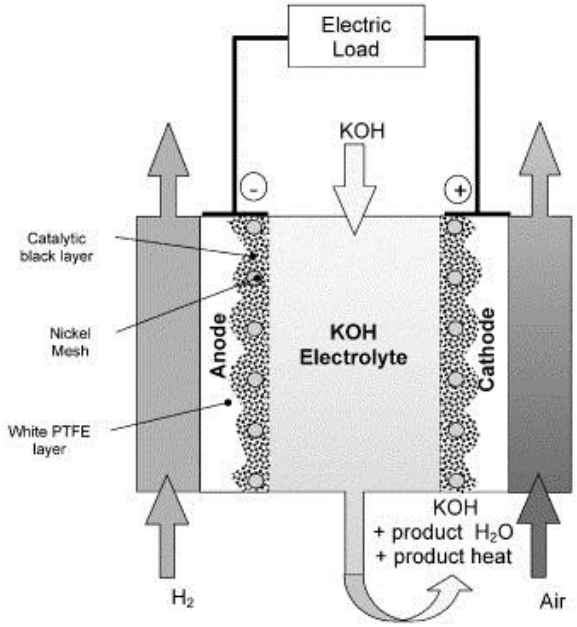

Figure 2.1 Schematic of an aqueous electrolyte AFC, reproduced from [47].

2.1.4 The AAEM Fuel Cell

Recent developments in alkaline anion exchange membranes (AAEMs) have opened up the possibility of an alkaline analogue of the acidic solid polymer electrolyte fuel cell. This could utilise the benefits of the alkaline cathode kinetics and at the same time eradicate the disadvantages of using an aqueous electrolyte. As the AAEM is also a polymer electrolyte membrane (sometimes abbreviated as PEM) some clarity in abbreviations is required. In this thesis, PEM refers only to the proton exchange membrane fuel cells (acidic), AAEM to the anion exchange membrane H_2/O_2 fuel cells, and AFC exclusively to the aqueous electrolyte alkaline H_2/O_2 fuel cells. Anion exchange membranes are also employed in alkaline direct alcohol fuel cells, discussion of which will refer to them as ADMFC/ADEFC (methanol/ethanol).

2.1.4.1. AAEM Principles

The AAEM fuel cell is based on the same fundamental principles of the PEM fuel cell; direct electrochemical conversion of H_2 to electricity using a solid electrolyte, with the key differences being the fundamental half equations (Equation 2.8 and Equation 2.9) and the hydroxide ion conducting membrane. The schematic of an AAEM fuel cell is shown in Figure 2.2:

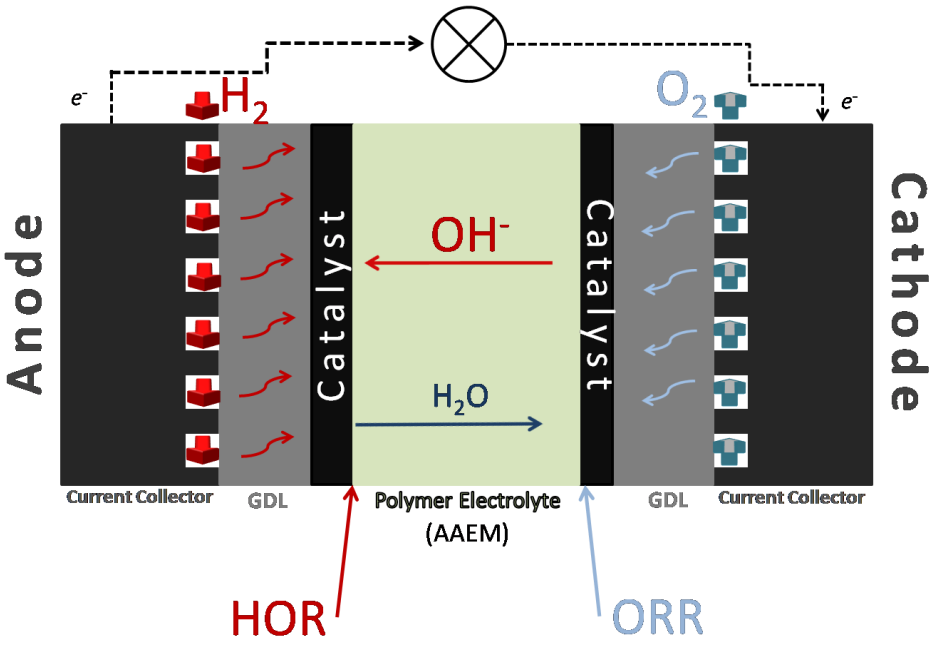

Figure 2.2 The outline of the AAEM alkaline fuel cell (cf. Figure 1.1).

The peripheral components of the AAEM fuel cell can be assumed to be the same as in PEM fuel cells, performing the same functions. Water management may be treated differently in AAEM as water is produced on the anode and consumed at the cathode, meaning there is the potential for flooding at the anode and insufficient humidification of the cathode. This is thought to offer the potential for more simple humidification, with the anode 'self-humidifying', it might be the case that only the cathode requires humidification (though an interesting recent study showed retained performance when using a dry cathode stream and humidifying the anode stream only, allowing diffusion of water through the membrane to be the sole source of cathode humidification [91]).

The other major difference from the PEM system is that the membrane conducts hydroxide ions. As diffusion coefficients are roughly 4 times larger for H^+ than OH^-, the ionic resistivity of AAEMs is often significantly higher than that of Nafion and may require doping of the membrane with KOH solution to increase conductivity [44].

2.1.4.2. Alkaline Membranes

Anion exchange membrane use in fuel cells is a relatively nascent technology and as such has no Nafion-like industry leader that is ubiquitous in the field [92]. A recent review of alkaline membranes by Merle [93] highlights

the vast number and variety of alkaline membranes in the literature, and the comparatively few commercially available membranes. As AAEMs are solid, they contain no mobile cations and so even though carbonates are still formed from the reaction of CO_2 with OH^-, there should be little precipitation of solid carbonates in the membrane. The prospect of reduced carbonate issues and lack of concentrated aqueous electrolyte in AAEMs has driven research into membrane development and solid alkaline fuel cell technology in recent years [93].

Just as Nafion contains negatively charged sulphonic acid groups to conduct positively charged protons, AAEMs must contain positively charged groups to conduct the negative hydroxide ion. As already mentioned, the conductivity of AAEMs is lower than that of PEMs [94]. One way of increasing the conductivity is to include more cationic groups in the polymer, but this often has the effect of reducing the mechanical strength and chemical stability of the membrane. The most common functional group in AAEMs is the quaternary ammonium group, R_4N^+ [95], which can undergo the following E2 elimination reaction (Hofmann elimination) in the presence of hydroxide:

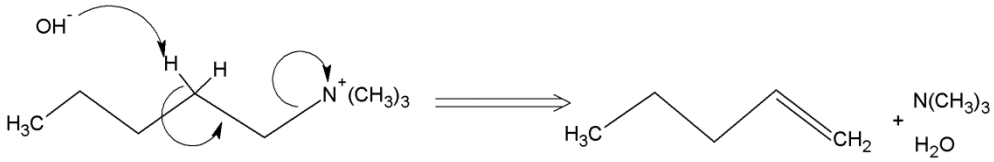

Figure 2.3 The Hofmann elimination of quaternary ammonium groups.

Most work at this point has suggested that this Hofmann elimination is slow below 60°C but much faster at higher temperatures, resulting in significant degradation to most AAEMs above 60°C [96]. This is an obvious limitation for current alkaline membranes as the kinetic benefit of operating at higher temperatures (PEM fuel cells are mostly operated at 80°C) is not obtainable. The weak basicity of R_4N^+ groups is also thought to contribute to the lower mobility of hydroxide in AAEMs compared to protons in PEMs. Also, though no solid carbonate precipitates, the carbonate anion is still formed, which serves to reduce the concentration of hydroxide in the membrane and may be a contributory factor to the reduced conductivity [93, 97].

There are many examples of anion exchange membranes in the literature, and of many different types as summarised by Merle [93] and Cou-

ture [98], but the most promising membranes for fuel cell applications are formed by radiation grafting of R_4N^+ groups onto polymer backbones [99-108] or chemical modification of existing polymers [92, 109-112]. A study by Varcoe in 2007 represented the first AAEM with conductivity over the desired mark of 10 $mScm^{-1}$ required for viable solid alkaline fuel cells, though the membrane required high levels of humidification to maintain good conductivity [113]. Studies previous to this often had to submerge membranes in KOH solution in order to attain sufficient conductivity [44, 114]. The highest conductivity membrane was reported in 2011 by Tanaka et al. for use in hydrazine fuel cells, with a maximum conductivity of 114 $mScm^{-1}$ at 80°C [115]. A good AAEM should have the following desirable properties:

High chemical, mechanical and thermal stability under operating conditions

High conductivity of OH^- ions, >10 $mScm^{-1}$

Low electrical conductivity

Low gas permeability

Low thickness

Good performance under various humidification levels

The electrodes in PEM fuel cells contain a certain amount of acidic ionomer (e.g. Nafion) solution to act as a binder in the ink and also to introduce some H^+ conductive substance to the triple phase boundary [9]. For AAEM fuel cells there is a need for an analogous ionomer solution for use in the catalyst layer [95] and so it is an important consideration for development of good electrodes for the alkaline fuel cell [106].

In summary, the improvement of AAEMs is an on-going area of research and development. There is no one membrane of choice currently and the conductivity and stability of some membranes is still an issue. However, there are signs in the recent work previously discussed that good AAEM performance is close and so catalyst development for the AAEM fuel cell is required to match performance and cost of the current PEM fuel cell technology.

2.1.4.3. AAEM Fuel Cell Examples

As a new and under-developed technology, there is a shortage of examples of AAEM fuel cells in the literature. Some of the pioneering work in alkaline membranes and AAEM fuel cells comes from the University of Surrey and the work of Varcoe and Slade [45, 50, 92, 99, 100, 102-104, 106-108,

113, 116-119]. They mainly use radiation grafted quaternary ammonium membranes. Peak power densities of around 55 $mWcm^{-2}$ were obtained using platinum cathodes and anodes and pure O_2 as an oxidant (corresponding to roughly 90 $mAcm^{-2}$ at 0.6 V) [108], with worse performance when employing Au or Ag cathode catalysts [45] (Figure 2.4). Operating a H_2/Air fuel cell with a carbonate-tolerant membrane yielded lower power densities of around 38 $mWcm^{-2}$ but showed better performance when the membrane was in carbonate form than when it was in hydroxide form, thought to be due to fact that the ORR proceeds more quickly in alkaline carbonate than aqueous KOH solution [116]. A similar trend was observed for Zhou et al. in 2009, though with very low power densities of only 4 $mWcm^{-2}$ [120].

Recent improvement in their membrane technology produced peak power densities of 230 $mWcm^{-2}$ (Figure 2.5) with Pt cathodes and pure O_2 for the thinnest of the membranes (17 μm fully hydrated) [50]. It is thought that the improved performance on decreasing membrane thickness is due to the increased water crossover from the anode to the cathode, where it is consumed (Equation 2.9). Au and Ag cathodes were again tested in this study, giving reduced performance compared to Pt.

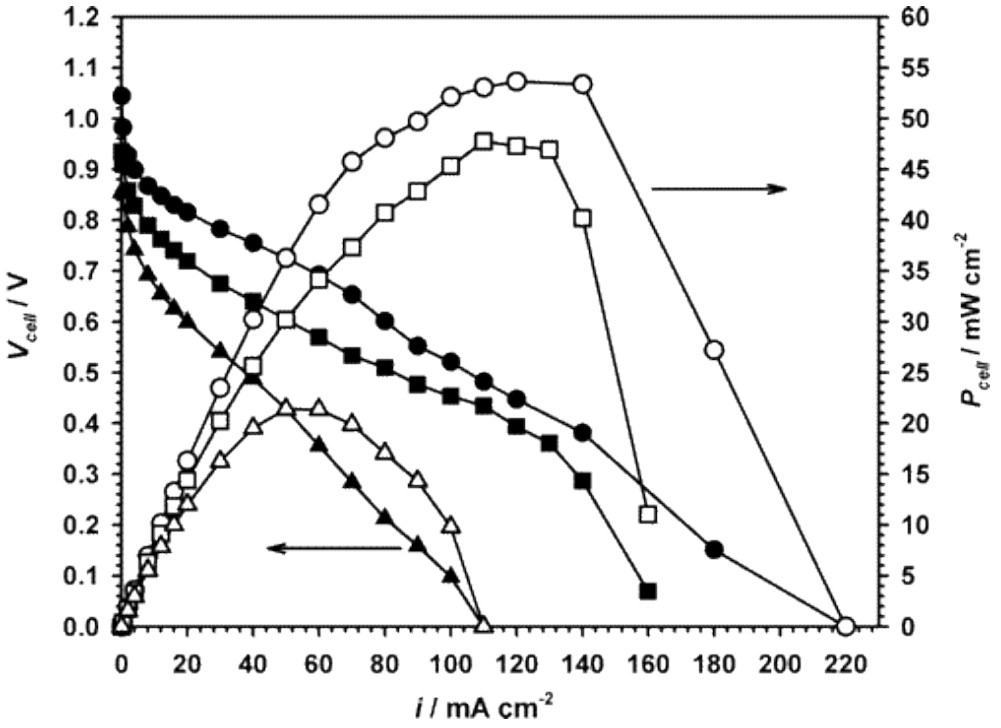

Figure 2.4 Fuel cell polarisation curves (filled symbols) and power densities (empty symbols) of Pt (circles), Ag (squares) and Au (triangles) cathodes using pure oxygen, reproduced from [45].

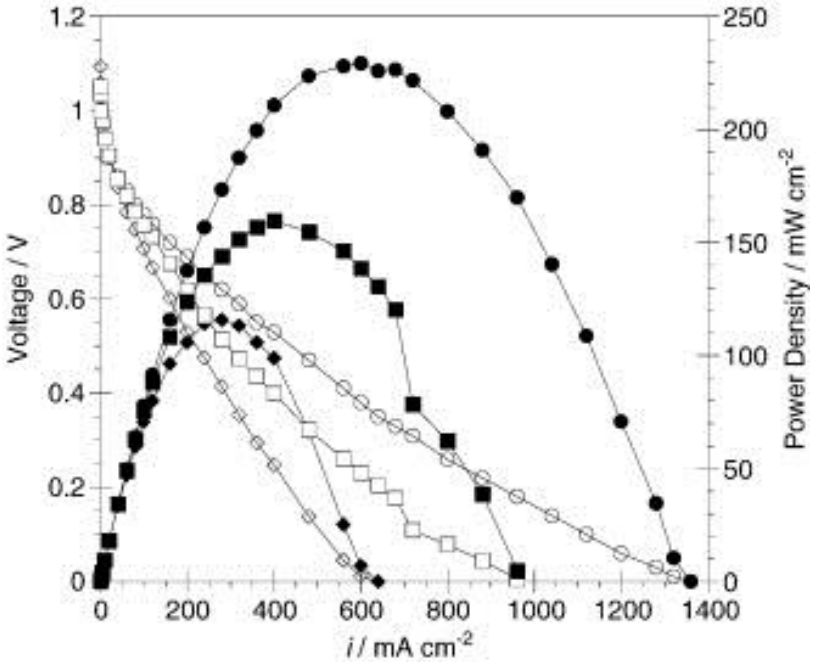

Figure 2.5 Fuel cell polarisation curves (empty symbols) and power densities (filled symbols) of Pt cathodes in pure oxygen showing the effect of membrane thickness on performance. The performance improves in the order 85 μm (diamonds), 46 μm (squares) and 17 μm (circles). Reproduced from [50].

They also developed a novel reference electrode for use in an AAEM fuel cell which allowed decoupling of the cathode and anode polarisations from the overall cell polarisation. It was shown that the anode polarisation was significantly higher than the cathode polarisation, contrary to the situation in PEM fuel cells (Figure 2.6). In addition to the already discussed slower HOR kinetics in alkaline, it is thought that flooding in the anode of AAEM fuel cells can cause high mass transport polarisation, even at low current densities (note that the thicker 80 μm membrane was used in this study). They also demonstrated that, as water is a reactant in the ORR (unlike in PEM), the cathode electrode design is important for good performance. Using PTFE free cathodes they achieved a power density of 125 $mWcm^{-2}$ and showed a small catalytic effect from carbon only in the alkaline cell [119]. This highlights the need for greater attention to water management and catalyst layers in AAEM FCs [117-119].

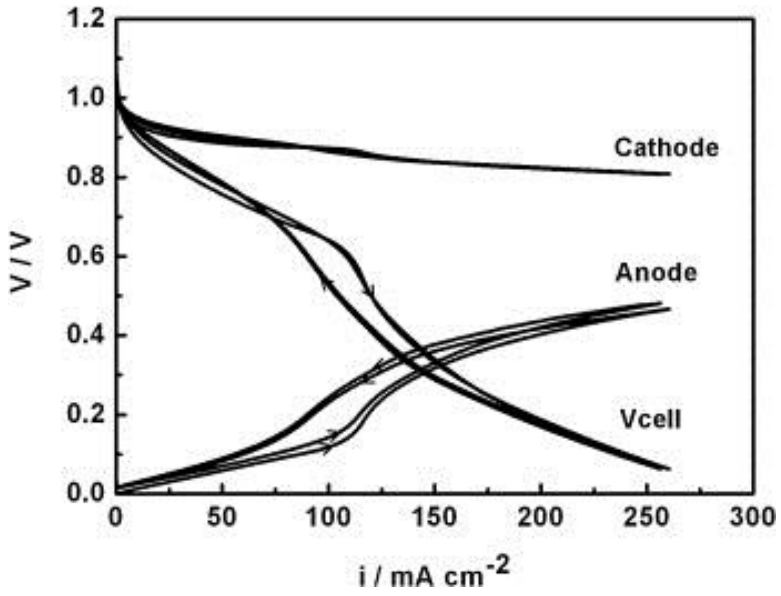

Figure 2.6 The overall polarisation curve (Vcell) and its cathode and anode constituents, obtained using a novel Pd coated Pt wire as a reference electrode. The anode polarisation is significantly greater than that of the cathode. Reproduced from [117].

Some of the earliest work on AAEM fuel cells was conducted by Agel et al. in 2001 [44]. They used a KOH doped membrane, carbon supported Pt on nickel foam electrodes and H_2/O_2 at atmospheric pressure and ambient temperature to obtain a current density of around 25 $mAcm^{-2}$ at 0.6 V. This study demonstrated the need for good ionic contact between the electrodes and the membrane, as the performance increased to just under 60 $mAcm^{-2}$ at 0.6 V when an interfacial KOH gel was applied between them.

Lu et al. demonstrated the first fully non-platinum AAEM cell in 2008 by using a chromium-decorated nickel cathode and a silver anode [121]. Their quaternary ammonium polysulphone membrane was dissolved in solvent allowing control of the thickness of the cast film and impregnation into the electrode layers. The peak performance of 50 $mWcm^{-2}$ was achieved using humidified H_2/O_2 at 60°C with a back-pressure of 1 atm (gauge).

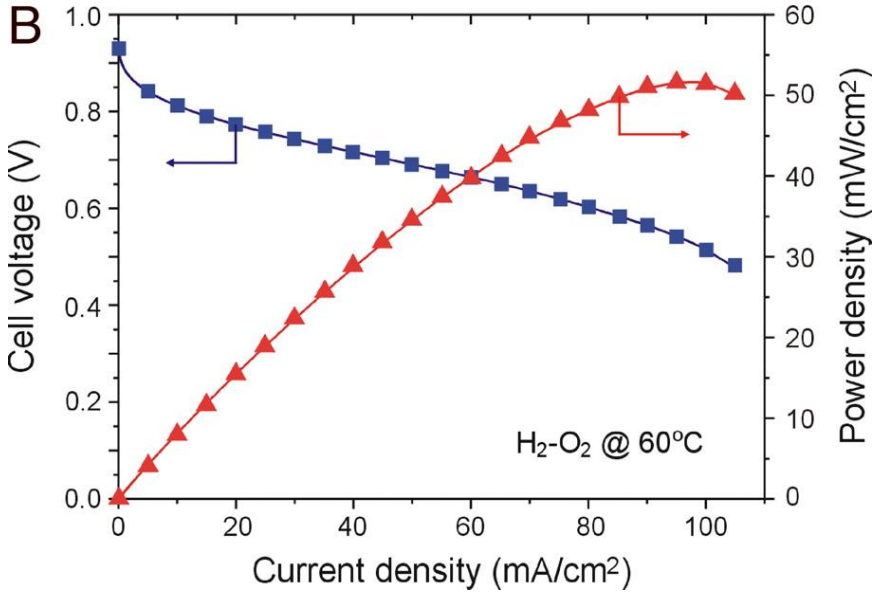

Figure 2.7 Polarisation curve (blue) and power density (red) of a fully non-Pt AAEM fuel cell at 60°C, reproduced from [121].

Park et al. showed that a high loading of silver (2.0 mg cm^{-2}) could produce a similar peak power density of 30 $mWcm^{-2}$ as a Pt cathode in their aminated polysulphone membrane fuel cells, using humidified H_2/air at 60°C [60]. They also observed a high OCV of around 1.05 V which, given the discussion in Section 1.4.4, might indicate higher exchange current densities or lower fuel crossover reducing the voltage loss from OCV (Varcoe also observed a similar effect [45]).

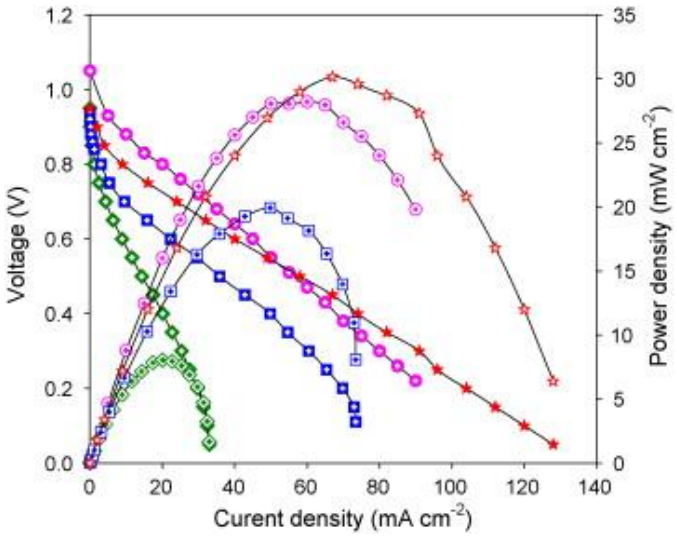

Figure 2.8 Polar curves and power densities of AAEM fuel cells with Pt anodes (0.5 mg cm^{-2}) and silver cathodes at 0.5 mg cm^{-2} (green), 1 mg cm^{-2} (blue), 2 mg cm^{-2} (red) and with a Pt cathode (0.5 mg cm^{-2}) (pink). Reproduced from [60].

In 2009 Gu et al. used a quaternary phosphonium containing ionomer solution in conjunction with a commercially available AAEM to again demonstrate the importance of good ionic conductivity between the electrode and membrane layers [95]. A marked difference in performance was seen between MEAs with and without the ionomer solution, with a peak power density of nearly 200 $mAcm^{-2}$ obtained at 80°C with back-pressurised H_2/O_2 gases. Mamlouk et al. showed a similar effect on their in-house membrane and concluded that the optimal ionomer content in the catalyst layer depended on several factors such as thickness of electrode and O_2 partial pressure. They also suggested that due to flooding problems the anode layer should be thicker than the cathode layer [122].

A year later in 2010, the best performance from an AAEM fuel cell was demonstrated by Piana et al. [123]. They used a commercially available membrane in conjunction with a novel in-house ionomer solution as a catalyst binder and H_2/air (CO_2-free) at 50°C. A peak power density of 400 $mWcm^{-2}$ was obtained when using Pt on the anode and cathode, and 200 $mWcm^{-2}$ when using a non-disclosed transition metal on carbon catalyst as the cathode. They also demonstrated the very interesting effect of CO_2 on the system; at low current densities CO_2 causes the expected drastic reduction in performance due to reaction with OH^- and subsequent reduction in conductivity. However, at higher current densities more OH^- ions are produced by the electrochemical half reactions which help to overcome this is-

sue by a so-called self-purging mechanism (Figure 2.9). There is a clear change in the polar curve representing an increase in membrane conductivity at higher current densities (though by this point a large amount of operating voltage has been lost). This has implications for the conditioning of AAEM fuel cells, with Varcoe suggesting that the cells should be quickly brought to high current densities and then polar curves taken by reducing the load back to OCV (this method produced better performance than increasing the current load from OCV) [119].

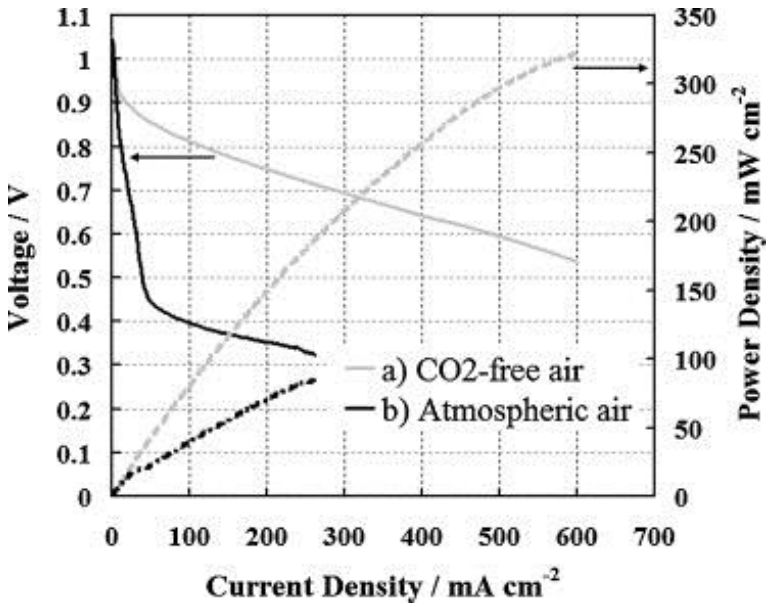

Figure 2.9 Polar and power density curves showing the effect of CO_2 on the performance of the membranes. The performance in CO_2-free air (grey) is good, but the carbonate effect has a drastic effect on performance in atmospheric air (black). On reaching higher current densities this effect is reduced, shown by the change in gradient of the black polar curve to match that of the CO_2-free air polar curve. Reproduced from [123].

The most recent work comes from Cao et al. in 2012 [92]. They developed a poly(methyl vinyl ether-alt-malic anhydride) (PMVMA) membrane by chemical grafting of ammonium groups to the polymer. The membrane was stable up to 150°C and showed increasing ion conductivity from room temperature to 60°C. Their peak power density of 155 $mWcm^{-2}$ was obtained at 35°C and on H_2/O_2 and demonstrated a vast improvement over lower temperatures (and hence higher Ohmic resistances, Figure 2.10).

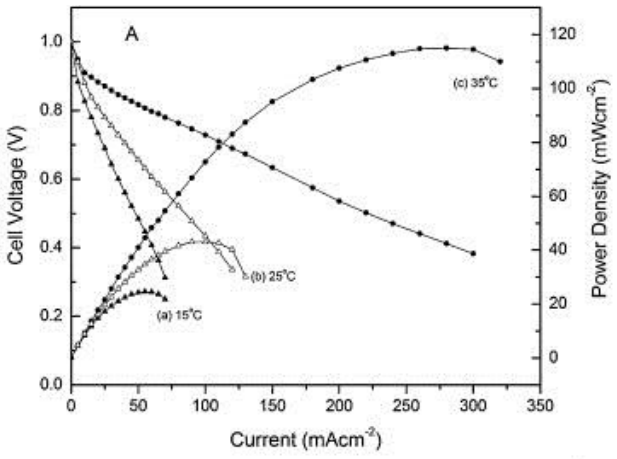

Figure 2.10 The effect of temperature on AAEM resistance and polarisation performance. Reproduced from [92].

Some of the most promising work on AAEM fuel cells comes from the Tokuyama Corporation, who are one of the commercial suppliers of alkaline membranes. Unfortunately they publish only short conference proceedings with little detail, but the work shows encouraging signs for solid alkaline fuel cells [46, 91, 97, 105, 124-126]. They have produced quaternary ammonium-containing membranes with good conductivity of around 40 $mScm^{-1}$ and can control the thickness between 10 and 40 μm [105]. They have achieved a peak power density of 325 $mWcm^{-2}$ using Pt/C anodes and cathodes and CO_2-free air as the oxidant and have also confirmed a similar self-purging effect, as discussed by Piana et al., at higher current densities [46, 124, 127]. Tokuyama were also the first to show elevated operating temperatures in AAEMs, getting improved performance and 200 hour stability from their membranes at 80°C [125]. In 2011 they demonstrated a very interesting, and ostensibly counterintuitive, comparative performance when there was no humidification of the cathode gas stream. As the ORR in alkaline consumes water as a reactant, it is assumed to need good humidification of the cathode, but this study showed that water flux from the anode to the cathode increases when the cathode is dry, compensating for the lack of water. They also showed the catastrophic effect of not humidifying either gas stream, proving that the 2 moles of water produced by the anode HOR is not enough in itself to provide sufficient humidification for the membrane [91]. The potential for partially non-humidified operation is important if AAEMs are to be used in portable devices such as automobiles.

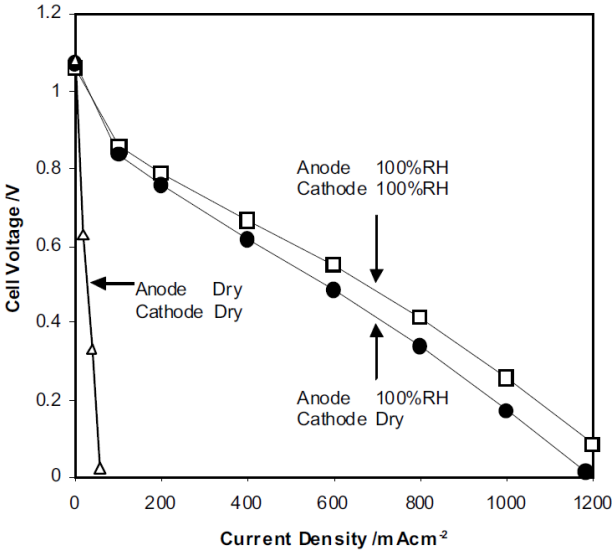

Figure 2.11 The effect of humidification on the Tokuyama AAEM. Humidification of the anode stream only (circles) shows comparable performance to humidification of both streams (squares). When there is no humidification of either gas stream (triangles), the performance is drastically reduced. Reproduced from [91].

In summary, solid alkaline fuel cells using hydrogen as a fuel represent a potential improvement in performance and reduction of cost over acidic PEM fuel cells. The technology is in the early stages of development, shown by the lack of studies to date and the variation in techniques and results in these studies, and requires further research with bespoke methods applied to the alkaline case (as opposed to trying to apply acid PEM principles to what might be a very different technology) to attain the performance levels achieved from state-of-the-art PEM fuel cells.

2.2 Catalysis

As already mentioned, the role of the catalyst in fuel cells is to reduce the activation energy of the electrochemical half reactions and therefore limit the voltage losses associated with the kinetics of these reactions. The catalyst achieves this in two ways; by providing a geometrically suitable surface for the reactants to adhere to, holding them in a favourable position for reaction, and by having an electronic structure and energy level suitable for the facile breaking and making of bonds. In this manner the energy of the transition state can be said to be stabilised, or lowered, and reaction can proceed more readily. Most fuel cell catalysts, being supported metal nanoparticles, are heterogeneous catalysts with the current state-of-the-art ma-

terials being carbon supported platinum. This work concentrates on a novel non-platinum catalyst based on palladium-iridium (PdIr/C), developed at Amalyst Ltd. [128] for use as an anode catalyst in alkaline fuel cells.

2.2.1 Palladium in Fuel Cell Catalysis

As platinum is an expensive and limited resource, its ubiquity in current fuel cell catalyst layers is seen as a major obstacle for widespread commercialisation. Thus, there has been a drive to develop electrocatalysts that contain little or no Pt in recent years [31, 129, 130]. Next to Pt, the catalytic activity of Pd is the highest for both the ORR and the HOR [18] and is significantly cheaper and more abundant than Pt, making it a good candidate for non-platinum fuel cell catalysts (Figure 2.12). Much of the development of Pd-based catalysts has focused on alloys and surface modified catalysts due to the low activity of Pd compared with Pt in acidic systems [131], but Pd is known to be much more active for the oxidation of many species in alkaline media [132] and so is considered a potential anode catalyst for ADMFC/ADEFCs where there are large anode overpotentials when using Pt catalysts [133, 134]. Palladium also suffers from electrodissolution to Pd^{2+} at low pH and potentials between 1.0 and 0.6 V (vs SHE) [135].

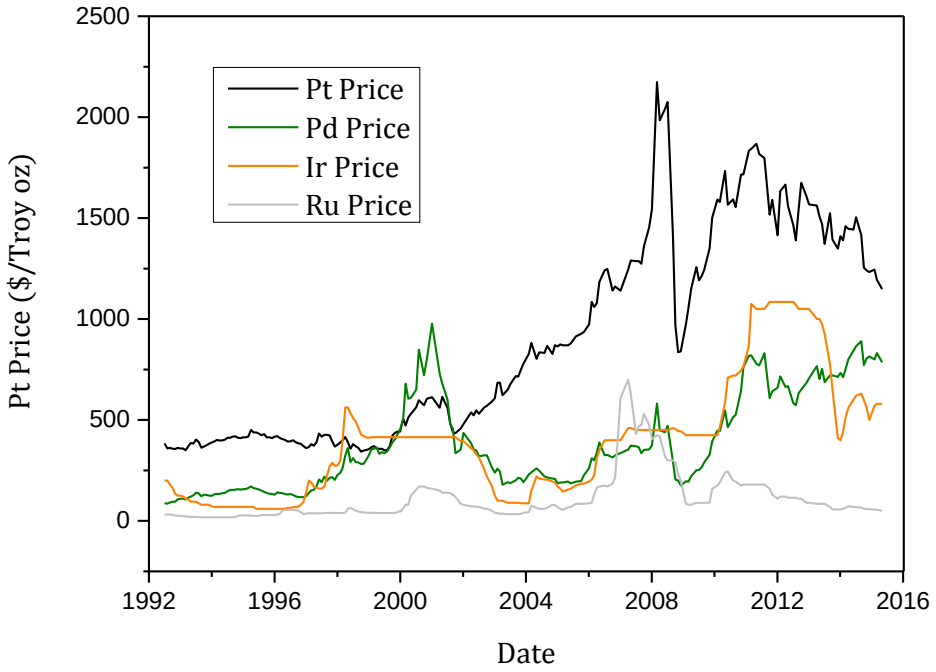

Figure 2.12 The variation of platinum group metal (PGM) prices in the last 20 years. Data from the Johnson Matthey website [136].

2.2.1.1. The HOR

As the rate determining step in the HOR reaction is the dissociative adsorption of the hydrogen, involving electron transfer into the antibonding H_2 orbital, the electronic properties of the catalyst have a large bearing on the ease of bond breaking and the strength of adsorption of atomic hydrogen on the catalyst surface. Pd is in the same periodic group as Pt and thus has similar valence electron behaviour, so is expected to have similar enthalpy of hydrogen adsorption. Indeed they have similar bond strengths with H and so reside close to each other on a volcano plot [137], with Pd having a slightly stronger bond strength (undesirable). The situation is similar for carbon supported catalysts with slightly lower, but comparable, performance achieved in fuel cell testing (PEM) using a Pd/C anode compared to a Pt/C anode by Grigoriev et al. [138], and Pronkin et al. [139] suggesting that the activity of the HOR is two orders of magnitude lower on Pd/C using RDE techniques (though RDE of HOR in acid is notoriously inaccurate due to the very fast kinetics).

In order to increase the activity of both catalysts, a weaker M-H bond is desired, so that the enthalpy of formation/breaking of the bond is zero (the

peak of a volcano plot). Markovic et al. [140] showed that depositing a monolayer of Pd onto a Pt (111) surface markedly increased the HOR reaction rate compared to the single crystal Pt (111) in acid, and the reason was attributed to a weaker M-H bond for the monolayer-modified Pt. Greely et al. [141] used density functional theory (DFT) to predict the bond strength of Pd monolayers on various transition metal substrates. It was shown that the electronic structure of the substrate can have a large effect on the Pd monolayer's d-band energy level, and thus the bond strength. This manifests itself in very different exchange current densities for the hydrogen evolution reaction (HER, the reverse of the HOR and considered almost identical in mechanism due to the high reversibility of the reaction) as shown in Figure 2.13. In other words, the ostensibly identical Pd surface layers have different electrocatalytic properties due to the change in their electronic structure induced by the bulk substrate's electronic structure.

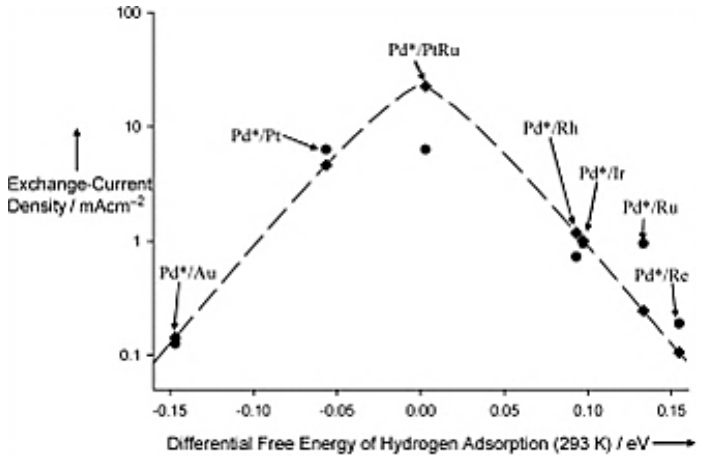

Figure 2.13 Volcano plot of Pd monolayers on various metal substrates. The dashed line represents the DFT model predicted exchange current densities for the HER, the square points represent specific modelled systems and the circles represent the experimental data for the corresponding examples. Reproduced from [141].

Cho et al. [142] have also shown that an anode catalyst of carbon supported Pd-Pt alloy containing only 5% Pt ($Pd_{19}Pt/C$) has the same performance as a Pt/C catalyst in the PEM fuel cell environment.

Although very low anode loadings of Pt have been achieved in PEM fuel cells [81], Pt suffers very easily from carbon monoxide (CO) poisoning. CO can strongly bind to the Pt surface and irreversibly block active sites for the HOR. This is a major concern for anode catalysts as the majority of hydrogen production is from hydrocarbon reforming which can leave traces of CO in the gas supply, enough to poison the catalyst and severely reduce

performance [134]. Pd has a similarly strong bond to CO and so is also easily poisoned, but Pd alloys have been shown to have superior CO tolerance compared to sole Pd or Pt [143]. Papageorgopoulos et al. [144] showed that PdPt/C has less CO coverage at 80°C than Pt/C (which has total coverage), and that CO tolerance in fuel cell testing is also superior (and superior to PtRu/C, the most widely used CO tolerant anode catalyst). The reason for this is due to a weaker bond with CO in Pd alloys. This was shown by Garcia et al. [145] who observed no CO_2 in the outlet anode stream when using PdPt/C as the catalyst, indicating no oxidation of CO and therefore that the enhanced CO tolerance must be due to the greater available sites by virtue of weaker M-CO bonds. Conversely they showed that CO_2 was present when using PtRu/C as the catalyst, indicating that the enhanced CO tolerance of this material is due to the so called bifuncional mechanism, where neighbouring Ru sites allow the adsorption of OH species which aid in the oxidation of CO adsorbed on adjacent Pt atoms to CO_2.

2.2.1.2. The ORR

The activity of Pd for the ORR is second only to Pt, but still has an exchange current density roughly an order of magnitude lower in acidic solution [146]. Recent results from Kondo et al. [147] have suggested that the Pd(100) facet has very high activity for ORR in acid (much higher than the other low index planes of Pd and roughly three times that of the most active Pt facet). Though it is very difficult to synthesise single crystal nanoparticles for fuel cell type catalysts, this interesting result has led to recent attempts to create palladium cathode catalysts supported on carbon nanotubes [148], carbon papers [149] and even nanocubes composed entirely of single crystals of Pd (100) [150].

The activity of Pd for the ORR in alkaline solution is more promising, with exchange current densities similar to that of Pt for other low index facets, and high activity for PdPt alloys which is thought to be due to the reduced effect of anion adsorption in alkaline [131]. Jiang et al. [151] found that the activity of carbon-supported Pd nanoparticles for ORR in alkaline is high, and studied the particle size effect showing that the mass activity peaked for particles of around 5 nm in size.

Again, alloying in Pd based catalysts is thought to change the energy level of the d-band of Pd, resulting in a lower bond strength with oxygen species and thus an increase in ORR activity [152]. Alloying may also pro-

duce smaller particles and change the lattice parameters of the metal structure, aiding in increased activity [153].

2.2.1.3. PdIr/C Anode Catalysts

There are no examples of a PdIr/C anode catalyst for hydrogen oxidation in the literature, and only two examples of its use for other oxidations in fuel cells; one for ethanol and one for formic acid. Though the mechanisms for these oxidations will be different than that of the HOR, they serve as the only examples of a similar catalyst to the one used for this work and so deserve some attention.

The first example came in 2008 when Wang et al. developed a PdIr/C catalyst for use on the anode of a direct formic acid fuel cell [154]. Due to CO poisoning effects (CO is an intermediate in the oxidation of formic acid) Pt is seen as an unsuitable catalyst for formic acid anode catalysts, and so the CO tolerance of Pd-based alloy catalysts have been investigated as a suitable replacement [155]. They showed improved activity when compared with Pd/C catalysts, despite the lack of activity of Ir for formic acid oxidation. Their catalyst was prepared by simultaneous reduction of $PdCl_2$ and $(NH_4)_2IrCl_6$ with sodium borohydride and deposition onto Vulcan carbon nanoparticles, with the precursor amounts adjusted in order to prepare catalysts with Pd:Ir ratios of 1:1, 3:1 and 5:1. The smallest particle size and biggest lattice parameter was observed for the 1:1 catalyst, indicating that a higher Ir content can help to control agglomeration of Pd and also expand the lattice of the Pd. Using CO stripping voltammetry they also showed that Ir has no affinity for CO and even a small amount of Ir in the Pd lattice can significantly weaken the CO bond strength. They suggested that increasing the amount of Ir in the alloy did not change the bond strength but did reduce the amount of CO adsorbed, and thus also the poisoning effect. This effect is balanced by the fact that increasing the amount of unreactive Ir reduces the electrocatalytic effect of the Pd, and so the 5:1 ratio was found to be the best for formic acid oxidation.

More recently in 2010 Shen et al. [156] synthesised PdIr/C catalysts in the ratios 5:1, 7:1 and 9:1 for use in ADEFCs, using a similar simultaneous reduction method with sodium borohydride, in addition to citrate as a complexing agent (which reduced the size of the particles from around 3.9 nm to 3.0 nm). They found that PdIr is better than Pd for ethanol oxidation, with a low amount of Ir again giving the best results in alkaline elec-

trolyte (Pd:Ir of 7:1). Conversely they found that the amount of Ir in the alloy did not affect the crystallite size in a significant way, but the lattice spacing was lower in the PdIr/C catalysts than the Pd/C, indicating an alloying effect from the smaller Ir lattice parameter. They suggested that the improved CO tolerance comes from the adsorption of hydroxyl species at low potentials by Ir, aiding in the oxidation of adsorbed CO on adjacent Pd sites (the bifunctional mechanism). X-ray photoelectron spectroscopy (XPS) suggested that the addition of Ir has very little effect on the electronic structure of Pd (though as only low amounts of Ir were used in this study, this may not be the case for lower Pd:Ir ratios), leading the authors to attribute the increased catalytic activity for ethanol oxidation to the bifunctional mechanism and reduced particle size of PdIr/C compared to Pd/C.

In summary, Pd-based alloys have shown potential for use as anode catalysts in alkaline media due to their enhanced activity, CO tolerance and lower cost. PdIr alloys have not been fully studied and no examples exist of their use for HOR in AAEM fuel cells, though they show promise for oxidation of small organic molecules.

3 Experimental and Theory

This chapter will outline the experimental details and materials used in the investigation of PdIr/C as an anode catalyst for alkaline HOR as well as background theory for many of the techniques used.

3.1 PdIr/C Catalyst Synthesis

The first iteration of the PdIr/C catalyst was synthesised using the simultaneous reduction method, where the metal precursors are reduced to zero oxidation state and deposited on the carbon support in one step (a common method, an example of which can be seen in Zhang et al's paper [157]). In an attempt to increase the surface area and improve the distribution of metal on carbon, a second method was deployed involving a carbon pretreatment to introduce functional groups. This catalyst will be denoted by $PdIr/C_{HSA}$ and the procedure explained in section 3.1.6. Pd/C, Ir/C and variations of PdIr/C with different Pd:Ir ratios were also synthesised using the methods described, with the quantities of precursor metal salts altered accordingly.

3.1.1 Materials

Below are details of all the chemicals and equipment used in the catalyst synthesis procedure.

3.1.1.1. Chemicals

Palladium (II) Nitrate: $Pd(NO_3)_2.xH_2O$ from Alfa Aesar, 99.9% purity and 39% minimum Pd by mass.

Palladium (II) Chloride: $PdCl_2$ from Alfa Aesar, 99.999% purity and 59.97% Pd by mass. This precursor was used for some of the first Pd/C catalysts synthesised; however, it required large amounts of hydrochloric acid in order to dissolve, and therefore a significant amount of sodium bicarbonate was required to adjust the pH of the solution. Also work by Serov et al. [158] suggested that using the nitrate precursor gave smaller particle sizes for their PdCo alloys, and

therefore better performance, than when the chloride precursor was used. For these reasons, use of $PdCl_2$ precursor was phased out.

Iridium (III) Chloride: $IrCl_3.xH_2O$ from Alfa Aesar, 99.9% purity. Both $IrCl_3$ and $Pd(NO_3)_2$ are hygroscopic so are carefully sealed when not in use and stored in a desiccator in order to reduce the amount of water absorbed, and therefore also the resultant inaccuracies in weighing of the chemicals. For this reason, weighing was also conducted in as short a time as possible.

Sodium Hypophosphite: NaH_2PO_2 from Sigma Aldrich, >99% purity. This is the reducing agent used to reduce the metal oxidation states to zero via the following electrochemical half reaction [159]:

$$H_2PO_2^- + H_2O \rightarrow H_2PO_3^- + 2H^+ + 2e^- \qquad \text{Equation 3.1}$$

Sodium Bicarbonate: $NaHCO_3$ from Sigma Aldrich, reagent plus grade >99.5% purity. A saturated solution is used to increase the pH of the reaction solution.

Hydrochloric Acid: HCl 2 molar solution from Fisher Scientific, 99.9% purity.

IPA: Isopropyl alcohol, $CH_3CH(OH)CH_3$ 70% solution in water from Sigma Aldrich.

Nafion Solution: A dispersion of Nafion ionomer in a water solution, 10.3% Nafion by mass, from Dupont. Used in ink preparation.

Tokuyama Solution: AS-4 dispersion of alkaline ionomer in a propanol solution, 5% ionomer by mass, from Tokuyama Corporation. Used in ink preparation.

Deionised Water: A Millipore Milli-Q machine was used to produce highly deionised water (18.2 MΩcm) for all experiments.

3.1.1.2. Carbon Supports

The carbon supports provide a highly conductive, stable substrate on which the catalyst nanoparticles are deposited. The carbon support chosen for the catalyst was Ketjenblack EC-600JD powder from Akzo Nobel [160]. It has a very high surface area of approximately 1400 m^2g^{-1} which aids in metal dis-

persion and small particle size (and therefore high electrochemical surface area).

3.1.1.3. Equipment

Weighing Balances: Two weighing balances were used; Ohaus Adventurer proAV264 and AND GR-200-EC, both accurate to $\pm$0.1 mg.

Hot Plates: For 1 g (1L) batches a RR98072 bowl-heater from Radleys was used in conjunction with a round-bottomed glass flask. For larger 4 L batches a flat Technico Cimaree hot plate was used in conjunction with a 5 L glass beaker.

Sonication Bath: Ultrasonic waves are used for agitation to aid dissolving of solutions. Supplied by VWR.

pH Meter: UP-5 electrode pH meter from Denver Instruments was used to monitor the pH of the solutions. Calibrated using standard buffer solutions of pH4.0, ph7.0 and pH10.0.

Pestle and Mortar: Agate pestle and mortars were used to grind samples to a fine powder

Tube Furnace: A CST 10/07 tube furnace from Carbolyte Furnaces was used in conjunction with a bespoke quartz tube from Cambridge Glassblowing for catalyst reduction.

Filtration: Millipore glassware and filterpapers (3 μm nitrocellulose) were used with a diaphragm vacuum pump from KNF Lab.

Glassware: all glassware was thoroughly cleaned using a sequence of hot water and soap, IPA, acetone and then deionised water. It was dried in an oven and stored in a clean cupboard, and given a further rinse with deionised water before use.

3.1.2 Methodology

The procedure used for catalyst synthesis is based on that of a patented commercial process [128] that involves a simultaneous reduction method. Described is the methodology for synthesis of 1 g of 1:1 PdIr/C catalyst. The method for Pd/C synthesis is identical except for the absence of any Ir precursors and subsequent adjustment of $Pd(NO_3)_2$ mass to give the desired metal loading. Larger batches than 1 g have been made using a direct proportional scale-up of the method.

3.1.3 Preparation

For 1 g of 40%metal catalyst (1:1) the following approximate target masses of chemicals are accurately weighed:

Carbon: 0.6 g

$Pd(NO_3)_2$: 0.309 g

$IrCl_3$: 0.400 g

NaH_2PO_2: 0.295 g (2.5 times the molar amount of palladium is used in order to provide the correct number of electrons for reduction of Pd(II) and Ir(III) to their zero oxidation state, according to Equation 3.11)

$NaHCO_3$: A saturated solution is prepared in deionised water

The metal precursor chemicals are fully dissolved in deionised water and sonicated for 30 minutes in separate beakers. One litre of deionised water is heated to 80°C (insulated using nitrile rubber insulation) on a hotplate and stirred with a magnetic bar. The carbon is added to the water and stirred at temperature overnight to allow ample time for dispersion in the solution.

3.1.4 Synthesis

Both precursor solutions are added to the slurry and the pH of the solution is increased to 7.0 by drop-wise addition of saturated sodium bicarbonate solution. The pH of the solution is monitored and maintained between 7.0 and 7.5 for one hour with further addition of bicarbonate if required. Sodium hypophosphite is added and the solution is maintained at 80°C for a further hour to allow electrochemical reduction of the metals. After this hour has elapsed the heat is removed and the mixture allowed to cool to room temperature.

3.1.5 Recovery

The cooled solution is then vacuum filtered and washed through with a further litre of deionised water. The filtrate is collected and dried overnight in an oven at 90°C. Once dried the catalyst is ground in a pestle and mortar to produce a fine powder.

The final stage is reduction to remove oxide and hydroxide species. The powder is placed in a ceramic boat and situated in the centre of a tube furnace in a nitrogen atmosphere as the temperature is brought up to 150°C.

Once up to temperature and purged with nitrogen the gas is changed to an $80\%N_2$:$20\%H_2$ mixture (achieved using flow meters and convergent piping) and maintained for one hour. The stream is then changed back to pure nitrogen as the furnace cools to room temperature. The reduced and annealed catalyst is recovered and weighed to calculate the overall yield for the synthesis.

3.1.6 $PdIr/C_{HSA}$

The catalyst synthesis was adapted in order to improve the electrochemical surface area of the metal and therefore performance. This was achieved by using the following carbon pre-treatment step and a more aggressive reducing agent ($NaBH_4$). The carbon was stirred in 1M KOH for 12 hours at 80 °C before being filtered and dried and then used in the synthesis in the same manner as described previously. Alkaline treatment of carbon supports increases the number of surface oxygen-containing functional groups and also the surface acidity of the carbon [161]. Excepting these two changes, the synthesis procedure is the same as for the PdIr/C catalyst. However, pre-treatment of carbon supports can have a significant effect on the activity, stability and therefore performance of the final catalyst, as well as improving dispersion adhesion in the slurry during synthesis, as outlined in this comprehensive review of pre-treatment in carbon supported Pt catalysts [162], and in the case of NaOH pre-treatment on Pt/C improving particle size, distribution and activity of the catalyst [163]. This improved surface area catalyst is denoted throughout at $PdIr/C_{HSA}$.

3.2 Inks

In order for the catalyst to be applied to electrodes for electrochemical and fuel cell testing, an ink must be created. The ink allows catalyst to be evenly and accurately distributed onto an electrode providing a secure bond and a triple phase boundary at which the HOR or ORR may occur.

3.2.1 Formula

The inks are created by mixing the catalyst with a polymer binder, deionised water and isopropyl alcohol (IPA). Initially, Nafion ionomer solution was trialled as the binder due to its wider availability and superior homogeneity of the inks produced with it. Improved electrochemical results were

seen when using the alkaline anion exchange ionomer AS-4 from Tokuyama, and so this was used as a binder in some inks. However, it produced generally poor ink quality than the Nafion binder, as discussed in Section 5.2.3.

3.2.1.1. Inks For Ex-Situ Electrochemical Testing

In order to create an electrode with an accurate catalyst loading, an ink of known concentration is prepared from the catalyst, acetone and IPA solvents and Nafion solution as a binder. The ink density (in terms of mass of metal in the catalyst) is calculated using the following equation:

$$\rho_{\text{ink}} = \frac{m_{\text{cat}} \cdot metal\ \%_{\text{wt}}}{V_{\text{sol}}} \qquad \text{Equation 3.2}$$

Where ρ_{ink} is the metal ink density (mg metal ml^{-1}), m_{cat} is the mass of the catalyst used in the ink (mg), $metal\ \%_{\text{wt}}$ is the weight percentage of the catalyst and V_{sol} is the total volume of solvent used, including the Nafion binder.

Around 7 mg of catalyst is accurately weighed in a glass vial, then 1 ml of acetone is used to wet the catalyst. This avoids oxidation of the IPA, of which 9 ml is added after the acetone. Finally, 39 µl of Nafion solution is added using a micropipette and the ink is sonicated for 30 minutes to ensure good homogeneity.

3.2.1.2. Inks For Fuel Cell Electrodes

It was found that a good consistency for airbrushing of the inks on to GDL material was obtained with a 10% solids ink (solids being the mass of the catalyst plus the total mass of the polymer in the binder solution), containing 80-100% binder mass relative to the mass of the carbon in the catalyst. Thus, the inks were prepared by accurately weighing masses of catalyst, binder solution, water and IPA such that an ink of the aforementioned consistency is achieved. The solution is then sonicated for 30 minutes to assure good homogeneity.

3.3 Imaging

3.3.1 Scanning Electron Microscopy

Scanning electron microscopy (SEM) uses an electron source for imaging, but it detects electrons that have either been backscattered or emitted from the sample as secondary electrons (depending on the operating mode) and builds up a topographic image from the data. The microscope used was a JEOL JSM6480LV SEM which was not capable of as high resolution imaging as TEM, so was therefore used primarily for its spectroscopic capabilities. It is equipped with an X-sight X-ray detector (Oxford Instruments) which allows energy dispersive X-ray spectroscopy (EDX) to be carried out using INCA software. This technique uses high energy electrons to eject inner-shell electrons from the sample atoms, leaving a hole which is then filled by an outer shell electron transition down. The difference in energy between the outer and inner electron shells is emitted as a photon (X-ray) and each element has a unique pattern of possible X-ray energies due to the discreet electronic structures of each element. Thus, by detecting the number of photons of each energy a fingerprint of the atomic make-up of the sample can obtained and also a rough idea of the relative amounts of each element in the sample. The technique is more accurate for heavier elements and for flat polished samples, but can still provide useful confirmation of expected elemental makeup of the catalysts.

The powder catalyst samples were mounted on carbon covered SEM tabs for imaging and EDX analysis. A suitable area of powder was located and EDX carried out over an area between 10-70 μm in order to get a good averaging of the catalyst and to take into account potentially poor distribution of metal nanoparticles.

3.3.2 Transmission Electron Microscopy

The catalysts were imaged using transmission electron microscopy (TEM) which uses a high energy electron beam and a detector to measure the electrons that are transmitted through the sample. Contrast in the image is generated as areas of the sample with greater thickness or higher atomic number appear darker than other areas due to electron absorption. In the case of fuel cell catalysts, the carbon particles appear lighter than the metal nanoparticles on them.

The TEM instrument used was a JEOL JEM1010 equipped with a Gatan Orius camera system and operated at a potential of 80 kV. The catalyst powders were highly dispersed in 70% IPA solution under sonication and applied to a carbon mesh TEM grid (Agar Scientific) using a micropipette and an optical microscope to ensure an disperse distribution of particles. Once prepared the sample was mounted in the TEM instrument as soon as possible to prevent contamination and an area of finely dispersed catalyst was sought out for clear imaging.

Particle size analysis was achieved using Image-J software and measuring the longest axis of any detached metal particles in the image. The data sets included over 200 particles in all cases.

3.3.3 High Resolution Transmission Electron Microscopy

High resolution transmission electron microscopy (HR-TEM) is an imaging mode that allows atomic level definition of features in crystalline samples. Samples were prepared by sonication in methanol and dispersion of two to three drops on a copper TEM grid. The instrument used was a JEOL JEM 2200FS microscope equipped with a Gatan camera and operating at 200 kV. Lattice spacing values were calculated using Image-J software.

3.4 X-ray Photoelectron Spectroscopy

3.4.1 Background Theory

X-ray photoelectron spectroscopy (XPS) is a spectroscopic technique that can give quantitative information about the elemental composition of a sample and the electronic structure of the constituent elements. The sample is irradiated with X-ray light under vacuum and electrons emitted by the photoelectric effect are measured by the instrument. The binding energy of the electron can be calculated using Equation 3.3 and the number of electrons detected is proportional to the amount of a specific element in the sample.

$$E_{\text{binding}} = h\nu - (E_{\text{k}} + \phi) \qquad \text{Equation 3.3}$$

Where $h\nu$ is the photon energy, E_k is the kinetic energy of the electron as measured by the instrument and ϕ is the work function, a correction factor that is dependent on surface structure and instrumentation.

As the ejected electrons are from core atomic orbitals and these orbitals have well defined energies, the binding energy of the electron is specific to a particular energy level within a particular element. This energy can also be affected by the atom's local environment, such as bonding or coordination, which manifests in slight shifts in energy of the peaks in an XPS spectrum. These shifts can be used to gain an insight into the change of energy levels that can occur from processes such as alloying – which is of particular interest in catalysis as the electronic structure of a material can change how active a certain catalyst is towards the reaction of interest [164]. The ejected electrons can be scattered by neighbouring atoms, and it is only electrons ejected without energy loss that contribute to the peaks in the spectrum, with those being scattered contributing to the background signal [165]. As the probability of electron scattering increases exponentially with depth in the sample, XPS is considered a surface sensitive technique with an electron mean free path of a few nanometres, depending on sample and equipment set up [166].

3.4.2 Spectra

XPS data is normally represented as a plot of decreasing binding energy (in eV) versus intensity or counts. Figure 3.1 shows an example XPS survey for a PdIr/C with characteristic peaks for each element present. Areas of interest within the survey can be studied at higher resolution to give more information about the particular element of interest. When these peaks are looked at closely a doublet is often observed due to spin-orbit coupling. For atomic orbitals with orbital angular momentum (L) greater than zero (p, d or f orbitals) the spin angular momentum (S) of the electron ($\pm 1/2$) can couple to the orbital angular momentum causing a split in energy of the final (excited) state of the atom such that $J = L + S$, where J is the total angular momentum quantum number. The degeneracy of the two states is such that a doublet is given by $2J + 1$, which also determines the probability of transition to a particular state and thus the peak ratio. For this reason, when fitting the peaks in an XPS spectrum, the peak

separation (determined by the difference in energy between the two possible J states) and relative peak ratios must be fixed.

For PdIr/C catalysts we are mainly concerned with excitations from the Pd 3d and Ir 4f orbitals. D orbitals (L=2) split in to a 5/2 sextet and a 3/2 quartet and F orbitals (L=3) into a 7/2 octet and a 5/2 sextet, with the higher J value having higher energy (and therefore lower binding energy). Thus, for Pd a doublet will be observed with $Pd\ 3d_{5/2}$ at low binding energy and $Pd\ 3d_{3/2}$ at high binding energy, with a peak ratio of 3:2 [167]. For Ir a doublet of $Ir\ 4f_{7/2}$ at low binding energy and $Ir\ 4f_{5/2}$ at high binding energy with peak ratio 4:3 is seen [156]. An example of this doublet structure can be seen in Figure 3.2.

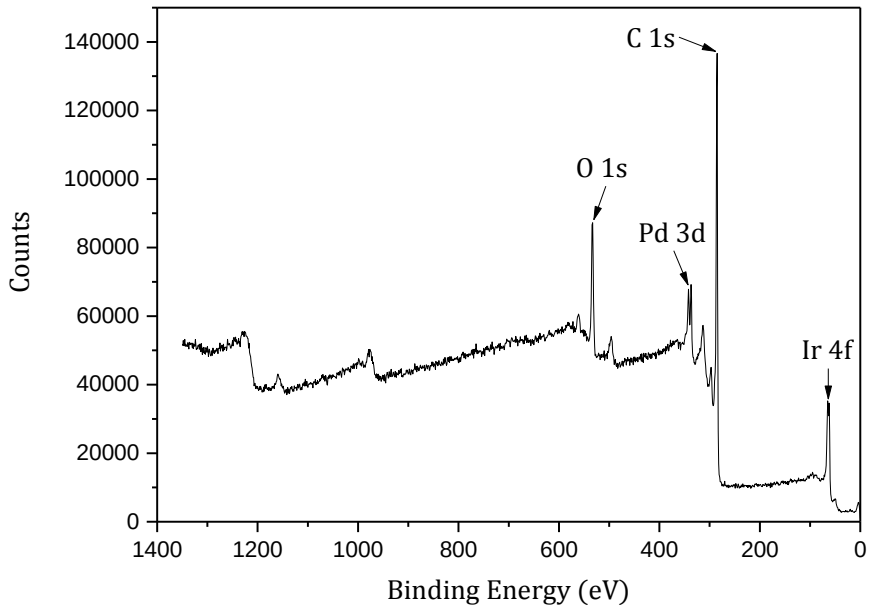

Figure 3.1 An Example XPS survey spectrum of PdIr/C highlighting characteristic peaks for the elements of interest.

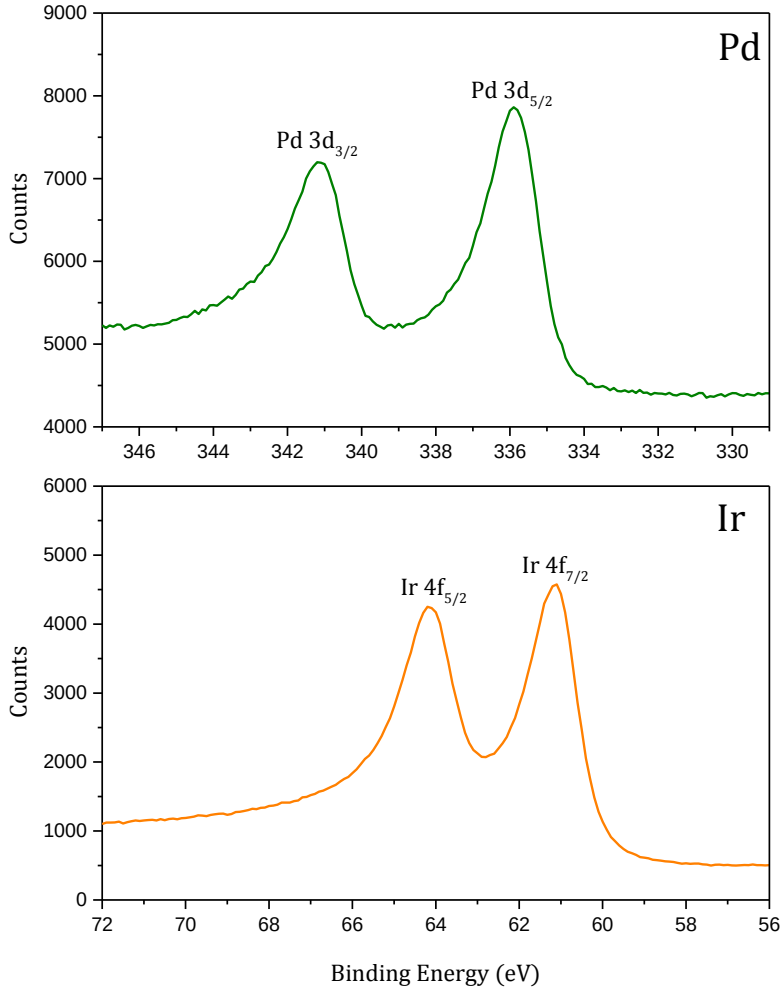

Figure 3.2 Detailed view of the Pd 3d and Ir 4f doublet peaks from the XPS of PdIr/C catalyst.

3.4.3 Experimental

XPS was carried out on a Thermoscientific K-alpha machine using a monochromatic Al Kα X-ray source of 1,486.68 eV energy and spot size of 400 µm. Powder samples were deposited on adhesive carbon tape with all excess removed to avoid cross contamination and areas of good catalyst coverage were selected for spectra acquisition. A total of five survey spectra, ten C spectra and 150 Pd/Ir spectra were taken for each sample to provide good signal to noise ratios. Data processing and peak fitting was carried out using CasaXPS software with Pd and Ir peak ratios set as described above, and peak separation for metallic and oxide peaks held at the same value.

All spectra were corrected such that the C 1s peak was set to 284.6 eV to normalise the data to that of graphitic carbon [168, 169], though in most cases the C 1s was very close to this value at around 284.68 eV ± 0.01. In order to try and reduce the extent of oxidation in the samples, reduction in a furnace at 80 °C and an 80% N_2 / 20% H_2 atmosphere for 1 hour was performed before all XPS experiments.

3.5 X-ray Diffraction

Due to the need to detect small changes in lattice parameter on alloying of the metals, synchrotron X-ray powder diffraction (SXPD) was used in preference to lab-based XRD in order to obtain a high enough resolution for accurate determination of this parameter.

3.5.1 Background Theory

X-ray diffraction (XRD) is a characterisation technique used to determine crystal structures, lattice parameters and crystallinity of samples. Incident monochromatic X-ray light is diffracted by crystalline compounds according to Bragg's law where constructive interference occurs when the following condition is met:

$$n\lambda = 2d\sin\theta \qquad \text{Equation 3.4}$$

Where λ is the X-ray wavelength, d is the spacing between diffraction planes and θ is angle between the incident light and the diffraction plane as shown in Figure 3.3.

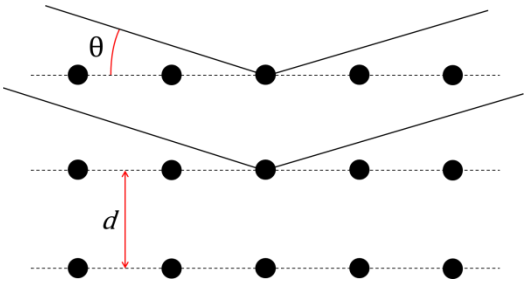

Figure 3.3 Diffraction in a crystal lattice according to Bragg's law.

The sample is normally scanned through a range of 2θ values where the intensity of the diffracted X-rays is recorded, though in some synchrotron ex-

periments a large 2D detector plate is sometimes used to collect the full diffraction ring structure, which is later processed into a 1D line. The diffraction pattern in powder XRD is a ring as there are many randomly oriented crystals in the sample and so all possible diffractions from lattice planes are present. Powder XRD can therefore be used to calculate the range of d-spacing in a crystal structure, and in conjunction with the Millar indices the lattice parameter can be calculated. For the case of a cubic structure, the following equation can be used to calculate the lattice parameter of a crystal:

$$d_{hkl} = \frac{a}{\sqrt{h^2 + k^2 + l^2}} \qquad \text{Equation 3.5}$$

Where h, k and l are the Millar indices of a specific crystal plane and a is the lattice parameter or constant.

Additionally, by using the Scherrer equation, a lower-bound of crystallite size can be determined:

$$\tau = \frac{K\lambda}{\beta \cos\theta} \qquad \text{Equation 3.6}$$

Where τ is the mean size of the ordered crystal domains, K is a shape factor (a dimensionless number used to correlate the crystallite size to the diffraction peak broadening), λ is the X-ray wavelength, β is the line broadening at half the peak height and θ is the Bragg diffraction angle. The Scherrer equation is only valid for particles smaller than 0.1 μm and can give deceptive results as it measures each crystallite and so does not take into account agglomeration. Nevertheless, it is often used for characterisation of fuel cell catalysts [170].

Shen et al. [156] used X-ray diffraction to confirm the alloying of Ir with Pd in their fuel cell catalyst by attributing a shift in the position of the Pd diffraction peaks to the incorporation of the smaller lattice parameter of the Ir. In this way they confirmed alloying of the two metals in their catalyst.

3.5.2 Experimental

Powder diffraction patterns were obtained using synchrotron radiation on beamline I11 [171] at the Diamond Light Source. The wavelength of the

incident radiation (λ = 0.826607(2) Å) was calibrated using Si standard powder (NIST SRM640c) and data collected for 2θ values between 0° and 150° in 1 mdeg steps (rebinned to 20 mdeg steps, only data up to 100° will be discussed in this thesis) using the high contrast multi-analysing crystal (MAC) detectors. The data were fitted using Le Bail refinement in TOPAS software (Bruker) in order to obtain crystallographic detail such as the lattice parameter. In addition, the refinement software can extract mechanical information such as apparent crystallite size using the Fundamental Parameter Method [172] calculated using the Double-Voigt Approach.

3.6 X-ray Absorption Fine-Structure

X-ray absorption fine structure (XAFS) describes how X-rays close to the core binding energy are absorbed by atoms and can give detailed information about chemical environment, coordination numbers and bond lengths. This technique is applied in a variety of fields, but of particular interest to the present work is the structural determination of fuel cell catalysts [173-178]. XAFS spectra are usually collected at a synchrotron light source due to the tuneable nature and intensity of the X-rays.

3.6.1 Background Theory

An incident monochromatic X-ray beam is shone onto a sample of known thickness and photons are absorbed by core electrons. The probability that an X-ray photon is absorbed is given by the absorption coefficient, μ described by Beer's Law:

$$I = I_0 e^{-\mu x} \qquad \text{Equation 3.7}$$

Where I_0 is the incident intensity, I is the transmitted intensity and x is the sample thickness. The absorption coefficient is measured at varying incident energies, with a sharp rise in absorption seen when the energy is close to that of the binding energy of a core electron. This is known as an absorption edge and can be clearly seen in Figure 3.4. Well defined core energy levels are known for the elements and therefore the X-rays can be tuned to energies at or above a specific edge for a specific element to probe its absorption structure. The XAFS spectrum is separated into two distinct

regions, the near edge spectra (XANES), which is typically within 30 eV of the absorption edge, and the extended fine structure (EXAFS) which appear as oscillations in μ, for reasons described later.

The ejected photoelectrons (produced by the photoelectric effect) will have an energy equal to that of the incident photon minus the binding energy of the electron $(E - E_0)$ and travel away from the excited atom with a wavenumber of $k = \sqrt{\frac{2m(E-E_0)}{\hbar^2}}$ (as it is a matter wave). The electron can be scattered by neighbouring atoms' electrons and return to the excited atom, interacting with the advancing wave, to produce an interference pattern or modulation in the absorption coefficient, μ (as μ is dependent on there being an appropriate available quantum state for the electron, the presence of a back-scattered electron will change the absorption coefficient). This is why fine structure arises in the absorption spectrum.

The fine structure in the EXAFS region has a fine structure function $\chi(E)$ defined as:

$$\chi(E) = \frac{\mu(E) - \mu_0(E)}{\Delta\mu_0(E)} \qquad \text{Equation 3.8}$$

Where $\mu(E)$ is the measured absorption coefficient, $\mu_0(E)$ is a background function representing the absorption of a single atom (with no neighbours causing modulation in the signal) and $\Delta\mu_0$ is the measured increase in absorption seen at the binding energy E_0 (shown on Figure 3.4). This function normalises the data and thus corrects for variations in the sample thickness, experiment set up and concentration of absorbing atoms so that different data sets can be compared (both within a single experiment set and between data collected on different machines).

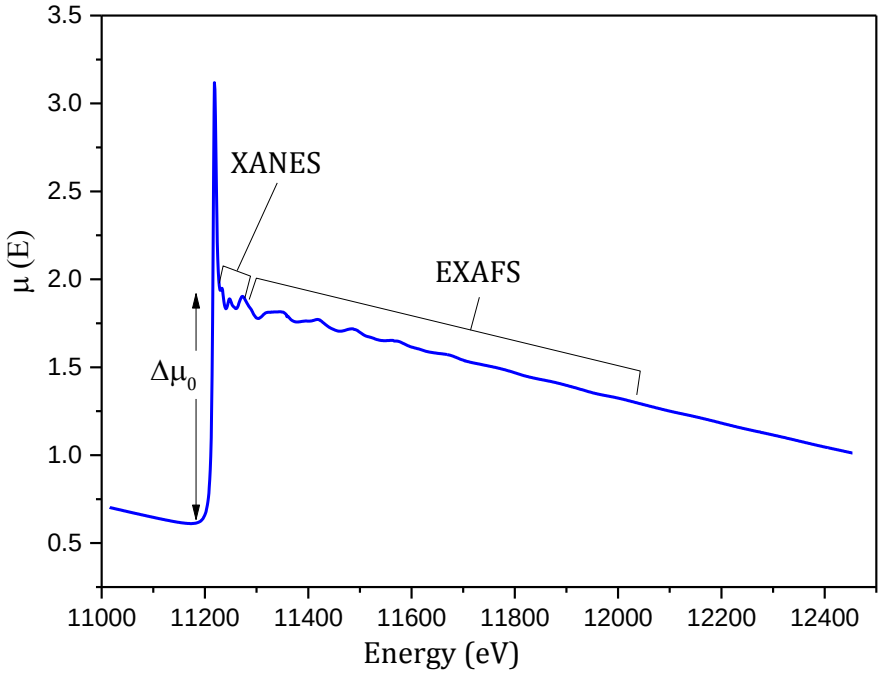

Figure 3.4 XAFS spectrum of the Ir L_3 edge of PdIr/C.

Different frequencies are seen in the EXAFS due to different near-neighbour coordination environments. This is modelled in the EXAFS equation given by:

$$\chi(k) = \sum_j \frac{N_j f_j(k) e^{-2k^2\sigma_j^2}}{kR_j^2} \sin\left[2kR_j + \delta_j(k)\right] \qquad \text{Equation 3.9}$$

Where $f(k)$ and $\delta(k)$ are scattering properties (amplitude and phase shift respectively) of the neighbouring atoms, N is the coordination number, R is the distance to the neighbouring atom, and σ^2 is the mean square disorder in R [179]. It should be noted that energy has been converted to k (wave-number) in this equation. This EXAFS equation averages many interacting atom pairs and accounts for different neighbouring atom types by summing contributions from all the different coordination shells, each one (of the same distance from the central atom) represented by j. This means that the EXAFS oscillation consists of many different frequencies, corresponding to all the different coordination shells, and therefore requires the use of Fourier transforms in the analysis.

To account for inelastic scattering and the lifetime of the hole created by ejection of a photoelectron (a back-scattered photoelectron must return to the atom before its excited state has decayed), the EXAFS equation is modified as follows:

$$\chi(k) = \sum_j \frac{N_j f_j(k) e^{-2k^2\sigma_j^2} e^{-2R_j/\lambda(k)}}{kR_j^2} \sin\left[2kR_j + \delta_j(k)\right] \qquad \text{Equation 3.10}$$

Where λ is the mean free path of the photoelectron, typically between 5 and 30 Å. The mean free path and R^{-2} terms mean that XAFS only probes the local environment of an atom to around 5 Å.

Extraction of these parameters from EXAFS data can provide very useful information about the structure of the catalyst, for example whether it has a core-shell structure or is a mixed alloy, and the degree of mixing therein [180-183]. A comprehensive overview of the modelling of structure and composition of nanoclusters via EXAFS can be found from Frenkel et al. [184].

Many empirical effects can affect the amplitude of the scattering, such as the detector setup and sample quality, as well as the nature of the absorbing element itself. For this reason, an amplitude reduction factor, S_0^2, is added as a multiplier of the amplitude function to give the final version of the EXAFS equation:

$$\chi(k) = \sum_j \frac{N_j S_0^2 f_j(k) e^{-2k^2\sigma_j^2} e^{-2R_j/\lambda(k)}}{kR_j^2} \sin\left[2kR_j + \delta_j(k)\right] \qquad \text{Equation 3.11}$$

3.6.2 Experimental

XAFS spectra were collected on the B18 beamline at the Diamond Light Source. 11 mm diameter pellets were prepared consisting of the catalyst and a cellulose power as a binder and pressed at 3 tonnes. The amount of catalyst in each pellet was determined by using HEPHAESTUS software [185] to calculate the desired absorption per unit area in order to give an edge jump between 0.25 and 1 for the edge of interest. For practical ease, the same pellets were used for the Pd and Ir edges, with a density selected as a compromise giving a sufficient jump at both edges.

Spectra were obtained at both the Pd K edge (24350 eV) and the Ir L_3 edge (11216 eV) in transmission mode for 300 s each in steps of 1 eV ms^{-1}. The beam operates with a ring energy of 3 GeV and a current of 300 mA and a Si(311) monchromator was used for all experiments. Calibration was performed on Pt and Pd foils, both of which were in place for every spectrum. At least 3 spectra were collected and merged for each sample in order to average the signal.

3.6.3 Data Analysis

Data analysis was carried out using the Demeter software suite [185] (consisting of ATHENA, ARTEMIS, HEPHAESTUS and ATOMS) implementing the FEFF6 and IFEFFIT codes [186, 187]. ATHENA is used to convert the raw data into absorption coefficient as a function of energy, $\mu(E)$. A background signal was generated using the AUTOBK method [188] in order to isolate the k-space EXAFS from the raw data and the data was normalised using ATHENA. Merging of multiple spectra was also carried out in ATHENA.

Fitting of the merged data was carried out using ARTEMIS software in conjunction with FEFF. FEFF is used to generate scattering paths for given structures and calculate theoretical scattering amplitudes and phase shifts which, along with $\lambda(k)$, are used in the EXAFS equation to predict and refine the structural parameters N, R and σ until a good fit to the experimental data is obtained. From Equation 3.11 it can be seen that both N and S_0^2 are multipliers of the scattering amplitude, and therefore cannot be independently determined without prior knowledge of the system. For this reason, the first fit conducted was on the Pd reference foil (Figure 3.5) as the coordination number can safely be assumed to be that of crystalline Pd, 12. By setting $N = 12$ the value of S_0^2 returned from the fit of the reference foil is equal to the amplitude reduction factor, determined to be 0.83 ± 0.05. This value is then used in the fitting of the catalyst sample data, where the coordination is unknown (there will be some degree of coordination of, say, a Pd absorber to all of Pd, Ir and O and therefore the Pd-Pd coordination is expected to be less than 12 as it is in a pure crystal). The value for S_0^2 is chemically transferable, meaning that the value calculated for Pd foil is applicable to all Pd compounds. For fitting of the catalyst

samples N is set to 1, meaning that the returned value of S_0^2 is actually the product of the coordination number and the amplitude reduction factor, and thus dividing this number by, in our case, 0.83 yields the coordination number for a given scattering path. In the absence of an Ir reference foil, the value of 0.83 was also used in fitting paths with Ir as the absorbing atom. Given that the empirical effects of the experimental setup and the sample inhomogeneity are consistent (the same pellet is used for both Pd and Ir edge measurements) this approach is generally valid, though it is likely to be a source of small error in the determined values of the parameters. Additionally, the S_0^2 for Pt foil was also calculated to be 0.80 ± 0.06 (a similar value was found by Nashner et al [189]) and given that Pd, Pt and Ir are all electronically similar it is a reasonable approximation to apply the value from Pd and Pt to the Ir fit.

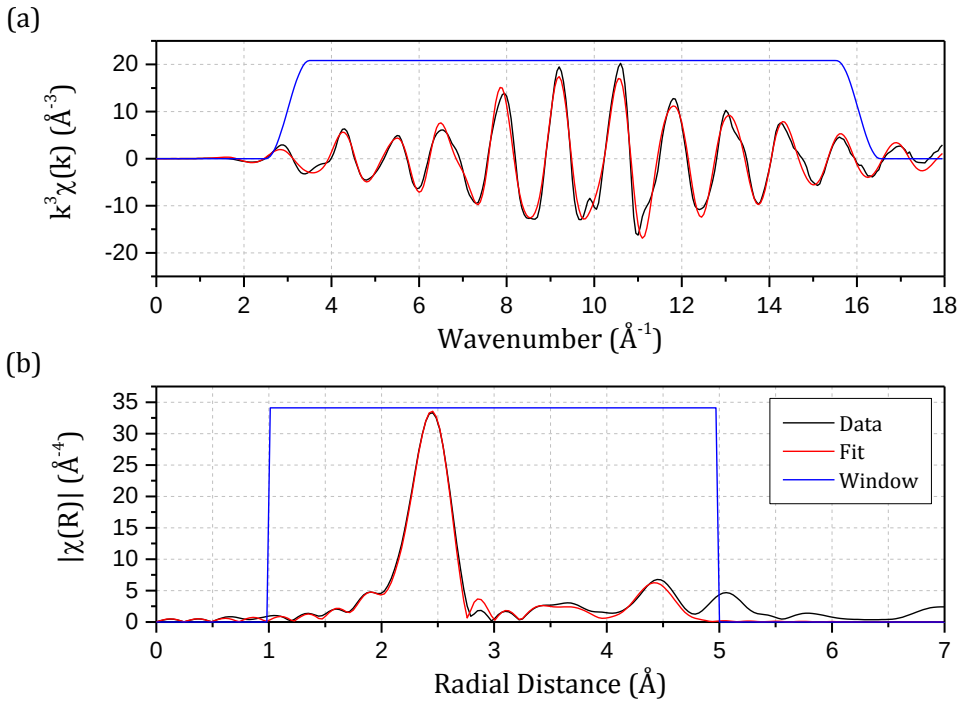

Figure 3.5 (a) The k^3 weighted Pd K edge experimental data (black) and fits (red) for the Pd reference foil from which the amplitude reduction factor of 0.83 was calculated and (b) the corresponding k^3 weighted Fourier transform.

With the amplitude reduction factor determined, modelling and fitting of the PdIr/C system was carried out. As no crystallographic data for PdIr alloy nanoparticles were found on the Crystallography Open Database (COD), some assumptions and modifications of extant structural infor-

mation were required in order to generate scattering paths through the ATOMS and FEFF programmes.

The first and main constraint applied to the model is to only look at the first coordination shell, i.e. the nearest neighbours of the absorbing atom, by selecting only the single scattering paths, from absorber atom to nearest scattering atom and back to the absorber atom (Figure 3.6). This is sufficient to ascertain the coordination of both absorbing atoms (Pd and Ir) to each of Pd, Ir and O and therefore deduce the structure of the catalyst, and keeps the number of variables in the fit as low as possible [190].

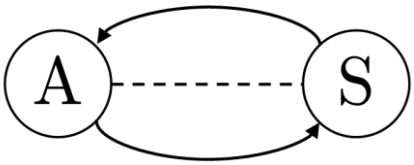

Figure 3.6 The single scattering path from absorber atom (A) to scattering atom (S) and back.

The following input structures from the COD were used in the ATOMS programme to generate structures for the FEFF calculations; Pd [191], Ir [192], PdO [193] and IrO_2 [194]. The lattice parameters of both Pd and Ir were adjusted to the value obtained from XRD for the PdIr/C 1:1 catalyst, 3.8851 Å. The paths used for the Pd edge data were: Pd*-Pd-Pd*, Pd*-Ir-Pd* and Pd*-O-Pd* and for the Ir edge; Ir*-Ir-Ir*, Ir*-Pd-Ir* and Ir*-O-Ir* where the asterisk denotes the absorbing atom. The Pd*-Ir-Pd* path was generated by exchanging the absorber atom in the Ir crystal structure for Pd in FEFF (and leaving all other atoms in the cluster as Ir), and vice versa for the Ir*-Pd-Ir* path.

With all the paths generated, the data for the Pd edge and Ir edge were simultaneously fitted using ARTEMIS. This model gives 18 separate parameters divided in the following way:

- $2 \times \Delta E_0$: The edge energy for Pd and Ir
- $6 \times S_0^2$: Amplitude reduction factor, effectively the coordination number as N is set to 1, for Pd-Pd, Pd-Ir, Pd-O, Ir-Ir, Ir-Pd and Ir-O
- $5 \times \Delta R$: The average variation in bond length from the theoretical bond length, R_0, calculated from the ATOMS input such that $R = R_0 + \Delta R$. The distinct bond lengths are; Pd-Pd, Pd-O, Ir-Ir, Ir-O and Pd-Ir (Ir-Pd is identical)

- $5 \times \sigma^2$: The mean square disorder in bond length for the 5 distinct bonds outlined above

All data were fitted for $3 \leq k \geq 17$ Å^{-1} (the range over which there were significant oscillations in the absorption coefficient) and $1 \leq R \geq 3$ Å, the latter constraining the fit to the first coordination sphere. None of the paths used in the fit had contributions above $R = 3$. A k^3 weighting was also used for all fits in order to amplify the spectrum at high wavenumber, which tends to attenuate rapidly with increasing k, giving a roughly equal amplitude of oscillation across the full k range and thus making sure the data across the full range contribute equally (Figure 3.5 (a)).

3.7 ICP-AES

Inductively coupled plasma atomic emission spectroscopy (ICP-AES) is often used for trace metal analysis. It uses ICP to excite ions that then emit characteristic energy spectra, of which the relative intensity can be used to calculate the concentration of the element in the sample. The catalysts were digested into their constituent elements using concentrated HNO_3 and HCl (3:1 ratio, aqua regia) under sonication for 1 hr and then the elemental make-up of the catalysts tested with ICP-AES at the Department of Civil Engineering Imperial College London. The instrument used was an Optima 7300 DV ICP-OES from Perkin Elmer (Massachuetts, USA).

3.8 Low Energy Ion Scattering

Low energy ion scattering (LEIS) is a surface sensitive spectroscopic technique that uses ionised atoms of the noble gases, He, Ne or Ar, to chemical and structural make up of surfaces by measuring the energy and position of the incident ions after interaction [195, 196]. As the energy of the scattered ion is directly related to the mass of the scattering atom, a spectrum of masses of surface elements can be developed [197]. Due to the high probability of neutralization of low energy noble gas ions, it is only ions scattered by the outermost surface atoms that have any chance of returning to the detector as ions, and thus the technique is inherently surface sensitive (compared with XPS which is often used for surface analysis yet probes a depth of around a dozen atomic layers [198]). This makes it a useful tool for the study of many surfaces, particularly catalysts where the surface struc-

ture and composition are integral to the performance of the material [199, 200]. LEIS does not have a high enough spatial resolution to measure individual particles and thus for these purposes is a bulk (surface) technique [201].

The instrument used for the LEIS experiments in this thesis was an IONTOF Qtac100 equipped with He, Ne and Ar primary ion sources with a fixed beam angle of 145° and scattered ions detected at the full azimuthal angle. Samples were prepared by compressing the catalyst powder into a thin disk pellet in order to give as flat a surface as possible.

As all catalyst samples had some element of surface oxidation or other contamination, sputtering was required to clean the surface and obtain a signal from the Pd and Ir in the nanoparticles. The sputtering beam used in all presented experiments was Ar, with Ne used as the primary beam at 5 keV. Spectra were collected using an alternating 30 s acquisition time followed by a 10 s sputtering. This cycle was repeated 131, 145 and 141 times for the PdIr/C, PdIr/C_{HSA} and PdIr/C 9:1 catalysts, respectively. The partial spectra were then totalled to give the accumulated spectrum. Background signals were removed to give a net intensity for the Pd and Ir peaks, which were then fit using the included instrument software in order to obtain the peak integral ratios. The partial spectra were also fit individually using this method in order to generate the sputtering profile data.

3.9 Electrochemical Testing

3.9.1 Materials and Equipment

3.9.1.1. Chemicals

Potassium Hydroxide: 38%$_{wt}$ solution of KOH in water, AnalR Normapur grade from Sigma Aldrich. A high purity KOH solution used as the electrolyte for all electrochemical experiments to minimise the effect of impurities.

Nafion Solution: A dispersion of Nafion ionomer in a water solution, 10.3% Nafion by mass, from Dupont. Used in ink preparation.

Acetone: >99.5% from Sigma Aldrich. Used in ink preparation.

IPA: Isopropyl alcohol, $CH_3CH(OH)CH_3$ >99.7% from VWR. Used in ink preparation.

Micropolish: A suspension of 1µm aluminium oxide particles used in conjunction with a microcloth for polishing of glassy carbon electrodes obtained from Buehler.

Gases: All gases used are from BOC and are zero grade. Gases used are: N_2, H_2 and CO.

Catalysts: The catalysts used for these experiments are the in-house PdIr/C, PdIr/C_{HSA}, Pd/C and Ir/C, and a commercially available Pt/C catalyst from Alfa Aesar. The commercial catalyst was 39.25% Pt by mass and with an XRD crystallite size of 3.5 nm.

3.9.1.2. Equipment

Piping and Fittings: Nylon 1/4in outer diameter piping is used all gas connections. Swagelock and Hamlet LetLock compression fittings are used for gas-tight connections. All piping and fittings are supplied by FTI Ld.

Glassware: Bespoke 3-electrode glass electrochemical cells were supplied by Adams and Chittenden. They consist of a main chamber surrounded by a water-jacket camber, a luggin capillary for the reference electrode chamber and a counter electrode chamber separated from the main chamber by a ceramic frit. There is a 24/40 ground glass opening to the main chamber allowing a good fit with the PTFE rotator sheath, and three threaded openings allowing a gas in tube, gas out tube and thermometer to be inserted.

PTFE Cell: A bespoke PTFE cell was also used for electrochemical experiments, more details of which are given in Section 3.9.3.

Rotator: A rotator and controller unit from Pine Instruments is used to control the rotation rate of the electrode.

Rotating Disk Electrode: A PTFE-encapsulated glassy carbon electrode is threaded onto the end of the rotator shaft and forms the working electrode.

Reference Electrode: A Hydroflex reversible hydrogen electrode (RHE) from Gaskatel was used as the reference electrode. The electrode consists of a platinum wire and a cartridge hydrogen supply. The PTFE shaft contains no electrolyte and so is designed to be used in a wide range of working electrolyte solutions. The reference electrode establishes the potential against which all other measurements are made.

Counter Electrode: Also called an auxiliary electrode, a high surface area Pt mesh (99.9% Pt, from Alfa Aesar) is used to counter any electrochemical-half reaction occurring at the working electrode (acting as a cathode when the working electrode is the anode and vice versa). The counter electrode must be of much greater surface area than the working electrode to ensure that the reaction occurring at it is fast and therefore does not impede the reaction at the working electrode [202].

Faraday Cage: Constructed using aluminium frame and galvanised wire mesh, the faraday cage is used to isolate electrical noise from the experiments.

Potentiostat: An Autolab PGSTAT302 from EcoChemie was used to control and measure the potential and current of the working electrode. It is connected to the working, reference and counter electrodes and grounded to the faraday cage.

3.9.2 Experimental

3.9.2.1. General Experimental Preparation

Before each experiment the glass cell and its components are thoroughly cleaned with acetone, deionised water and then 100 ml of 1M KOH solution. To ensure that all parts of the cell are covered by KOH, it is tilted side to side to remove any air bubbles in the luggin capillary and other electrode chambers. The cell is then rinsed and filled with deionised water for storage. This cleaning procedure is repeated weekly or whenever an impurity is encountered.

The pre-prepared electrode is then wetted with deionised water and attached to the rotator shaft and the cell is assembled with a RHE reference electrode and a Pt mesh counter electrode and 125 ml of 1M KOH solution. The working electrode is lowered to within 5 mm of the luggin capillary opening to negate any electrode resistances. Any air bubbles in the cell, luggin capillary or on the surface of the working electrode are removed by tilting the cell or rotation of the electrode.

Nitrogen gas is bubbled through the solution for 20 minutes via a glass tube containing a frit to reduce the bubble size and increase dissolution and therefore deaerating the solution. The final preparation step is electrochemical cleaning of the electrode. This is accomplished by potential cycling be-

tween 0 – 1.2 V vs RHE at 20 mVs^{-1} for 10 cycles, or until the CV is stable and repeatable. The system is now ready for electrochemical experiments.

3.9.2.2. Electrode Preparation

Glassy carbon electrodes are cleaned and polished using a figure of eight motion on a micropolishing cloth and with 1 μm alumina solution for five minutes, or until a mirror finish is obtained. The electrode is then washed with acetone and thoroughly rinsed with deionised water before drying under a glass beaker.

The volume of ink required to make the electrode is calculated by using the desired metal loading and the metal ink density (from Equation 3.2):

$$V_{\text{ink}} = \frac{m_{\text{metal}}}{\rho_{\text{ink}}} \qquad \text{Equation 3.12}$$

This volume of ink is then deposited on the glassy carbon electrode surface with a micropipette in such a way that it is in contact with the glassy carbon only, and not the PTFE sheath, and left to dry at room temperature under a glass beaker. Garsany et al. [203] showed that the quality of the catalyst layer of the electrode can have a large bearing on the electrochemical performance, and so a uniform layer covering the entire surface of the glassy carbon is desired. The loading of metal in the experiments used is 35 $\mu g\ cm^{-2}$.

3.9.3 PTFE Cell

Strong alkaline solutions can corrode glass and so all electrochemical experiments were conducted as swiftly as possible to minimise contamination from the glass cell. Mayrhofer et al. [204] studied the effect of glass corrosion on the electrocatalysis of Pt and suggested use of a PTFE electrochemical cell in order to improve the reproducibility and quality of the electrochemical results. A bespoke PTFE cell was manufactured to the specifications outlined by Mayrhofer et al. to allow more stable and repeatable results, as well as the ability to conduct long term durability experiments (see Section 5.2.7).

The PTFE cell includes separate reference and counter electrode compartments, the former connected to the main cell chamber via a narrow bore that acts as a luggin capillary. The hydrogen concentration in the elec-

trolyte was initially found to be too low when using the PTFE and so a lid designed to perfectly fit the conical sheath of the RDE was constructed. This improved the hydrogen pressure in the cell and therefore the hydrogen saturation in the electrolyte, and consequently the HOR results. All parts of the cell including the frits and gas diffusion structures were constructed of PTFE.

In a further attempt to increase stability and repeatability, and also to more closely reflect the majority of the work in the literature, the KOH solution used the subsequent PTFE cell experiments was reduced to 0.1 M.

The lack of protruding luggin capillary in the cell could mean that there is less travel distance for the electrolyte flow towards the electrode surface (directed by the rotation of the disk electrode) than in the glass cell set up. This means that the practice of placing the electrode as close to the luggin as possible might not be valid or desirable in the PTFE cell. Indeed, it was found that when the electrode was placed too close to the luggin hole the HOR activity was artificially low, giving a similar effect to that seen when H_2 concentration is low. Thus, the electrode was placed around 10 mm away from the luggin and its position on the clamp stand marked in order that all subsequent experiments were conducted with a similar distance to the luggin.

3.9.3.1. Alkaline inks

Nafion was originally used as a binder in the RDE inks, as in some examples in the literature [205-207], but as the electrochemical surface area derived from alkaline experiments was lower than for the same catalysts in acid (see Section 5.1.1) (these results not shown in this thesis) it was suspected that the Nafion binder might be inhibiting the OH^- mediated HOR in alkaline. Therefore, an alkaline anion ionomer solution (AS-4, Tokuyama Corporation) was obtained and used in further testing.

Excepting the differences mentioned above, all other gases, reagents and experimental conditions were consistent with the testing in a glass cell.

3.10 Electrochemical Impedance Spectroscopy

Electrochemical impedance spectroscopy (EIS) is a powerful diagnostic tool for electrochemical systems or reactions. It involves imposing a perturbing sinusoidal signal of either voltage or current and measuring the corresponding response in either current or voltage over a range of frequencies of the

applied signal. Different processes will have different responses at different frequencies due to the time constant of their response, and so ohmic, charge transfer and mass transport losses (resistances) can be inferred and modelled from EIS.

3.10.1 EIS Background Theory

Taking the example of applying a voltage signal and measuring the current response, a sinusoidal perturbation in V is applied over a wide range of frequencies (typically between 100 kHz and 0.1 mHz) and the current response is measured at each frequency. The voltage and current signals are described by the following equations, respectively, as a function of time:

$$V(t) = V_0 \cos \omega t \qquad \text{Equation 3.13}$$

$$I(t) = I_0 \cos(\omega t + \phi) \qquad \text{Equation 3.14}$$

Where V_0 and I_0 are the amplitudes of the signals, ω is the angular frequency and ϕ is the phase shift of the measured response with respect to the applied signal. This can be seen in Figure 3.7.

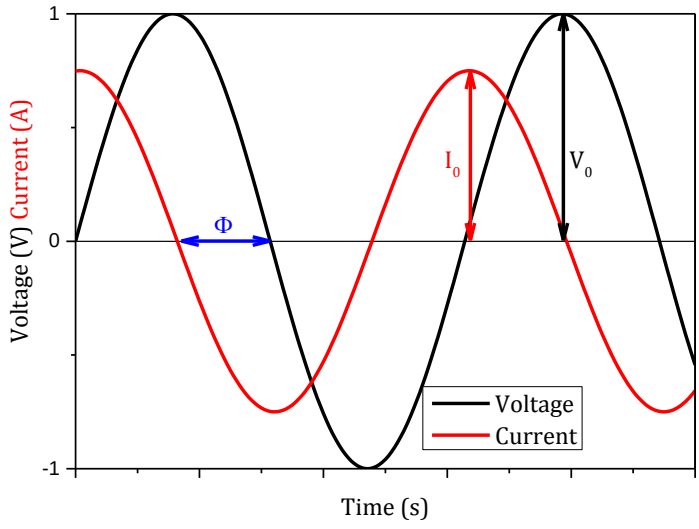

Figure 3.7 The applied voltage signal (black) and corresponding current response (red).

Impedance is a complex property and is composed of a real component (resistance) and an imaginary component (reactance – capacitance or inductance). This can be represented in Cartesian form as:

$$Z = Re\{Z\} + Im\{Z\} = R + iX \qquad \text{Equation 3.15}$$

Or in polar coordinates as:

$$Z = |Z|e^{i(\phi)} \qquad \text{Equation 3.16}$$

Where Z is the complex impedance, R is the resistance, X is the reactance, $i = \sqrt{-1}$, $|Z|$ is the magnitude of the impedance and ϕ is the phase shift between the voltage and current signals.

Expressing the voltage and current in the polar forms, and noting that via Euler's relationship $\cos(\omega t + \phi) = Re\{e^{i(\omega t+\phi)}\}$ (the real part of a complex function), gives representations of the voltage and current as follows:

$$V(t) = V_0 e^{i\omega t} \qquad \text{Equation 3.17}$$

$$I(t) = I_0 e^{i(\omega t-\phi)} \qquad \text{Equation 3.18}$$

The impedance of a system, Z, is defined in an analogous way to Ohm's law as:

$$Z(\omega) = \frac{V(t)}{I(t)} = \frac{V_0 e^{i\omega t}}{I_0 e^{i(\omega t-\phi)}} = |Z|e^{i\phi} \qquad \text{Equation 3.19}$$

It can therefore be seen that the magnitude of the impedance ($|Z|$) is the ratio of the amplitudes of voltage and current. Impedance spectra are often represented as Nyquist plots with $Re\{Z\}$ on the x-axis, $-Im\{Z\}$ on the y-axis and $|Z|$ and ϕ shown by the length and anticlockwise angle to the x-axis of a vector drawn to any data point, respectively. This is shown in Figure 3.8. Each data point on a Nyquist plot is the impedance at a single frequency and as such is not explicit in showing frequency information. For this, a Bode plot is used whereby the frequency is plotted against both magnitude and phase (Figure 3.9). By Euler's relationship:

$$|Z|e^{i\phi} = |Z|(\cos\phi + i\sin\phi) = R + iX \qquad \text{Equation 3.20}$$

Therefore magnitude and phase are given by:

$$|Z| = \sqrt{R^2 + X^2} = \sqrt{(Re\{Z\})^2 + (Im\{Z\})^2} \qquad \text{Equation 3.21}$$

$$\tan\phi = \frac{\sin\phi}{\cos\phi}, \phi = \tan^{-1}\left(\frac{Im\{Z\}}{Re\{Z\}}\right) \qquad \text{Equation 3.22}$$

Therefore the magnitude and phase at each frequency can be calculated from the real and imaginary components of the impedance, obtained from the x and y values of a data point on a Nyquist plot. In practice, the phase and magnitude of the applied and measured signals are recorded by the impedance analyser and the Nyquist plot is constructed from these values [208].

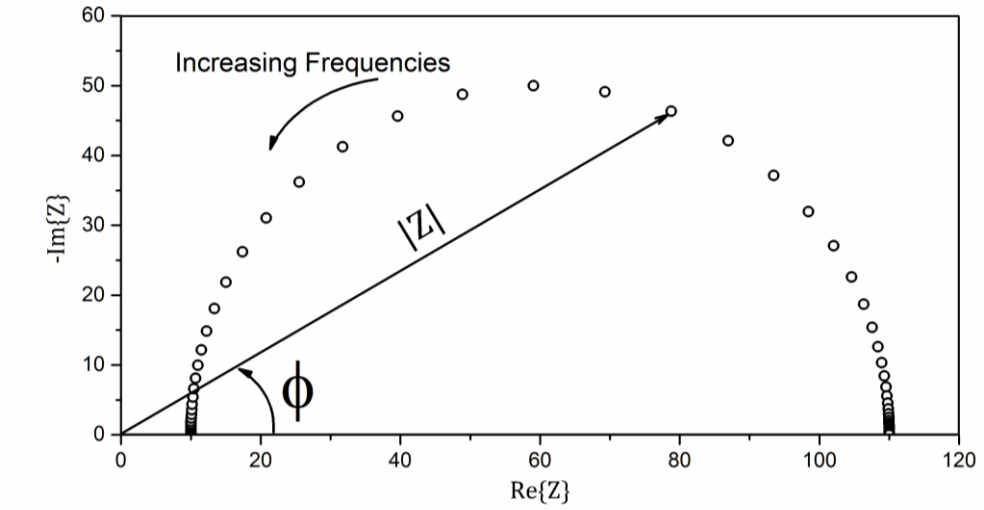

Figure 3.8 Nyquist plot of impedance data simulated using Z view software for a Randles circuit with elements $R_1 = 10\ \Omega$, $R_2 = 100\ \Omega$ and $C = 10^{-6}$ F and frequencies from 1 mHz to 1 MHz.

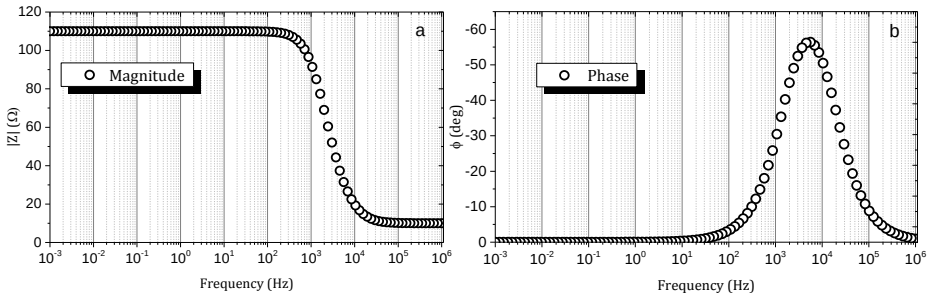

Figure 3.9 Bode plots of the same simulated circuit as in Figure 3.8 showing the variation in (a) magnitude and (b) phase with frequency.

3.10.2 Equivalent Circuits

Impedance data can be used to model electrochemical processes as electrical circuits consisting of ideal resistors (R), capacitors (C), and inductors (L). This allows parameters such as solution resistance, charge transfer resistance and double-layer capacitance to be extracted from fitting of impedance data and therefore a powerful insight into the various processes occurring in an electrochemical reaction unavailable from, for example, a polarisation curve. The impedance of each element is shown below:

$$Z_{\mathrm{R}} = R \; ; \; V = IR \qquad \text{Equation 3.23}$$

$$Z_{\mathrm{C}} = \frac{1}{i\omega C} \; ; \; I = C\frac{\mathrm{d}V}{\mathrm{d}t} \qquad \text{Equation 3.24}$$

$$Z_{\mathrm{L}} = i\omega L \; ; \; V = L\frac{\mathrm{d}I}{\mathrm{d}t} \qquad \text{Equation 3.25}$$

One of the most common equivalent circuits is the Randles circuit (Figure 3.10), used to simulate the Nyquist plot shown in Figure 3.8. It consists of a resistor (R_{EL}) representing the electrolyte resistance in series with a parallel combination of a capacitor (C_{DL}) representing the double-layer capacitance at an electrode surface and a resistor (R_{CT}) representing the Faradaic charge transfer resistance. This circuit produces a perfect semi-circle on a Nyquist plot, with the offset from the origin being equal to R_{EL} (the high frequency intercept) and the diameter of the semi-circle being equal to R_{CT} (the low frequency intercept, minus R_{EL}).

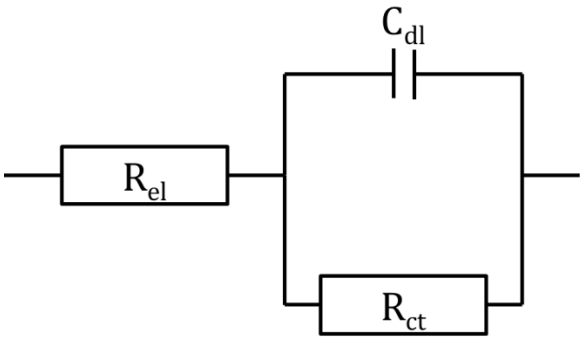

Figure 3.10 An ideal Randles circuit

In reality, electrochemical reactions at electrode surfaces are complex and do not behave ideally and modifications of the circuit elements are made to account for this. One such modification is to use a constant phase element (CPE) in place of a capacitor. The CPE models the behaviour of a double-layer in that it acts as an imperfect capacitor in the following way:

$$Z_{\mathrm{CPE}} = \frac{1}{Q(i\omega)^n} \qquad \text{Equation 3.26}$$

Where Q is the CPE's admittance and n is an integer value $0 \leq n \leq 1$. When $n = 1$ the CPE is an ideal capacitor with capacitance of Q and when $n = 0$ it is an ideal resistor. When using a CPE to model a non-ideal capacitor, n should be > 0.75, or else the CPE element is far from behaving as a capacitor. The CPE, when in parallel combination with a resistor, causes a depression in the semi-circle of the Nyquist plot. The phase of a CPE is independent of frequency and is equal to $-(90° \times n)$, where $0 \leq n \geq 1$, and $n = 0$ behaves like a pure resistor and $n = 1$ an ideal capacitor.

When diffusion resistance, or mass transport resistance, exists in an electrochemical system a Warburg element with the following impedance is used:

$$Z_{\mathrm{W}} = \sigma\omega^{-1/2} - i\sigma\omega^{-1/2} \qquad \text{Equation 3.27}$$

Where σ is the Warburg coefficient. When placed in series with the charge transfer resistance (Figure 3.11) an infinite Warburg element produces a 45° line after the charge transfer arc (Figure 3.12 a). A similar effect can be produced when $n = 0.5$ for a CPE. This Warburg impedance only applies when there is an infinite diffusion layer thickness. In the case of limited diffusion, such as that created by the well-defined diffusion boundary layer in an RDE experiment, a bounded transmissive Warburg element is used, with impedance of:

$$Z_{\mathrm{BW}} = \frac{R_{\mathrm{D}}\tanh(\sigma\omega)^{1/2}}{(\sigma\omega)^{1/2}} \qquad \text{Equation 3.28}$$

Where R_D is the mass transport resistance [209]. This has the effect of forming a second arc after the charge transfer arc on the Nyquist plot (Figure 3.12 b) with a diameter of R_D.

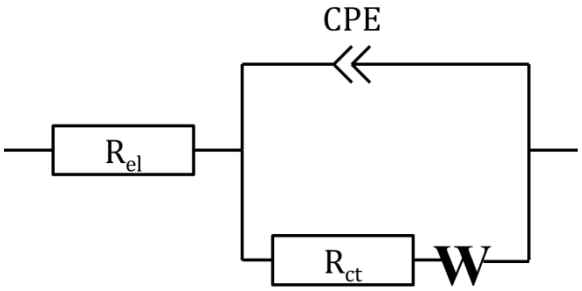

Figure 3.11 A Modified Randles circuit with a CPE replacing the ideal capacitor and a Warburg element (infinite or finite) in series with the Faradaic resistance.

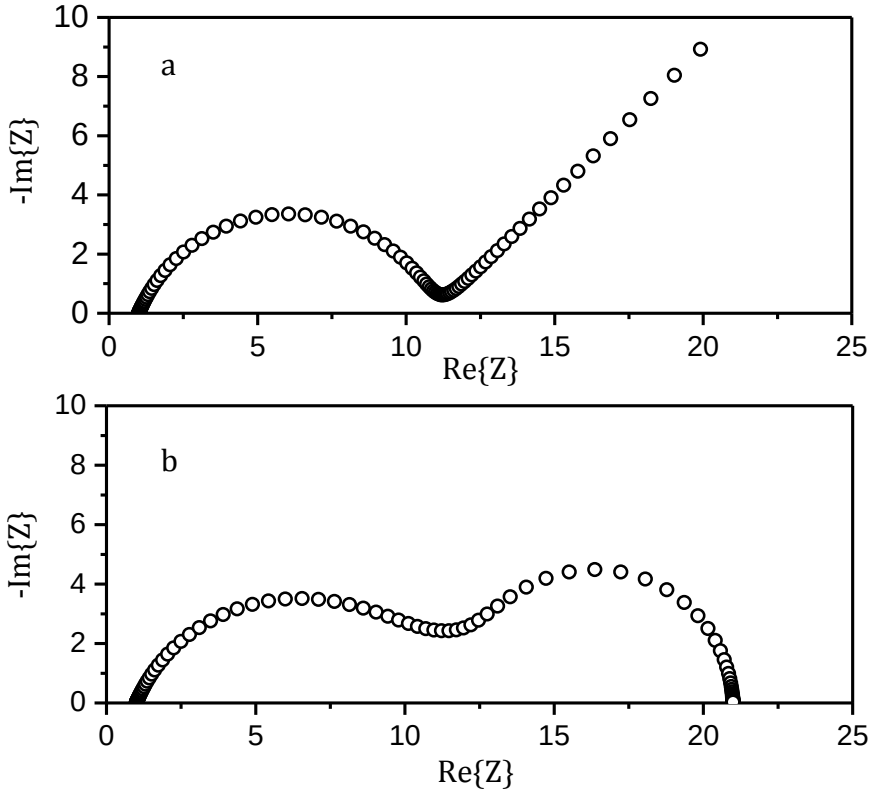

Figure 3.12 Nyquist plots for simulated Randles circuits with (a) an infinite Warburg element and (b) a finite Warburg element with frequency range 1 mHz to 1 MHz. Both show depressions of the charge transfer arc due to the use of a CPE in place of an ideal capacitor.

The preceding treatments apply to an electrochemical reaction at a single electrode. In the case of a fuel cell a second Randles circuit can be placed in series to the first in order to model both the anode and the cathode, with a single series resistor giving the sum total ohmic resistance of the cell.

When a suitable equivalent circuit is chosen, based on the data obtained and the expected electrochemical setup (for example, noting if diffusion limitation is likely to apply and the number of reactions occurring) a complex non-linear least-squares method can be used to fit the equivalent circuit to the experimental data and therefore obtain the relevant parameters of the model. In particular, calculating the charge transfer and mass transport resistances can give vital information about the performance of a catalyst and electrode in a fuel cell.

3.10.3 Experimental

Impedance data were collected using an Autolab potentiostat and FRA software in potentiostatic mode over a frequency range of 0.1 Hz to 100 kHz with an amplitude of 10 mV. ZView software (Scribner) was used to model and fit the equivalent circuits. All impedance measurements were taken with respect to open circuit potential, as measured by the potentiostat.

3.11 Durability Experiments

The stability of the PTFE cell set up compared with the glass cell affords the ability to study the durability of the catalysts under accelerated stress testing. Many accelerated test protocols exist for acidic PEM fuel cells, however, to the author's knowledge no standardised tests exist for alkaline catalyst durability. For this reason, the standard protocols for PEM testing were followed, and detail of the electrochemical procedures used is given in Section 5.2.7. The PTFE cell was prepared in the same way as for all other electrochemical testing.

3.12 Fuel Cell Testing

Initial in situ fuel cell testing of the catalysts was conducted using two main systems; a bespoke Whistonbrook system consisting of automated load, valves, flow meters and cell heaters, and a commercial Scribner test station that also included a humidification system.

3.12.1 Materials

Below are details of all materials and equipment used for fuel cell testing.

3.12.1.1. Chemicals

Sulphuric Acid: H_2SO_4 for Nafion membrane preconditioning, from Sigma Aldrich, ≥97.5% assay.

Hydrogen Peroxide: H_2O_2 for cleaning Nafion membranes, 3% solution in water from Sigma Aldrich.

Potassium Hydroxide: KOH for Tokuyama membrane preconditioning, from Sigma Aldrich, ≥85% hydrated.

Gases: All gases used are from BOC and are zero grade. Gases used are: O_2, N_2, H_2, Air and CO_2-free air.

3.12.1.2. MEA Materials

Nafion 212: Proton conducting membrane from Dupont.

Tokuyama A006: OH^- conducting polymer membrane from Tokuyama Corporation.

Tokuyama A201: OH^- conducting polymer membrane from Tokuyama Corporation.

Gas Diffusion Material: GDM consisting of Toray macroporous carbon paper (GDL) coated in a PTFE-based carbon ink, total thickness ≈ 190 μm. Used as a base for the catalyst coating in order to make fuel cell electrodes. JM v2 GDM obtained from Johnson Matthey.

Platinum Electrodes: Commercial fuel cell electrodes from Alfa Aesar consisting of Toray GDL, carbon ink layer bound by PTFE and catalyst layer containing a loading of 0.54 mg cm^{-2} of catalyst and the same mass of Nafion binder. The product name is 'H_2 Electrode/Reformate Cathode'.

Tygaflor: A PTFE coated woven fabric used to protect the MEA during the hot-pressing process.

3.12.1.3. Equipment

Piping and Fittings: Nylon 1/4in outer diameter piping is used for room temperature gas connections, PTFE 1/8in piping is used for gas connections in and out of the test cell where temperatures might exceed 65°C and steel piping is used for permanent fittings (1/4" and 1/8"). Swagelock and Hamlet LetLock compression fittings are used for gas-tight connections. All piping and fittings are supplied by FTI Ltd.

Hot Press: Carver pneumatic hot press with 12×12 inch pressing area used to laminate MEAs. Fitted with oil pressure gauges for monitoring applied force.

Bespoke Test Station: Fuel cell testing is carried out with a bespoke fuel cell test station created by Whistonbrook. It consists of a 10 A load bank, a potentiostat to measure the cell voltage, 5 thermocouple inputs, two electric heating cartridges and electronic valves for the following gases: Air, Helox, Oxygen, Nitrogen, Hydrogen and 'Mixed'. All flow rates are regulated via software-controlled

electronic mass flow meters (Bronkhorst) except hydrogen gas which is controlled manually with an acrylic flow meter. It also has a software-controlled peristaltic pump for methanol delivery and a manual bladder valve for cell compression with N_2 gas (see Figure 3.13). The system is capable of impedance measurements via the current interrupt method.

Commercial Test Station: Improved fuel cell testing was performed using the commercial Scribner 840 fuel cell test system (Scribner Associates). The unit comprises controlled and programmable load, fuel and temperature controls and dew-point humidification control of all gases. The improved humidification in particular leads to higher performing fuel cells. The same single cell test cell was used for this system as for the Whistonbrook system.

Humidification: For the Whistonbrook system, humidification of the gas streams is achieved by bubbling the gas through Schott bottles (through a bed of glass beads to help diffusion) held in a water bath at 10 °C higher than the cell operating temperature. The gas enters the humidification system after exiting the Whistonbrook test station and the humidified gas flows through insulated PTFE tubing directly into the test cell. As already mentioned, the Scribner system has integrated dew-point humidification control and provides much improved humidification.

Test Cell: Single MEA test cell of active area 10.9 cm^2 shown in Figure 3.13.

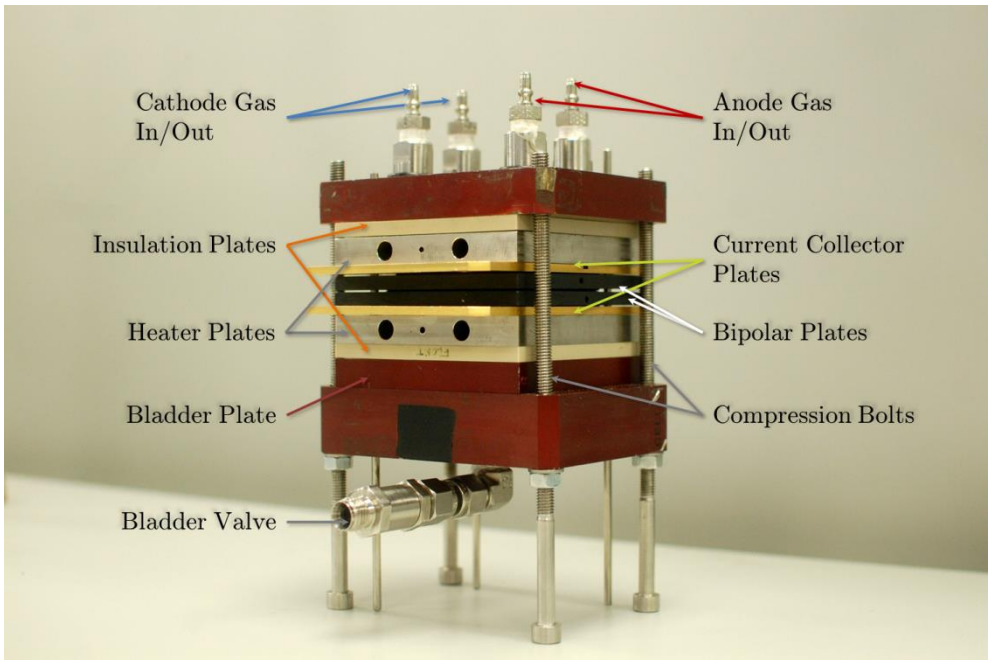

Figure 3.13 Test cell for single MEA testing. The MEA is sandwiched between the two bipolar plates which contain two holes for the voltage sensor leads (seen on the right of the image) and the load is applied to the gold current collector plates. Heating cartridges are inserted into the large holes in the heating plates and thermocouples in the smaller holes. Cell compression is achieved through gas pressure (usually 4 bar) applied to the bladder plate via the one-way bladder valve, and the compression bolts tightened to 2 Nm using a torque wrench.

Current Collection Plates: The current collection plates allow the conduction of electrons to and from the MEA and have flow channels machined in them to allow the delivery of gas to the GDL surface of the MEA. The plates are shown in detail in Figure 3.14 in the orientation they would be in the test cell, i.e. the anode plate view is of the 'outside' and the cathode plate of the 'inside'. When assembling the cell the MEA is placed on the cathode plate and then the anode plate placed on top. The anode gas is delivered in the 'gas in' port on the right of the anode plate, around the flow channel (not shown) and out of the 'gas out' port on the anode plate. The cathode gas has to pass through the anode plate ('gas through' holes) and is delivered to the 'gas in' port of the cathode plate, travels through the serpentine flow channels and out of the 'gas out' port of the cathode plate (where it must again pass through the anode plate to exit the test cell).

Waterbath: Used for preparation of membranes, has a working range of 20-100°C.

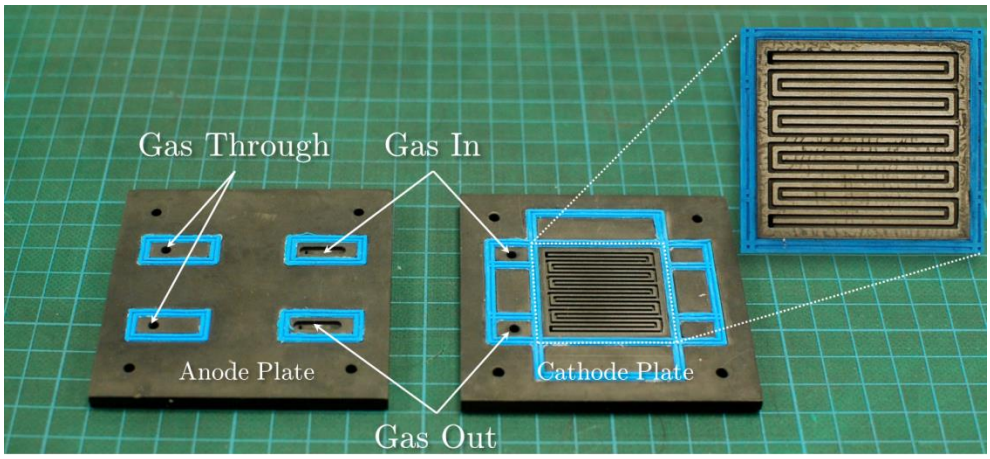

Figure 3.14 The bipolar plates showing the gas in and out ports, holes for the gas to pass through the anode plate to the cathode plate, the serpentine flow channel (detail inset) and the silicon rubber seals. The holes in the four corners of the plates are for alignment pins used for correct and consistent assembly of the test cell.

3.12.2 Electrode Preparation

In-house fuel cell electrodes are prepared by cutting 3.3×3.3 cm squares of GDM (using a steel template and a scalpel) and coating them with catalyst inks (section 3.2) applied with an airbrush. In order to get an accurate idea of the loading of the catalyst, the GDM is weighed before application of the ink and the total mass of dried ink required for a desired loading is calculated (based on the formula in Section 3.2.1.2). The ink is then applied and left to dry until the mass of the electrode is unchanging. Multiple coatings of ink are applied until the desired catalyst loading is achieved.

Though it is difficult to obtain the exact loading desired (as such small amounts of catalyst are applied to the GDM), the mass is always accurately recorded, enabling an accurate calculation of the actual loading of a particular electrode.

Whenever a platinum electrode is mentioned, it is simply prepared by cutting the commercial platinum electrodes obtained from Alfa Aesar.

3.12.3 MEA Manufacture

The 'working part' of the fuel cell is the membrane electrode assembly. As the name suggests, it consists of an anode and cathode electrode sandwiching a membrane and is manufactured in the following way:

3.12.3.1. Membrane Preconditioning

The membranes as received contain no water molecules and are likely contaminated with dust or organic detritus. For this reason the Nafion membranes are preconditioned before used in MEA manufacture. Membranes are cut into 8×8 cm pieces, the backing layers removed and treated with 3% H_2O_2 solution at 80°C for one hour. Samples are then rinsed thoroughly in deionised water and treated with 1M H_2SO_4 at 80°C for a further hour, before being rinsed again in deionised water. The Nafion is then clean and fully protonated. If an MEA is not pressed immediately the membranes are stored in sealed plastic bags containing deionised water for later use.

The Tokuyama membranes can be damaged by peroxide and are vulnerable to degradation at elevated temperatures, so are preconditioned simply by submersion in 1M KOH solution for 2 hours at room temperature, then thoroughly washed in deionised water.

3.12.3.2. Hot Pressing

Once the membranes have been prepared and the electrodes made, the MEA can be manufactured by laminating in a hot press under temperature and pressure. The MEA is prepared for hot pressing by creating a sandwich as follows;

12×12 inch titanium plate,

12×12 inch PTFE sheet,

10×10 cm Tygaflor sheet,

Cathode electrode with catalyst layer facing upwards,

Preconditioned membrane,

Anode electrode with catalyst layer facing downwards (i.e. the catalyst layers of both electrodes are in contact with the membrane),

Tygaflor sheet,

PTFE sheet,

Titanium plate.

In the case that the anode and cathode electrodes are different, an asymmetric pattern was cut out of the excess membrane area to distinguish the anode and cathode sides (Figure 3.15), and by convention the anode is always kept facing upwards throughout the pressing procedure.

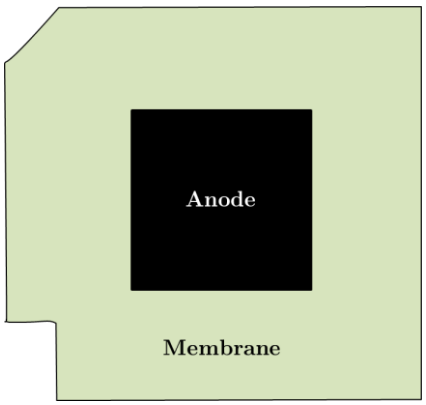

Figure 3.15 An asymmetric MEA to distinguish the anode side from cathode side. If the membrane shape above is replicated, the side facing upwards will be the anode and the side facing downwards will be the cathode.

3.12.3.3. List of MEAs

Table 3.1 shows the details of all the MEAs involved in experiments in Chapter 6. Pressure, temperature and duration refer to the hot-pressing settings used to bind the MEAs. Many more MEAs have been manufactured during this project, for various reasons, but are not shown here.

Table 3.1 Details of MEAs used in fuel cell experiments

MEA No.	Membrane	Anode Loading (mg cm^{-2})	Cathode Loading (mg cm^{-2})	Pressure (PSI)	Temperature (°C)	Duration (s)
1	Nafion 212	Pt 0.54	Pt 0.54	450	170	180
2	Tokuyama A006	Pt 0.54	Pt 0.54	450	70	240
3	Tokuyama A006	PdIr 0.72	Pd 0.68	1000	70	240
4	Nafion 212	Pt 0.54	Pt 0.54	450	170	180
5	Touyama A201	Pt-AAEM 0.16	Pt-AAEM 0.16	700	50	240

3.12.4 Fuel Cell Test Stations

3.12.4.1. Bespoke System

Once the MEA is prepared and the test cell fully assembled, it is connected to the bespoke Whistonbrook test station. The load is connected to the current collection plates and secured with gold-plated nuts; voltage sensing leads are inserted in the holes in the bipolar plates and K-type thermocouples are inserted into both heating plates and the head of the humidification bottles. Inlet gases from the humidification bottles are connected to the inlet ports of the test cell and the outlet ports are connected to the extraction system via quick connections (Swagelok). The exhaust gases are bubbled through deionised water in Schott bottles before entering the extraction system to avoid back-flow of air into the system and to remove any water

from the exit gas. This also serves as a useful visual indicator that all gasses are flowing correctly through the system.

Nitrogen gas is flown over the anode to purge all oxygen before hydrogen is introduced and the oxidant gas (air, CO_2-free air or O_2) is flown over the cathode. The system is fully leak tested regularly using a detergent solution that produces bubbles where leaks exist, but it is also tested for hydrogen leaks before every operation using an electronic hydrogen sensor along all points in the hydrogen stream. This sensor is then placed near the test cell for the duration of the experiment as a safety measure. The system is then fully set up and ready for testing (Figure 3.16).

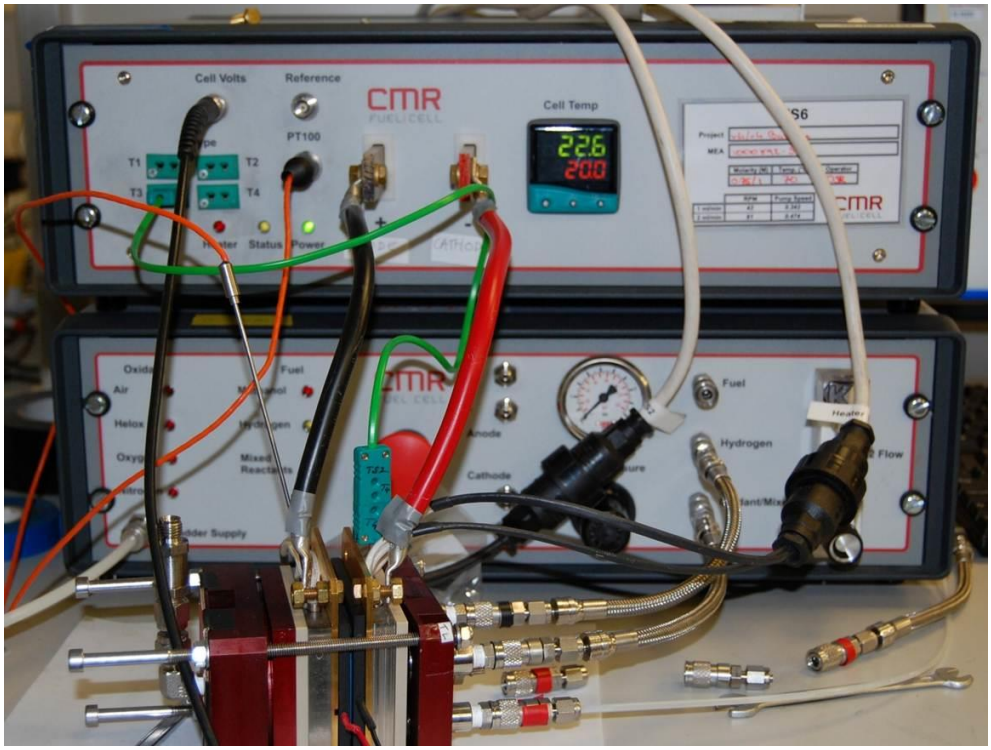

Figure 3.16 The fuel cell test station showing load, thermocouple and voltage sensing connections and inlet an outlet gases. The humidification system is not shown here.

3.12.4.2. Commercial

The setup for the commercial Scribner test station is much the same as for the bespoke system except the gases exit the unit already humidified, via heated lines. The commercial test station can be seen in Figure 3.17.

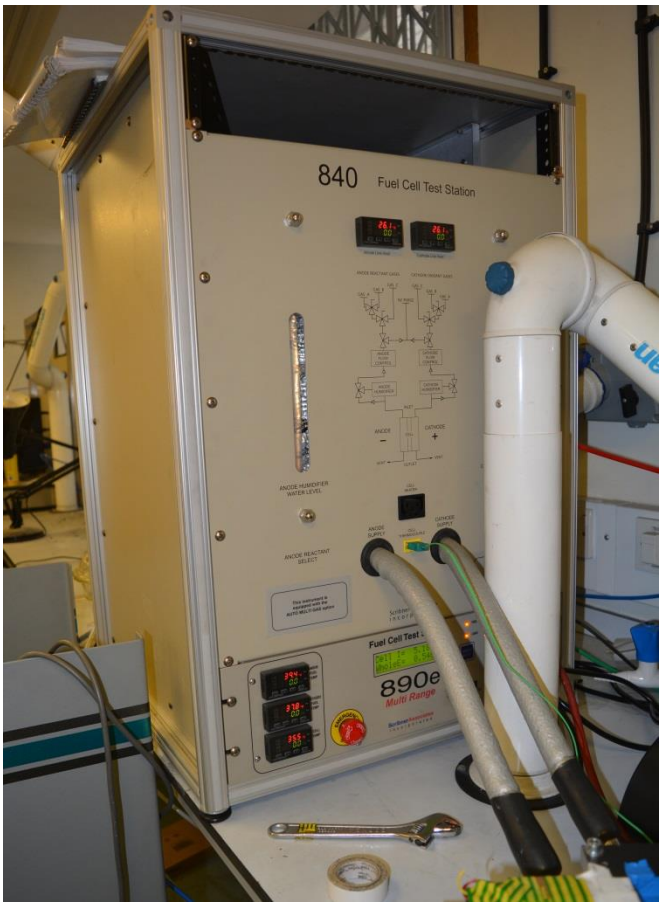

Figure 3.17 The commercial Scribner fuel cell test system.

4 Characterisation

4.1 Compositional Analysis

PdIr/C catalyst samples were analysed using thermogravimetric analysis (TGA) and inductively coupled plasma atomic emission spectroscopy (ICP-AES) in order to confirm the metal loading and Pd:Ir ratios, respectively, were as they should be from the precursor amounts used in synthesis. TGA involved heating the samples at 5 °C/min under a flow of ambient air such that all the carbon support is oxidised and removed, leaving a metal residue, all the while the mass of the sample is accurately monitored. Figure 4.1 shows an example TGA profile for the PdIr/C powder (red) and the filtered and washed remainder after the acid digestion treatment performed for ICP-AES experiments (black) (see Section 3.7). TGA of the powder samples confirmed the metal loading to be $40\%_{wt} \pm 2\%$ and the total loss of mass for the samples after acid digestion confirmed that all of the metal had gone into solution, and therefore that the ICP-AES results are valid.

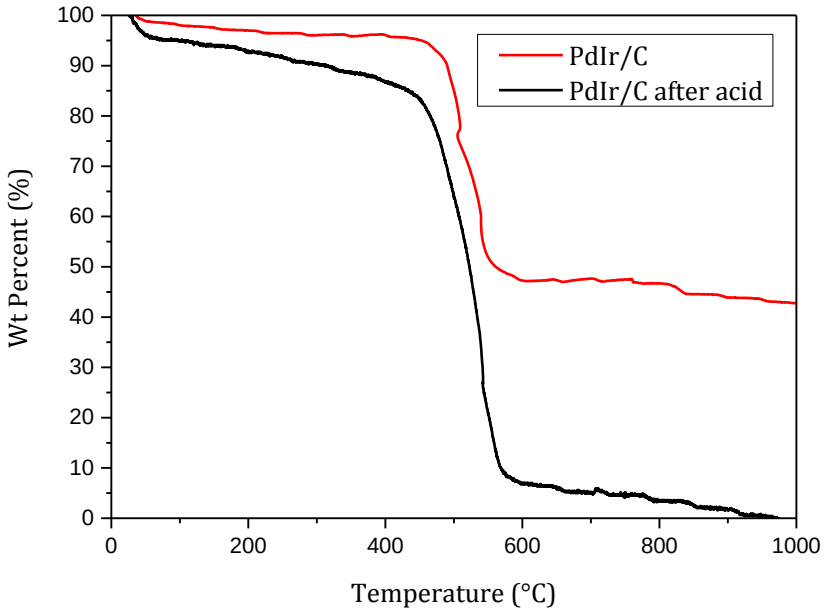

Figure 4.1 TGA profiles for a PdIr/C catalyst before (red) and after (black) acid digestion

ICP-AES of various PdIr/C samples showed a 1:1 ratio was obtained in the metal nanoparticles after synthesis. The average discrepancy from the calculated metal ratio (based on precursor amounts used in each synthesis) and the ratio obtained from ICP-AES for the range of PdIr/C samples studied was 3.7%.

Given the metal loading and atomic ratios were close to those expected from the synthesis, the method was deemed valid for preparing PdIr/C catalysts of known loading and atomic makeup.

4.2 Imaging

4.2.1 Scanning Electron Microscopy

Scanning Electron Microscopy (SEM) was primarily used for its energy dispersive X-ray spectroscopy (EDX) capabilities as the imaging resolution is too low to provide any useful information about metal particle size or distribution.

4.2.1.1. EDX Results

Figure 4.2 shows an example EDX spectrum of PdIr/C. It confirms the presence of expected elements in all catalysts tested. The INCA software was also used to give a quantitative analysis of the elementary make-up of the catalyst, specifically the metal weight percentage and Pd:Ir ratio. The results are averaged from at least 3 spectra in different areas of the sample. The rated accuracy of the software's calculations is relatively low at around $\pm$ 3% points, depending on the element in question, and the technique is further reduced in accuracy due to the fact that a powder sample is used and not a polished one. Nevertheless, it serves as a useful first idea of the rough elemental makeup of the catalysts produced. In all PdIr/C catalysts tested, the iridium amount is lower than the palladium, varying from around 2:1 to 3:1, despite the precursor chemicals added at an amount that should give a 1:1 ratio. This suggests that incomplete iridium reduction in the synthesis process, but a more accurate quantitative elemental analysis is needed before this conclusion can be made.

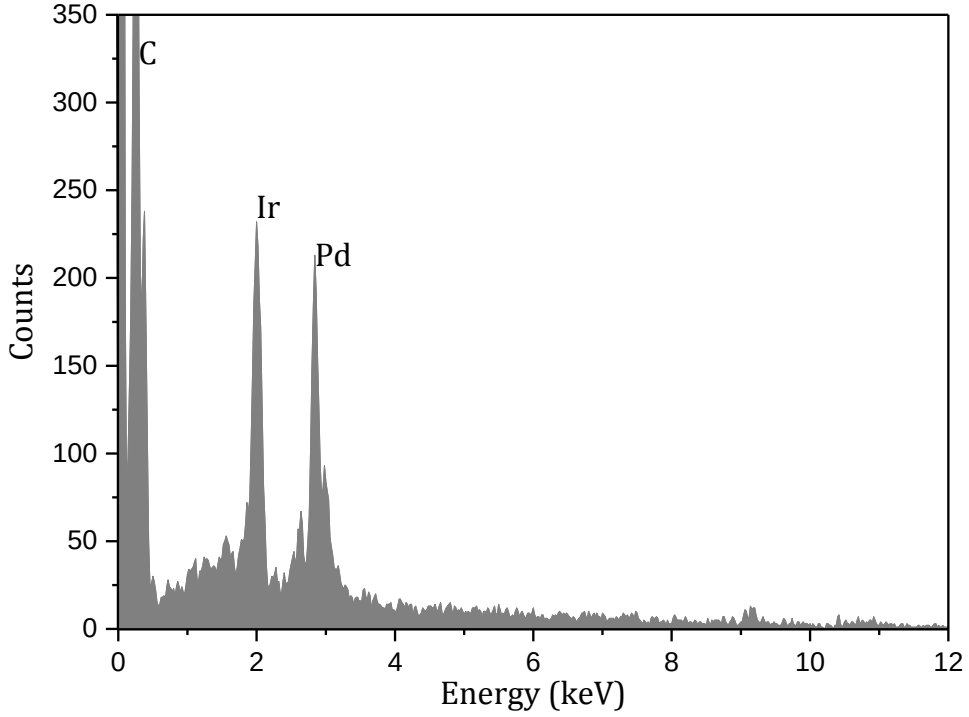

Figure 4.2 EDX Spectrum of PdIr/C catalyst showing the peaks for carbon, palladium and iridium.

4.2.2 Transmission Electron Microscopy

The first step in evaluating the quality of a catalyst is through high resolution imaging. From this an idea of the distribution and size of the catalyst nanoparticles is attained.

4.2.2.1. PdIr/C

Figure 4.3 shows selected TEM micrographs of the PdIr/C catalyst. The darkness of the image is dependent on atomic weight, so the larger, lighter particles represent the carbon supports and the smaller, darker particles the metal catalyst particles.

In all samples some areas of agglomeration of the metal particles and inhomogeneity of metal distribution was seen. Figure 4.3 shows a representation of the different areas of metal seen in the PdIr/C catalyst, showing areas of good particle size distribution (bottom right) as well as large areas of agglomeration (top right). On the whole, the presence of agglomeration, at least in parts of all the samples, suggests that optimisation of the cata-

lyst synthesis process ($PdIr/C_{HSA}$) should yield improved performance (and thus increased utilization of the catalyst).

Figure 4.4 shows the particle size distribution taken from all the particles in Figure 4.3. The average particle size is 12 nm; however, the broadness of the distribution shows the issues with agglomeration and particle size control in this catalyst.

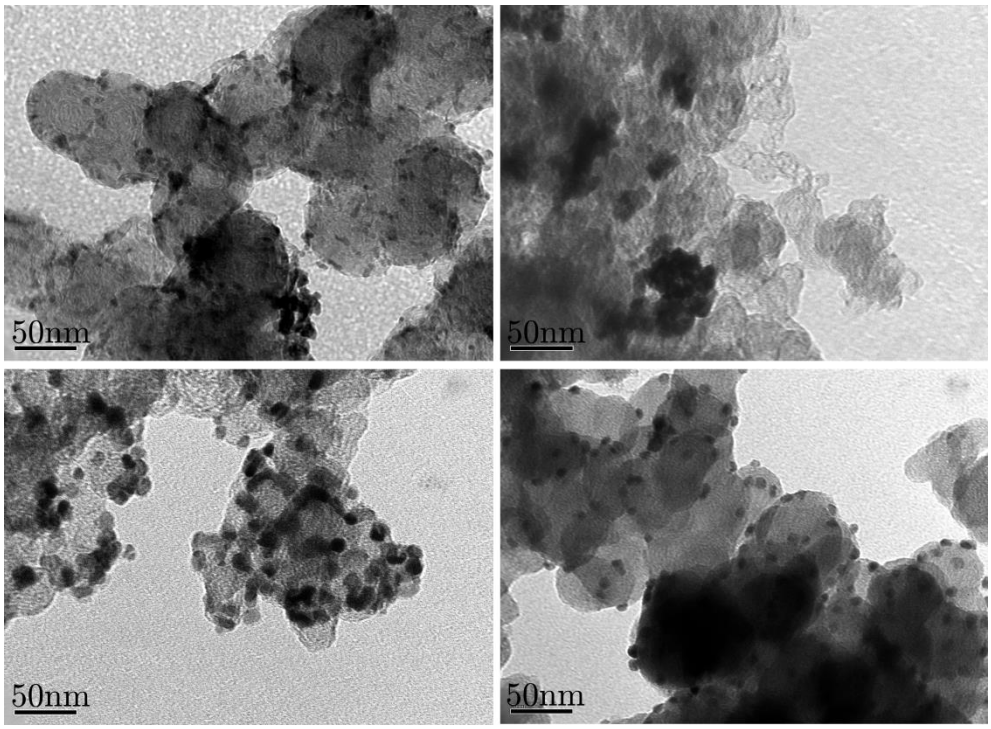

Figure 4.3 TEM micrographs of PdIr/C showing varying degrees of agglomeration and particle distribution. The scale bar on all images is 50 nm. Darker contrast in the images represents higher density areas and so the metal nanoparticles are shown as small, dark circles on the larger, lighter carbon particles.

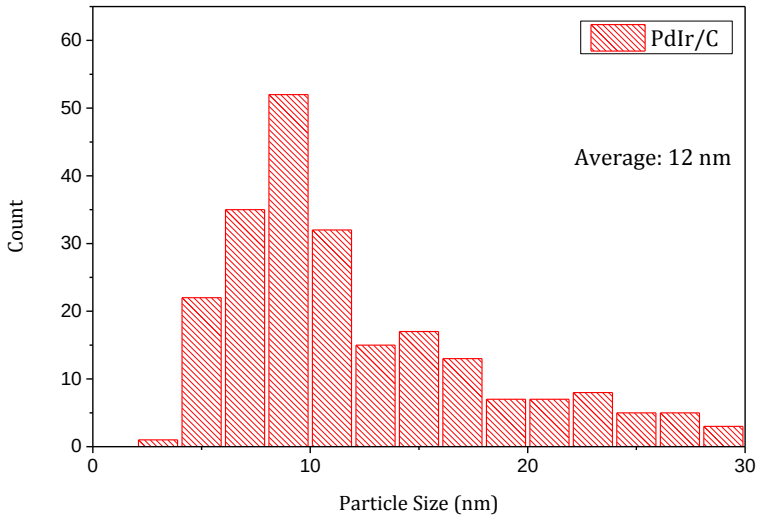

Figure 4.4 Histogram showing the particle size distribution for the images shown in Figure 4.3. TEM images reveal an average particle size of 12 nm for PdIr/C.

4.2.2.2. $PdIr/C_{HSA}$

Figure 4.5 and the corresponding histogram of particle sizes in Figure 4.6 show the improvement in particle size distribution and dispersal on the carbon support on change of the catalyst synthesis procedure (see Section 3.1.6). This yields an average particle size of 3.8 nm, which is much more akin to the size of particles found in commercially available Pt/C catalysts (3.5 nm in the case of the Pt/C used in this study). However, there are still areas of particle agglomeration seen and further improvements could be made to the dispersion. In particular, using a lower metal loading weight than 40% is expected to vastly improve the size distribution and dispersal (TEMs of $5\%_{wt}$ PdIr/C not discussed in this thesis showed an even distribution of metal particles of similar sizes, though it was decided that for a better comparison with the commercially available Pt/C, focus should remain on the $40\%_{wt}$ catalysts). A study of the effect on catalytic activity of particle size, inter-particle distance and metal loading can be found from Corradini et al. [210].

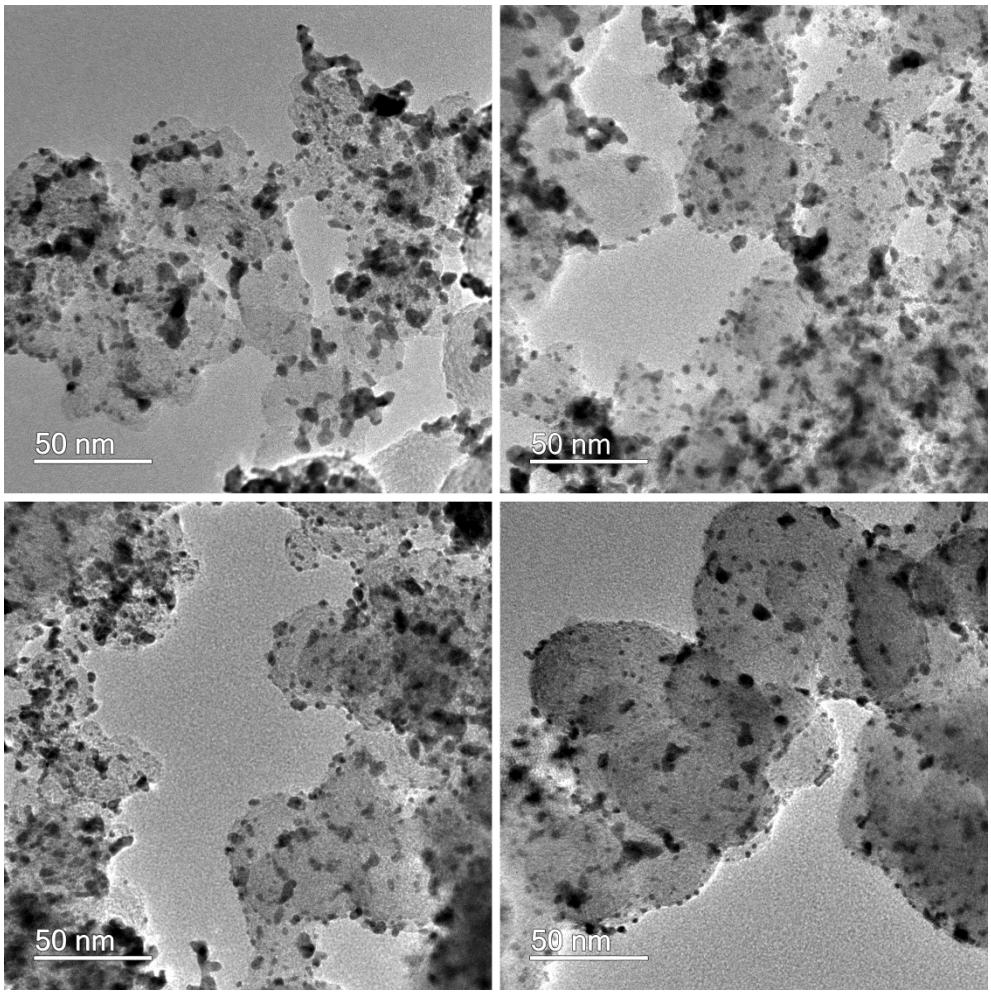

Figure 4.5 TEM Micrographs of $PdIr/C_{HSA}$.

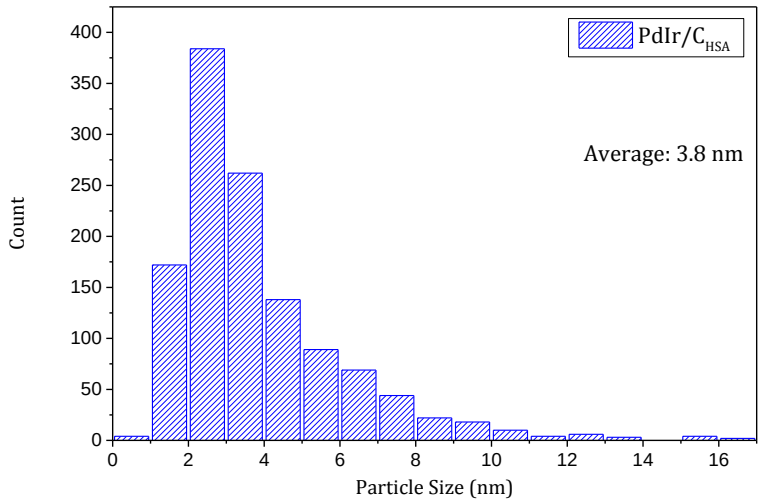

Figure 4.6 Histogram showing particle size distribution for the $PdIr/C_{HSA}$ catalyst.

4.2.3 HR-TEM

4.2.3.1. PdIr/C

High resolution TEM microscopy was used to obtain information about the crystal structure of the catalyst. Figure 4.7 shows an example HR-TEM micrograph of PdIr/C in which the 2D projection of the 3D lattice of the metal particles, as well as the layered structure of the carbon support, can clearly be seen. A cross section of a particle was taken (indicated by the yellow line on Figure 4.7) and is shown in Figure 4.8. The lattice spacing (averaged over the whole cross section) was calculated to be 2.23 Å, which is very close to the value of 2.24 Å for the (111) plane obtained from X-ray diffraction (Section 4.4).

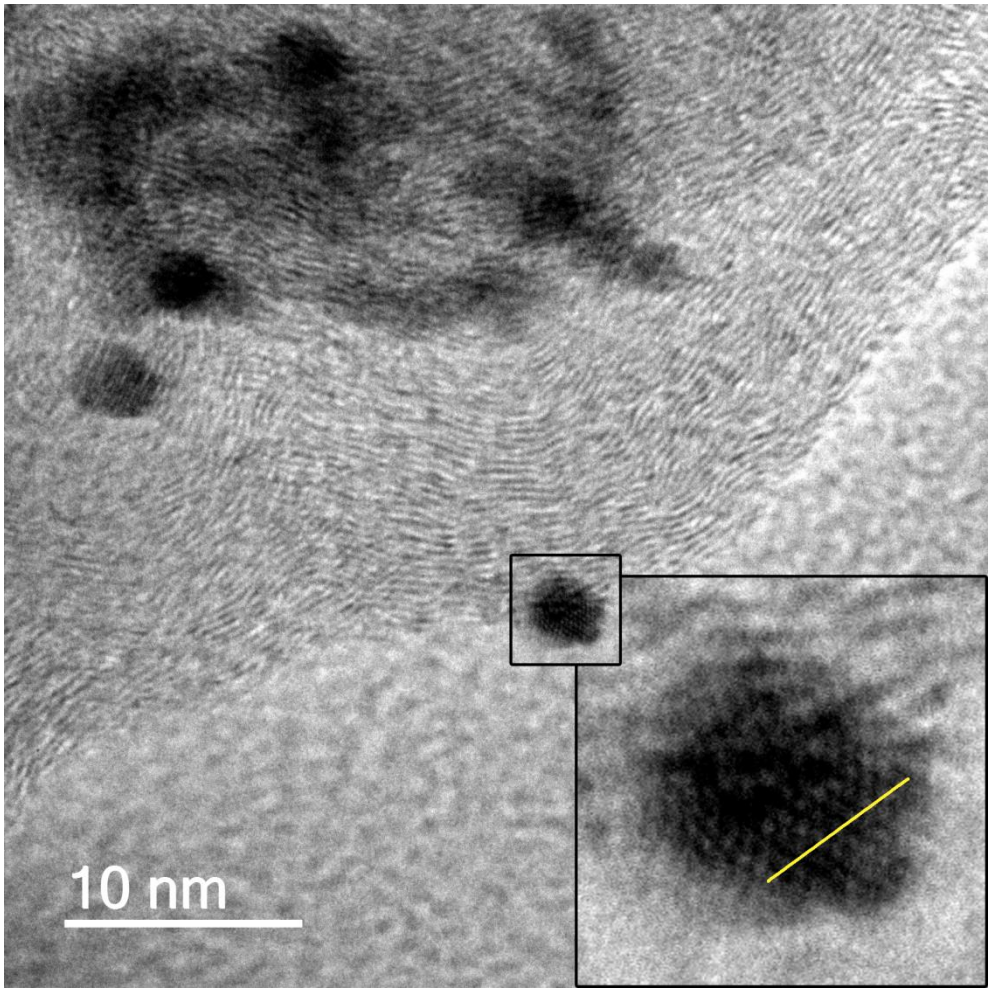

Figure 4.7 HR-TEM of PdIr/C showing the lattice structure of the metallic nanoparticle and the layered structure of the carbon support.

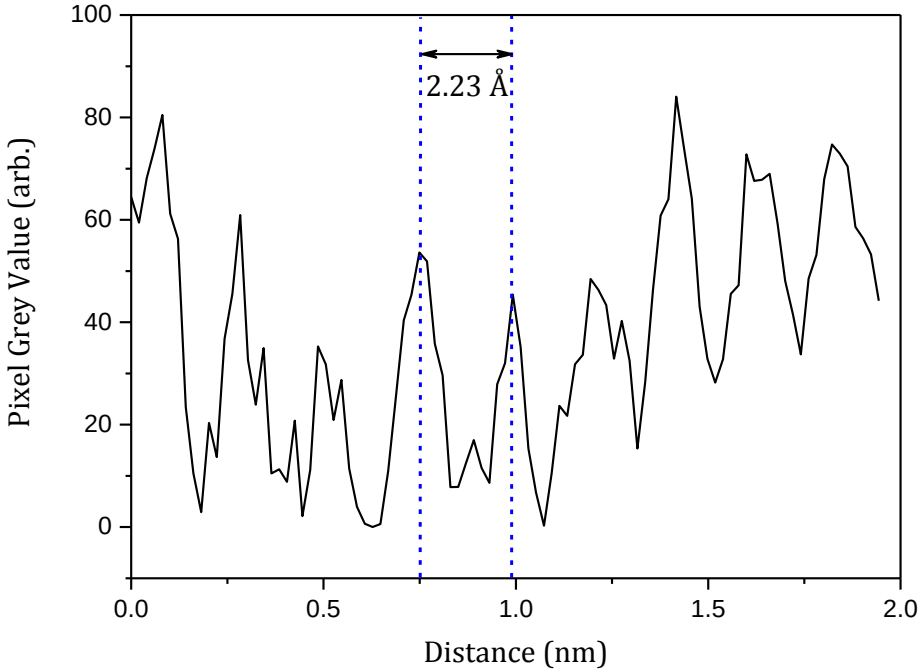

Figure 4.8 Cross section of the PdIr particle shown by the yellow line in Figure 4.7, showing the lattice spacing of the particle.

4.2.3.2. $PdIr/C_{HSA}$

HR-TEM was also used to examine the high surface area catalyst. Figure 4.9 shows an area of well distributed metal nanoparticles at increasing magnification, including one crystallite that appears to contain three different crystal facets. Taking cross sections, as indicated by the yellow lines, showed two of the facets to be the (111) plane with spacing of 2.23 Å, and one the (002) with spacing of 1.95 Å (compared to 1.94 Å from XRD). The cross sections are shown in Figure 4.10 and the whole section was averaged in order to obtain the lattice spacing.

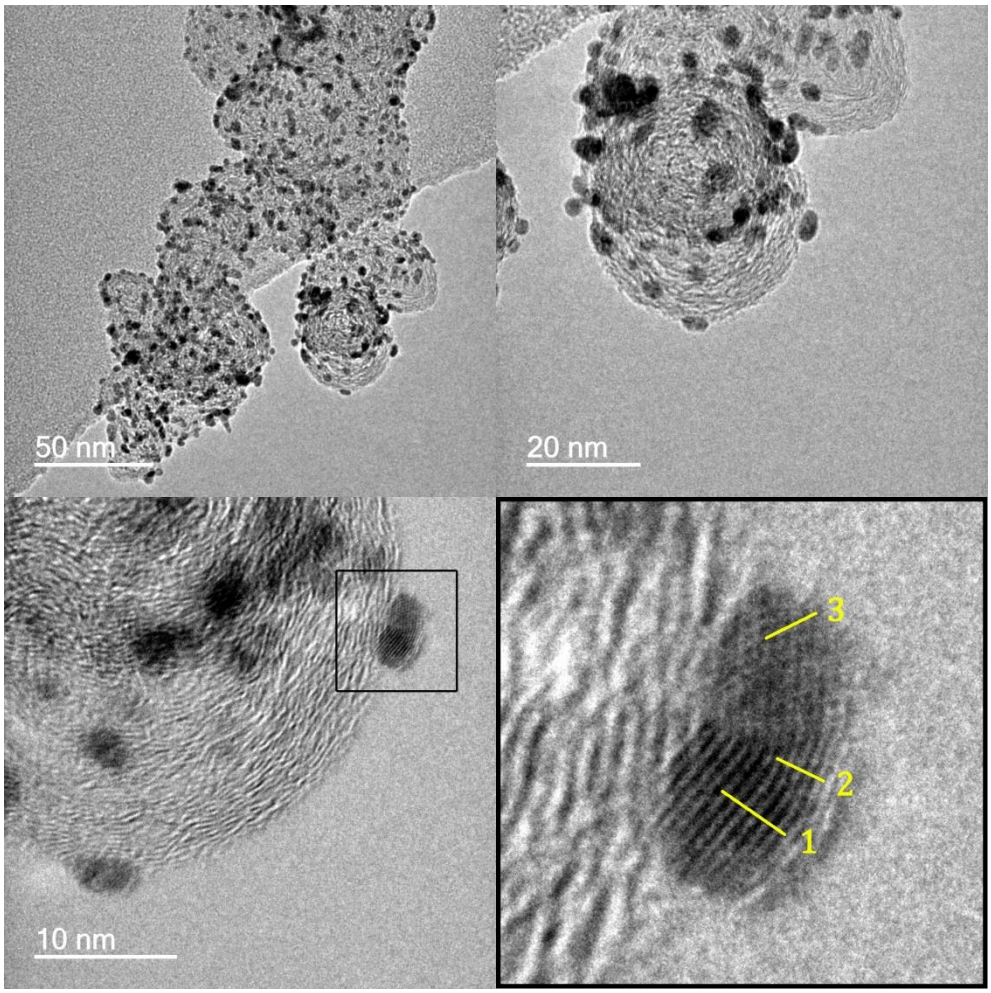

Figure 4.9 HR-TEM image of the PdIR/C_{HSA} catalyst at various magnifications. Three different cross sections indicated by the yellow lines were taken to examine the three different facets seen in this crystallite.

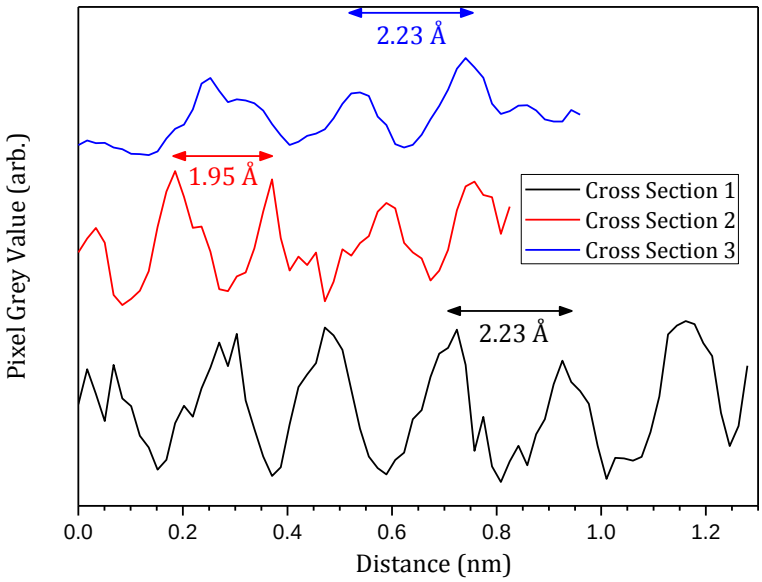

Figure 4.10 Three cross sections from Figure 4.9 stacked on an arbitrary axis. The lattice spacing (averaged over the whole length of the cross section) shows cross sections 1 and 3 to correspond to the (111) plane and cross section 2 the (002).

4.2.3.3. HR-TEM EDX

As with the SEM, EDX was performed using the HR-TEM instrument. However, a much greater special resolution is achievable with this measurement, allowing elemental mapping of the sample. Three areas of the catalyst were studied as indicated by the white boxes in Figure 4.11 and all gave slightly Pd rich atomic Pd:Ir ratios of 1.1, 1.2 and 1.1. The results of the largest mapping area are shown in Figure 4.12 and show that the Pd and Ir elements are found in areas corresponding to the metal nanoparticles, as expected. The distribution of Pd and Ir is relatively even with no areas dominated by any one element; however, a much more comprehensive mapping study would be required to obtain more useful information about the distribution of elements within individual particles.

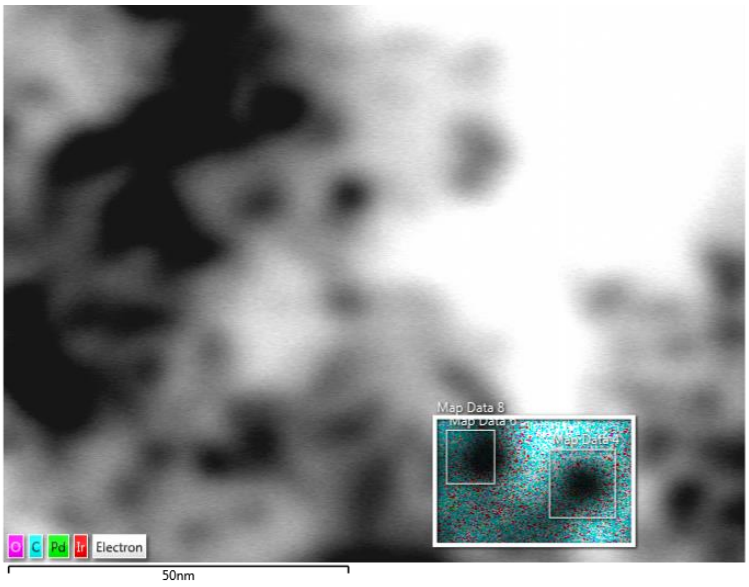

Figure 4.11 The three areas of EDX mapping indicated by the white boxes. Fine focus is not possible when imaging in EDX mode, thus the quality of the image is lower than that from the HR-TEM. Nevertheless, it is still possible to identify areas of metal nanoparticles and thus map individual crystallites.

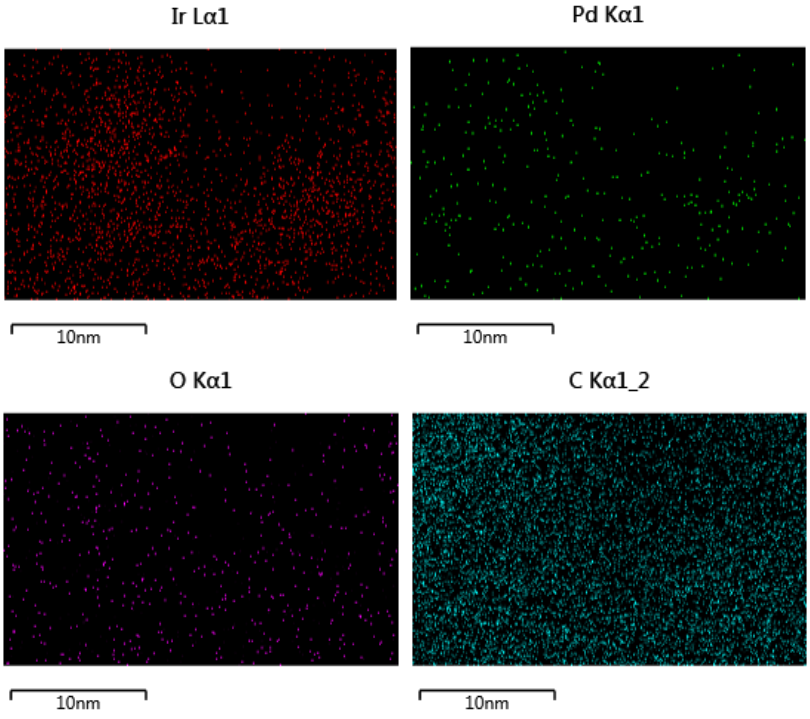

Figure 4.12 The results of EDX mapping for the largest area shown in Figure 4.11, indicating the locations of Ir (top left, red), Pd (top right, green), O (bottom left, pink) and C (bottom right, cyan).

4.3 X-ray Photoelectron Spectroscopy

X-ray photoelectron spectroscopy (XPS) was carried out on PdIr/C and PdIr/C_{HSA} catalysts as well as Pd/C and Ir/C monometallic catalysts in order to determine if there are any changes in electronic structure when compared to the individual constituents of the alloy. Three variations of the PdIr/C catalyst with higher Pd contents (3:1, 5:1 and 9:1 ratios of Pd:Ir) were also synthesised and examined with XPS. An example full survey spectrum of PdIr/C can be seen in Figure 4.13 showing the characteristic C 1s, Pd 3d and Ir 4f peaks, as expected. There is also an O 1s peak present due to oxidation of the catalysts due to a small amount of oxidation of the samples between reduction and the XPS measurements. The presence of oxides is to be expected as the catalysts are stored under ambient conditions and should not pose a problem for fuel cell operation in a hydrogen environment as reduction would be expected to occur under operating conditions.

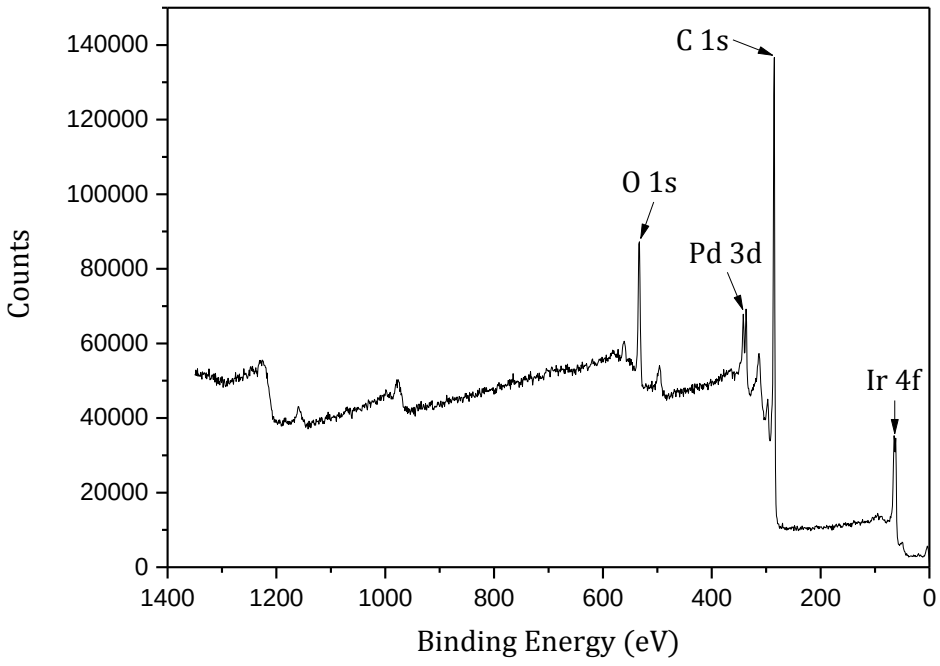

Figure 4.13 An example XPS survey spectrum of the PdIr/C catalyst showing the characteristic peaks for the elements of interest.

When all bimetallic catalysts are compared to the monometallic Pd/C and Ir/C standards, a clear shift in peak position can be seen for both the

Pd 3d and Ir 4f peaks, with the Pd peaks shifting to higher binding energy and the Ir peaks to lower binding energy (Figure 4.14). This suggests a change in electronic structure of the elements within the bimetallic catalysts compared to their monometallic analogues and provides evidence of alloying in all samples. Specifically, the Ir becomes more electron rich and the Pd more electron poor in the bimetallic catalysts. The highest Pd content catalyst exhibits the smallest shift in Pd 3d peak position and the low Ir content means that the Ir spectrum is noisy compared to the other samples (all spectra are normalised using CasaXPS such that the highest peak is set to 1 and the spectra for all samples are stacked on an arbitrary axis in Figure 4.14). For a quantitative description of the peak shifts the spectra were fitted using CasaXPS software in order to deconvolute the metallic and oxide contributions to the peak, with the metallic peak positions being used to assess the shift (see Section 4.3.1).

As mentioned in Section 1.4.1.4, the location of the d-band centre plays an important role in catalyst-adsorbate interaction and therefore also in catalytic activity. Yoo and Sung studied PdIr alloy electrodes grown by magnetron sputtering with high resolution synchrotron XPS in order to determine the valence band centres and showed that the d-band centre shifted to higher binding energy with an increase in Pd content [164]. They found that the catalyst most active for HOR (in acidic media) was $Pd_{59}Ir_{41}$, the closest example to a 1:1 atomic ratio. This coincided with an intermediate d-band centre, compared to pure Pd or pure Ir, and they concluded that the enhanced activity was due to an intermediate binding of adsorbates, allowing for the best combination of enhanced dissociation kinetics and enhanced bond formation of products. The importance of the strength of adsorbate binding in activity of surfaces was previously demonstrated by Marković et al. on Pt single crystals [86] and applied to the PdIr case, with the same trend being seen. The resolution of the XPS instrument used in this work is not high enough to accurately study the valence band, and the lower density of metal in the carbon supported nanoparticles compared with the sputtered alloys of Yoo and Sung gives a lower signal in the spectra. However, some useful comparisons can be drawn, namely that the shifts in Pd and Ir binding energy shown in Figure 4.14 are likely to produce a more intermediate bond with adsorbates than either pure Pd or pure Ir, which contributes to the enhanced activity for HOR seen in Chapter 5. Yoo and Sung suggested that the higher Pd content electrodes bind hydrogen too

strongly and so the more electron-poor Pd seen in the PdIr/C catalysts in this work can be assumed to bind hydrogen less strongly than Pd/C and therefore show a greater activity towards the HOR.

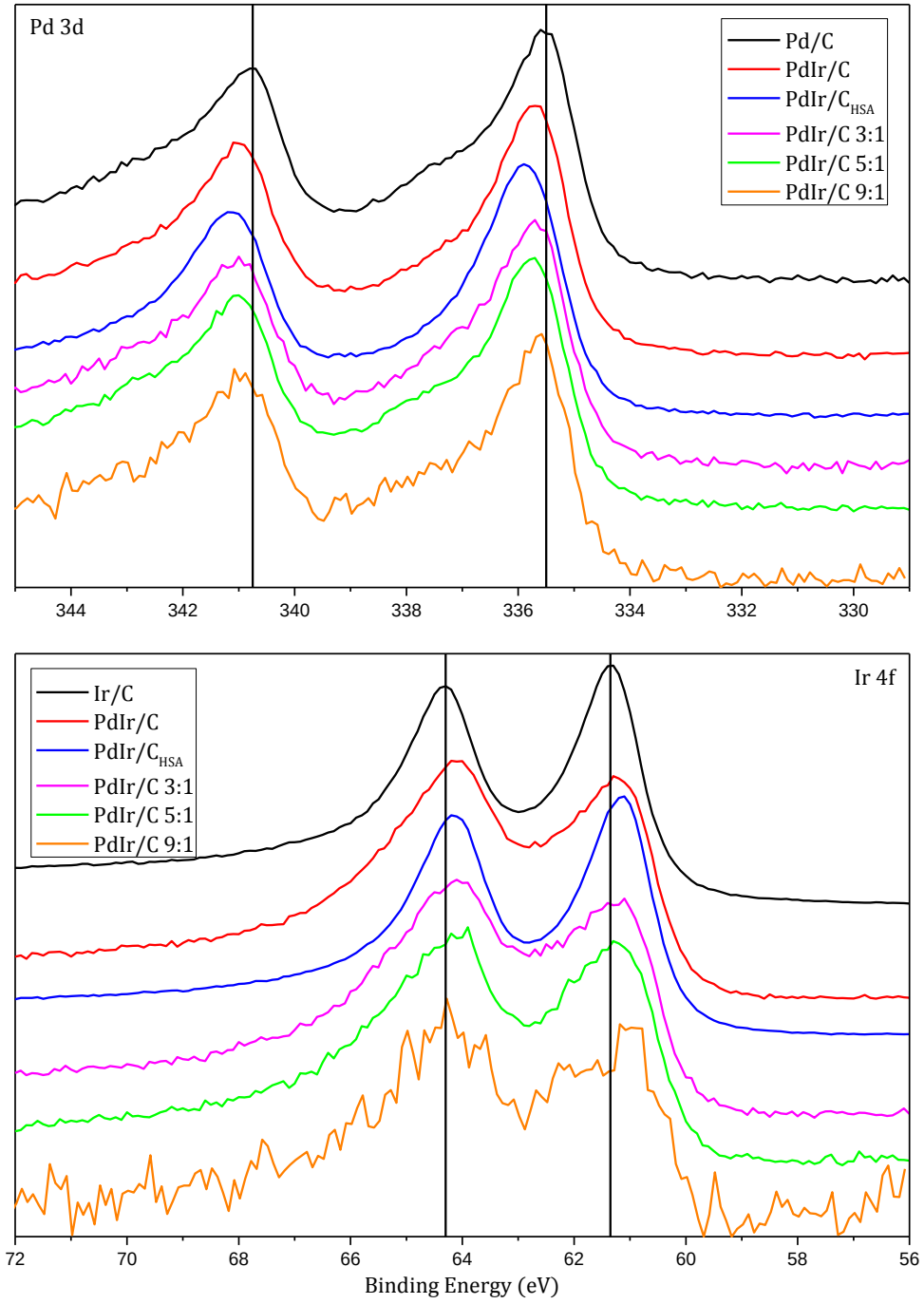

Figure 4.14 Normalised high resolution XPS spectra of the Pd 3d (top) and Ir 4f (bottom) doublets for single metallic Pd and Ir (black), PdIr/C (red), PdIr/C$_{HSA}$ (blue), PdIr/C 3:1 (magenta), PdIr/C 5:1 (green) and PdIr/C 9:1 (orange). The peaks are shifted to higher binding energy for Pd and lower binding energy for Ir.

4.3.1 Fitting

All spectra were fitted using CasaXPS software. As can be seen from Figure 4.15, the doublet peaks for Pd 3d and Ir 4f contained a metallic (e.g. Pd^0) and oxide species (e.g. Pd^{2+}) component [211]. The peak ratios were constrained for both the metallic and oxide species to reflect the respective degeneracies of each doublet peak such that Pd $3d_{3/2}$ was 2/3 the area of Pd $3d_{5/2}$ and Ir $4f_{5/2}$ was 3/4 the area of Ir $4f_{7/2}$. The full width at half maximum (FWHM) was constrained to be the same for pairs of metallic peaks and pairs of oxide peaks and a Shirley background subtraction was employed. Fitting the XPS data allows extraction of peak positions (binding energies) and areas, which, when divided by the relative sensitivity factor (16 for Pd and 13.9 for Ir), gives a quantitative measure of elemental composition. All catalyst samples were fitted but only the $PdIr/C_{HSA}$ fits are shown here. A summary of the peak positions and atomic ratios of the elements extracted from the fit is shown in Table 4.1.

Table 4.1 Summary of peak positions and shifts in binding energy (eV) extracted from fitting with CasaXPS software

Catalyst	Pd $3d_{5/2}$ (eV)	Pd $3d_{3/2}$ (eV)	Ir $4f_{7/2}$ (eV)	Ir $4f_{5/2}$ (eV)	Pd Peak Shift (cf. Pd/C)	Ir Peak Shift (cf. Ir/C)
Pd/C	335.48	340.78	-	-	-	-
Ir/C	-	-	61.41	64.31	-	-
PdIr/C	335.66	340.96	61.39	64.29	+0.18	-0.02
$PdIr/C_{HSA}$	335.89	341.19	61.32	64.22	+0.41	-0.09
PdIr/C 3:1	335.64	340.94	61.26	64.16	+0.16	-0.15
PdIr/C 5:1	335.67	340.97	61.33	64.23	+0.19	-0.08
PdIr/C 9:1	335.60	340.90	61.32	64.22	+0.12	-0.09

Although some of the shifts in peak positions are small and perhaps within the experimental error, there is a clear trend shown for positive Pd and negative Ir peak shifts, with larger shifts seen for the Pd peaks. The largest shift in Pd peak position is seen for $PdIr/C_{HSA}$ which could be due to the more aggressive reducing agent used in synthesis leading to a higher degree of alloying and therefore also modification of electronic structure. It is also possible that the pre-treatment of the carbon in this catalyst leads to a shift in the C 1s peak compared to the untreated catalysts and, because all spectra were normalised to the position of the C 1s peak, a shift in the Pd and Ir peak positions [212]. However, there was not a significantly different shift in C 1s peak position for $PdIr/C_{HSA}$ and a negative shift of the Ir peak suggests that the effect of the normalisation to C 1s is negligible.

The atomic ratios of the catalysts were also calculated from the XPS fits and broadly agreed with the expected ratios from precursor quantities used in synthesis, but a significant error is expected (if the particles have a degree of inhomogeneity in their structure) due to the catalyst particles being larger than the penetrating depth of the instrument (especially considering the thickness of the powered sample which is, atomically, mainly carbon and not homogenous) [166]. A higher resolution synchrotron XPS experiment would be required to gain any useful information about the atomic amounts in the catalysts.

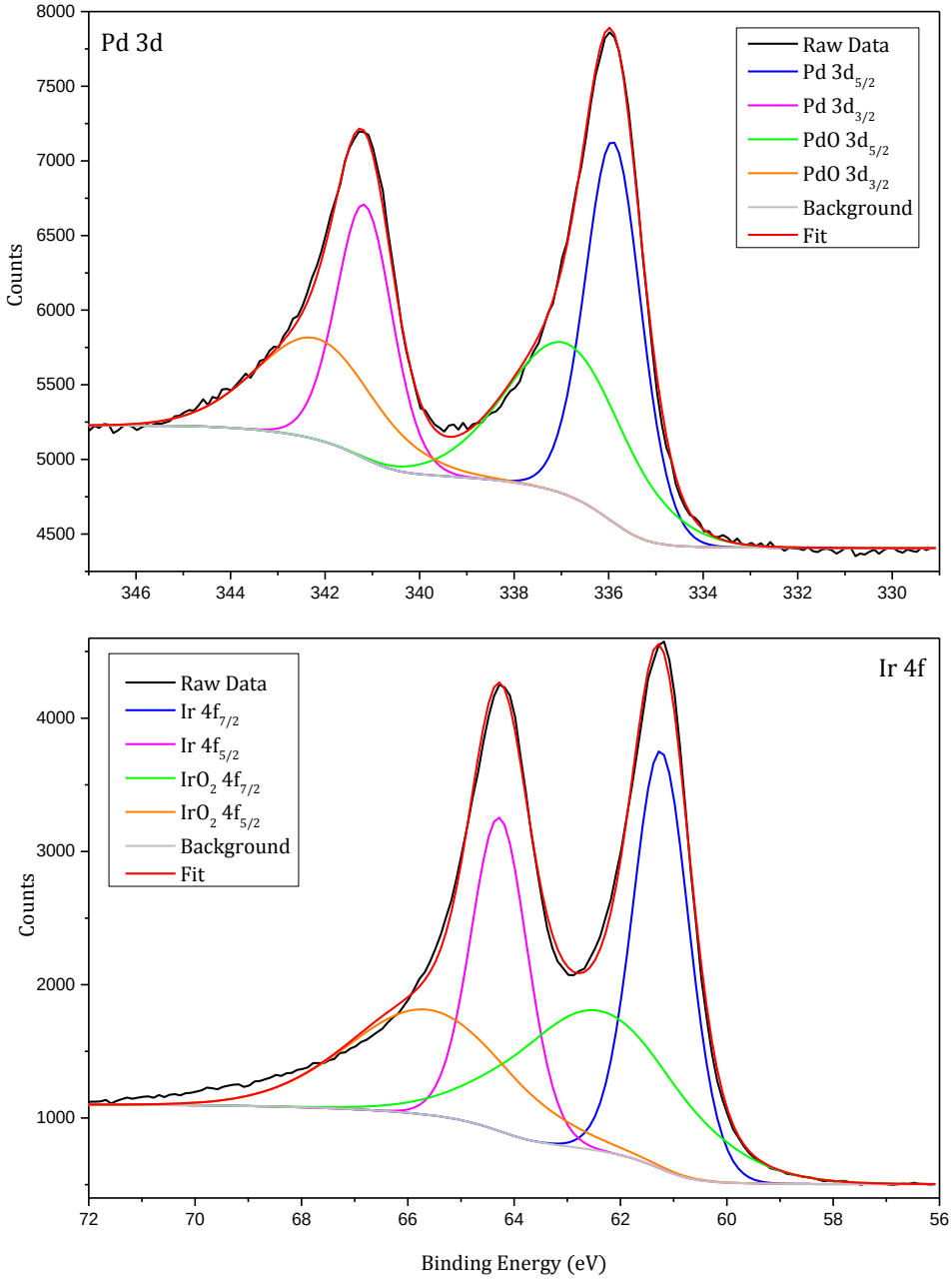

Figure 4.15 Fitting of the high resolution XPS spectra of the Pd 3d (top) and Ir 4f (bottom) doublets in the $PdIr/C_{HSA}$ catalyst. The raw data is shown by the black line with the overall fit in red. The fit consists of metallic doublet (low binding energy, blue, and high binding energy, magenta) and a doublet from an oxide species (low binding energy, green, and high binding energy, orange).

4.4 X-ray Diffraction

Due to the expected small changes in lattice parameter on alloying of Pd and Ir and the low metal content in the catalysts, synchrotron X-ray powder diffraction (SXPD) was used in preference to a lab XRD instrument in order to attain a high-signal-to-noise ratio and accurate extraction of lattice parameters using a Le Bail fit. The SXPD pattern shown in Figure 4.16 exhibits broad peaks (full-width at half maximum (FWHM) ~ 0.7 °) indicative of small crystallite size. The PdIr/C catalyst particles have a face-centred cubic structure (space group Fm-3m) with a lattice parameter of 3.8851(1) Å consistent with the results found by Raub on bulk PdIr alloys [213], though the lattice parameter for the bulk alloy is smaller at 3.862 Å. Both Pd (ICSD PDF 46-1043) and Ir (ICSD PDF 6-598) also have face-centred cubic lattices, but with different lattice parameters (3.8898 Å and 3.8394 Å, respectively); thus the absence of additional peaks in the diffraction pattern suggests alloying in the sample as opposed to an unalloyed mixture of Pd and Ir nanoparticles. The FWHM of the peaks in the Le Bail fit was used to obtain an apparent crystallite size of 6.6(2) nm. This is consistent with the TEM average of 12 nm as the crystallite size calculated from XRD is likely to be smaller than the total grain size seen in TEM imaging as a grain may be composed of more than one crystallite.

In order to obtain further evidence of alloying within the sample, Pd-rich particles were also synthesised and analysed using SXPD. The lattice parameters of carbon supported particles with Pd:Ir ratios of 3:1, 5:1 and 9:1, as well as pure Pd/C, were determined using the refinement procedure described above and the results are shown in Figure 4.17. The value for Ir was taken from Fonseca et al. [214] as it is a value for Ir nanoparticles and not bulk metal. There is a general increase in lattice parameter with increasing Pd content and the Pd:Ir 1:1 sample has an intermediate value between that of pure Pd and Ir, as with the bulk metal standards mentioned previously, suggesting alloying of the two metals in the catalyst samples. As well as the intermediate electronic density inferred from the XPS results, it is possible that the intermediate lattice size in PdIr/C has an effect on catalytic activity for the HOR. In addition, there is no evidence of bulk oxide in the XRD patterns, suggesting that the presence of oxygen seen in XPS is surface oxide only. This has implications for the interpretation of the following X-Ray absorption fine-structure results (see section 4.5).

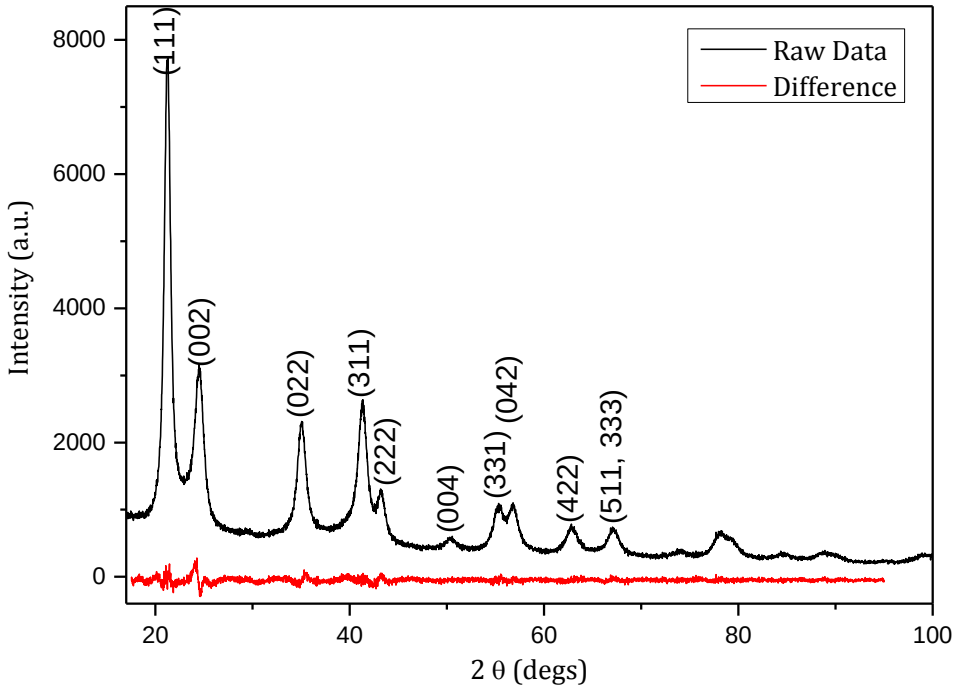

Figure 4.16 SXPD pattern of PdIr/C showing characteristic peaks of the FCC lattice and corresponding Miller indices (black). The difference trace is shown below in red.

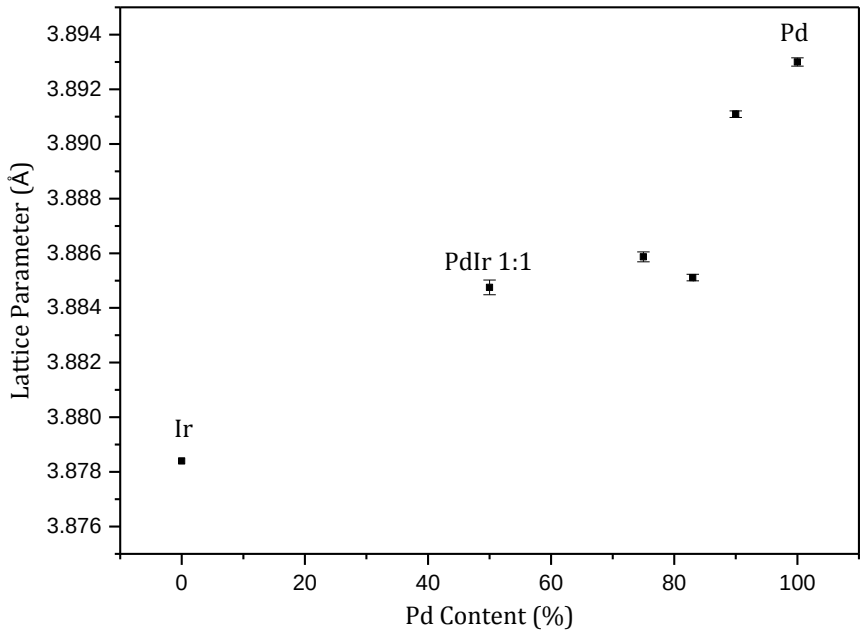

Figure 4.17 The increasing lattice parameter with Pd content. The value for Ir was taken from [214].

4.5 X-Ray Absorption Fine-Structure

It is known from XRD and XPS experiments that the PdIr/C catalysts consist of nanoparticle clusters of Pd and Ir with some degree of alloying present. However, information about the composition and homogeneity of the cluster can only be obtained by X-ray absorption fine-structure (XAFS) experiments, which can reveal the local coordination environment of an absorbing atom. XAFS spectra of PdIr/C, PdIr/C_{HSA} and PdIr/C 9:1 were obtained on the B18 beamline at the Diamond Light Source synchrotron.

The extended XFAS (EXAFS) data were modelled and fitted using the Demeter software suite [185] in order to extract information about the coordination and bond lengths in the catalysts. The full details of the fit can be found in Section 3.6.3 but it should be emphasised here that fitting of the EXAFS data was conducted by considering only the first coordination shell of the material as this is sufficient to obtain a nearest neighbour coordination number for each element and thus elucidation of the average structure of the catalyst [190]. Initial attempted fits included only Pd and Ir coordination, but a much better fit was obtained when including PdO and IrO_2 structures and scattering paths. Given the presence of significant oxide contribution to the XPS spectra (Figure 4.15) this is to be expected, and has been shown to be the case in Pt/C catalysts [178, 215], particularly in the work of Herron et al. [176] where varying the potential of the electrode during XAFS experiments produced a significant increase in oxygen neighbours on increasing the potential to the oxidation region. Significantly, however, the FCC structure of Pt is maintained under these conditions, indicating a thin film of oxide on the surface of the particles. It is therefore a fair assumption that the oxides present in the PdIr/C catalysts are also in the form of a surface thin-film.

4.5.1 Results

Good fits were obtained for all catalyst samples, indicating a good instrumental set up and sample preparation, as well as a valid model for the fit. Table 4.2 shows the extracted parameters from the fitting; N (coordination number of various shells), R (bond distance) and σ^2 (mean squared disorder in bond length), as well as the R-factor (R_f) which is a percentage measurement of the difference between the data and the theoretical EXAFS signal. All fits have low R_f, again indicating a good fitting model. For discus-

sion of the results it should be emphasised that EXAFS spectra arise from absorption throughout the whole sample and as such any parameters extracted from the data are average values.

Observing the total coordination numbers for either Pd or Ir ($N\Sigma_{Pd\text{-}X}$ and $N\Sigma_{Ir\text{-}X}$, respectively) it can be seen that all catalysts have lower coordination than would be expected for bulk FCC metal (12) due to the small size of the nanoparticles resulting in a larger proportion of the atoms in a cluster residing at the surface, and therefore having lower coordination [190, 216, 217].

$N\Sigma_{Pd\text{-}X}$ and $N\Sigma_{Ir\text{-}X}$ have similar values in all samples of around 8, which rules out a core-shell structure for these catalysts. In a perfect core-shell catalyst the core metal would have a coordination of 12 with the shell metal being much lower (around 6, depending on shell thickness) [183, 218, 219].

Considering only the 1:1 alloys (PdIr/C and $PdIr/_{HSA}$), both catalysts have higher Pd-Pd or Ir-Ir coordination than Pd-Ir, indicating a low level of mixing of the two elements within the alloy. However, the Pd-Ir coordination in both cases is high enough to rule out separate Pd and Ir clusters and therefore provides proof of alloying, at least to some degree [218, 220]. The slightly higher Pd-Ir coordination in $PdIr/C_{HSA}$ suggests a higher degree of mixing in this catalyst than in the PdIr/C.

Assuming that there is only surface oxide in the catalyst samples (no evidence of bulk oxide is seen in the XRD data, and previous work has shown that the oxide formation is restricted to the surface of Pt/C catalysts [176]), the higher Ir-O coordination in PdIr/C suggests that there is a greater amount of Ir at the surface than Pd, contrasted with the $PdIr/C_{HSA}$ catalyst which has a more even amount of oxide on both elements. The slightly higher total Pd coordination could suggest a more Ir rich (though still mixed with Pd) shell in the PdIr/C catalyst; however, the difference is small and within the error of the fit.

Beale and Weckhuysen simulated EXAFS spectra for many different bimetallic alloy structures (PtPd in their case) and showed the expected coordination numbers for, amongst others, core-shell, random and bicluster catalysts (Figure 4.21) [218]. Using this modelling as a guide, the PdIr 1:1 catalysts in this study seem to fit the 'single-half' structure most closely (Figure 4.21 (d)). That is to say, the catalyst is composed of a single cluster with a high degree of segregation between the Pd and Ir within the cluster. However, the PdIr 1:1 catalysts have an appreciably higher degree of mix-

ing than in the 'single-half' model and thus a slightly modified structural model is proposed, shown in Figure 4.22 (a).

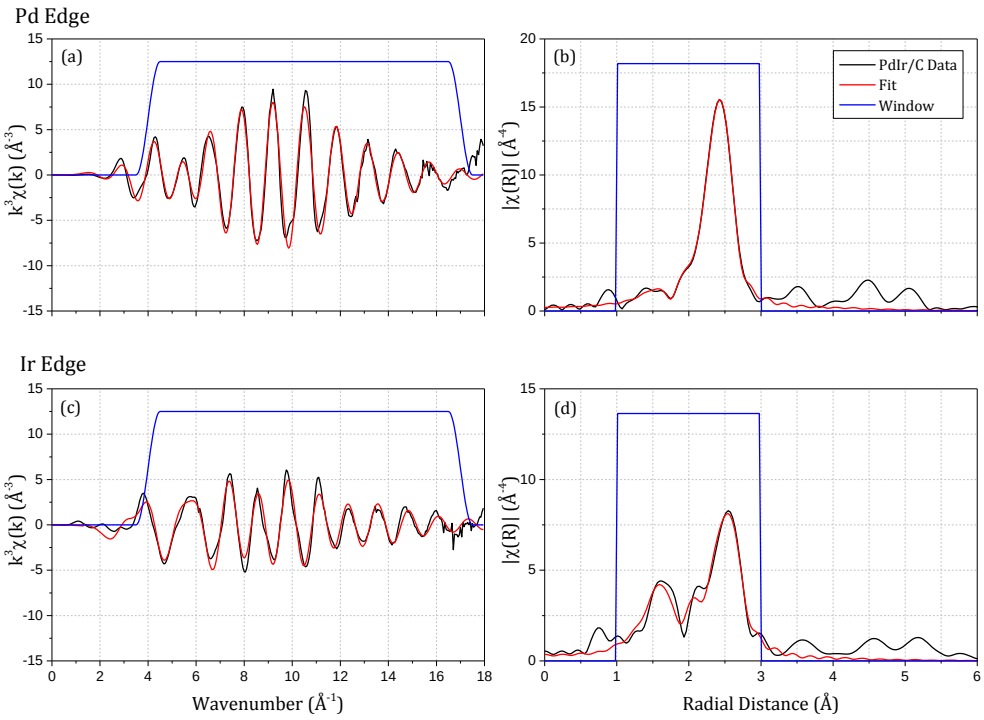

Figure 4.18 EXAFS data (black) and fits (red) for the PdIr/C catalyst showing; (a) the k^3 weighted Pd K edge and (b) corresponding k^3 weighted Fourier transform, and (c) the k^3 weighted Ir L_3 edge and (d) corresponding k^3 weighted Fourier transform.

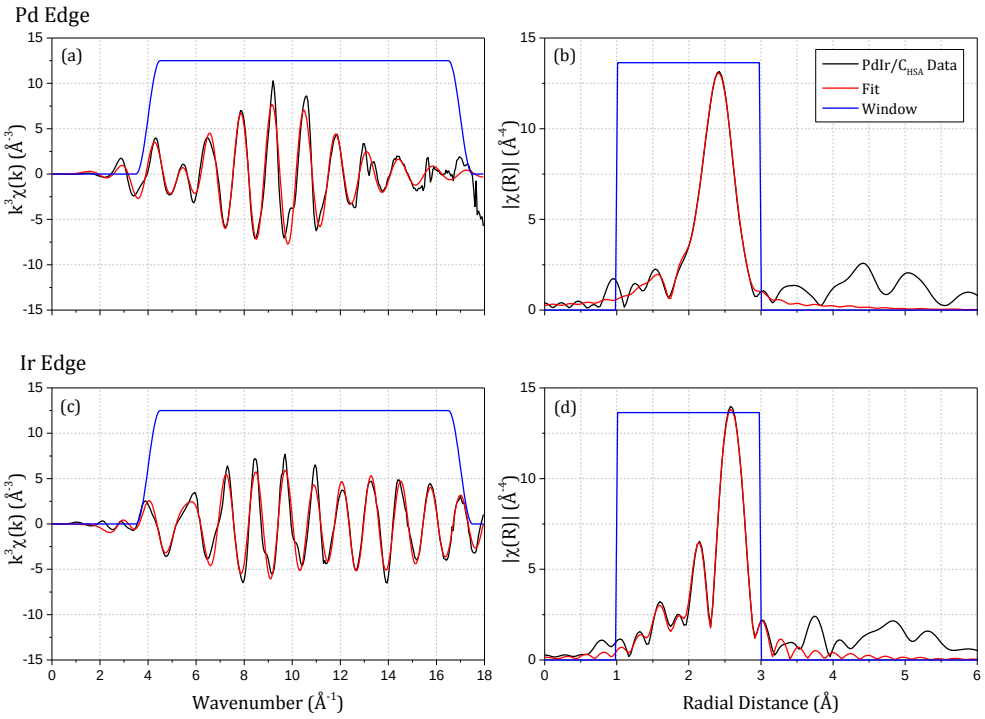

Figure 4.19 EXAFS data (black) and fits (red) for the PdIr/C$_{HSA}$ catalyst showing; (a) the k^3 weighted Pd K edge and (b) corresponding k^3 weighted Fourier transform, and (c) the k^3 weighted Ir L3 edge and (d) corresponding k^3 weighted Fourier transform.

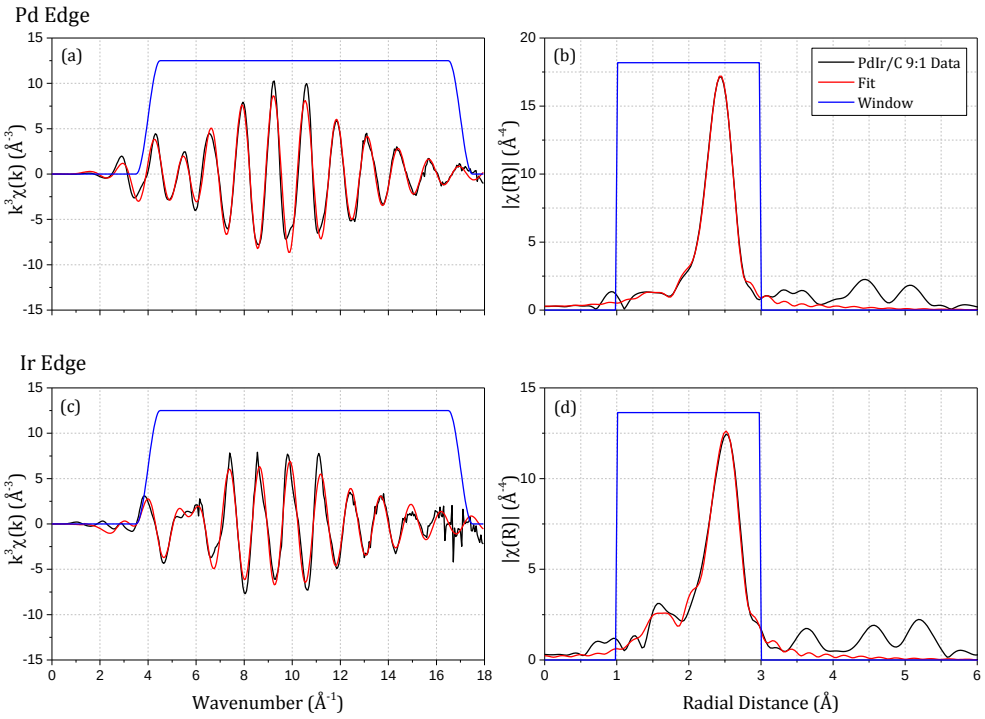

Figure 4.20 EXAFS data (black) and fits (red) for the PdIr/C 9:1 catalyst showing; (a) the k^3 weighted Pd K edge and (b) corresponding k^3 weighted Fourier transform, and (c) the k^3 weighted Ir L_3 edge and (d) corresponding k^3 weighted Fourier transform.

The PdIr/C 9:1 catalyst has low Pd-Ir coordination, as would be expected due to the low amount of Ir in the sample. The intermediate and similar values for Ir-Ir and Ir-Pd coordination suggest a decoration of Ir on the Pd. Though the $N\Sigma_{Pd\text{-}X}$ and $N\Sigma_{Ir\text{-}X}$ coordination is ostensibly similar, there is a significant contribution to $N\Sigma_{Ir\text{-}X}$ from IrO_2 which, if assumed to be at the surface, can be thought of as additional Ir coordination that would not be present in a fully reduced sample, thus lowering the total coordination for Ir. With this consideration, the PdIr/C 9:1 catalyst most closely fits the 'decorated' model of Beale and Weckhuysen. Indeed, this could also be applied to the PdIr/C catalyst suggesting a degree of decoration of Ir at the surface of the 'single-half' cluster. The equal Ir-Pd and Ir-Ir coordination, low Pd-O and high Ir-O coordination in the 9:1 sample also resembles a PdAu alloy structure in the work of Price et al., where a well-mixed shell of PdAu (PdIr in this case) surrounds a core mainly composed of Pd [180] (Figure 4.22 (b)).

In all cases the metallic bond lengths agree very well with those expected form the lattice parameter obtained via XRD (2.747 Å). As the

structure is FCC and the bond length obtained is that of the nearest neighbour, the value should be $^{1}/_{\sqrt{2}}$ times that of the lattice parameter (3.8851 Å). In all catalyst samples the Pd-Pd and Pd-Ir bond lengths are the same, within error. However, there is a difference in the Ir-Ir bond length for PdIr/C_{HSA} compared to both PdIr/C and PdIr/C 9:1 (which have the same Ir-Ir bond length as each other within error). This could be due to there being an element of Ir decoration in the latter two samples as opposed to a greater fraction of the Ir in PdIr/C_{HSA} being incorporated in the body of the cluster.

The mean squared disorder values and errors for all bond lengths are reasonable and mean that the structural model proposed in the fit is valid, the exception being the Pd-O bond in the PdIr/C sample, though the amount of PdO is low and so difficult to fit accurately.

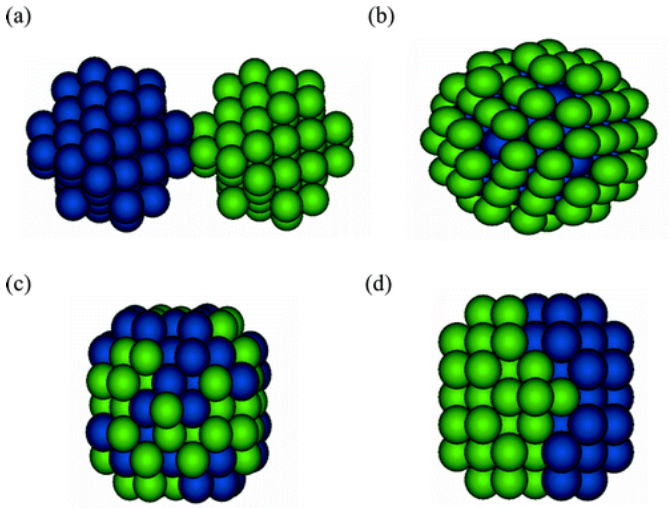

Figure 4.21 The hypothetical bimetallic structures proposed by Beale and Weckhuysen for Pt (blue) and Pd (green) alloys; (a) bi-cluster, (b) core-shell, (c) random and (d) single-half). Diagram from [218].

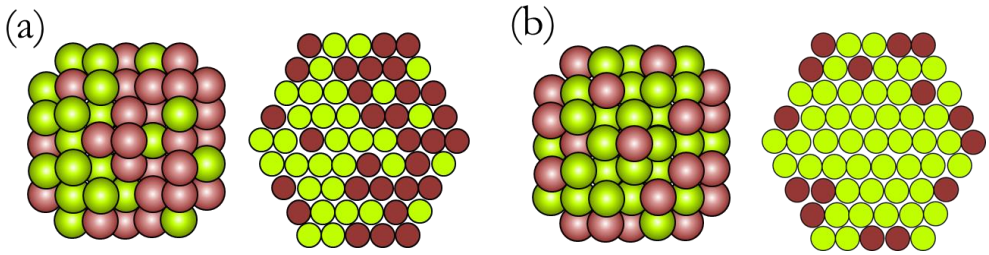

Figure 4.22 Depictions of possible arrangement of Pd (green) and Ir (red) atoms in the PdIr alloy clusters; (a) a single-half structure and cross-section with a higher degree of mixing than in Figure 4.21d and (b) a Pd cluster with Ir decoration, showing Ir mainly situated on the surface, with the corresponding cross-section highlighting the Pd-rich core.

In summary, both core-shell and well mixed alloy structures can be discounted from the EXAFS results. The PdIr/C and PdIr/C_{HSA} catalysts most closely resemble the 'single-half' structure, with a higher degree of mixing in the latter and an element of surface Ir decoration in the former. The Pd rich 9:1 catalyst consists of a well-mixed PdIr shell decorated on a core of Pd.

Table 4.2 Structural parameters obtained from the EXAFS fits to both the Pd K and Ir L_3 edge data.

Catalyst	Shell	N	R (Å)	σ^2 x 10^{-3} (Å^2)	R_f
PdIr/C	Pd-Pd	6.3 ± 0.5	2.736 ± 0.004	6.54 ± 0.43	0.009
	Pd-Ir	1.5 ± 0.6	2.718 ± 0.010	6.54 ± 1.29	
	Pd-O	0.5 ± 0.3	2.004 ± 0.022	3.57 ± 4.74	
	Ir-Ir	3.6 ± 0.7	2.657 ± 0.011	7.51 ± 0.99	
	Ir-Pd	2.0 ± 0.4	2.718 ± 0.010	6.54 ± 1.29	
	Ir-O_2	2.6 ± 0.5	1.974 ± 0.010	7.40 ± 1.96	
	Σ_{Pd-X}	8.4 ± 1.5			
	Σ_{Ir-X}	8.1 ± 1.7			
PdIr/C_{HSA}	Pd-Pd	5.0 ± 0.3	2.738 ± 0.002	5.40 ± 0.31	0.003
	Pd-Ir	2.3 ± 0.4	2.724 ± 0.004	4.95 ± 0.55	
	Pd-O	0.7 ± 0.2	1.997 ± 0.009	3.08 ± 1.83	
	Ir-Ir	5.7 ± 0.4	2.692 ± 0.002	5.34 ± 0.25	
	Ir-Pd	1.4 ± 0.2	2.724 ± 0.004	4.95 ± 0.55	
	Ir-O_2	1.0 ± 0.6	1.974 ± 0.013	5.27 ± 2.65	
	Σ_{Pd-X}	8.0 ± 0.8			
	Σ_{Ir-X}	8.1 ± 1.2			
PdIr/C 9:1	Pd-Pd	7.0 ± 0.2	2.737 ± 0.002	6.80 ± 0.18	0.004
	Pd-Ir	0.8 ± 0.3	2.715 ± 0.007	6.34 ± 0.81	
	Pd-O	0.5 ± 0.2	1.996 ± 0.013	4.39 ± 2.96	
	Ir-Ir	3.1 ± 0.8	2.651 ± 0.013	7.21 ± 1.33	
	Ir-Pd	3.7 ± 0.5	2.715 ± 0.007	6.34 ± 0.81	

	Ir-O_2	1.5 ± 0.7	1.978 ± 0.018	7.96 ± 4.52
	$\Sigma_{\text{Pd-X}}$	8.2 ± 0.7		
	$\Sigma_{\text{Ir-X}}$	8.3 ± 2.0		

4.6 Low Energy Ion Scattering

Low energy ion scattering (LEIS) is a surface sensitive spectroscopic technique used to investigate the elemental makeup of the catalysts' surface. Figure 4.23 shows the cumulative raw spectra (red) and background corrected net spectra (black) obtained for the PdIr/C, PdIr/C_{HSA} and PdIr/C 9:1 catalysts, as well as the fitting curves used to calculate the integrated Pd (green) and Ir (orange) peak areas. Pd Peaks are seen around 2400 eV and Ir peaks around 3275 eV. The cumulative spectra were summed from partial spectra following an acquisition-sputtering cycle, the details of which can be found in Section 3.8.

From integration of the fitted Pd and Ir accumulated peaks the Pd:Ir ratio was calculated to be roughly 3:1, 1:1 and 10:1 for the PdIr/C, PdIr/C_{HSA} and PdIr/C 9:1 catalysts respectively. The significantly higher Pd amount seen for PdIr/C and, to a lesser extent, PdIr/C 9:1 is unexpected for the bulk material compositions verified with ICP-AES and so the partial spectra were studied with increasing sputtering cycles and discussed below.

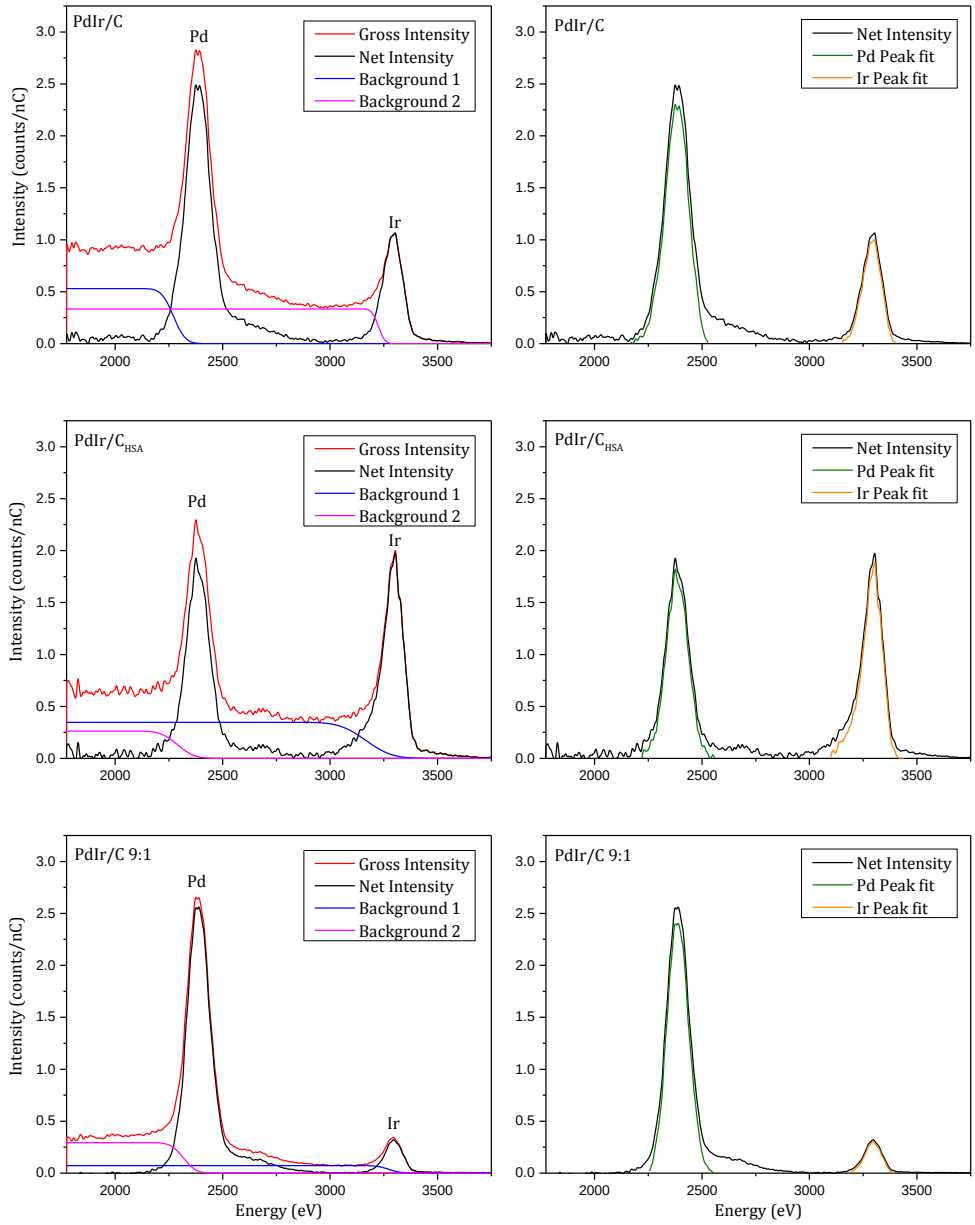

Figure 4.23 LEIS spectra of PdIr/C (top), PdIr/C_{HSA} (middle) and PdIr/C 9:1 (bottom). Showing: in the left column; the gross intensity (red), two background corrections applied (blue and pink) and the resulting corrected net intensity spectrum (black); and in the right column the net intensity (black), Pd peak fit (green) and Ir peak fit (orange).

Figure 4.24 shows the sputtering profiles for the catalysts; that is, the peak integrals for Pd (green) and Ir (orange) of each partial spectrum taken after each 10 s sputtering event. There is a general trend of increasing amounts of Pd and Ir appearing in the first few cycles, as would be expected due to removal of surface contaminants, after which the profiles

plateaux to reflect the relative peak integrals of the accumulated spectra previously discussed. Given the roughly 1:1 Pd:Ir ratio seen for PdIr/C in ICP-AES experiments, the disparity between the Pd and Ir amounts is notable. The estimated total sputtering depth for the PdIr/C sample was 1.6 nm and so, given the average particle size of 12 nm and significant agglomeration issues seen in the TEM, this is likely to represent only the outer 10% or so of most catalyst particles. It must be noted that, certainly for the similar technique of secondary ion mass spectrometry (SIMS), sputtering of nanoparticles for depth profiling may be significantly different to that of flat surfaces [201] and medium energy ion scattering (MEIS) would be more suited to depth profiling of bimetallic catalysts [199]. Nevertheless, assuming the profile for PdIr/C represents mainly the outer surface of the nanoparticles, it would seem that there is a Pd-rich outer layer with an, assumed, Ir-rich core (in order for the 1:1 atomic ratio to hold, further sputtering depth would have to show a decrease in Pd and increase in Ir amounts). This is contrary to the results from EXAFS experiments which showed this catalyst to have a slight Ir decoration in the surface layers of a poorly mixed bimetallic cluster. Unless there is a preferential anchoring of Ir to the carbon support over Pd (leaving the exposed side of the bi-cluster as the Pd-rich half), and to the author's knowledge there is nothing to suggest that this is the case, this result is unexplained. A full sputtering depth profile would reveal more information; however, this was not possible due to the sputtering dose exceeding that recommended for the instrument. MEIS experiments could provide more illumination for this catalyst.

Conversely, the PdIr/C_{HSA} catalyst shows a profile much more similar to that expected from a 1:1 catalyst; after surface decontamination is achieved the amounts of Pd and Ir plateaux to similar values relatively quickly. This is expected due to the smaller and more dispersed nanoparticles and the slightly better mixing of elements in the crystallites seen from TEM and EXAFS, respectively.

As expected, there is a higher amount of Pd than Ir seen for the PdIr/C 9:1 catalyst, though the ratio is still slightly Pd rich. Again, this does not correspond with the results of the EXAFS experiments which suggested that most of the Ir in this catalyst is at the surface. The reason for this result is likely the same as for the PdIr/C catalyst and requires further investigation to fully elucidate.

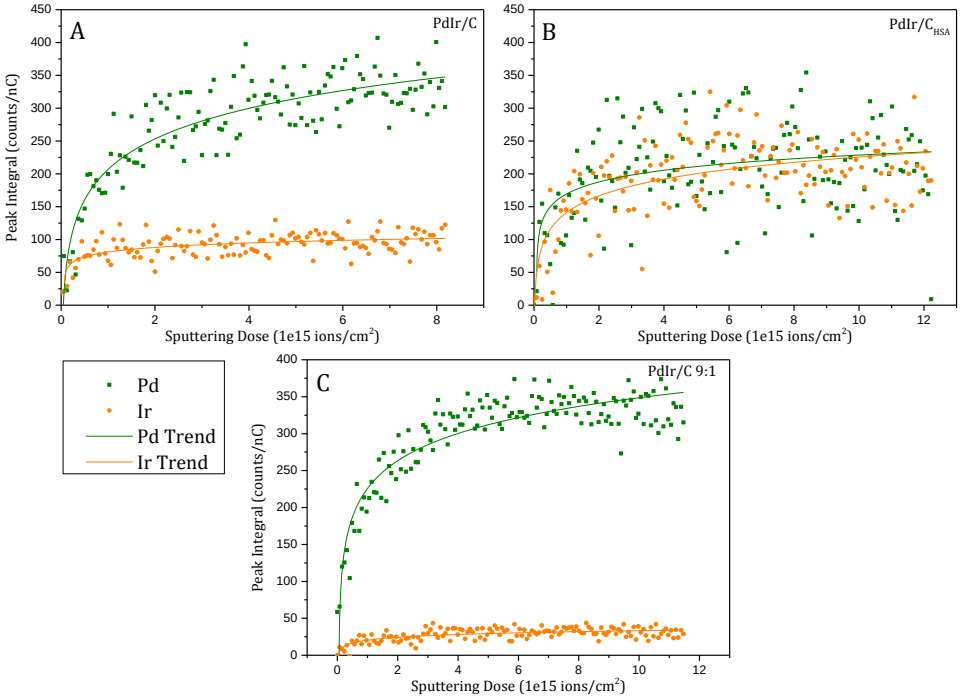

Figure 4.24 Sputtering profiles for PdIr/C (A), PdIr/C_{HSA} (B) and PdIr/C 9:1 (C) showing the integrated areas of the Pd (green, squares) and Ir (orange, circles) peaks with increasing sputtering dose.

5 Electrochemical Testing

To measure the inherent catalytic activity of a catalyst the redox reaction kinetics can be studied using a variety of electrochemical techniques. Cyclic voltammetry (CV), carbon monoxide stripping (CO CV) and rotating disk electrode (RDE) experiments were conducted to assess the physical and kinetic properties of the PdIr/C catalyst and compare them with that of a commercially available Pt/C catalyst. Electrochemical impedance spectroscopy (EIS) was employed in order to separate the charge and mass transfer resistances of the catalysts, and the catalyst durability was also measured over long potential cycling.

5.1 Glass Cell

Initial experiments were conducted in a three-electrode glass cell as it is based on a common design for RDE experiments and produces reliable results due to the positioning of the luggin capillary and gas inlet pipe.

5.1.1 Cyclic Voltammetry

Cyclic voltammetry was conducted on Pt/C and PdIr/C catalysts in 1M KOH alkaline medium. The main purpose of the CV is to calculate an electrochemical surface area for the catalysts. There are four main regions in the CVs shown in Figure 5.1;

The hydrogen desorption region at low potentials and positive current which represents the removal of adsorbed hydrides,

The oxide formation region at high potentials and positive currents which represents the formation of M-OH and MO_x species,

The oxide removal region at high potentials and negative current where reduction of the surface oxide species occurs,

The hydrogen adsorption region at low potentials and negative current where hydrides are formed on the electrode surface.

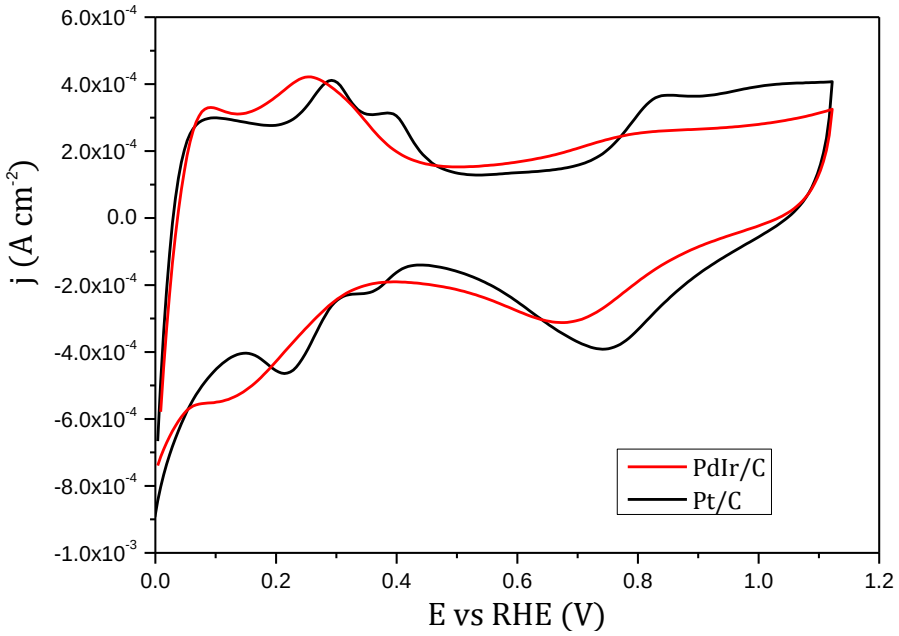

Figure 5.1 Cyclic voltammograms of commercial Pt/C Catalyst (black) and PdIr/C catalyst (red). The current is normalised to the geometric surface area of the electrode.

Autolab GPES software was used to integrate the area under the hydrogen desorption region to give the total columbic charge (after baseline correction for the double layer charge) and the electrochemical surface area (ECSA) was calculated from this value using a common method in the literature [221]. The ECSAs calculated were 13.79 m^2g^{-1} and 8.10 m^2g^{-1} for the Pt/C and PdIr/C catalysts respectively. The lower surface area for the PdIr/C catalyst corroborates the suspected agglomeration problems seen in the TEM imaging of the catalysts. The ECSAs derived in alkaline solution were lower for both catalysts than they were in acidic solution (not discussed in this work) which might suggest that the ionic transport is worse in alkaline solution, most likely due to the use of a proton-conducting ionomer as a binder in the catalyst layer.

5.1.2 Carbon Monoxide Stripping Voltammetry

Carbon monoxide is a strongly binding ligand and can therefore poison a catalyst by binding to and blocking active sites, preventing catalyst atoms from being used in the desired reaction. Currently, much of the hydrogen produced commercially is generated from reforming of hydrocarbons and so contains traces of CO. Even small amounts of CO can greatly hinder the

performance of a fuel cell catalyst, so CO tolerance is a highly desired property. To test the CO tolerance of the catalysts carbon monoxide stripping cyclic voltammetry (CO CV) is employed. CO is irreversibly adsorbed to the catalyst surface and then electro-oxidation removes it as CO_2. If the potential at which this electro-oxidation occurs is lower than the normal operating potential expected of a fuel cell (around 0.6 V), any CO adsorbed during operation will be oxidised and therefore will not hinder the HOR or ORR, or affect fuel cell performance.

5.1.2.1. Experimental

After the general experimental preparation (Section 3.9.2.1), carbon monoxide is bubbled into solution for 10 minutes, while the electrode is held at 18 mV to force electrodeposition of CO. Following this, the electrolyte is purged with nitrogen gas for 25 minutes to remove all CO from the cell, leaving only adsorbed CO on the electrode surface. A CV is then taken to observe the CO stripping behaviour.

5.1.2.2. Results

Figure 5.2 shows the CO CVs for Pt/C (black) and PdIr/C (red) along with an overlay of a CO-free Pt/C CV (grey). The positive CO oxidation peaks are seen at 0.71 V and 0.75 V for the Pt/C and PdIr/C catalysts respectively. The peak is more positive for the palladium-containing catalyst, which is expected as previous studies have suggested a stronger bonding of CO on palladium [144] (requiring a higher overpotential to remove and oxidise it). However, the peak potential of both catalysts is too positive to enable removal of CO during normal fuel cell operation. As a general rule, the lower the potential for the CO oxidation peak, the less the anode needs to be polarised in order to remove CO and so the less the fuel cell performance is compromised due to overpotential losses. For this reason, PtRu/C catalysts are often used on the anode electrodes in fuel cells. The Ru helps promote the oxidation of CO at a lower peak potential of around 0.5 V via the bifunctional mechanism, where Ru-OH is formed adjacent to Pt-CO sites and aids in the oxidative removal of CO from the Pt [222]. The peak potentials of both Pt/C and PdIr/C in this experiment are higher than generally seen for PtRu/C [223], and so the CO tolerance of both is lower in this respect.

However, a non-zero current is seen in the hydrogen desorption region of the PdIr/C CO CV (cf zero current for Pt/C and the higher current, and therefore hydrogen coverage, in the CO-free CV). This suggests that a proportion of hydrogen species remains on the electrode surface, despite carbon monoxide presence. Using relative electrochemical surface area calculations, the coverage of CO on PdIr/C catalyst was found to be only 74%, as opposed to 100% coverage for Pt/C. This means that not all of the PdIr/C catalyst is poisoned, despite saturation with carbon monoxide. Yepez and Scharifker [224] suggested that the ability of Pd to store hydrogen could help to reduce the surface coverage of CO, and a similar sub-monolayer coverage of CO was found by Papageorgopoulos et al. on PtPd alloy catalysts [144]. They found that increasing both the temperature and Pd content decreased the fractional coverage of CO, with the lowest coverage of 73% achieved for pure Pd at 80°C. However, a much higher coverage was seen at 25°C (the same temperature as this experiment) with 95% coverage for pure Pd and 93% coverage for $PtPd_6$. As well as decreasing the CO coverage, the peak potential increased with increasing Pd content in their alloys. The lowest peak potential at 25°C was for PtPd 1:1 at 0.775V – higher than that of the PdIr/C catalyst in this experiment.

The lower peak potential and CO coverage of PdIr/C compared to PtPd suggests that the presence of Ir might aid carbon monoxide tolerance and shows potential for application of the novel PdIr/C catalysts in place of more widely used PtPd alloys.

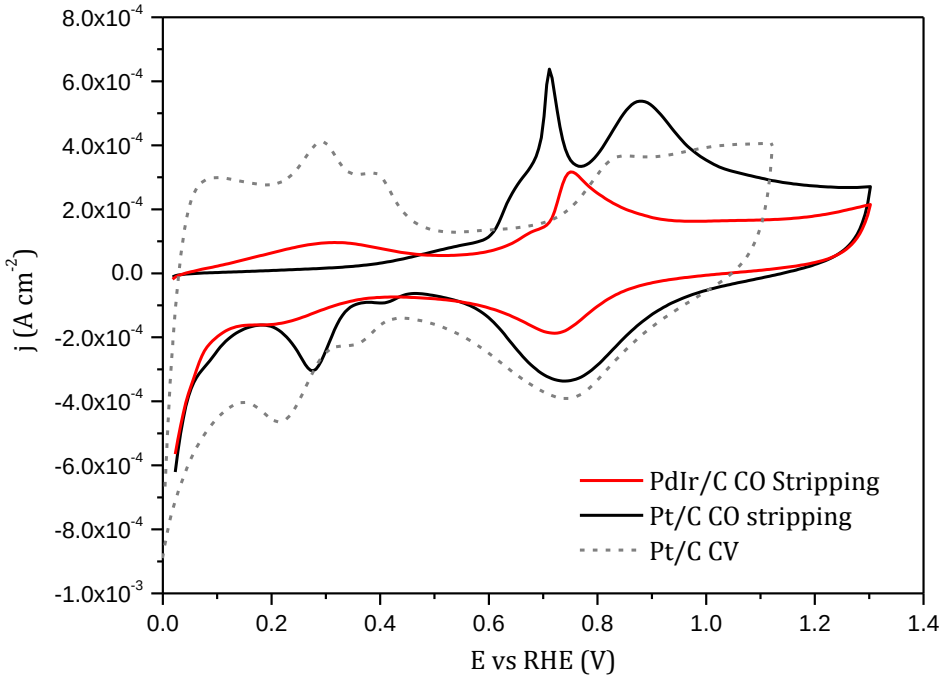

Figure 5.2 CO stripping voltammograms of commercial Pt/C catalyst (black) and PdIr/C catalyst (red). A CO-free CV of Pt/C is shown (grey) to contrast the hydrogen desorption region. The current is normalised to the geometric area of the electrode.

5.1.3 Rotating Disk Electrochemistry

Cyclic voltammetry is conducted with a stationary electrode and in a deaerated electrolyte. For the RDE experiments, hydrogen gas is used in conjunction with rotation of the electrode to study the kinetics of the HOR. The rotation of the electrode serves to create a convection current, delivering the reactant to the electrode surface with a well-defined laminar flow, and removing the reaction products. This allows control of the mass transport aspect of performance of the catalyst, and thus deconvolution of this from the inherent electrochemical activity is possible. RDE has been widely used to study high surface area fuel cell catalysts, beginning with the pioneering work of Schmidt, Gasteiger et al. [225].

5.1.3.1. Experimental

The cell is set up as described in Section 3.9.2.1, then the gas stream is switched from nitrogen to hydrogen. Hydrogen is bubbled through the solution for 40 minutes (hydrogen is not very soluble in strong alkaline solutions) to saturate the solution with reactant. H_2 is also bubbled slowly dur-

ing the experiments. The electrode is rotated at 1600 rpm, as the faster rotation creates a larger diffusion limited current value and so a greater potential region over which the kinetic current has an influence. At higher rotation rates than 1600 rpm there is a chance of cavitation occurring in the solution, creating radicals and affecting the results as well as potentially corroding the catalyst layer. Linear sweep voltammetry is used to scan between -0.015 V and 0.4 V at 5 mV cm^{-2}, producing a RDE voltammogram.

5.1.3.2. Results

Figure 5.3 shows an example RDE voltammogram for the HOR at both the commercial Pt/C and PdIr/C catalysts. The high rotation rate of the electrode controls the thickness of the reactant diffusion layer at the electrode, and thus the rate of diffusion of H_2 to the electrode surface is fixed [202]. At low polarisations the diffusion rate is more than fast enough to supply ample reactant for the reaction to take place, and so the reaction is said to be under kinetic control in the low polarisation region. As the overpotential is increased the reaction is driven harder and so requires more reactant to produce the kinetically desired current. Eventually the fixed diffusion rate is not high enough to supply sufficient reactant and the reaction becomes diffusion controlled, up to the point where the polarisation is sufficient to make the reaction completely diffusion-limiting and the current plateaus at a maximum value. This gives the characteristic shape of the curves seen in Figure 5.3.

The diffusion-limiting current value is slightly higher for Pt/C than PdIr/C, but this is determined by factors such as catalyst layer thickness and structure and so is very hard to repeat accurately between two samples (the metal loading of both electrodes is the same at 35 μg cm^{-2}). Additionally, there may be variations in the saturation of H_2 in the electrolyte which can change the limiting current value. What is more important when evaluating the catalyst activity is the kinetic component of the current, which is indicated in the gradient of the curve at potentials before the diffusion-limited value is reached. The gradient of the PdIr/C catalyst's curve (red) is steeper than that of the Pt/C (black), but a Tafel analysis of the data is required for quantitative evaluation (Figure 5.4).

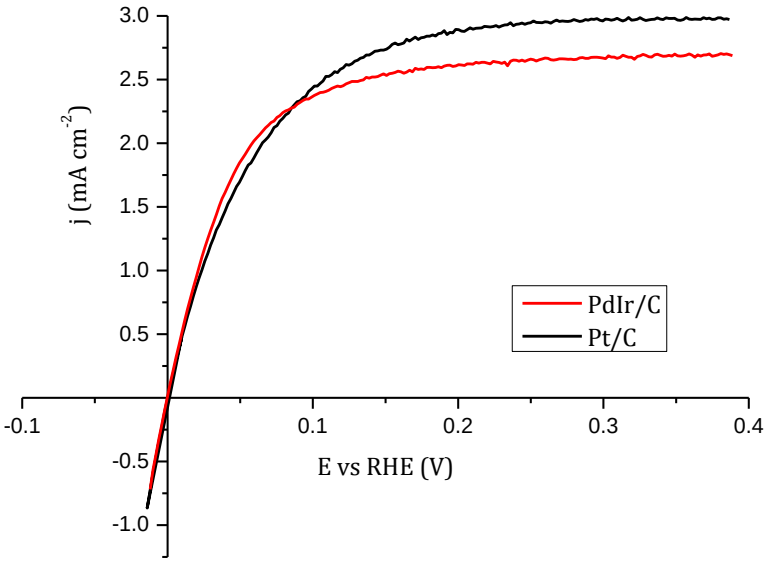

Figure 5.3 RDE voltammograms of the HOR at Pt/C catalyst (black) and PdIr/C catalyst (red) obtained at a rotation rate of 1600rpm in 1 M KOH (aq). The current is normalised to the geometric area of the electrode.

5.1.3.3. Tafel Analysis

As discussed in Section 1.4.1.6, the Tafel approximation can be used to simplify the B-V equation:

$$\eta = a + b \log j \qquad \text{Equation 5.1}$$

Where $a = 2.303 \frac{RT}{\alpha_i nF} \log j_0$ and $b = -2.303 \frac{RT}{\alpha_i nF}$. For simplification, this is often rearranged to:

$$\log j = \frac{\eta}{b} - \frac{a}{b} \qquad \text{Equation 5.2}$$

From the definitions of a and b it is seen that $\frac{a}{b} = -\log j_0$ and thus:

$$\log j = \frac{\eta}{b} + \log j_0 \qquad \text{Equation 5.3}$$

Therefore, the linear region of a plot of log current density vs potential (Figure 5.4) has a gradient of $\frac{1}{b} = -\frac{\alpha_i nF}{2.303RT}$ and an intercept of $\log j_0$ allow-

ing calculation of the exchange current density (j_0) and the charge transfer coefficient (α).

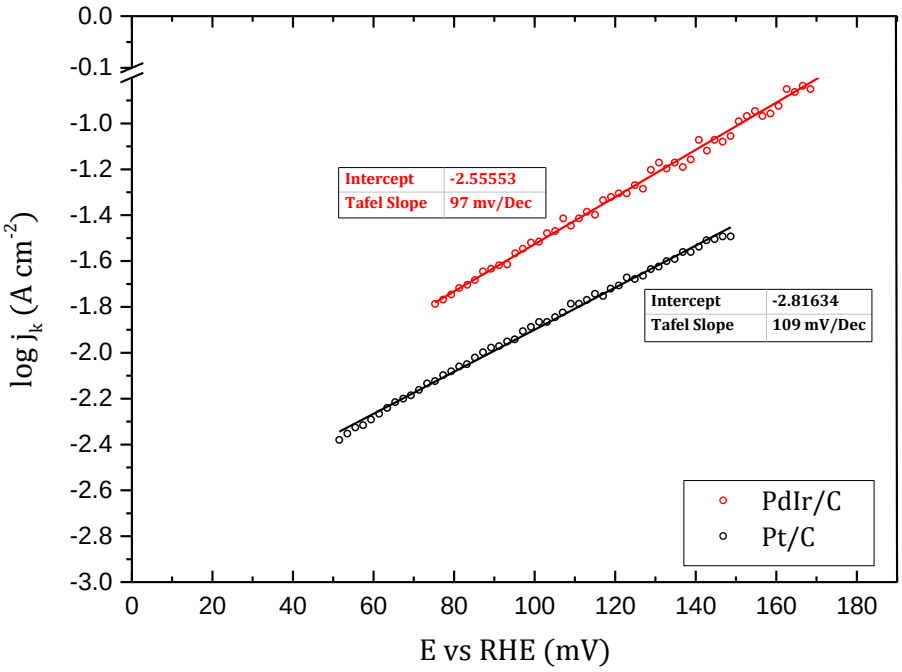

Figure 5.4 Tafel plot of Pt/C catalyst (black) and PdIr/C catalyst (red) obtained from the data shown in Figure 5.3. The current is normalised to the geometric area of the electrode.

The data in Figure 5.4 yield j_0 values of 1.53 mA cm^{-2} and 2.78 mA cm^{-2} for Pt/C and PdIr/C respectively. As shown in Figure 1.9, the effect of j_0 on activation potential losses is very strong and so as high a j_0 as possible is desired for good catalyst performance. The in-house PdIr/C catalyst has an increase in exchange current density of over 80% compared to the commercially available Pt/C catalyst and so is a promising candidate for replacement of platinum-based catalysts in AAEM fuel cells.

Also from this data, the Tafel slopes give αn values of 0.54 and 0.61 for Pt/C and PdIr/C respectively. Assuming the same mechanism on both catalysts where the number of electrons in the rate determining charge transfer step, n, is 1 [86], this suggests that the PdIr/C catalyst has a higher charge transfer coefficient, meaning that a larger percentage of the overpotential favours the forward reaction than the reverse (HER).

5.1.4 Koutecky-Levich Analysis

The Koutecky-Levich equation (Equation 5.4) can be used to determine the kinetic contribution to the overall current density by obtaining RDE voltammograms at multiple rotation rates [226]:

$$\frac{1}{i} = \frac{1}{i_k} + \frac{1}{i_d} = \frac{1}{i_k} + \frac{1}{Bc_0\omega^{\frac{1}{2}}} \qquad \text{Equation 5.4}$$

Figure 5.5 shows an example of such data obtained for the HOR on PdIr/C at rotation rates of 400, 600, 900, 1200 and 1600 rpm.

The rotation of the electrode serves to deliver reactant to the electrode surface via forced convection in a controlled and well defined manner, as well as maintaining homogeneity in the electrolyte. Adjacent to the electrode surface is a stagnant layer called the Levich layer where, as opposed to convection, the main mode of mass transport is diffusion.

$$\delta_L = 1.61\ \mathrm{D}^{1/3}\omega^{-1/2}\nu^{1/6} \qquad \text{Equation 5.5}$$

Equation 5.5 governs the thickness of the Levich layer, δ_L, where D is the diffusion coefficient, ω is the rotation rate of the electrode (rad/s) and ν is the kinematic viscosity of the electrolyte. The limiting current value, i_{lim}, is inversely proportional to the thickness of the Levich layer, as described by the Levich equation:

$$i_{lim} = 0.62\ nFA(\mathrm{D}/\delta_L)C \qquad \text{Equation 5.6}$$

Where n is the number of electrons transferred in reaction, F is Faraday's constant, A is the area of the electrode and C is the concentration of reactant. As the rotation rate is increased the thickness of the Levich layer decreases and therefore the diffusion rate and mass transport limiting current (the point where the curve levels off at higher polarisations) increases.

At low polarisations only a small amount of reactant is required and so the current is said to be under total kinetic control. This is manifested in the convergence of all the curves near to the origin, and as the polarisation is increased from here the mass transport controlled current has increasing influence, leading to divergence of the curves until complete mass transport limited behaviour is reached. Thus, the overall current density is composed

of a rotation-rate-dependant mass transport current, i_d, and a rotation-independent kinetic current, i_k which is dependent on the activity of the catalyst [227-229].

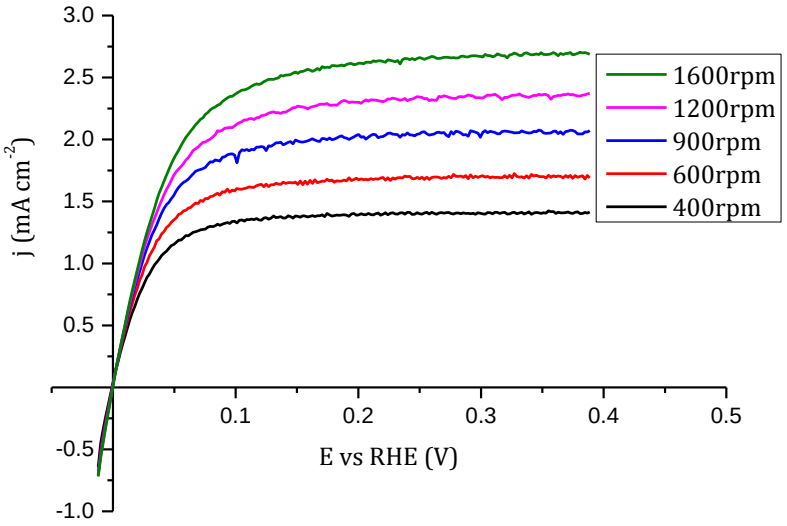

Figure 5.5 A plot of multiple RDE voltammograms for the HOR at PdIr/C catalyst with rotation rates varying from 400 rpm (black) to 1600 rpm (green). The current is normalised to the geometric area of the electrode. These data are used for the Koutecky-Levich analysis.

The data in Figure 5.5 are used to construct plots of $\frac{1}{i}$ vs $\frac{1}{\omega^{1/2}}$ at the potentials 0.025, 0.05, 0.075, 0.1 and 0.125 V (Figure 5.6). In accordance with the Koutecky-Levich equation they yield intercepts of $\frac{1}{i_k}$, and therefore the kinetic currents, for each potential point. That is, extrapolating the current at a theoretical infinite rotation rate removes all restriction from the diffusion limitation and gives a purely kinetic current which is defined by the heterogeneous rate constant for the reaction, k_f (forward reaction):

$$i_k = nFAk_fC \qquad \text{Equation 5.7}$$

The above potentials were chosen as they represent the parts of the curve in Figure 5.5 where the trend is neither linear nor in the diffusion-limited region, i.e. there is both a kinetic and diffusion contribution to the overall current density. The area of mixed control exists over a relatively large region of overpotential compared to what is typically found in acid

HOR experiments, meaning the Koutecky-Levich analysis is valid for alkaline HOR but not for acid HOR [73, 84, 230].

Extracting values for i_k at different potentials can yield kinetic parameters such as the standard rate constant, k^0, and the symmetry factor, α via the following equations (and following Equation 5.7):

$$k_f = k^0 e^{\left(\frac{F}{RT}\eta(1-\alpha)\right)} \qquad \text{Equation 5.8}$$

$$\ln k_f = \ln k^0 + \frac{F}{RT}\eta(1-\alpha) \qquad \text{Equation 5.9}$$

Where η is the polarisation. Thus, a plot of $\ln k_f$ vs η gives a straight line and allows calculation of k^0 from the intercept and α from the gradient, provided the diffusion constants are known. However, this calculation is rarely performed in the literature and for most purposes, comparisons of i_k suffice for comparing the performance of different catalysts [230]. In particular, the apparent rate constant from Koutecky-Levich analysis can differ from the actual rate constant due to the difference in actual catalyst surface area and geometric area of the (catalytically) inert electrode substrate, as outlined in the analysis by Masa et al. [231]. For this reason, the method of application of the catalyst layer to the electrode surface is maintained as consistently as possible between experiments and the values obtained for kinetic currents of different catalysts are used for comparative purposes and are not intended as absolute rate constants for each catalyst.

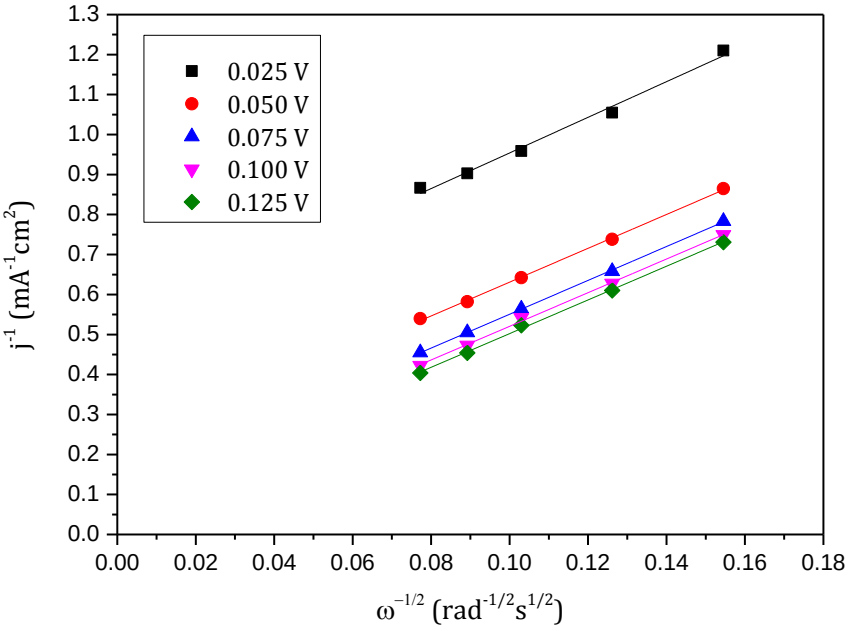

Figure 5.6 Koutecky-Levich plot of RDE data of the HOR on PdIr/C in 1M KOH and using a glass cell. The inverse of the current density is ploted at different roation rates for a series of polarisations, producing straight lines of similar gradient for each potential.

This treatment is repeated for the Pt/C data (see Appendix 9.2) and the kinetic currents are then normalised for mass activity (the metal loading of the electrode, Figure 5.7) and specific activity (the electrochemical surface area of the catalyst, Figure 5.8) and compared, in accordance with the method of Garsany et al. [203]. In both cases the PdIr/C catalyst has a higher kinetic current at any given potential than the commercial Pt/C catalyst, indicating that it is more active for the HOR in alkaline solution than platinum. The exception is at 0.125 V for the mass activity data where the higher diffusion-limited current value for Pt/C (Figure 5.3) means that the current is still increasing at this potential, whereas the PdIr/C is close to its diffusion-limited value. The improved activity of the PdIr/C catalyst is more exaggerated when normalised to electrochemical surface area as the agglomeration issues resulted in a much lower surface area than that of the commercial Pt/C. This means that although the utilization of the PdIr/C catalyst is low, its performance still exceeds the commercial Pt/C catalyst and so the potential for improvement with optimization of the synthesis procedure is promising.

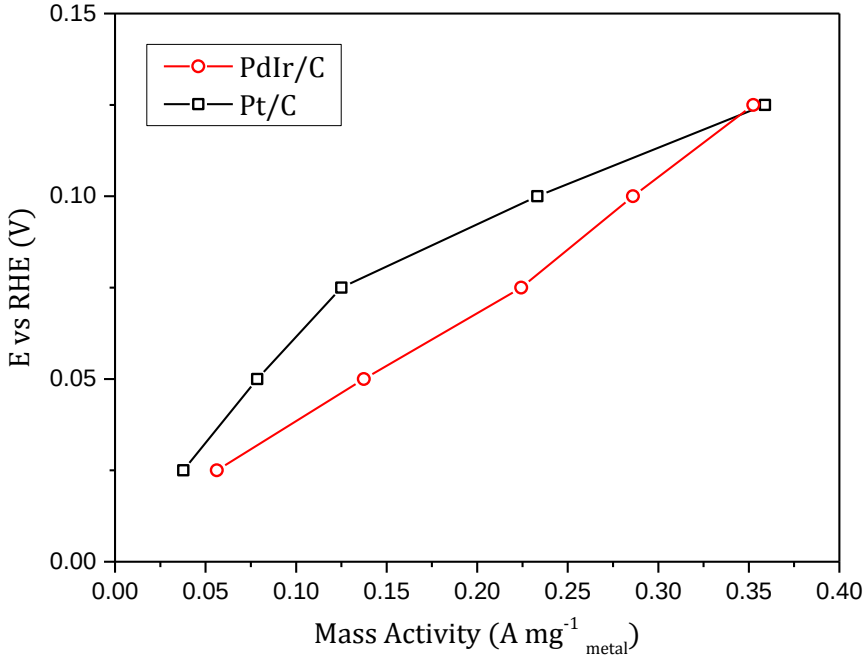

Figure 5.7 Plot showing the kinetic current normalised to mass of metal on the electrode at various potentials of the RDE voltammograms for Pt/C (black) and PdIr/C (red). The kinetic current is higher for any given potential for PdIr/C than Pt/C except at 0.125 V where the current is similar, showing that it has higher mass activity for the HOR.

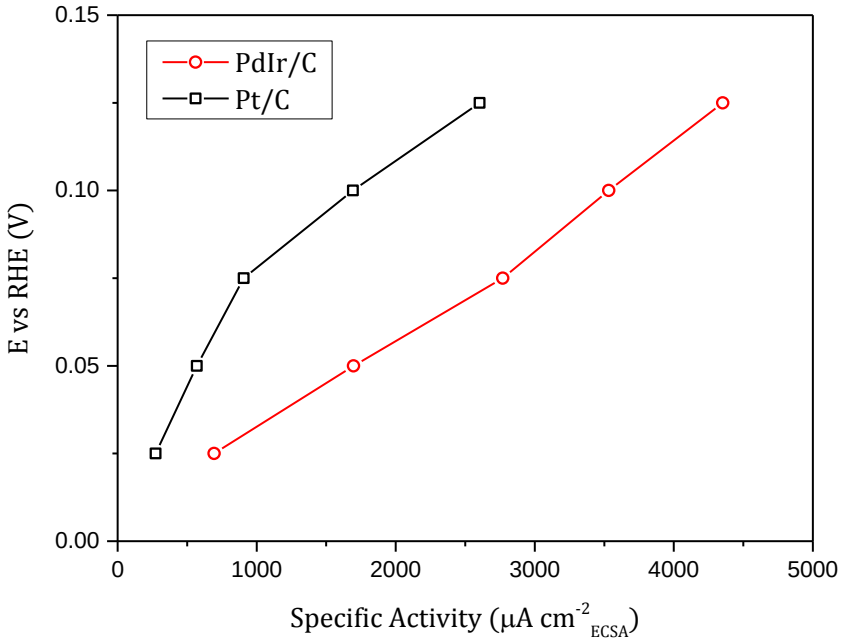

Figure 5.8 Plot showing the kinetic current normalised to electrochemical surface area of the catalysts at various potentials of the RDE voltammograms for Pt/C (black) and PdIr/C (red). The kinetic current is again higher for PdIr/C than Pt/C showing that it also has a higher specific activity for HOR in alkaline.

5.2 PTFE Cell

As alkaline solutions can corrode glass, releasing silicates into solution [232], and give rise to possible contamination of the electrode, further experimentation was conducted in a PTFE cell made to the same specifications as that of the cell used by Mayrhofer et al. [204]. The concentration of the electrolyte in the following experiments was also reduced to 0.1 M KOH to more closely reflect the majority of the literature on alkaline electrochemistry. A further change was made in using an alkaline ionomer as a binder for the inks (AS-4, Tokuyama) in place of Nafion, to see if improvements to the HOR could be seen with suspected lower diffusion resistance (see Section 5.2.6.1). All these changes to the experimental procedure were expected to improve apparent performance of the catalysts (thus more closely representing their inherent activity) and the stability of the experimental setup. The stability of the experiment is particularly important for durability or carbon corrosion studies (Section 5.2.7) where long-term experimentation would not be possible in the glass cell (electrolyte must be replaced after a couple of hours or so as the electrode becomes contaminated).

Improvements to the PdIr/C were also made by pre-treating the carbon with a solution of KOH and using a more aggressive reducing agent in an attempt to increase the surface area (see Section 3.1.6). This catalyst will be denoted as PdIr/C_{HSA} and is compared with the original PdIr/C and Pt/C catalysts in this section of experiments. The use of the alkaline binder, as opposed to Nafion, generally decreased the quality of the prepared inks, in that the catalyst powders tended to disperse less well in the alkaline binder. This effect was more pronounced with the PdIr/C catalyst than the Pt/C and PdIr/C_{HSA}, possibly due to carbon pre-treatment in the latter two that could aid in hydrophilicity in the presence of the alkaline binder. In Section 5.2.3 comparison is made between electrodes created with catalyst inks containing the alkaline AS-4 binder and those using Nafion as a binder, the latter being denoted as PdIr/C-Naf and Pt/C-Naf. In-house Pd/C and Ir/C catalysts were also synthesised in order to gauge the level of improvement on alloying of the two metals in comparison to the mono-metallic catalysts.

5.2.1 Cyclic Voltammetry

CVs of the PdIr/C, PdIr/C_{HSA} and commercial Pt/C catalysts are shown in Figure 5.9. Though the CVs have similar features as those conducted in the glass cell (Figure 5.1), it is noticeable that the peaks are far more defined and a relatively smaller double-layer capacitance is seen when using the PTFE cell and alkaline binder in the ink. This is likely due to contaminants from the corrosion of glass being absorbed on the catalyst surface and the positively charged Nafion binder having a blocking effect on ion transport. The hydrogen desorption region yields electrochemical surface areas (ECSAs) of 18.16, 28.28 and 33.99 m^2g^{-1} for PdIr/C, PdIr/C_{HSA} and Pt/C, respectively. This represents a significant increase in ECSA from those obtained in the glass cell using Nafion as the binder, and confirms the adjustment to the synthesis procedure for PdIr/C_{HSA} has improved the surface area of the catalyst (though it is still not as high as the commercially synthesised Pt/C).

Figure 5.10 shows the CVs of Pd/C and Ir/C in comparison with the PrIr/C_{HSA} catalyst, which resemble those obtained by Durst et al. at pH 13 [233]. The PdIr catalyst CV has features from both the Ir and Pd CVs, notably the hydrogen desorption peak from Ir and the oxide reduction peak from Pd. However, these features are shifted in potential in the PdIr

CVs, representing a distinct voltammetric response from that of its constituent elements.

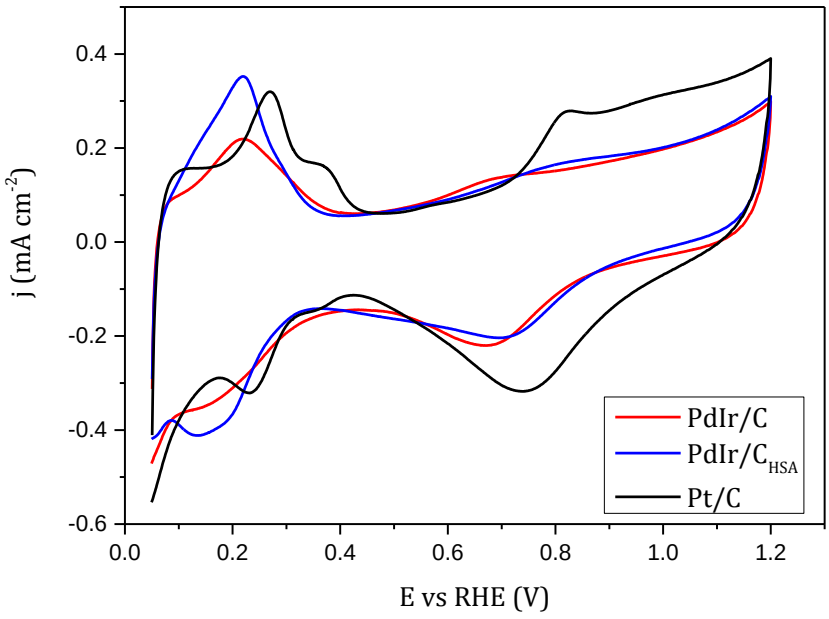

Figure 5.9 Cyclic voltammograms of PdIr/C (red), PdIr/C_{HSA} (blue) and Pt/C (black) recorded at a scan rate of 20 mV s^{-1} in 0.1M KOH and using a PTFE cell. The current density is normalised to the geometric area of the electrode.

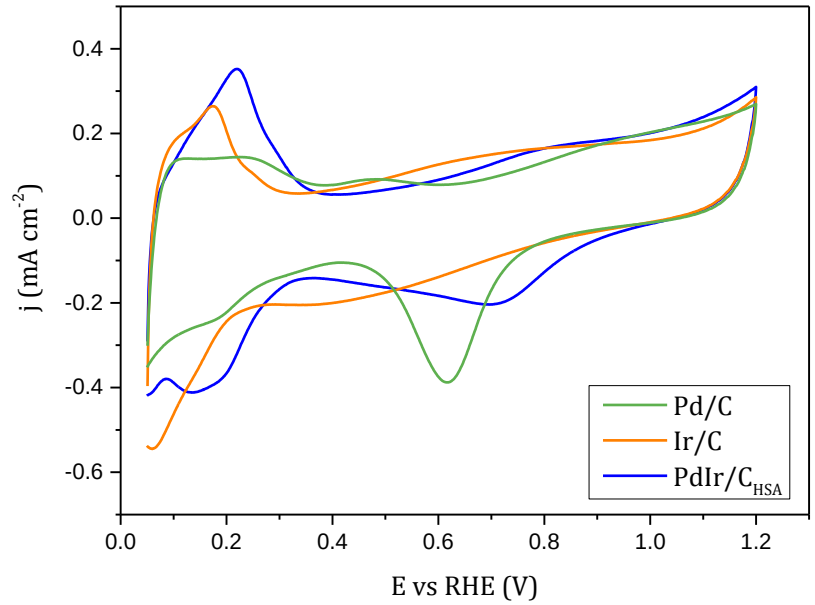

Figure 5.10 Cyclic voltammograms of Pd/C (green) and Ir/C (orange) recorded at 20 mV s^{-1} in 0.1M KOH. The CV of PdIr/C_{HSA} (blue) from Figure 5.9 is also shown as a comparison.

5.2.2 Rotating Disk Electrochemistry

RDE experiments in the PTFE cell were conducted in in the same manner as the glass cell (Section 5.1.3.1). The design of the PTFE cell incorporates a small hole in the base of the main chamber as a luggin capillary, as opposed to a separate luggin suspended midway up the chamber in the glass cell. This meant that RDE experiments in the former were more sensitive to distance between the electrode and luggin capillary and thus a marker was used to ensure the same separation existed for all experiments.

Figure 5.11 shows example HOR curves for various catalysts at 1600 rpm rotation rate. The data suggest an order of activity towards hydrogen oxidation of $PdIr/C_{HSA} > PdIr/C \approx Pt/C > Ir/C > Pd/C$, with the improved $PdIr/C_{HSA}$ catalyst having a clearly higher current at all potentials than the alternatives. The diffusion limiting current for PdIr/C is slow to plateau, possibly due to a resistance in the experimental set-up. The shape of the Pd/C curve is also significantly different to the other catalysts and includes a peak around 0.2 V, before the limiting current is reached which could be attributed to oxidation of absorbed hydrogen in the form of palladium hydride, which has been previously observed on carbon supported Pd [234]. Once this absorbed hydrogen is fully depleted, the current decreases until the diffusion limited value is reached at higher polarisations. This effect is more highly pronounced at lower rotation rates (and therefore lower limiting current values), and HOR curves at a range of rotation rates from 400 rpm can be seen in Appendix 9.1. Shao reported that the strong adsorption of hydride on the surface of palladium causes a slow reaction rate for the oxidation of H_{ad} (the Volmer reaction), and thus a slow HER/HOR, explaining the poor RDE performance of Pd/C seen in Figure 5.11 [131]. The characteristic shape of the Pd/C is also observed in this paper, for both experimental and theoretical data and matches that of the data in Figure 5.11. The decrease in current beyond 0.25 V for Ir/C is attributed to absorption of OH species at lower potentials than for the other catalysts due to the highly oxophilic nature of Ir [233].The data show that there is a significant improvement in HOR activity on alloying of Pd and Ir compared to the constituent monometallic catalysts.

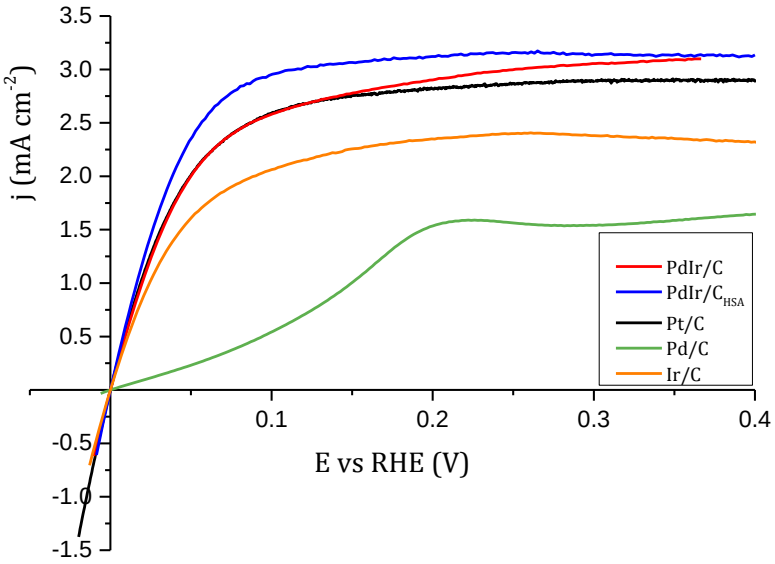

Figure 5.11 RDE voltammograms of the hydrogen oxidation reaction on PdIr/C (red), PdIr/C_{HSA} (blue), Pt/C (black), Pd/C (green) and Ir/C (orange) catalysts at 5 mV s^{-1} scan rate and 1600 rpm rotation rate.

5.2.2.1. Tafel Analysis

Again, in order to extract the exchange current density values from the HOR data, a Tafel plot is constructed as in Section 5.1.3.3 for the 1600 rpm voltammograms and the linear portion of the curve is fitted to give j_0 and αn (Figure 5.12). The less negative the intercept of the Tafel slope, the higher the catalyst's exchange current density (j_0) and therefore the higher inherent activity for hydrogen oxidation. Table 5.1 shows the values extracted from the Tafel analysis of the catalyst and supports the order of activity proposed from the HOR curves in Figure 5.11. The best performing catalyst, PdIr/C_{HSA}, has an exchange current density double that of PdIr/C or commercial Pt/C and thus represents a promising improvement for anode catalysts in alkaline environments. The j_0 values for PdIr/C and Pt/C are similar to one another, in contrast to the results obtained in the glass cell (Section 5.1.3.3) which is most likely due to the poor quality of the electrode layer obtained with the alkaline binder for PdIr/C. Both Pt/C and PdIr/C_{HSA} made much more homogeneous inks due to the carbon pre-treatment step making the catalyst more miscible in the alkaline solution (it is assumed that the commercial Pt/C catalyst is synthesised using a carbon pre-treatment step, though exact details are not known). Conse-

quently, the electrode layers produced with PdIr/C contained areas of catalyst agglomeration and should not be expected to perform as well for the same mass loading as the other catalysts. This issue did not exist to the same extent when using Nafion as the binder and so the relative performance of PdIr/C and Pt/C in Nafion is closer to the inherent value than in AS-4. However, there is a general increase in exchange current density for the PTFE/AS-4 experiments over the glass/Nafion ones.

The monometallic catalysts have decreasing exchange current densities in the order Pt/C > Ir/C > Pd/C, with the latter having more than an order of magnitude lower j_0 than Pt/C and Ir. This trend agrees well with that seen in the recent experiments of Durst et al. [233], giving more credence to methods employed in these experiments and therefore also the viability of the PdIr/C_{HSA} as an improved anode alkaline catalyst.

All catalysts had similar Tafel slopes and therefore αn values around 0.5, except PdIr/C, which is low. This could again be due to the poor electrode layer produced for this catalyst in the alkaline based ink, and indeed the value obtained when using Nafion in the same setup (see Section 5.2.3.2) was close to 0.5.

Table 5.1 Summary of exchange current density and αn values extracted from the Tafel analysis of each catalyst.

	PdIr/C	PdIr/C_{HSA}	Pt/C	Pd/C	Ir/C
j_0 (mA cm^{-2})	3.07	6.14	2.99	0.12	1.85
αn	0.35	0.56	0.53	0.52	0.55

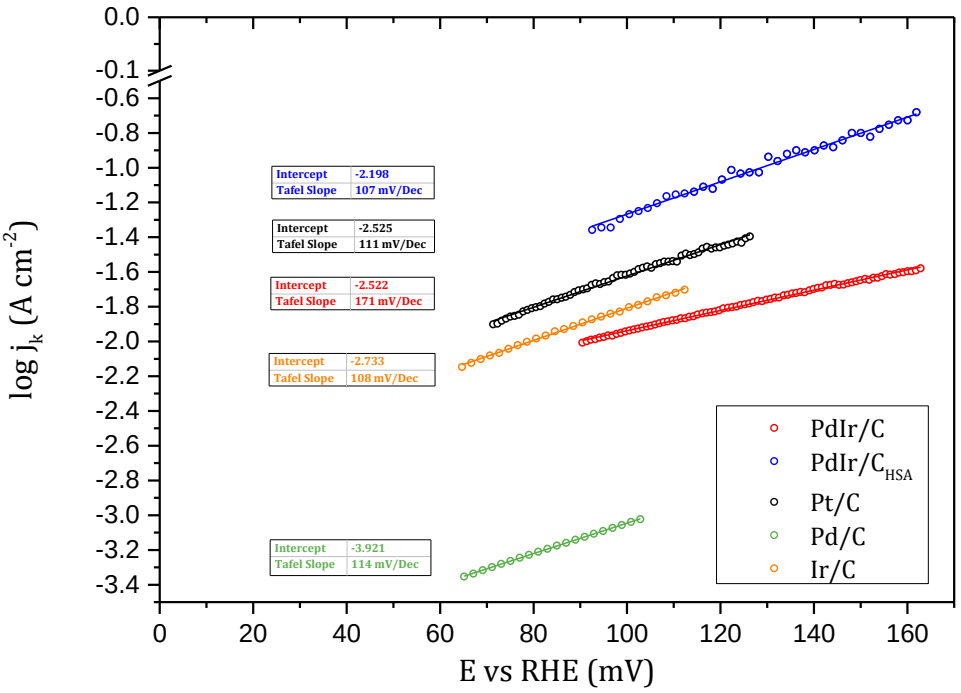

Figure 5.12 Tafel plots of PdIr/C (red), PdIr/C_{HSA} (blue), Pt/C (black), Pd/C (green) and Ir/C (orange) catalysts for the HOR at 1600 rpm in 0.1M KOH and the PTFE cell. The data is fit to a straight line and the intercepts and Tafel slope values are shown in the corresponding coloured tables. Current density is normalised to geometric area of the electrode.

5.2.3 Nafion as a Binder in the Ink

In order to ascertain if the improved performance of the catalysts in the PTFE/AS-4 set up compared to the glass/Nafion was due to the electrochemical cell or the use of alkaline binder, Nafion based inks were also tested in the PTFE cell.

5.2.3.1. Cyclic Voltammetry

Figure 5.13 shows the CVs for PdIr/C-Naf and Pt/C-Naf and yields ECSAs of 17.15 and 28.99 m^2g^{-1}, respectively. The surface areas obtained are both lower than those with the alkaline binder in the ink, indicating that the use of Nafion hinders the hydrogen desorption and gives too-low values for ECSA; however, they are both significantly higher than those of the glass/Nafion experimental set up, meaning that the use of glass in alkaline experiments produces a prohibitively large contamination effect that masks the true surface area of the catalysts, as seen by Mayrhofer et al. [204, 235]. The reduction in ECSA for PdIr/C-Naf compared with PdIr/C in alkaline

binder is small, but this is expected due to the aforementioned poor electrode layers created with the AS-4 based inks. In general, the features of the CVs when using Nafion based inks do not differ from those seen in alkaline based inks, the most significant factor in quality of CV being the use of the PTFE cell in place of glass.

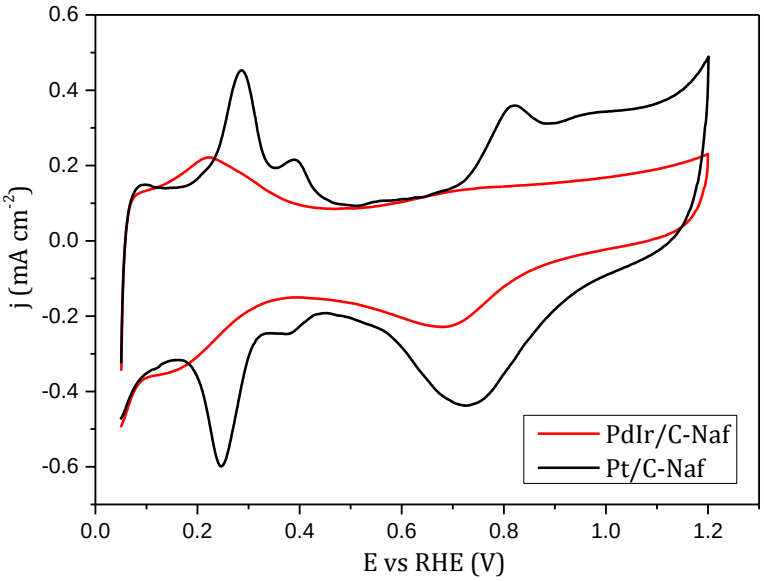

Figure 5.13 Cyclic voltammograms of PdIr/C-Naf (red) and Pt/C-Naf (black) in 0.1M KOH and the PTFE cell, recorded at 20 mV s^{-1}.

5.2.3.2. Hydrogen Oxidation Reaction

The HOR curves for PdIr/C-Naf and Pt/C-Naf are shown in Figure 5.14. Interestingly, the Nafion based inks have higher limiting current densities than those of the alkaline based inks, which might be expected as they produce better quality electrode layers, therefore increasing the diffusion current limiting value. However, there is a clear reduction of the gradient approaching this limiting current for the Nafion based inks in the region of mixed kinetic and diffusion control, indicating that there is a hindrance to the kinetics of the HOR when using Nafion in the electrode layer.

Tafel analysis (Figure 5.15) yields j_0 values of 2.91 and 2.01 mA cm^{-2} and αn values of 0.53 and 0.43 for PdIr/C-Naf and Pt/C-Naf respectively. The exchange current densities have intermediate values between the higher PTFE/AS-4 and glass/Nafion experimental setups, as might be expected, though PdIr/C-Naf has only a slightly lower j_0 than PdIr/C but, again, it is suggested that the inhomogeneity in the alkaline based ink for this cata-

lyst leads to artificially low exchange current densities. There is a general trend of activity for the PdIr/C and Pt/C catalysts of: PTFE/AS-4 > PTFE/Nafion > glass/Nafion, with a more stark difference seen in the commercial Pt/C.

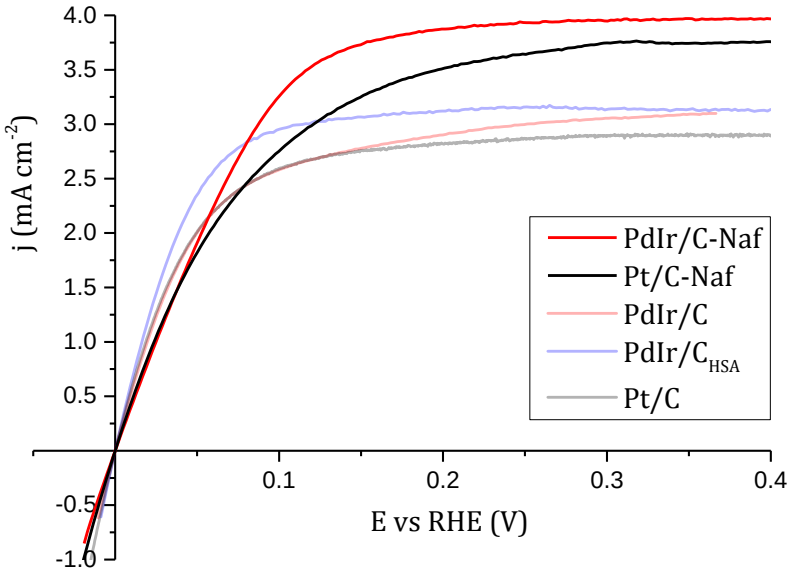

Figure 5.14 Hydrogen oxidation reaction on PdIr/C-Naf (red) and Pt/C-Naf (black) at 1600 rpm in hydrogen-saturated 0.1M KOH and the PTFE at a scan rate of 5 mV s^{-1}. The linear sweep voltammograms of the alkaline based inks from Figure 5.11 are also shown as a comparison (faded lines).

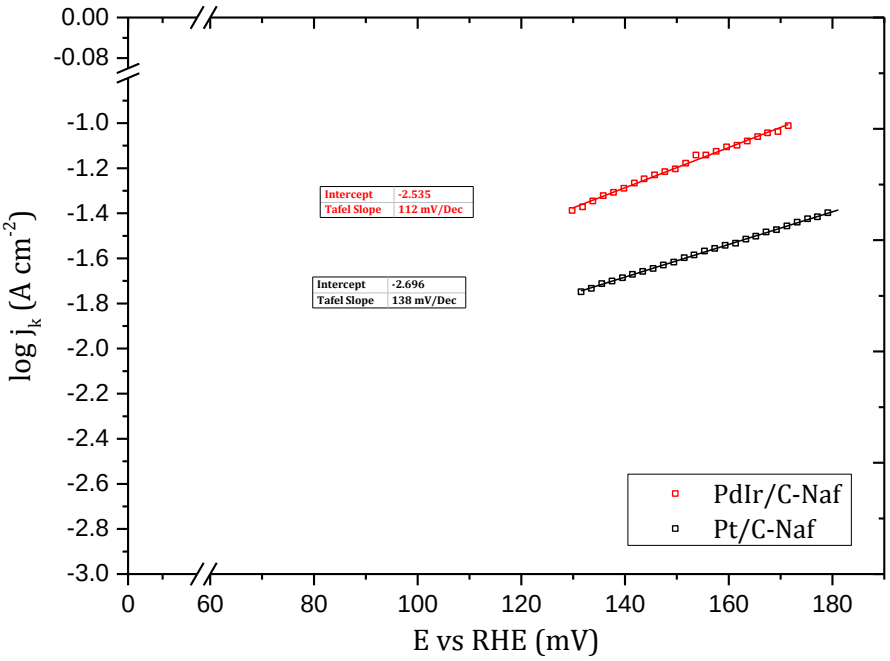

Figure 5.15 Tafel plots of the HOR at 1600 rpm for PdIr/C-Naf (red) and Pt/C-Naf (black) and the corresponding intercepts and Tafel slopes.

5.2.4 Koutecky-Levich Analysis

As with the experiments in the glass cell, the rotation rate of the electrode is varied during HOR linear sweep voltammetry in order to extract the kinetic currents at various potentials, and therefore ascertain the mass activity and specific activity of the catalysts. Figure 5.16 shows an example of the HOR data at varying rotation rates for the PdIr/C_{HSA} catalyst, and the corresponding Koutecky-Levich plot is displayed in Figure 5.17. The inverse of the intercept of the Koutecky-Levich plots is used in the same manner, as described in Section 5.1.4, to produce mass and specific activity plots (Figure 5.18 and Figure 5.19) for all catalysts used in this study. Other Koutecky-Levich plots can be found in Appendix 9.2.

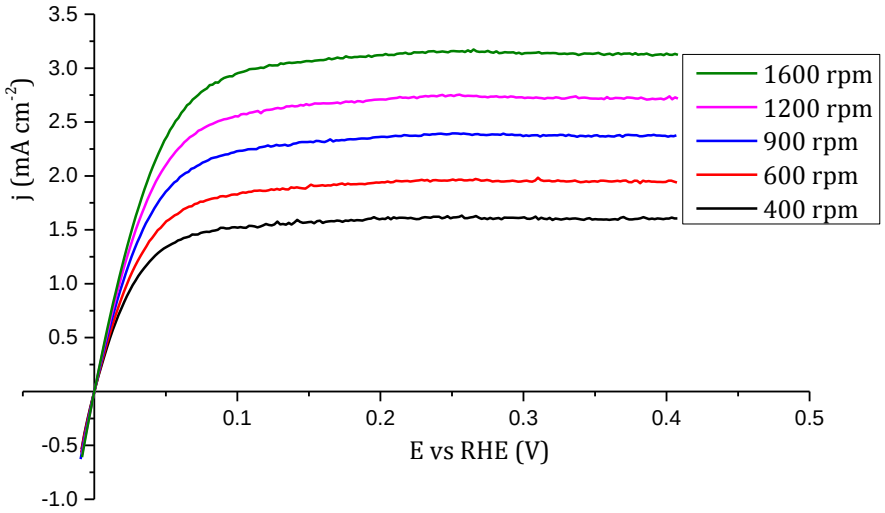

Figure 5.16 RDE voltammograms of the HOR on PdIr/C$_{HSA}$ in 0.1M KOH and the PTFE cell, recorded at a scan rate of 5 mV s^{-1} at rotation rates varying from 400 rpm (black) to 1600 rpm (green).

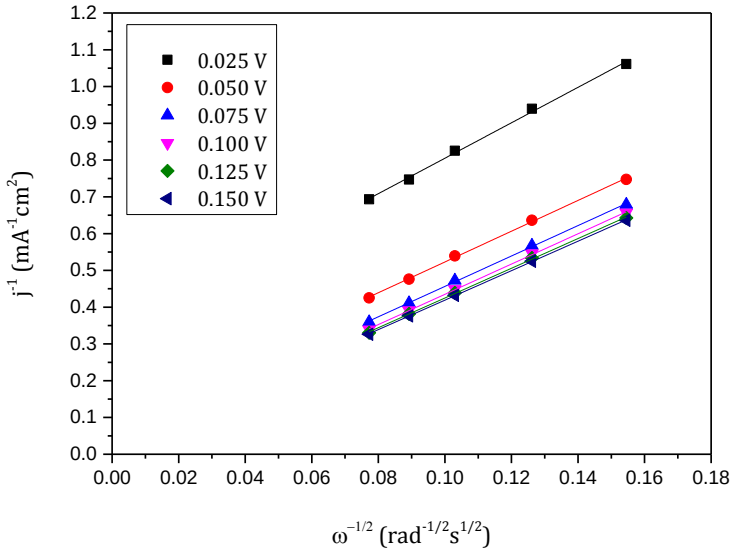

Figure 5.17 Koutecky-Levich plot of the HOR data of PdIr/C$_{HSA}$ in 0.1M KOH and the PTFE cell.

PdIr/C$_{HSA}$ has the highest kinetic current at all potentials, when normalised to both mass loading and ECSA, reinforcing its credentials as the superior anode catalyst in this study. For the mass activity, there is a trend of PdIr/C$_{HSA}$ > PdIr/C ≈ Pt/C > PdIr/C-Naf > Pt/C-Naf, which follows the results of the exchange current density derived from the 1600 rpm HOR experiments, as expected given the similar mass loadings used in all elec-

trodes. The reasons for this trend, and in particular the unrealistically low performance of PdIr/C due to the quality of the alkaline ink with this catalyst, have previously been discussed. The relatively low ECSA of PdIr/C compared with Pt/C and PdIr/C_{HSA} accentuates the performance of the former when normalised for specific activity, showing good performance despite low utilisation of the catalyst and suggesting a higher inherent activity for PdIr alloys than Pt (which is confirmed by the clearly superior performance on increasing the surface area in the PdIr/C_{HSA} catalyst).

The Nafion based inks generally perform more poorly than their alkaline counterparts, except for PdIr/C-Naf, which out-performs PdIr/C at higher polarisations. This is, again, likely due to the agglomeration issues suffered particularly by this catalyst when using AS-4 as the binder. Given the better dispersion of PdIr/C-Naf on the electrode surface, it is expected to perform better when the reaction is driven harder, as there are more reaction sites available. It is also possible that Nafion has a lower resistance to diffusion of hydrogen than AS-4, yet a higher resistance to hydroxide transport (which mediates the HOR in alkaline) and thus there are two competing factors with the former being more influential at higher polarisations. However, this is largely speculation and more would need to be known about the properties of the ionomers before this conclusion could be drawn, though having a hydroxide conducting ionomer in the electrode layer has been shown to enhance the triple-phase boundary, as might be expected [236].

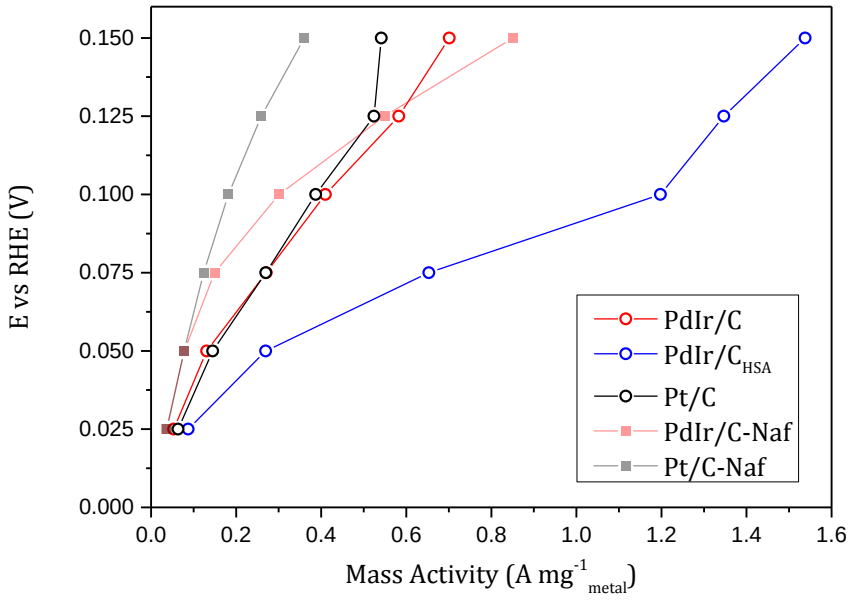

Figure 5.18 Mass activity plot showing the activity of electrodes made with AS-4 (empty circles) and Nafion (filled squares, faded) binders in hydrogen-saturated 0.1M KOH and the PTFE cell. The kinetic currents at various potentials of PdIr/C (red), PdIr/C_{HSA} (blue) and Pt/C (black) are normalised to the metal loading of the electrode.

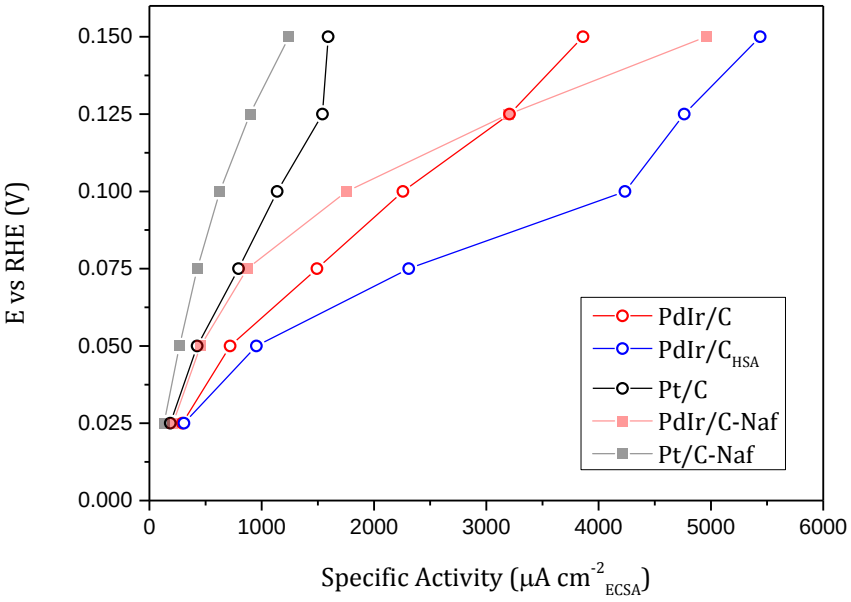

Figure 5.19 Specific activity plot showing the activity of electrodes made with AS-4 (empty circles) and Nafion (filled squares, faded) binders in hydrogen-saturated 0.1M KOH and the PTFE cell. The kinetic currents at various potentials of PdIr/C (red), PdIr/C_{HSA} (blue) and Pt/C (black) are normalised to the electrochemical surface area of the electrode.

5.2.5 RDE Summary

Table 5.2 and Figure 5.20 summarise the values obtained from the preceding electrochemical analysis of the electrodes used in this study. The $PdIr/C_{HSA}$ shows the greatest activity for HOR in alkaline, with a two-fold increase in exchange current density over the next best performing catalyst. There is a general trend in performance for experimental set up in the order PTFE/AS-4 > PTFE/Nafion > glass/Nafion, with a larger difference seen for the Pt/C than the PdIr/C catalyst, likely due to the inherent performance of the latter being masked by varying electrode quality depending on experimental set up. Performance of the individual catalysts generally decreases in the order $PdIr/C_{HSA}$ > PdIr/C > Pt/C > Ir/C > Pd/C showing the improved activity of the alloyed PdIr over all other monometallic catalysts studied.

These results demonstrate the importance of using an inert electrochemical cell (such as PTFE) and an alkaline exchange ionomer (such as AS-4) as a binder in order to most closely represent the inherent activity of the metals under investigation. A consideration may need to be made in the formulation of inks made using an alkaline binder to improve the homogeneity of the solution and produce the best quality electrodes, particularly with catalysts employing non-pre-treated carbon supports.

Table 5.2 Summary of the values obtained from electrochemical analysis for the various electrodes discussed in this study.

Electrode	ECSA (m^2g^{-1})	j_0 (mA cm^{-2})	αn
PdIr/C	18.16	3.07	0.35
$PdIr/C_{HSA}$	28.28	6.14	0.56
Pt/C	33.99	2.98	0.53
Pd/C	n/a	0.12	0.52
Ir/C	n/a	1.85	0.55
PdIr/C-Naf	17.15	2.91	0.53
Pt/C-Naf	28.99	2.01	0.43
PdIr/C glass	13.79	2.78	0.61
Pt/C glass	8.10	1.53	0.54

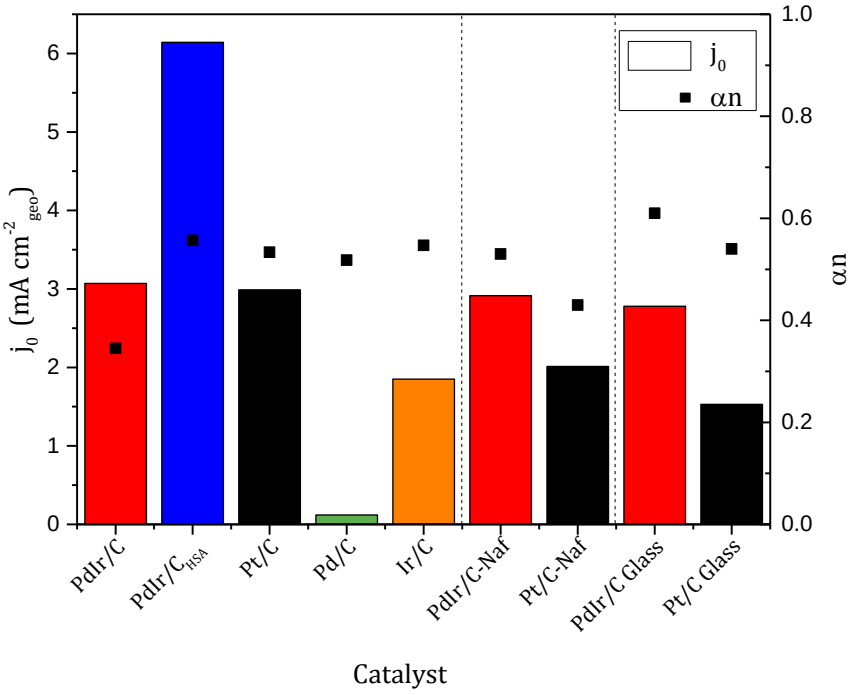

Figure 5.20 Summary of the exchange current density (bars) and αn (black squares) values obtained from electrochemical analysis of PdIr/C (red), PdIr/C_{HSA} (blue), Pt/C (black), Pd/C (green) and Ir/C (orange).

5.2.6 Electrochemical Impedance Spectroscopy

Electrochemical impedance spectroscopy (EIS) was used to gain more of an insight into the processes occurring during the HOR on PdIr/C and Pt/C catalysts. The technique can be used to see how properties such as charge transfer resistance and mass transport resistance change with polarisation or rotation rate of the electrode.

5.2.6.1. Catalyst Comparisons

Figure 5.21 shows EIS data for PdIr/C, PdIr/C_{HSA} and Pt/C catalysts at 0.025 V polarisation under hydrogen (HOR) at 1600 rpm. The total size of the arcs (total impedance, Z) in the Nyquist plot gives an indication of the activity of the catalysts, as $V = IZ$ and all spectra were taken at the same polarisation, a smaller total impedance represents a higher current and therefore performance.

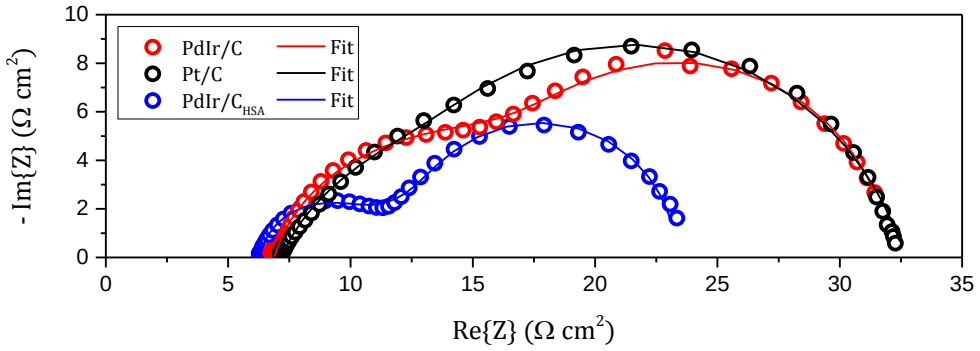

Figure 5.21 EIS for PdIr/C (red), Pt/C (black) and PdIr/C_{HSA} (blue) catalysts taken at 0.025 V and with a rotation of 1600 rpm. The data were fitted using ZView software and the fits are shown by the corresponding lines.

For the PdIr/C and PdIr/C_{HSA} catalysts, two clear arcs can be seen due to two distinct processes occurring with different time constants; charge transfer at high frequencies and mass transport at low frequencies (further evidence that these are the processes involved is provided in Sections 5.2.6.2 and 5.2.6.3). The profile for the Pt/C catalyst is less well resolved, though it is clearly not composed of a single arc. This suggests two possible scenarios: the charge transfer is much larger and at a lower frequency for Pt/C than for PdIr/C and therefore the arcs overlap considerably, or the charge transfer is much faster for Pt/C than for PdIr/C and there is a very small high frequency arc that is dwarfed by the mass transport arc. Given that it has already been shown that the PdIr/C catalysts have comparable, if not higher, activity to Pt/C, the former scenario is more likely. Additionally, the diffusion to the electrode surface is controlled by the rotation rate of the electrode (which is the same in all cases and given by Equation 3.11). The mass transport through the electrode layer to the active sites could differ from catalyst to catalyst, however, and is dependent on the quality of the deposited layer on the electrode. As the Pt/C is commercially synthesised and produces a more homogeneous ink, and therefore a more even electrode layer, it is likely that the mass transport resistance would be, if anything, lower for Pt/C electrodes than PdIr/C ones.

One possible explanation for the difference in EIS results for Pt/C and PdIr/C was postulated; due to the aforementioned hydrogen storage capabilities of Pd (and possibly Pd alloys), the mass transport resistance could be significantly lower in PdIr due to the readily accessible Pd-H stored in the lattice. This would mean that PdIr could still have a larger R_{CT} than Pt, but have an overall smaller impedance due to its lower R_D. In order to

test this hypothesis, chronoamperometry was carried out on PdIr/C_{HSA} and Pt/C. The cell was saturated with hydrogen gas for an hour in order to form absorbed hydrogen in the catalyst structure. The cell was then purged with nitrogen for one hour to remove any dissolved hydrogen in the electrolyte before high speed chronoamperometry at 0.3 V was carried out. It was hypothesized that if PdIr/C was absorbing hydrogen that Pt/C was not, there would be a larger current observed in the chronoamperometry for PdIr/C than Pt/C, and the decay of the current should also be slower for PdIr/C. Figure 5.22 shows that there was a slightly higher current observed for PdIr/C_{HSA} compared Pt/C; however, this current decayed rapidly and reached 0 A after only 2 s. Chronoamperometry was repeated after the first scan for PdIr/C_{HSA} and shows a lower current, suggesting that the higher current could have come from absorbed hydrogen (not present in Pt/C) that is subsequently depleted after the first scan. Ultimately, the effect is small so it is inconclusive as to whether possible hydrogen absorption properties of PdIr are the reason for the double arc being seen for PdIr and not for Pt. As previously mentioned, H_{ad} has been shown to hinder the HOR on Pd surfaces [131], and so if this effect was also common to Pd alloys the activity of PdIr/C towards HOR should also be hindered. Again, given the superior activity already shown for the HOR on PdIr/C and PdIr/C_{HSA} through RDE studies, it is more likely that the charge transfer arc is larger for Pt/C and has significant overlap with the low frequency mass transport arc.

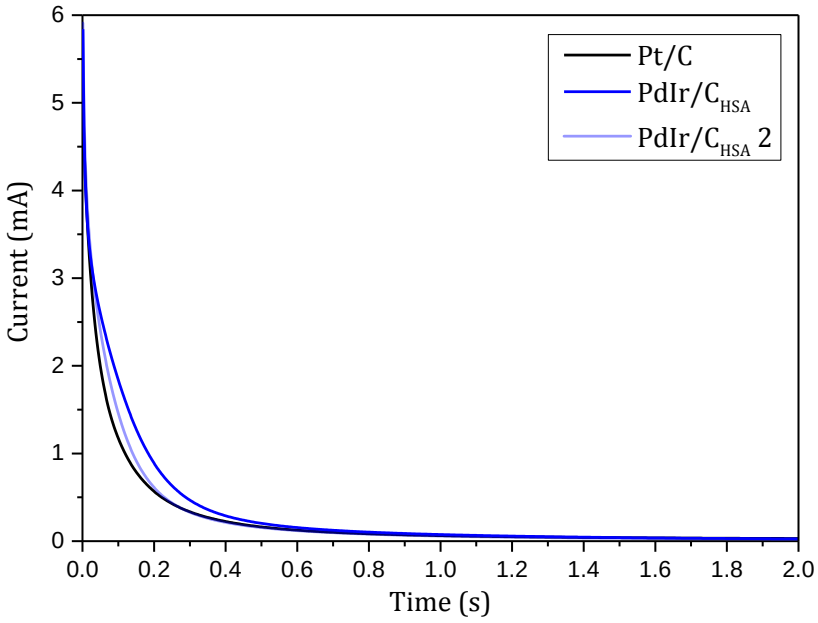

Figure 5.22 Chronoamperometry of Pt/C (black), PdIr/C$_{HSA}$ (blue) and the second run of PdIr/C$_{HSA}$ (light blue). 0.1M KOH was saturated with H$_{2\ (g)}$ for one hour before purging with N$_{2\ (g)}$ for a further hour, after which the potential was switched to 0.3 V and the current response measured.

Figure 5.23 shows the EIS of the HOR on Pt/C. For potentials negative of 0 V (HER), increasing polarisation reduces the size of the arc and thus shows that it is a charge transfer process with minimal mass transport resistance (as would be expected as there is no delivery of reactant required for the HER). However, for potentials positive of 0 V, increasing polarisation increases the size of the arc, implying that mass transport limitation is being instigated, even at low polarisation, and is providing increasing resistance with increasing polarisation. Throughout the whole potential range the apparent single arc holds, even though it is evident that both charge transfer and mass transport resistance must exist to varying extents across the range. This is further evidence of the fact that the mass transport and charge transfer processes for Pt/C must have similar time constants and thus a high degree of overlap of the two arcs in the Nyquist plots, with the effect of producing an apparent single arc that is not present in the PdIr catalysts (where a difference of time constants results in two distinct arcs being observed as in Figure 5.21).

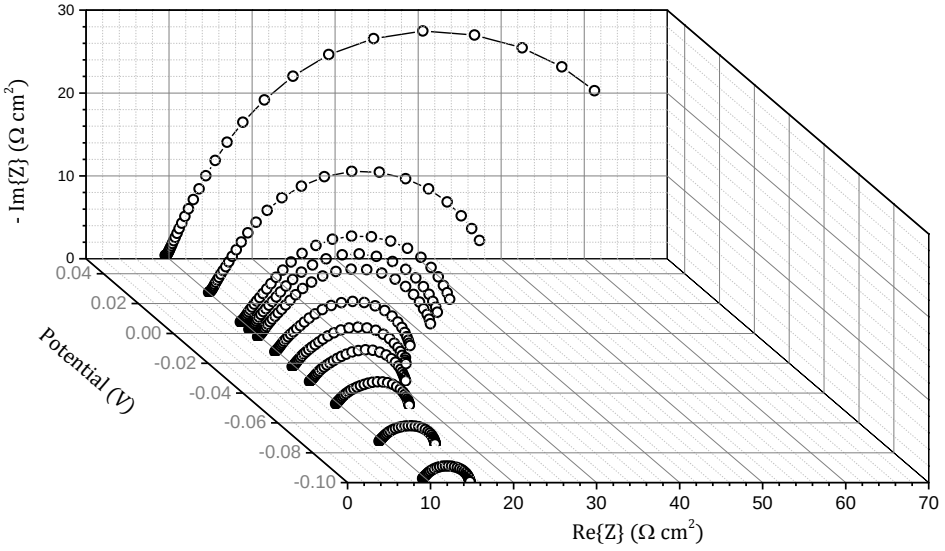

Figure 5.23 EIS of the HOR on Pt/C at varying potential. Data were collected at 1600 rpm and at potentials with respect to OCV. Positive potential represents the HOR and negative potential represents the HER. Connecting lines between data points are a guide for the eye only and do not represent any fitting of the data.

In order to ascertain the effect of the polymer binder used in the ink on electrode performance, PdIr/C and Pt/C inks with Nafion (a proton exchange ionomer) instead of the Tokuyama AS-4 (hydroxide exchange ionomer) were studied in the same PTFE cell with 0.1 M KOH electrolyte. It is clear that the larger impedance arcs for the Nafion based inks (Figure 5.24, squares) indicate worse performance for these electrodes. It is assumed that the difference should largely be due to the increased diffusion resistance of hydroxide through the Nafion layer compared with the alkaline anion exchange ionomer. The total impedance is larger for the PdIr/C-Naf catalyst than for the Pt/C-Naf, contrary to the result of the Tafel analysis (Section 5.2.3.2). This could be due to the impedance data being collected after the HOR experiments and a possible degrading of the electrode layer, or catalyst itself, that might be more severe for PdIr/C than Pt/C. However, it is clear that the increased resistance involved with using a Nafion binder means that an alkaline ionomer should be used where possible in alkaline experiments and this effect should be taken into account for studies using Nafion in an alkaline electrolyte [205-207].

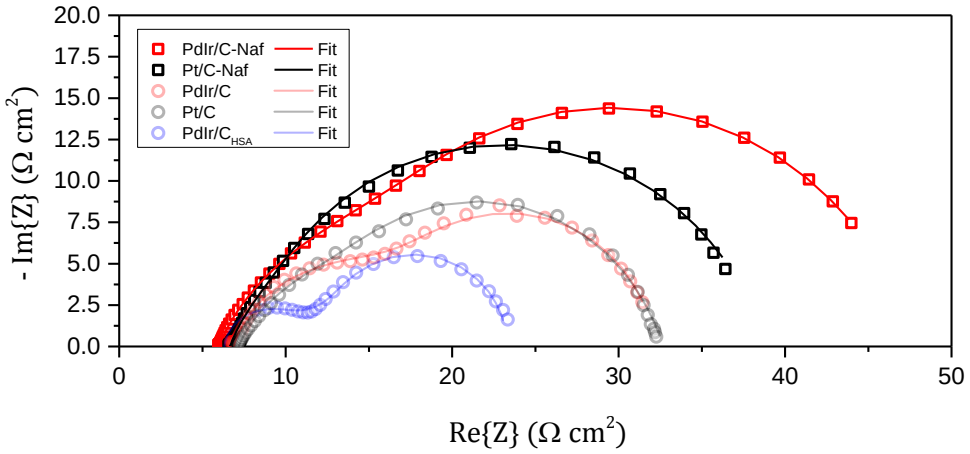

Figure 5.24 EIS data showing the effect of using Nafion as a binder in the ink (squares) as compared to the AS-4 based inks previously discussed (Figure 5.21). All spectra were collected at 0.025 V and 1600 rpm in a H_2 saturated electrolyte. Fits obtained with ZView software are shown as corresponding lines.

In order to get an idea of the resistances due to charge transfer (R_{CT}) and diffusion (R_D) the EIS data were fitted to the modified Randels circuit shown in Figure 5.25. All fits are shown on Figure 5.21 and Figure 5.23, and good fits to the data were obtained using the same equivalent circuit design in each case. Simulated impedance arcs for both infinite and finite diffusion using the Randels circuit in Figure 5.25 were previously shown in Figure 3.12. The data in Figure 5.24 clearly show finite diffusion behaviour, as would be expected for a RDE experiment, and thus the bounded transmissive Warburg element was used in the EIS fit in order to obtain the R_D values.

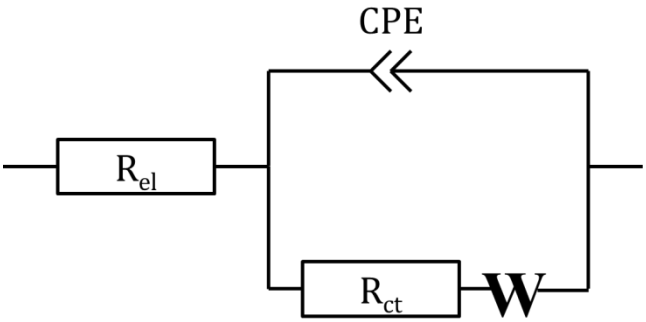

Figure 5.25 The modified Randels circuit used to fit EIS data for the HOR on all catalysts, where W represents a bounded transmissive, or finite, Warburg element, from which R_D is obtained.

Figure 5.26 shows the values obtained for R_{CT} and R_D for all catalysts (R_{EL} is not shown as all values are roughly the same, with any differences being attributable to slight variations in electrode placement relative to the luggin capillary, and can be easily seen by the high frequency intercept of the EIS data). As expected, PdIr/C_{HSA} shows the lowest overall resistance, as well as the lowest values for both R_{CT} and R_D, and therefore superior performance. The slightly higher R_{CT} for Pt/C over PdIr/C compares well with the slightly superior exchange current densities obtained for PdIr/C in the Tafel analysis, but it should be noted that there is little separation for the two arcs of the Pt/C EIS spectrum and therefore the model might not be as physically valid, despite a good fit to the data being possible. Nevertheless, the general trends in R_{CT} values from the modelling match the activity trends from Tafel analysis for these catalysts: PdIr/C_{HSA} > PdIr/C ≈ Pt/C. Figure 5.26 also shows that the mass transport resistance, R_D, is similar for all AS-4 based inks. The slightly lower value for PdIr/C_{HSA} is attributed to the fact that, as the most active catalyst, at the same polarisation (0.025 V) the total current is higher and therefore the diffusion limitation of the current will be proportionally less than for more active catalysts.

R_D is significantly higher for the Nafion based electrodes due to the higher resistance to diffusion of hydroxide ions through the cationic ionomer than for the anionic exchange AS-4 ionomer. The R_{CT} values for Pt/C and Pt/C-Nafion are similar, indicating that the poorer performance of the latter catalyst in alkaline electrolyte is purely due to higher mass transport resistances in the electrode (as would be expected for the highly consistent commercially prepared catalyst). This effect is not seen for the PdIr/C and PdIr/C-Nafion but, as mentioned previously, this could be due to degradation of the catalyst following previous experimentation and would explain the larger EIS arc for PdIr/C-Nafion than Pt/C-Nafion, despite the former showing greater activity for HOR in Tafel analysis.

Though overall performance of the catalyst is dependent on the total impedance of the whole system, conducting EIS can be a useful diagnostic step to help ascertain the quality of the prepared electrode (affecting R_D) and therefore separate the inherent activity of the catalyst (R_{CT}) from any systematic or experimental artefacts that might give a lower activity in Tafel analysis. As with all RDE experiments, it is not possible to obtain an activity greater than the actual activity of the catalyst and therefore as

much care as possible should be taken to prepare a good quality electrode in a clean cell so as to minimize any effects that mask the true performance of the catalyst. The importance of using an alkaline exchange membrane binder in place of Nafion for alkaline experiments is also highlighted by these data.

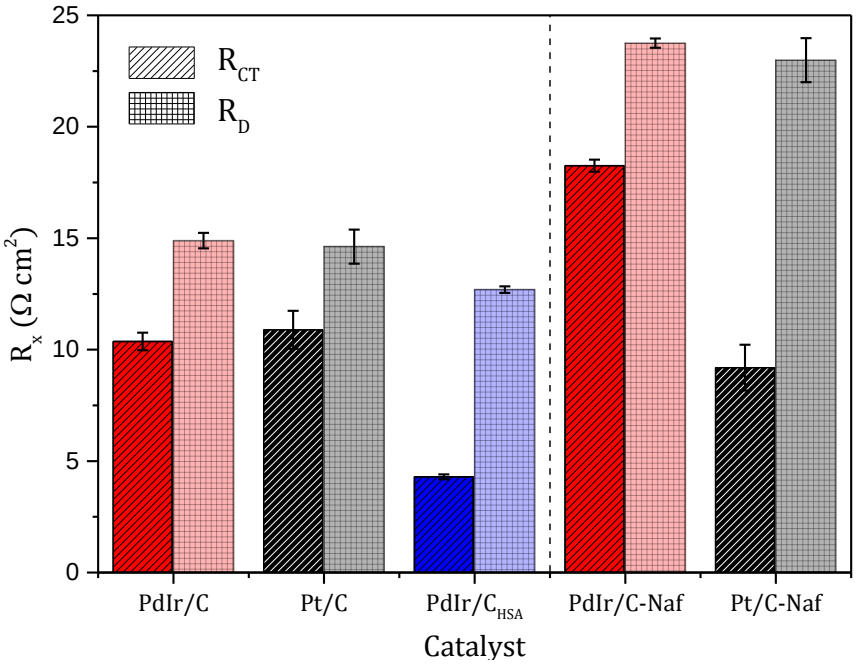

Figure 5.26 Values for charge transfer resistance (R_{CT}, diagonal pattern) and mass transport resistance (R_D, square pattern) for all catalysts for PdIr/C (red), Pt/C (black) and PdIr/C$_{HSA}$ (blue) catalysts. Values were obtained by fitting a modified Randels circuit (Figure 5.25) to the EIS data using ZView software. Error bars represent the error in value as given by the model.

5.2.6.2. Rotation Rate

As well as changing the rate at which reactant is brought to the surface of an electrode and keeping the electrolyte homogenous, varying the rotation rate of the electrode has the effect of changing the diffusion layer thickness, or Levich layer (δ_L). This is given by Equation 5.5. As the rotation rate increases the diffusion layer thickness decreases and therefore the diffusion limiting current increases. In terms of equivalent circuit modelling (see Section 3.10.2), this has the effect of moving from an infinite Warburg element to a finite one as the electrode is rotated from a static position, and a decreasing Warburg mass transport resistance as the rotation rate increases. This manifests itself as a decreased low frequency arc in a Nyquist plot with increasing rotation rate, as shown in Figure 5.27, and, though not shown

here, a static electrode would produce a straight line characteristic of an unbound Warburg element.

The data in Figure 5.27 show that, for a given polarisation, changing only the rotation rate affects only the second, mass transport, arc in the Nyquist plot. The charge transfer arc remains the same, as shown by the perfect overlap of data points at all rotations. At both 0.05 V and 0.015 V the two arcs overlap significantly, indicating that the time constants for the charge transfer and mass transport processes are of a similar order. The total impedance is larger for the 0.15 V polarisation as the contribution from the diffusion limiting part of the current is increased at higher polarisations (as it tends to purely diffusion limited current). However, the charge transfer resistance should decrease with increasing polarisation. This is suggested to be the case in Figure 5.27 by noting that the overlap of the charge transfer arc proceeds to lower frequencies for 0.05 V than for 0.15 V, suggesting a larger diameter arc for the former. Indeed, fitting of the data gave R_{CT} values of 35 $\Omega\,cm^2$ and 32 $\Omega\,cm^2$ for 0.05 V and 0.15 V, respectively. However, as the overlap of the two arcs is significant, the results of this fit should not be overly relied upon.

What can be said with confidence is that the data show that increasing the rotation rate decreases the mass transport resistance, and the overall shape of the impedance arc is described by a static charge transfer arc and a mass transport arc that varies with rotation rate. This is described by the modified Randles circuit with a finite Warburg element, as shown in Figure 5.25.

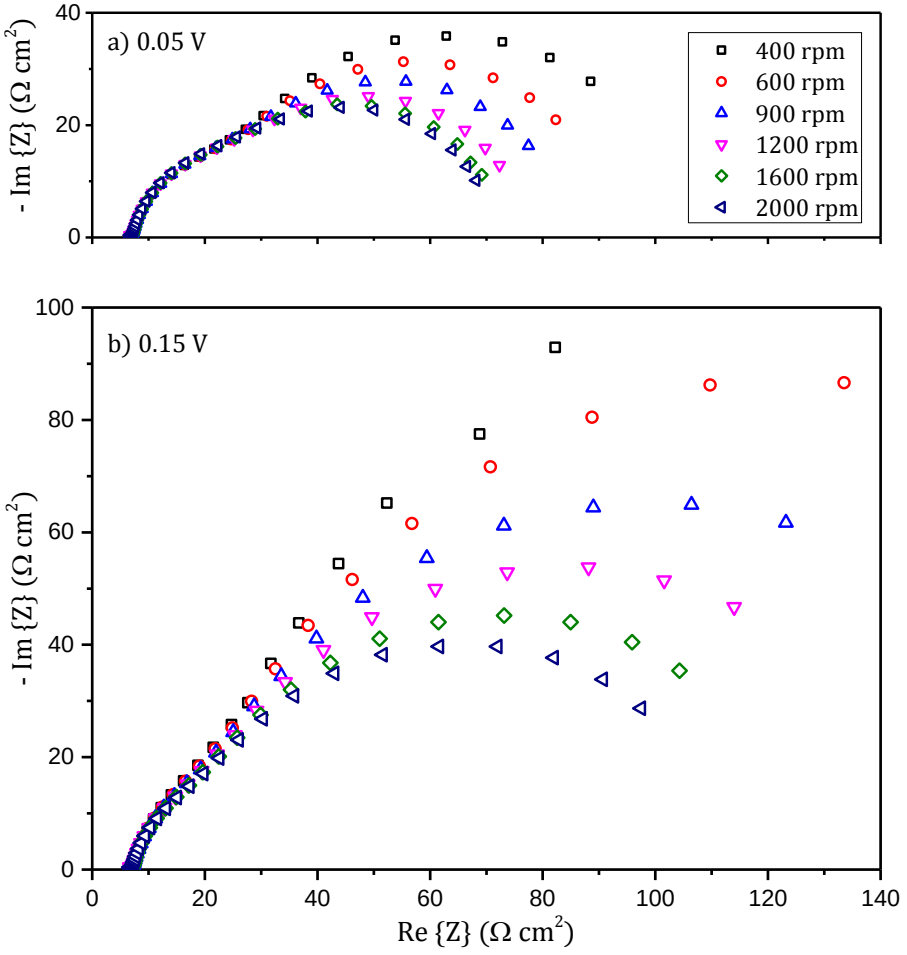

Figure 5.27 EIS of HOR at PdIr/C with varying rotation rates at a) 0.05 V and b) 0.15V with respect to OCV showing decreasing mass transport resistance with increasing rotation rate.

5.2.6.3. Polarisation

As already discussed, increasing polarisation of the electrode decreases the charge transfer resistance for a particular reaction. In the case of the HOR, a positive potential drives the reaction towards hydrogen oxidation, and a negative potential towards the HER. Additionally, as the potential is increased, the contribution of the diffusion controlled current for the HOR increases and so the mass transport resistance increases until the point of diffusion limited current, where it dwarfs the charge transfer resistance. This is shown in Figure 5.28. For the HER (negative potentials) there is no mass transport limitation as no dissolved reactant is required to travel to

the surface of the electrode for this reaction to occur. As the electrode is polarised more negatively, the charge transfer resistance decreases. Conversely, for the HOR, even at low polarisations, as dissolved H_2 gas needs to diffuse to the electrode there is a clear mass transport arc that increases as the polarisation increases. This was also shown previously to be the case for the Pt/C catalyst in Figure 5.23.

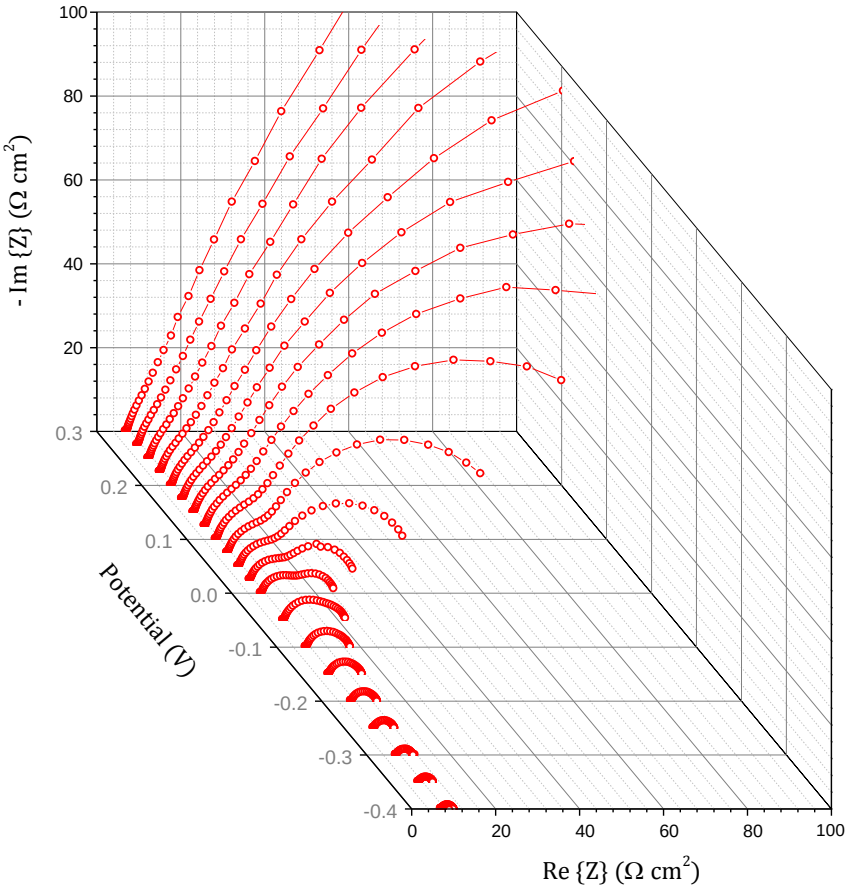

Figure 5.28 EIS for the HOR on PdIr/C at 1600 rpm with varying potential from -0.4 V to 0.3 V. The lines connecting the symbols are simply a guide for the eye and do not represent fitting of the data.

Fitting the data for the positive polarisation from 0.0 V using the modified Randles circuit as in Figure 5.25 gives values for this effect (Figure 5.29) and shows decreasing R_{CT} and increasing R_D with increasing polarisation. Beyond 0.0125 V it is no longer possible to attempt to fit an R_{CT} value due to the high degree of overlap between the two arcs and increasingly diminished charge transfer arc. Because R_{CT} decreases up to this point, and

because it should be negligible at high polarisations, R_{CT} was set to zero for all fits more positive than 0.0125 V.

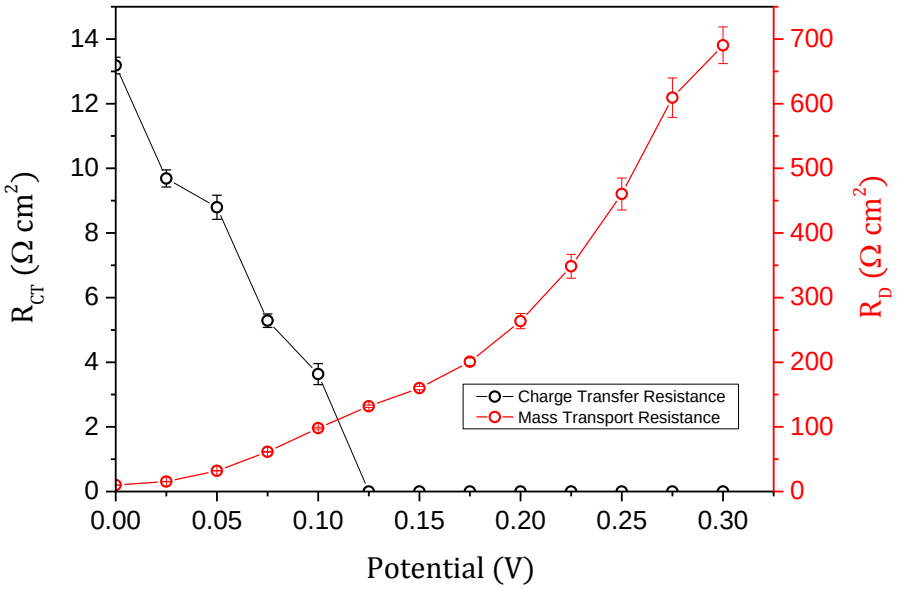

Figure 5.29 Fitting parameters for the HOR on PdIr/C data shown in Figure 5.28. Values for the charge transfer resistance (black) and mass transport resistance (red) are shown. R_{CT} was set to zero at 0.0125 V in order to improve the fit.

Figure 5.30 shows two examples of the fitting of data shown in Figure 5.28, at 0.00 V and 0.275 V. There is a good fit obtained for the modified Randles circuit in Figure 5.30 a) and by setting R_{CT} to zero in Figure 5.30 b).

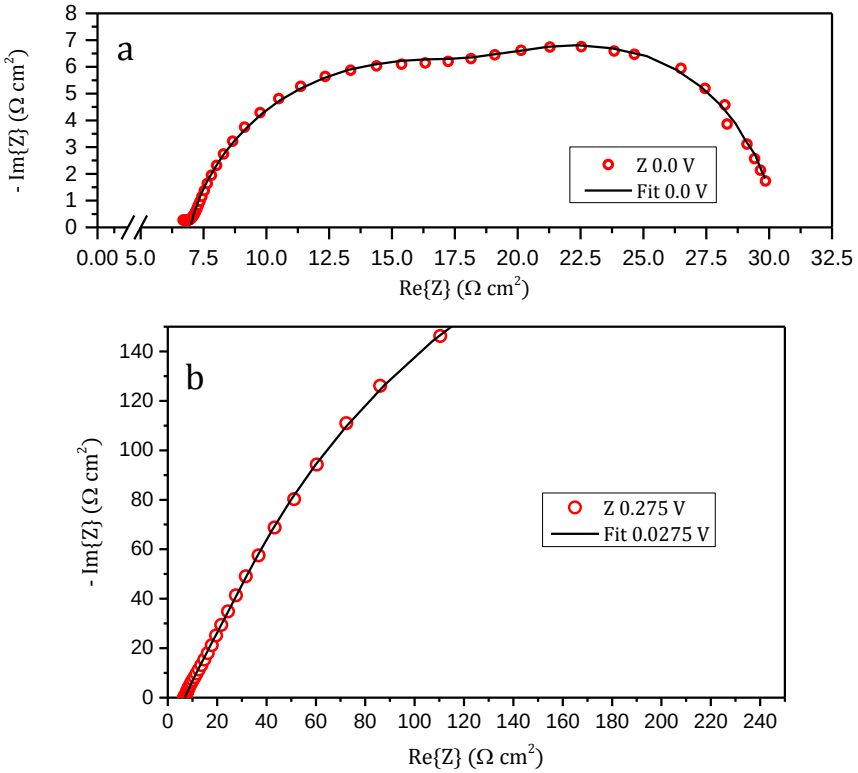

Figure 5.30 Example fittings (black lines) and raw data (red circles) for the two extremes of the HOR; (a) 0.00 V and (b) 0.0275 V. Data were collected at 1600 rpm in 0.1M KOH in the PTFE cell on PdIr/C and at potentials with respect to OCV.

5.2.7 Catalyst Durability

In order for a catalyst to be viable for long-term use in a fuel cell, it must be durable over conditions experienced in real-world operation. There are two main routes to catalyst degradation: corrosion of the support material (carbon in this case, and in most fuel cell catalysts) or dissolution of the metal particles. Carbon corrosion causes irreversible loss of carbon as CO_2 and subsequent aggregation of metal, and therefore reduction in ECSA. Dissolution of the metal can also lead to agglomeration, via Ostwald ripening, but also reduces ECSA simply through loss of mass into the electrolyte or, in a fuel cell, migration of catalyst material to areas of an MEA where it is unutilised [237, 238].

Degradation in operational scenarios such as automotive fuel cell use occurs on a timescale too long for useful laboratory testing, and thus accelerated test protocols have been developed to measure catalyst durability.

However, even these protocols require greater time than is afforded by the corrosion of glass in alkaline electrolyte. Therefore, it is necessary to conduct long-term experiments in the corrosion-resistant PTFE cell in order that any decrease in the ECSA of the catalyst can be attributed to electrochemical degradation and not contaminants from the corrosion of glass. Figure 5.31 shows the initial CV of PdIr/C in the PTFE cell (red) and the CV after leaving the electrode in the cell for 24 hours (grey). The CV shows very little change in this time, save a slight shift in potential of the peaks likely due to a small shift in potential of the reference electrode, and shows no loss of ECSA, demonstrating the suitability of the PTFE cell for durability experiments in alkaline electrolyte.

Many established accelerated stress tests for catalyst degradation exist for acidic PEM electrodes, such as those used in the US department of energy benchmarks [239, 240]. However, there are no equivalent protocols designed specifically for alkaline environments and thus the degradation studies in this work are based on the conventional PEM methods. Most of the work in the literature involving durability of catalysts in an alkaline medium is based on methanol fuel cells [241, 242], and though some AAEM fuel cell literature looks at the durability, it is often based on in-situ testing where the membrane stability is a larger issue [123, 243, 244]. To the author's knowledge, no ex-situ catalyst durability studies exist in alkaline media.

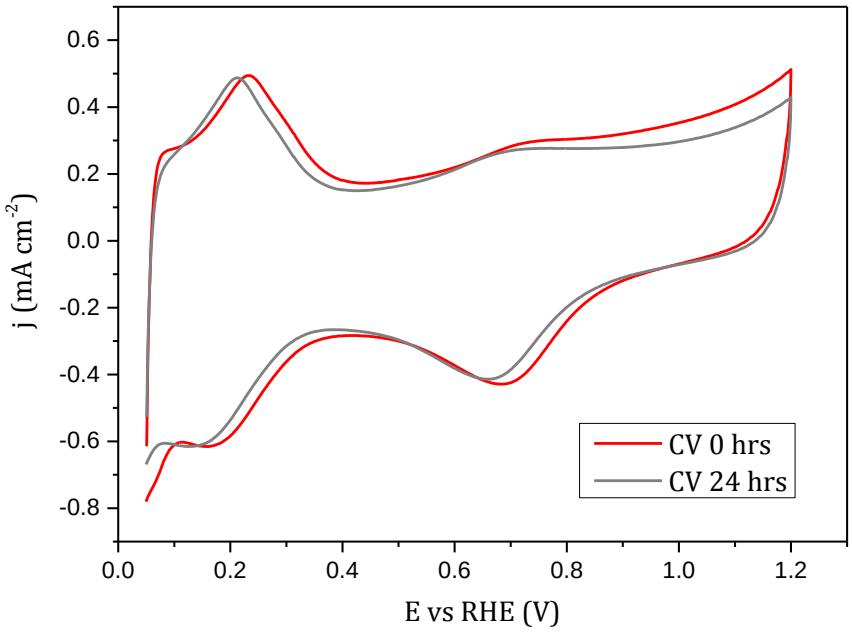

Figure 5.31 Cyclic voltammograms of PdIr/C in nitrogen saturated 0.1M KOH and the PTFE cell at 20 mV s^{-1} initially (red) and after 24 hours (grey).

5.2.7.1. Stop-Start Protocol

The first accelerated degradation protocol applied to the catalysts was the stop-start procedure developed first by Nissan which employs a fast (0.5 V s^{-1}) triangular wave scan between 1.0 and 1.5 V. This accelerated stress test is designed to mimic cell reversal and fuel starvation conditions experienced during startup and shutdown of automotive fuel cells [245]. CVs are taken following varying numbers of 1.0-1.5 V scans in order to measure the ECSA loss of the catalysts. Figure 5.32 and Figure 5.33 show the CVs and percentage ECSA loss respectively during the start-stop experiment. The Pt/C catalyst lost only 15% of the original ECSA during this test, with the PdIr/C and PdIr/C_{HSA} losing 73% and 89% respectively. Though in acidic environments carbon is unstable at these potentials [240], it is expected to be stable in alkaline conditions [246] (ref. 21) and so the loss of ESCA could be expected to be due to instability of the metal particles in these conditions.

Figure 5.34 shows the Pourbaix diagrams for various noble metals, depicting the thermodynamic stability of various species under different potential and pH conditions. The white parallelogram in these diagrams represents the stable region of water, and it should be noted that because the reversible hydrogen electrode used in these experiments is submerged in the

common electrolyte, the potential relative to the reference electrode remains constant along the slope of the base of the parallelogram. That is, at the operating pH of roughly 13, the potential relative to the reference electrode used is 1.2 V at the top edge and 0 V at the bottom edge of the white region in Figure 5.34. Therefore, it is predicted by the Pourbaix diagram that Pt and Pd will form stable passivation layers at potentials above 1.2 V, whereas Ir forms a soluble species, and therefore is expected to be lost to the bulk electrolyte during the start-stop protocol. This would explain the drastic decrease in ECSA for the PdIr based catalysts after 2,000 cycles compared to the comparatively stable Pt/C. The smaller particle size of the PdIr/C_{HSA} catalyst makes it more susceptible to corrosion and therefore loses the most ECSA in this test.

Both Pt/C and PdIr/C_{HSA} show an initial increase in ECSA on potential cycling. This increase in ECSA in the first few cycles was also observed by Wang et al. for Pd-based core-shell catalysts and was attributed to roughening of the surface and removal of contaminants [247]. They also observed a high stability for their Pt decorated catalyst, as seen in these results.

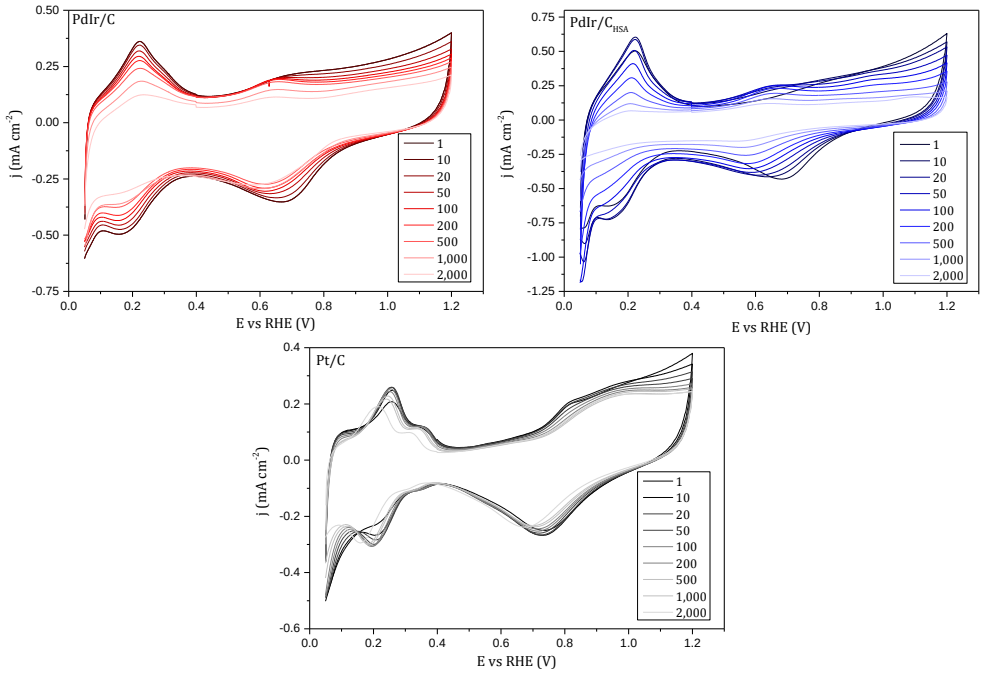

Figure 5.32 Cyclic voltammograms taken during the stop-start degradation test on PdIr/C (top left, red), PdIr/C_{HSA} (top right, blue) and Pt/C (bottom, black). The CVs displayed span from the initial CV (lightest) to the CV following 2,000 stop-start cycles (lightest).

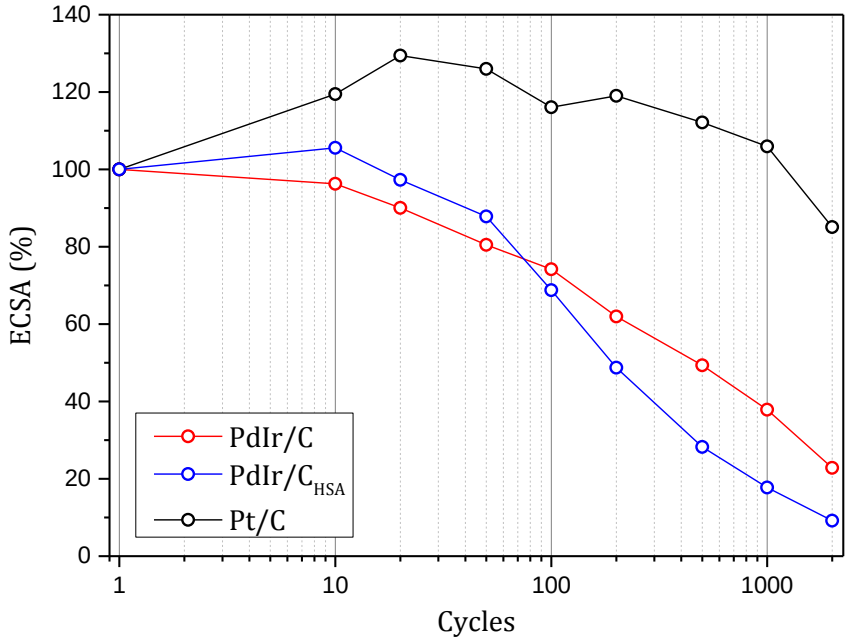

Figure 5.33 ECSA loss for PdIr/C (red), PdIr/C_{HSA} (blue) and Pt/C (black) using the stop-start procedure cycling from 1 V to 1.5 V vs RHE.

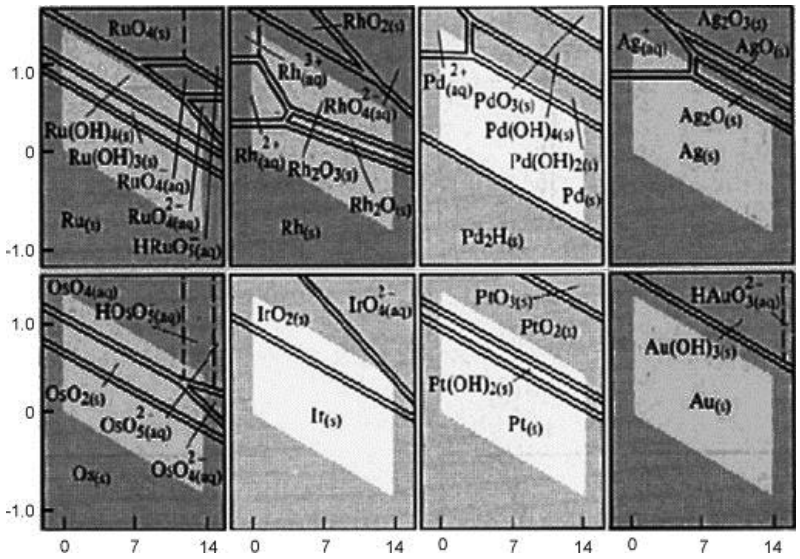

Figure 5.34 Pourbaix diagram of a selection of noble metals from Gu et al. showing the stability of various species at different potentials and pH values [248]. The metals Pt, Pd and Ir are highlighted. The white area represents the stable region for water.

5.2.7.2. Metal Dissolution Protocol

The second accelerated test protocol employed was based on the Pt dissolution test of the Fuel Cell Tech Team (FCTT) whereby the potential was

cycled between 0.6 V and 1 V at 0.5 V s^{-1} and the ECSA recorded at various points up to 10,000 cycles [239, 249].

Figure 5.35 shows the CVs obtained during the metal dissolution protocol and the corresponding ECSA loss in Figure 5.36. The less extreme conditions of this test lead to a smaller loss of ECSA for the PdIr/C_{HSA} and Pt/C catalysts at 51% and 58% respectively, and a similar loss of 81% for the PdIr/C catalyst. Though the Pourbaix diagram in Figure 5.34 predicts thermodynamic stability for all three metals under these conditions, the ECSA loss can only be attributed to mechanisms involving metal dissolution. Indeed, the PdIr/C CVs in particular show large peak shift and change of form for 5,000 and 10,000 scans, more reminiscent of the Pd/C CV shown in Figure 5.10 than the PdIr/C CV. This suggests loss of Ir from the PdIr/C catalyst, and to a greater extent than that seen for the PdIr/C_{HSA} catalyst. There is a suggestion from the EXAFS results in Section 4.5.1 that PdIr/C_{HSA} might have a higher degree of mixing of the component metals which could lead to greater electrochemical stability in these conditions. Regardless, the PdIr/C_{HSA} possesses the greatest stability of all catalysts tested under this protocol and, given that the potential range of 0.6 V to 1 V more closely represents the potentials experienced at the anode in normal fuel cell operation (as opposed to cell reversal/fuel starvation in the start-stop protocol), shows promise for long term operation in alkaline fuel cells.

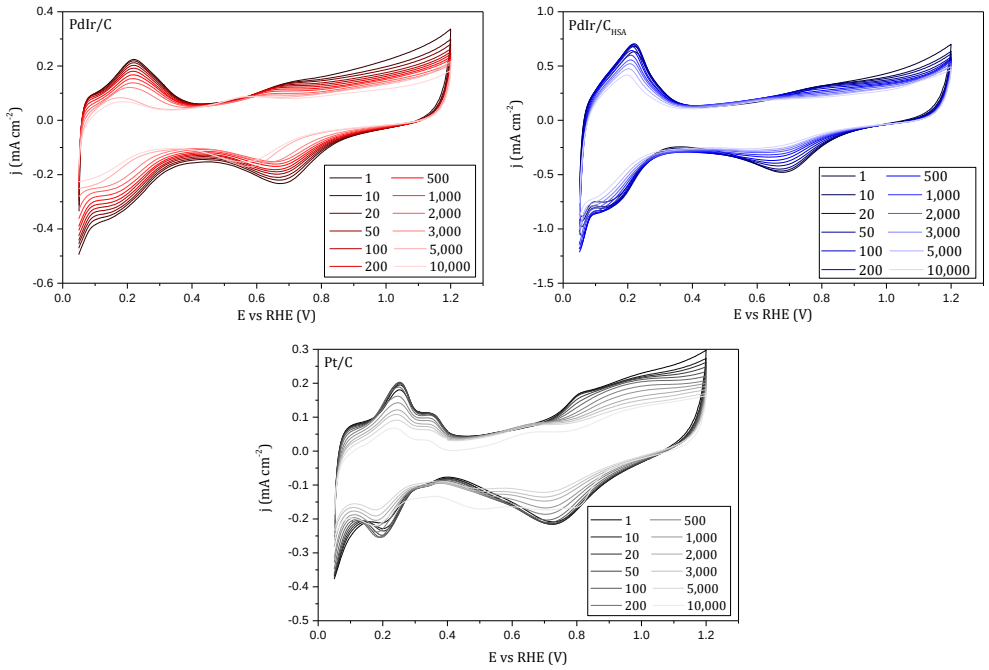

Figure 5.35 Cyclic voltammograms taken during the metal dissolution degradation test on PdIr/C (top left, red), PdIr/CHSA (top right, blue) and Pt/C (bottom, black). The CVs displayed span from the initial CV (lightest) to the CV following 2,000 stop-start cycles (lightest).

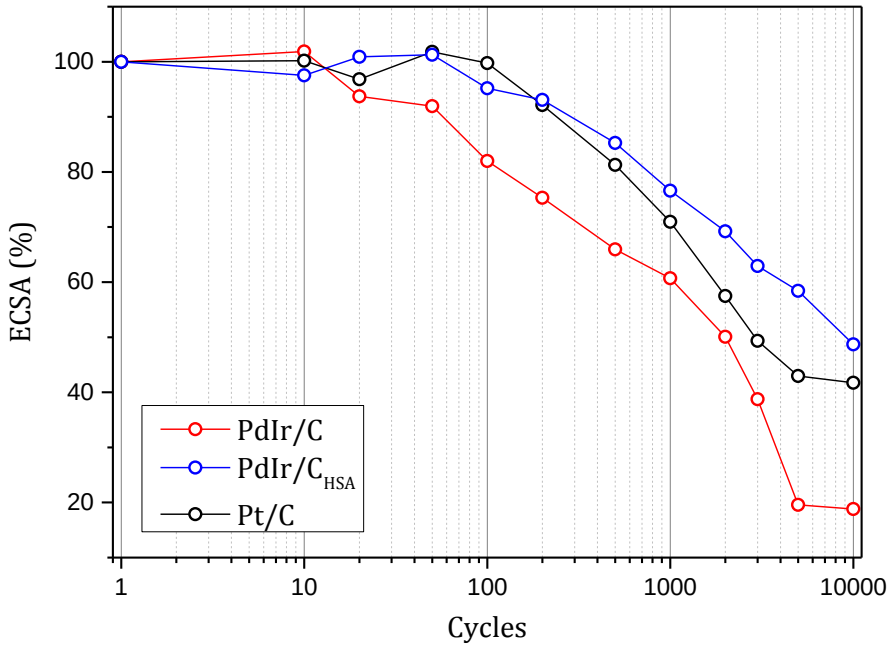

Figure 5.36 ECSA loss for PdIr/C (red), PdIr/C$_{HSA}$ (blue) and Pt/C (black) using the metal dissolution procedure cycling from 0.6 V to 1 V vs RHE.

5.3 Conclusions

Electrochemical characterisation has shown that the novel PdIr/C catalyst has a higher mass activity, specific activity and exchange current density than that of a commercially available Pt/C catalyst. These fundamental electrochemical tests show potential for the use of PdIr/C as an anode catalyst in platinum-free AAEM fuel cells. Imaging and cyclic voltammetry suggest an agglomeration problem that requires optimisation of the synthesis procedure to rectify. The low surface area of the PdIr/C catalyst compared to that of the Pt/C means the electrochemical performance is all the more notable. Indeed, increasing the surface of the catalyst in the case of $PdIr/C_{HSA}$, a significant increase in the mass activity of the catalyst was shown, relative to the both the PdIr/C and commercial Pt/C catalysts. Given the PdIr/C and $PdIr/C_{HSA}$ structures from EXAFS (Section 4.5.1) differ only slightly, it is assumed that the two-fold increase in activity for the latter over the former is due, in the main, to the increase of surface area on improvement of the synthesis procedure.

EIS results show both mass transport and charge transfer resistances for all catalysts and provide further explanation for the respective performance of the catalysts towards HOR in alkaline media.

A clear need to use an alkaline anion exchange ionomer as the binder in inks used for RDE in alkaline media has been shown. However, there is significant room for improvement in the formulation of said inks as the homogeneity of the solutions, and thus the quality of the electrode catalyst layer produced, was less satisfactory than that of the inks using Nafion as a binder. Increasing the surface groups on the carbon using pre-treatment improved this; however, further improvement could potentially be seen on addition of a surfactant to the mixture. A comprehensive ink formula study is suggested for future work.

The carbon monoxide tolerance of the PdIr/C catalyst is potentially better than that of Pt/C by virtue of sub-monolayer coverage of CO on its surface.

A summary of all parameters obtained via electrochemical testing is shown in Table 5.3:

Table 5.3 Electrochemical properties of the catalysts

Catalyst	ECSA (m^2g^{-1})	CO Peak η (V)	j_0 (mA cm^{-2})	αn	R_{CT} (Ω cm^2)	R_D (Ω cm^2)
Pt/C (glass)	13.79	0.71	1.53	0.54		
PdIr/C (glass)	8.10	0.75	2.78	0.61		
Pt/C	33.99		2.99	0.53	10.9	14.6
PdIr/C	18.16		3.07	0.35	10.4	14.9
$PdIr/C_{HSA}$	28.28		6.14	0.56	4.3	12.7
Pd/C			0.12	0.52		
Ir/C			1.85	0.55		
Pt/C-Naf	28.99		2.01	0.43	9.2	23.0
PdIr/C-Naf	17.15		2.91	0.53	18.3	23.8

6 Fuel Cell Testing

Electrochemical characterisation is a vital measure of the inherent activity of a catalyst, but it is not necessarily an indication of how well it will perform in a functioning fuel cell environment. The added complications of fuel cell systems as a whole mean that factors such as gas humidification, membrane condition, flow-field design, MEA manufacture and electrical connections can conspire to produce an overall performance lower than one might expect from otherwise promising electrochemical activity results. The catalyst is also in a different environment when in a solid-electrolyte-MEA as opposed to an aqueous electrochemical cell. For these reasons, testing a catalyst's ability to function within a working fuel cell is essential.

6.1 Experimental

6.1.1 Conditioning

In order to get the best performance out of an MEA it must go through a conditioning procedure which serves to bring the cell up to operating temperature, fully hydrate the MEA and allow the system to acclimatise to fuel cell operating conditions. Once the humidification water bath and cell temperatures where at operating values, the following electrical cycling was used to condition the membrane:

Cell held at 0.8 V for 30 minutes
Cell held at 0.4 V for 30 minutes
Cell held at 0.6 V for 30 minutes
Procedure repeated a further two times

This conditioning 'works' the MEA and a drastic increase in performance (current density) is often seen throughout the process, most likely down to good humidification of the membrane and catalyst layers through a combination of gas humidification and self-humidification with water generated by the electrochemical reaction. Occasionally a longer humidification procedure is needed to get the best MEA performance, but once a stable and acceptable performance is reached, a polarisation curve can be taken.

6.1.2 Polarisation Curves

Fuel cell testing can be carried out either potentiostatically (varying the voltage) or galvanostatically (varying the load current), and the voltage and current values are plotted to form a polarisation curve. The current is normalised to cell area to allow comparison with other experiments.

Polarisation curves were largely taken using an automated galvanostatic procedure that increased the load in increments of 50 $mAcm^{-2}$ from OCV, holding at each point for 30 seconds, then recording 5 data points at 5 second intervals (which are averaged) before moving to the next load. Occasionally a manual method was used where the system was not as stable in order to allow greater time for the cell to equilibrate at each load point. At each data point a current interrupt measurement of the resistivity of the system (both electronic and ionic) is made.

6.1.3 Shut-down Procedure

Once testing is complete it is imperative to use a proper shut-down procedure to protect the health of the MEA. If the MEA is left at OCV with hydrogen on the anode the high polarisation can lead to degradation and corrosion of the catalyst layers. For this reason, at the end of each experiment the temperature of the cell and humidification is reduced to room temperature and the anode stream in switched to nitrogen to purge all hydrogen from the system. The cell is held at a small load of 50 $mAcm^{-2}$ to consume any hydrogen left in the catalyst layers until the voltage of the cell is reduced to zero. This is repeated until the OCV is also zero and the MEA is safe to be stored for re-use.

6.2 Bespoke System

Fuel Cell Polarisation Curves

Figure 6.1 shows the results of fuel cell testing of MEAs 1, 2 and 3 (see Table 3.1 for details of MEAs) – acidic Pt/Pt, alkaline Pt/Pt and alkaline non-Pt (PdIr/C anode and Pd/C cathode) respectively. The test conditions for each MEA are shown in Table 6.1.

Table 6.1 Test conditions for MEA testing

MEA	Cell Temperature (°C)	Anode Gas	Cathode Gas
MEA1	80	H_2, 200 ml/min	Air, 500 ml/min
MEA2	60	H_2, 200 ml/min	O_2, 500 ml/min
MEA3	60	H_2, 200 ml/min	O_2, 500 ml/min

The polarisation curves have been resistivity-corrected by using the resistivity values from the current interrupt measurements and calculating the voltage loss attributable to it (via $V = IR$) and adding it to the voltage reading obtained. In this way the different conductivities of the two types of membrane are negated and a better comparison of the MEAs can be made. The alkaline membranes were much more resistive than that of the Nafion (see Section 6.2.1) and required priming with KOH solution in order for polar curves to be obtained. In the case of MEA 2 and MEA 3 the pump was used to deliver a 2M KOH solution, along with the O_2 in a mixed stream, at 0.1 ml/min for 5 minutes, then turned off before the polar curve measurements were taken.

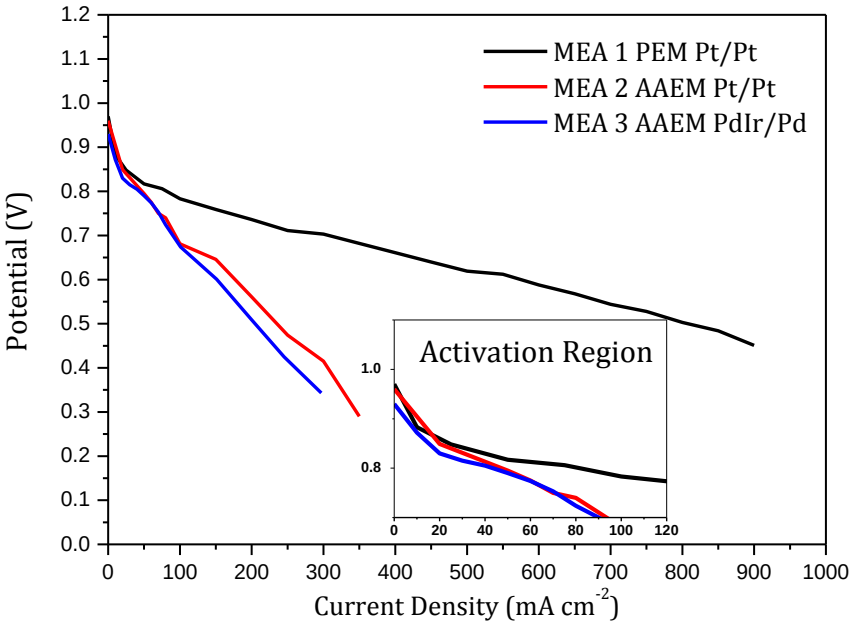

Figure 6.1 Fuel cell polarisation curve comparisons. Curves are shown for an acidic PEM Pt/Pt MEA1 (black), an alkaline AAEM Pt/Pt MEA2 (red) and an alkaline PdIr/Pd MEA3 (blue). Inset shows a detailing of the activation region of the polar curve where the catalyst properties have most influence. All curves are resistivity corrected.

The overall performance of the two AAEM cells is worse than that of the acidic PEM MEA, which is not surprising as the catalyst layers contain proton-conducing ionomer binders instead of hydroxide conducting ones. Much of the processes and techniques used to make the MEAs are based on those of the more well-known PEM fuel cells and as such the AAEM testing is highly unoptimised, as is much AAEM fuel cell research in the literature, so the poor performance relative to that of the PEM MEA is to be somewhat expected.

What is more interesting is the comparable performance of the fully platinum MEA2 and the fully non-platinum MEA3. This suggests that the novel anode catalyst, in conjunction with an in-house Pd/C cathode, has comparable activity in a fuel cell environment to commercially available platinum catalysts. The inset of Figure 6.1 shows the detail of the activation region of the fuel cell polar curve. This is the region in which the catalyst has most influence on the voltage losses and again the results are promising, showing similar trends for all three MEAs. Though much more work needs to be done on the MEA manufacturing and fuel cell testing, the initial results seem to corroborate those of the electrochemical experiments

and suggest the novel low-cost catalyst could prove a suitable replacement for platinum in AAEM fuel cells.

6.2.1 Membrane Resistivity

In order to study the resistivity issues and carbonation effect with the Tokuyama alkaline membranes the effect of carbon dioxide containing air on the conductivity of a sample of A201 membrane was tested. Using a potentiostat the high frequency intercept of impedance spectra were used to assess the resistivity of the membrane under different conditions. The membrane was soaked in 0.5M KOH at room temperature for two hours then rinsed with deionised water and placed in the cell at 60°C. Nitrogen gas humidified at 90°C was flowed over both the anode and cathode for nearly two hours before the stream was changed to air (also humidified at 90°C). As can be seen in Figure 6.2, the introduction of CO_2 in the air caused a dramatic increase in the resistivity of the membrane to levels far beyond that acceptable in a fuel cell. The gradual increase in resistivity seen while still under nitrogen is most likely due to removal of any KOH left in the membrane by the humidified stream.

Though pure O_2 was used for the fuel cell experiments, these results show the importance of not allowing any air into the system and swift set up of the test cell so as to minimise the exposure to CO_2. They also confirm that even the lowest resistivity seen is higher than that of a typical Nafion membrane.

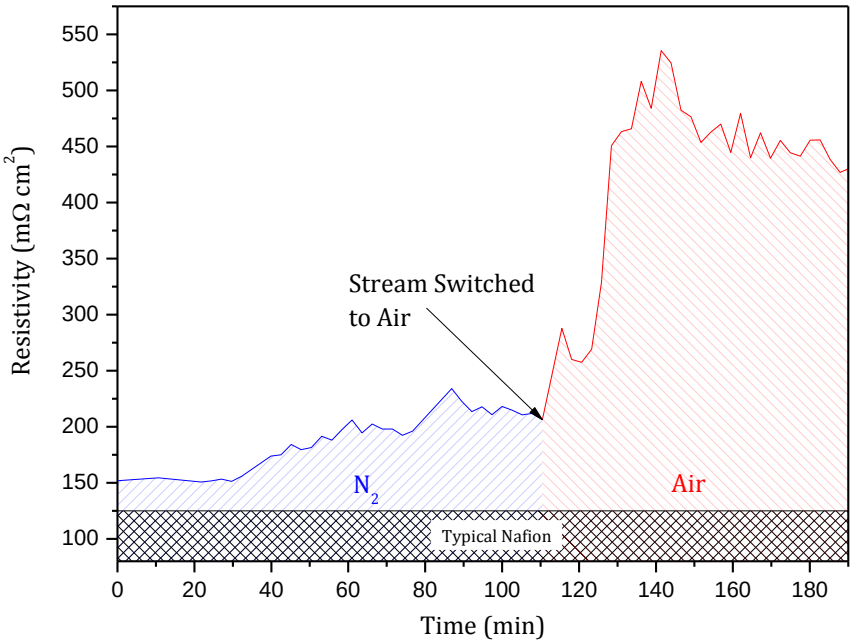

Figure 6.2 Membrane resistivity results. When the gas stream is switched from nitrogen (blue) to CO_2 containing air (red), the resistivity of the membrane increases sharply. A typical Nafion resistivity is shown in comparison (black).

This phenomenon is also observed in a more detailed experiment involving quartz crystal microbalances (QCMs) conducted by others in the group. The QCM allows small mass loadings, on the order of nanograms, to be detected by observing reductions in the resonant frequency of the crystal. A thin AAEM (30 nm) was cast on the surface of the QCM from a solution of AS-4 alkaline ionomer, and humidified nitrogen, followed by humidified CO_2-containing air, is flowed through a temperature controlled gas-tight chamber at 55 °C and 100% relative humidity. The humidified gases negate the drying effect seen in the initial stages of Figure 6.2. As Figure 6.3 shows, a stable resonance frequency under nitrogen immediately reduces on the introduction of air with a corresponding mass increase of 41.6 ng detected over the course of the experiment. In this way, the increase in the resistivity of the membrane on introduction of CO_2-containing air is shown to be coupled with an increase of mass on the QCM, attributed to the formation of carbonates in the membrane structure.

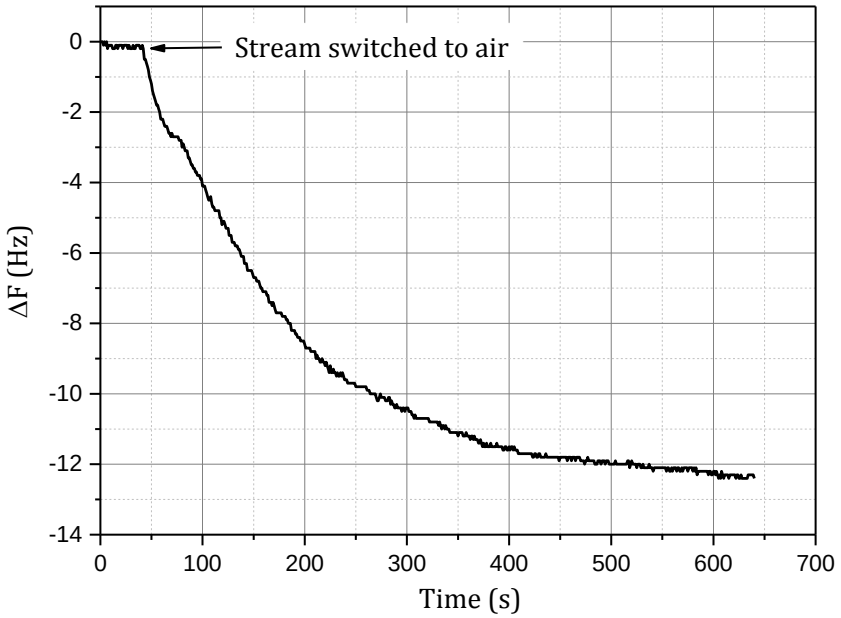

Figure 6.3 The reduction in frequency of a QCM with cast AAEM layer on the surface, corresponding to an increase in mass, on introduction of CO_2-containing air at 45 s, indicating formation of carbonates in the membrane. All gases are humidified at 100% relative humidity at 55 °C.

6.3 Commercial System

6.3.1 PEM Testing

The humidification system employed in the bespoke fuel cell test system is inadequate for high end fuel cell performance. The commercial fuel cell test station from Scribner Associates includes a dew point humidifier and, as can be seen in Figure 6.4, produced a much better PEM fuel cell performance.

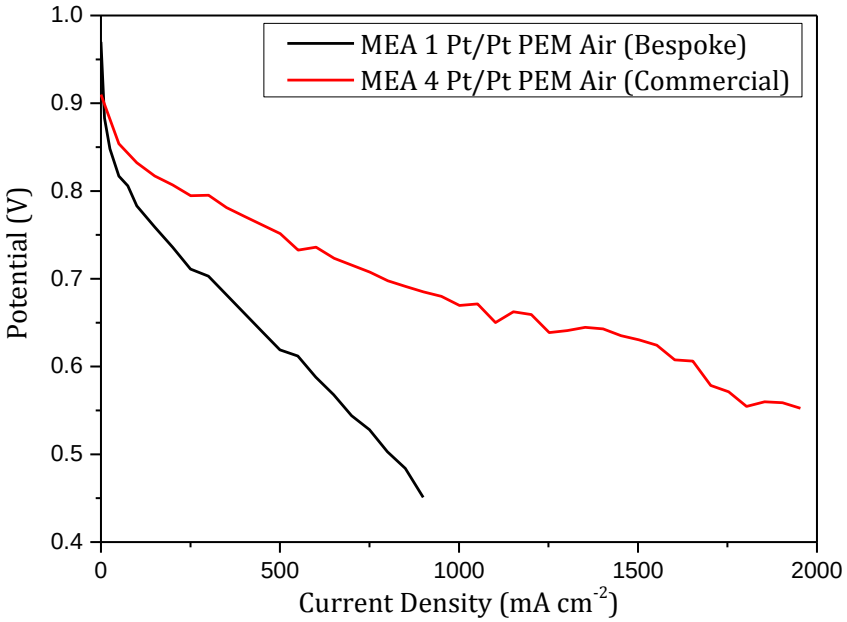

Figure 6.4 The performance of Pt/Pt PEM MEAs in the bespoke (black) and commercial (red) systems. Both polarisation curves were obtained with hydrogen on the anode and air on the cathode at 80 °C with 100% relative humidity and resistivity corrected.

With this in mind, a performance baseline for a Pt/Pt PEM was set in order for comparison with AAEM performance under oxygen. Figure 6.5 (a) shows the resistivity-corrected performance of MEA 4, a Pt/Pt PEM MEA, at 55 °C (blue) and 80 °C (red), and also with backpressure of 150 kPa applied to the cathode (dashed). The best performance is obtained using backpressure, as would be expected due to the enhancement of thermodynamics via increasing the Nernstian potential (as discussed in Section 1.3.3) and also enhancement of the kinetics via increase of the exchange current density (as discussed in Section 1.4.1.4) [17]. There is little difference in the 55 °C and 80 °C polarisation curves when operated under backpressure, possibly due to the enhancement effects of the pressure dwarfing any temperature effects. There is a greater difference seen at atmospheric pressure, as indicated by the solid blue and red polarisation curves in Figure 6.5 (a). Initially, the higher temperature has superior performance in the activation region due to improved kinetics at 80 °C. However, the 55 °C polarisation curve has lower potential losses at higher current densities. This could be due to the fact that the thermodynamic potential is higher for the lower temperature; however, such a large difference is not expected. Figure 6.5 (b) shows the same data as in Figure 6.5 (a), but without the resistivity correc-

tion, and gives a more comparable performance for the two operating temperatures. This is because at 55 °C, 100% relative humidity translates as a lower hydration level than at 80 °C, and therefore the membrane is more resistive and so overcompensated for when resistivity correction is applied. The thermodynamic advantages of lower temperature are more accurately represented in this uncorrected figure, and indeed for the backpressured experiments (where there is a thermodynamic enhancement of potential for both 55 °C and 80 °C anyway) it is the higher temperature, and more conductive membrane, that shows the best performance at high current densities.

These baseline tests show the benefit of the improved hydration system in the commercial unit as well as using backpressure. The effect of elevated temperature is less clear; however, given the instability of AAEMs at high temperature, 55 °C is chosen as the operating temperature for alkaline fuel cell testing.

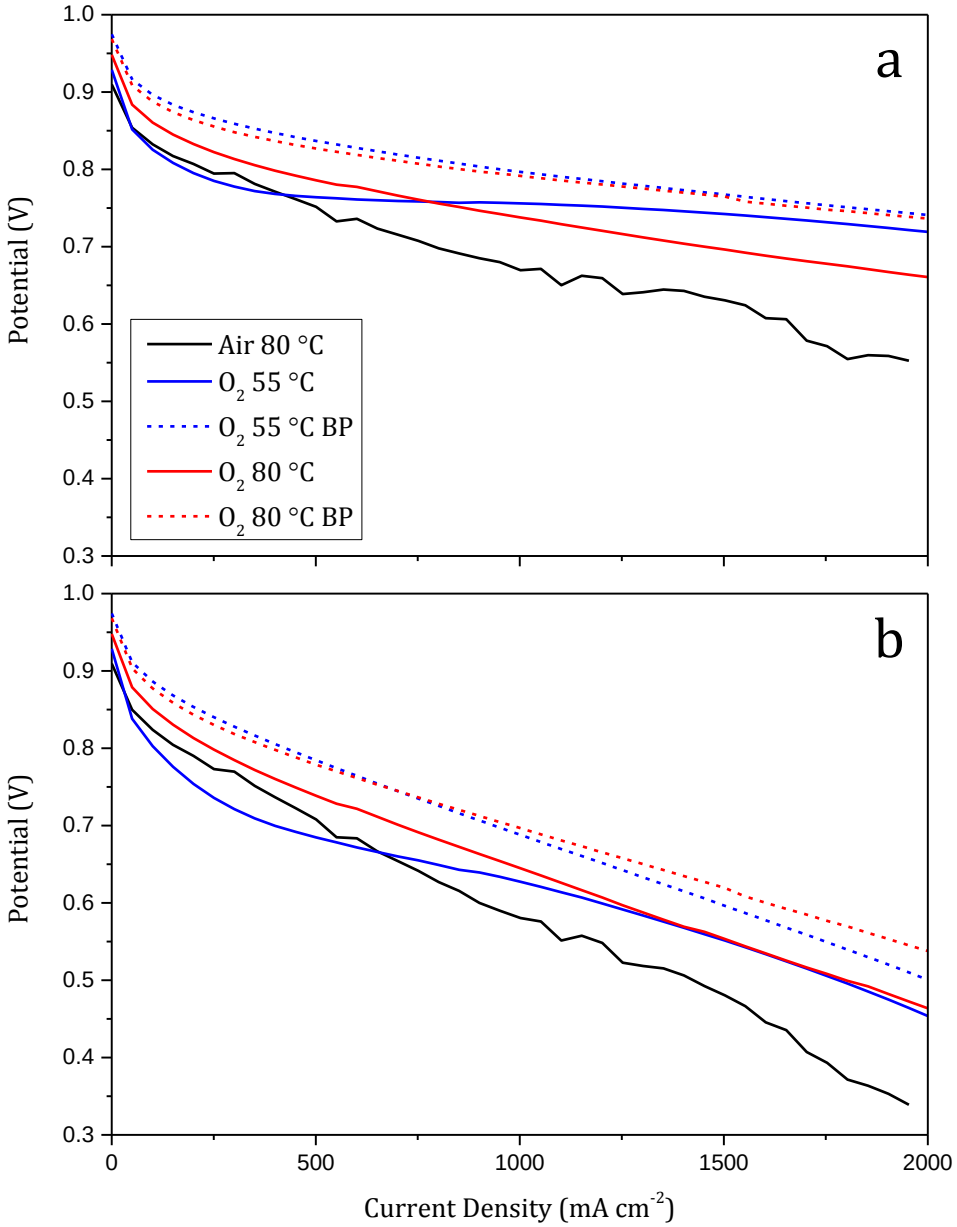

Figure 6.5 The resistivity corrected (a) and uncorrected (b) polarisation curves of MEA 4, Pt/Pt PEM, using air (black) and oxygen at both 55 °C (blue) and 80 °C (red) as the cathode gas, including the effect of 150 kPa of back pressure applied to the cathode (dashed).

6.3.2 AAEM Testing

Given the importance of using an alkaline binder in the inks shown in Section 5.2.3, a Pt/C catalyst ink was prepared with 25%$_{wt}$ alkaline ionomer with respect to the carbon mass. The carbon-coated GDM substrates, on

which all previous inks where applied to form electrodes, also contain Nafion as they are designed for use in PEM systems; for this reason the Pt-AAEM ink was applied directly to Toray paper GDL material in order to produce a Nafion-free electrode layer. It has been suggested that hotpressing the MEA when the membrane is in hydroxide form can be damaging, due to acceleration of Hoffmann elimination [96], and that hydroxide can be generated in situ when conditioning in the fuel cell set-up by holding at a potential of around 0.2 V, the MEA was initially tested in chloride form. However, it was not possible to generate enough current to transform the membrane into hydroxide form and so the MEA was soaked in 1M KOH for two and a half hours before placing it in the cell. Attempts at conditioning the MEA were made by holding the potential at 0.5 V, 0.4 V and eventually 0.2 V, with a stable, albeit low, current of 100 mA cm^{-2} achieved at the latter potential. A polarisation curve was attempted with oxygen at atmospheric pressure as the cathode gas and a cell temperature of 55 °C, with the results shown in Figure 6.6 (a). The performance of the MEA was poor, with stability also a major issue. When compared with a PEM MEA operating under the same conditions (Figure 6.6 (b)), the low current densities achieved are even starker. It should be noted that this is a highly unoptimised alkaline fuel cell given there is no GDM, an unoptimised ink formula, low loading on the electrodes (it was difficult to adhere much ink directly to the GDL without a carbon layer and a peak amount of 0.16 mg cm^{-2} was reached for this electrode), unconditioned membranes, lack of standard procedure for reliable AAEM FC testing and under-developed membrane technology. Many of the improvements necessary to obtain improved AAEM performance were deemed to be beyond the scope of the investigation of this thesis and so comparison of the Pt/C performance with that of PdIr/C in situ was not thought worthwhile until a much improved baseline performance for AAEM fuel cells is achieved. This will be the subject of further work beyond that presented here; nevertheless, the activity of $PdIr/C_{HSA}$ shown in Chapter 5 suggests that when improvements in alkaline membranes, and AAEM FCs in general, arrive there are promising alternatives to Pt ready to make AAEM FCs a viable alternative to PEM FCs, and a possible route to cost reduction.

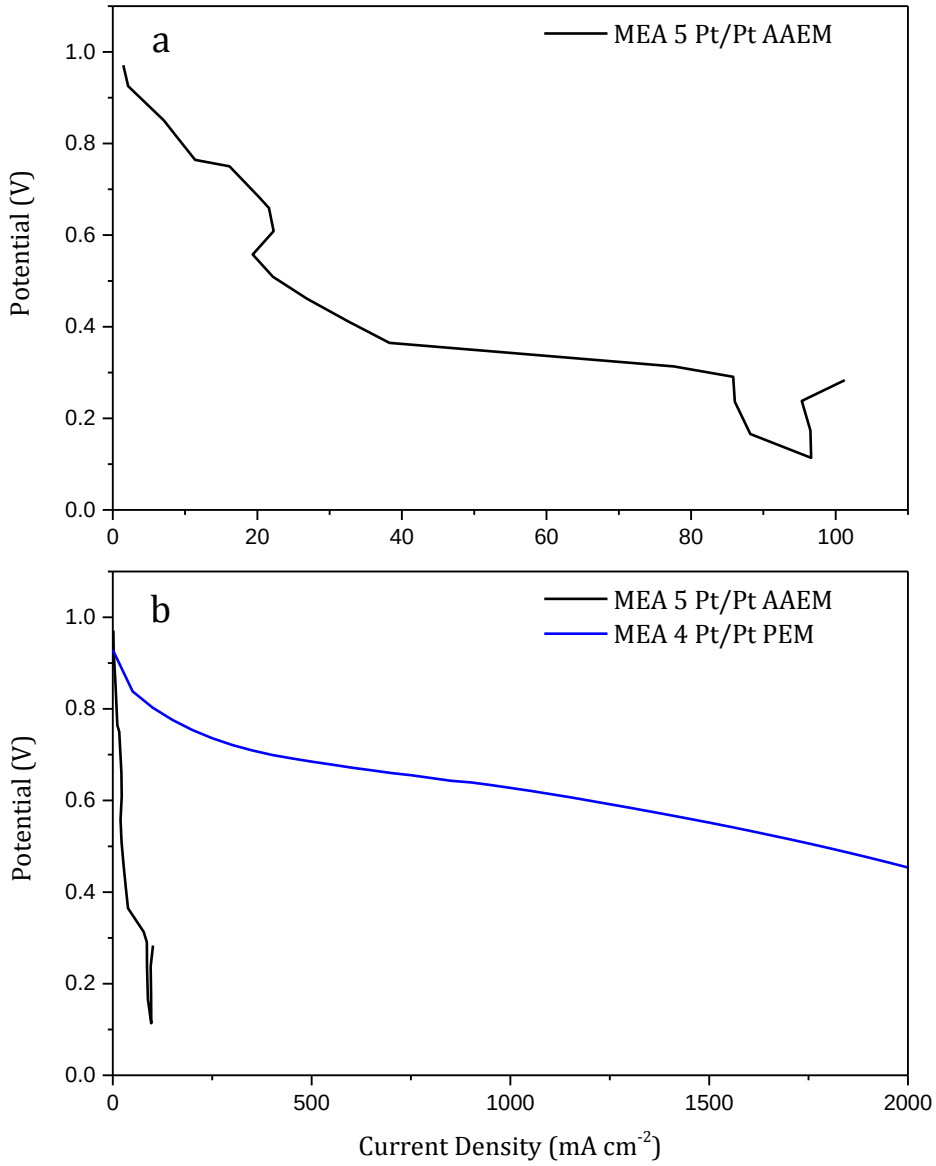

Figure 6.6 (a) Polarisation curve for MEA 5, a Pt/Pt AAEM with alkaline binder using oxygen as the cathode gas and at 55 °C, and (b) the same curve compared to a PEM MEA under the same conditions.

6.4 Conclusions

A fully non-platinum AAEM MEA consisting of the novel PdIr/C anode catalyst and a Pd/C cathode was manufactured and tested in a fuel cell test station, along with Pt AAEM and PEM MEAs. The performance of the two alkaline MEAs was comparable as was the activation region of all

three, suggesting that the activity of the catalyst is comparable with that of a commercially available Pt/C catalyst.

The performance of the alkaline membranes is an issue when compared to Nafion and they are highly sensitive to CO_2 and subsequent carbonation. Optimisation of the catalyst layers and fuel cell testing techniques is required in order to obtain matching performance for alkaline fuel cells.

A good baseline PEM performance has been achieved using the improved fuel cell testing system; however, the AAEM performance is too poor to allow valid comparison of PdIr/C with Pt/C without substantial improvements to the baseline performance.

7 Conclusions and Future Work

A novel PdIr/C catalyst for the HOR in AAEM fuel cells has been synthesised and its performance tested in both aqueous electrolyte and fuel cell environments. Initial fundamental electrochemical testing showed a slightly higher mass and specific activity than that of a commercially available Pt/C catalyst. TEM imaging and cyclic voltammetry showed that the surface area of the PdIr/C catalyst is lower than that of the Pt/C, due to agglomeration of the metal nanoparticles. For this reason, a higher surface area version, PdIr/C_{HSA}, was synthesised using an alkaline carbon pretreatment step and a more aggressive reducing agent.

Characterisation of the catalyst using ICP-AES showed the atomic ratios of Pd and Ir to be close to 1:1, and though EDX and LEIS showed some discrepancy from this ratio, in general they back up the elemental analysis of the catalyst. For future improvements to the catalyst, regular access to ICP-AES needs to be available in order to be able to rapidly screen new iterations and validate changes in synthesis procedure as it represents the most reliable method for determination of the atomic ratio in the catalyst samples.

TEM confirmed that the PdIr/C_{HSA} catalyst had greatly improved surface area, with an average particle size of 3.8 nm and greater dispersion of metal on the carbon support. However, some areas of agglomeration still exist and there is scope to further improve the distribution of metal by employing methods such as sonication or sequential reduction in the synthesis phase [250]. HR-TEM was also used to study the catalysts, and allowed determination of the exposed facets of the crystallites as well as high-resolution EDX mapping of individual particles. A longer mapping of a larger area, or multiple areas of the catalyst, would allow any significant areas of poor homogeneity to be identified. Although the particle studied in this work showed good distribution of Pd and Ir, it might not be the case for the whole sample, as was suggested by the EXAFS results.

EXAFS experiments allowed determination of local coordination numbers of Pd, Ir and O, and thus elucidation of the average structure of the

catalyst. Core-shell and well mixed alloy structures were discounted from the EXAFS results, with a 'single-half' structure most closely representing the PdIr/C catalysts and the PdIr/C_{HSA} version having a slightly higher degree of mixing. XRD and XPS confirmed the change in crystal and electronic structures on alloying of the two metals, compared with their monometallic equivalents. This could explain the great increase in activity for the alloy catalyst over both Pd/C and Ir/C and shows that even small changes in structure can have a drastic effect on the performance of the catalyst, with more improvements potentially to be made if a well-mixed alloy can be synthesised. In situ fuel cell EXAFS of the catalyst, such as those performed by Price et al. [180], would provide much more information on the behaviour of the materials in an operating environment and with varying potential. This would be particularly interesting with Pd based catalysts as they may possess the ability to adsorb hydrides in a similar manner to bulk Pd metal. A full in situ study of the PdIr/C catalysts by EXAFS is planned for future work.

LEIS was used to study the outermost surface layer of the catalysts, however, sputtering was required to clean the surface of oxides and other materials before significant Pd and Ir signals were seen. As such, there is an element of depth profiling to the results and so the results cannot be said to be purely surface specific. If non-destructive plasma cleaning could be employed in situ it might be possible to study purely the surface layer and compare with the structural modelling from the EXAFS experiments. Deliberately synthesising a core-shell structure, via methods such as sequential reduction or sacrificial replacement of metals, would allow a depth profiling experiment to be conducted on the LEIS equipment, with a 'high-low-high' signal expected from the shell metal, and vice versa for the core metal. However, this would require a greater control of particle sizing than achieved thus far, and would be further complicated by the powder samples not necessarily providing a flat surface for the LEIS study. Nevertheless, LEIS is an under-utilised technique for electrocatalyst characterisation and has much room for further study.

Electrochemical testing in a three-electrode glass cell showed the PdIr/C catalyst to have comparable, if not better, activity for the HOR in alkaline than Pt/C. In order to overcome contamination effects from the corrosion of the glass a bespoke PTFE cell was made for further electrochemical testing, also allowing for long term durability experiments [235]. The PdIr/C_{HSA}

catalyst showed the greatest activity with a two-fold increase in exchange current density over that of Pt/C, demonstrating its potential as an anode replacement and thus a route to cost reduction in fuel cells. The choice of binder used in making inks for the RDE was shown to be very important, with the electrodes incorporating the alkaline binder having superior performance to those with Nafion. Lima et al. [251] made electrodes for RRDE studies of carbon-supported catalysts without using any binder, and so this could be a route to overcoming the homogeneity issues experienced with the alkaline inks, though it represents a further removal from fuel cell-like conditions. A full ink optimisation study is required to improve electrochemical testing for future work, and to set a benchmark for alkaline based inks. Electrochemical impedance spectroscopy was also used to better understand the contribution of activation and mass transport losses to the overall performance of the catalyst. This further emphasised the need for an alkaline binder in the ink as the Nafion based inks displayed significantly greater mass transport resistances. Again, the $PdIr/C_{HSA}$ catalyst showed the lowest overall resistance from EIS, as well as having the lowest charge transfer resistance (a measure of inherent catalytic activity). In general, a greater separation for the two arcs in the Nyquist plots existed for the PdIr catalysts than the Pt/C, indicating that there is a greater difference between the time constants involved for the two processes for the former than the latter. The trends in charge transfer resistance from EIS matched well with that seen in the Tafel analysis of the RDE experiments. Varying the polarisation and rotation rate while conducting EIS proved that the two distinct arcs seen for PdIr were attributable to charge transfer and mass transport resistances, respectively. Finally, the catalyst durability was studied using two different procedures based on standard PEM durability tests. The $PdIr/C_{HSA}$ showed the best durability for the metal dissolution protocol, however, there is a significant difference between acidic and alkaline environments when it comes to catalyst and support stability and therefore there is a need for an alkaline specific benchmark to be set for AAEM fuel cells. Given the relative lack of study of AAEM FCs compared with the predominant PEM FC technology it is not surprising that there is no existing benchmark, and so if there is to be more research focused on catalysts for alkaline environments this must be addressed. Very recent work has used a scanning He ion microscope to study Pt/C catalysts with a much higher resolution than afforded by standard SEM instruments, allowing in-

dividual nanoparticles to be resolved in the imaging. This will be used to study catalyst degradation at various stages of the durability protocols, allowing the same region to be imaged and therefore follow the change in nanoparticle geometry, agglomeration or migration. This would provide excellent information as to whether metal is lost in solution, or suffers from Ostwald ripening or similar agglomeration mechanisms (or the extent to which is it a combination of both). Other work conducted in the group has shown carbon nitride materials to be more corrosion resistant supports for electrocatalysts and so this will be applied to the PdIr alloy as a route to improved durability, and possibly activity, in an alkaline environment [252-255].

Though fuel cell testing showed worse performance for AAEM fuel cells compared to PEM testing, the performance of a Pt/Pt AAEM MEA was comparable to that of a fully non-platinum Pd/PdIr AAEM MEA and the activation region of all three fuel cells tested showed a similar performance, suggesting that the activity of the PdIr/C in a fully non-platinum MEA is comparable to the industry-standard Pt. This has shown the potential for future of reduction of catalyst cost in fuel cells by employing PdIr/C anode catalyst in alkaline exchange membrane fuel cells.

Attempts at improved fuel cell performance using the commercial test station provided excellent baseline PEM results but satisfactory performance of AAEMs was not achieved in the timescale of this work. For AAEM fuel cells to match the performance achieved by PEM fuel cells, an improvement in membrane resistivity and use of anion exchange polymers in the catalyst layers is needed, as highlighted by EIS and QCM investigations into carbonation of the membranes. Due to the different half reactions, and therefore water management, in alkaline fuel cells many changes from the established PEM practices may be required for better AAEM performance; for instance, having more asymmetric electrodes where PTFE is removed from the cathode, loading is altered or gas diffusion layers are different on each side may help with water management. Varying humidification could also be considered, with dry cathode performance showing promise, possibly as it promotes the self-purging effect [91]. More generally, there is a definite need to remove all acid-based ionomers from the MEAs and to fully optimise inks, electrodes and gas diffusion layers for AAEM FCs before they can realistically be considered as alternatives to the established PEM technology. Nevertheless, should these improvements be made in the

coming years, the work in this thesis provides a promising catalyst to be employed on the anode as an alternative to platinum.

Additionally, the scope of the project is expected to expand to include use of the catalysts in electrolysers and methanol fuel cells. Electrolysers (essentially a fuel cell operating in reverse to evolve hydrogen and oxygen gas from water) might be a more promising application for the catalyst as the aqueous operating environment should help to negate many of the resistivity issues seen with the membranes. If fuel cell technology is to be adopted in such large sectors as the automobile industry, the demand for clean hydrogen will increase accordingly. In this way, electrolysers are seen as a vital element in a future hydrogen economy and could be required in an equal number to fuel cells. Also, the current platinum loading of electrolyser MEAs is significantly higher than the state of the art fuel cell MEAs, so there is arguably greater scope for price reduction using non-platinum catalysts in electrolysers.

Methanol has many potential benefits over hydrogen as a fuel for fuel cells, including a higher energy density, easier storage and transport, and the ability for production via biomass. However, the overpotentials involved in the oxidation of hydrocarbons are many times larger than those of the more kinetically facile HOR. This puts a greater emphasis on anode catalyst cost reduction as the low loadings achieved in some PEM fuel cell anodes will not be possible when using methanol as a fuel. For this reason, a non-platinum anode catalyst is predicted to have even more significant improvements for methanol fuel cells than PEM or AAEM.

Further down the line, incorporating graphene into fuel cell catalysts is something that is seen as having huge promise. Particularly because a method used for production of graphene is via intercalation of graphite with metal ions, followed by exfoliation and removal of the ions. If the ions are chosen to be Pt, or similarly catalytically active metals, it could be possible to reduce the ions on the surface of the graphene, rather than removing them, and thus have highly ordered distributions of small nanoparticles of catalyst on graphene.

Improvements in electrocatalysis in the coming years will have huge impact on many electrochemical technologies, many of which (fuel cells, electrolysers, redox flow batteries) are expected to be integral to a reduction in use of fossil fuels and a shift towards a greener electricity-based economy.

8 References

[1] S. Bilgen, "Structure and environmental impact of global energy consumption," Renewable and Sustainable Energy Reviews, vol. 38, pp. 890-902, 10// 2014.

[2] S. J. Davis, K. Caldeira, and H. D. Matthews, "Future CO2 Emissions and Climate Change from Existing Energy Infrastructure," Science, vol. 329, pp. 1330-1333, September 10, 2010 2010.

[3] J. Zhang, PEM Fuel Cell Electrocatalysts and Catalyst Layers: Fundamentals and Applications, Chapter 1: Springer, 2008.

[4] C. Pak, S. Kang, Y. Suk Choi, and H. Change, "Nanomaterials and structures for the fourth innovation of polymer electrolyte fuel cell," Journal of Materials Research, vol. 25, pp. 2063-2071, 2010.

[5] Y. Wang, K. S. Chen, J. Mishler, S. C. Cho, and X. C. Adroher, "A review of polymer electrolyte membrane fuel cells: Technology, applications, and needs on fundamental research," Applied Energy, vol. 88, pp. 981-1007, 2011.

[6] X. Li and I. Sabir, "Review of bipolar plates in PEM fuel cells: Flow-field designs," International Journal of Hydrogen Energy, vol. 30, pp. 359-371, 2005.

[7] A. El-kharouf and B. G. Pollet, "Chapter 4 - Gas Diffusion Media and their Degradation," in Polymer Electrolyte Fuel Cell Degradation, M. Matthew, K. Emin Caglan, and T. N. Veziroglu, Eds., ed Boston: Academic Press, 2012, pp. 215-247.

[8] A. El-kharouf, T. J. Mason, D. J. L. Brett, and B. G. Pollet, "Ex-situ characterisation of gas diffusion layers for proton exchange membrane fuel cells," Journal of Power Sources, vol. 218, pp. 393-404, 11/15/ 2012.

[9] E. Passalacqua, F. Lufrano, G. Squadrito, A. Patti, and L. Giorgi, "Nafion content in the catalyst layer of polymer electrolyte fuel cells: Effects on structure and performance," Electrochimica Acta, vol. 46, pp. 799-805, 2001.

[10] K. H. Kim, K. Y. Lee, H. J. Kim, E. Cho, S. Y. Lee, T. H. Lim, et al., "The effects of Nafion® ionomer content in PEMFC MEAs prepared by a catalyst-

coated membrane (CCM) spraying method," International Journal of Hydrogen Energy, vol. 35, pp. 2119-2126, 2010.

[11] J. Zhang, PEM Fuel Cell Electrocatalysts and Catalyst Layers: Fundamentals and Applications, Chapter 1 pg 13: Springer, 2008.

[12] J. T. A. Zawodzinski, C. Derouin, S. Radzinski, R. J. Sherman, V. T. Smith, T. E. Springer, et al., "Water Uptake by and Transport Through Nafion 117 Membranes," Journal of The Electrochemical Society, vol. 140, pp. 1041-1047, 1993.

[13] J. T. A. Zawodzinski, T. E. Springer, J. Davey, R. Jestel, C. Lopez, J. Valerio, et al., "A Comparative Study of Water Uptake By and Transport Through Ionomeric Fuel Cell Membranes," Journal of The Electrochemical Society, vol. 140, pp. 1981-1985, 1993.

[14] K. C. Neyerlin, H. A. Gasteiger, C. K. Mittelsteadt, J. Jorne, and W. B. Gu, "Effect of relative humidity on oxygen reduction kinetics in a PEMFC," Journal of the Electrochemical Society, vol. 152, pp. A1073-A1080, 2005.

[15] T. A. Davis, A first course in ion permeable membranes, 1997.

[16] B. Frano, "Chapter 2 - 2. Fuel Cell Basic Chemistry and Thermodynamics," in PEM Fuel Cells, ed Burlington: Academic Press, 2005, pp. 17-32.

[17] J. Zhang, H. Li, and J. Zhang, "Effect of Operating Backpressure on PEM Fuel Cell Performance," ECS Transactions, vol. 19, pp. 65-76, November 30, 2009 2009.

[18] R. P. O'Hayre, Fuel cell fundamentals, Chapter 3, 2006.

[19] M. M. Mench, "Performance Characterization of Fuel Cell Systems," in Fuel Cell Engines, ed: John Wiley & Sons, Inc., 2008, pp. 121-190.

[20] W. F. K. Wynne-Jones and H. Eyring, "PAPER 5 - THE ABSOLUTE RATE OF REACTIONS IN CONDENSED PHASES†," in Selected Readings in Chemical Kinetics, M. H. B. J. Laidler, Ed., ed: Pergamon, 1967, pp. 68-90.

[21] C. M. A. Brett and A. M. O. Brett, Electrochemistry: Principles, Methods, and Applications, Chapter 4: Oxford University Press, 1993.

[22] M. M. Mench, "Thermodynamics of Fuel Cell Systems," in Fuel Cell Engines, ed: John Wiley & Sons, Inc., 2008, pp. 62-120.

[23] R. P. O'Hayre, Fuel cell fundamentals, Chapter 2, 2006.

[24] J. K. Nørskov, J. Rossmeisl, A. Logadottir, L. Lindqvist, J. R. Kitchin, T. Bligaard, et al., "Origin of the Overpotential for Oxygen Reduction at a Fuel-Cell Cathode," The Journal of Physical Chemistry B, vol. 108, pp. 17886-17892, 2004/11/01 2004.

[25] V. Stamenkovic, B. S. Mun, K. J. J. Mayrhofer, P. N. Ross, N. M. Markovic, J. Rossmeisl, et al., "Changing the Activity of Electrocatalysts for Oxygen Reduction by Tuning the Surface Electronic Structure," Angewandte Chemie, vol. 118, pp. 2963-2967, 2006.

[26] B. Hammer and J. K. Norskov, "Why gold is the noblest of all the metals," Nature, vol. 376, pp. 238-240, 07/20/print 1995.

[27] B. Hammer and J. K. Nørskov, "Electronic factors determining the reactivity of metal surfaces," Surface Science, vol. 343, pp. 211-220, 12/10/ 1995.

[28] J. K. Nørskov, F. Abild-Pedersen, F. Studt, and T. Bligaard, "Density functional theory in surface chemistry and catalysis," Proceedings of the National Academy of Sciences, vol. 108, pp. 937-943, January 18, 2011 2011.

[29] GreeleyJ, I. E. L. Stephens, A. S. Bondarenko, T. P. Johansson, H. A. Hansen, T. F. Jaramillo, et al., "Alloys of platinum and early transition metals as oxygen reduction electrocatalysts," Nat Chem, vol. 1, pp. 552-556, 10//print 2009.

[30] J. K. Norskov, T. Bligaard, J. Rossmeisl, and C. H. Christensen, "Towards the computational design of solid catalysts," Nat Chem, vol. 1, pp. 37-46, 04//print 2009.

[31] B. Wang, "Recent development of non-platinum catalysts for oxygen reduction reaction," Journal of Power Sources, vol. 152, pp. 1-15, 2005.

[32] S. Chen and A. Kucernak, "Electrocatalysis under Conditions of High Mass Transport: Investigation of Hydrogen Oxidation on Single Submicron Pt Particles Supported on Carbon," The Journal of Physical Chemistry B, vol. 108, pp. 13984-13994, 2004/09/01 2004.

[33] X. Li, "Principles of fuel cells," Platinum metals review, vol. 50, p. 200, 2006.

[34] J. Tafel, "Über die Polarisation bei kathodischer Wasserstoffentwicklung," Zeitschrift für physikalische Chemie, vol. 50, p. 641, 1905.

[35] S. Slade, "Ionic conductivity of an extruded Nafion 1100 EW series of membranes," Journal of The Electrochemical Society, vol. 149, 2002.

[36] B. Frano, "Chapter 3 - 3. Fuel Cell Electrochemistry," in PEM Fuel Cells, ed Burlington: Academic Press, 2005, pp. 33-72.

[37] R. P. O'Hayre, Fuel cell fundamentals, Chapter 5, 2006.

[38] H. Wroblowa, M. L. B. Rao, A. Damjanovic, and J. O. M. Bockris, "Adsorption and kinetics at platinum electrodes in the presence of oxygen at zero net current," Journal of Electroanalytical Chemistry, vol. 15, pp. 139-150, 1967.

[39] J. P. Hoare, "Rest potentials in the platinum-oxygen-acid system," Journal of The Electrochemical Society, vol. 109, p. 858, 1962.

[40] J. Zhang, Y. Tang, C. Song, J. Zhang, and H. Wang, "PEM fuel cell open circuit voltage (OCV) in the temperature range of 23°C to 120°C," Journal of Power Sources, vol. 163, pp. 532-537, 2006.

[41] S. A. Vilekar and R. Datta, "The effect of hydrogen crossover on open-circuit voltage in polymer electrolyte membrane fuel cells," Journal of Power Sources, vol. 195, pp. 2241-2247, 2010.

[42] S. Srinivasan, M. A. Enayetullah, S. Somasundaram, D. H. Swan, D. Manko, H. Koch, et al., "Recent advances in solid polymer electrolyte fuel cell technology with low platinum loading electrodes," in Energy Conversion Engineering Conference, 1989. IECEC-89., Proceedings of the 24th Intersociety, 1989, pp. 1623-1629 vol.3.

[43] A. J. Appleby, "Electrocatalysis of aqueous dioxygen reduction," Journal of electroanalytical chemistry and interfacial electrochemistry, vol. 357, pp. 117-179, 1993.

[44] E. Agel, J. Bouet, and J. F. Fauvarque, "Characterization and use of anionic membranes for alkaline fuel cells," Journal of Power Sources, vol. 101, pp. 267-274, 2001.

[45] J. R. Varcoe, R. C. T. Slade, G. L. Wright, and Y. Chen, "Steady-State dc and Impedance Investigations of H2/O2 Alkaline Membrane Fuel Cells with Commercial Pt/C, Ag/C, and Au/C Cathodes," The Journal of Physical Chemistry B, vol. 110, pp. 21041-21049, 2006/10/01 2006.

[46] H. Yanagi, S. Watanabe, K. Sadasue, T. Isomura, H. Inoue, and K. Fukuta, "Improved Performance of Alkaline Membrane Fuel Cells Based on Newly Developed Electrolyte Materials," ECS Meeting Abstracts, vol. 902, pp. 341-341, 2009.

[47] G. F. McLean, T. Niet, S. Prince-Richard, and N. Djilali, "An assessment of alkaline fuel cell technology," International Journal of Hydrogen Energy, vol. 27, pp. 507-526, 2002.

[48] B. B. Blizanac, P. N. Ross, and N. M. Markovic, "Oxygen electroreduction on Ag(111): The pH effect," Electrochimica Acta, vol. 52, pp. 2264-2271, 2007.

[49] B. B. Blizanac, P. N. Ross, and N. M. Marković, "Oxygen Reduction on Silver Low-Index Single-Crystal Surfaces in Alkaline Solution: Rotating Ring DiskAg(hkl) Studies," The Journal of Physical Chemistry B, vol. 110, pp. 4735-4741, 2006/03/01 2006.

[50] S. D. Poynton, J. P. Kizewski, R. C. T. Slade, and J. R. Varcoe, "Novel electrolyte membranes and non-Pt catalysts for low temperature fuel cells," 14th International Conference on Solid State Protonic Conductors, Kyoto, Japan, 7-11 September 2008, vol. 181, pp. 219-222, 2010.

[51] F. Bidault, D. J. L. Brett, P. H. Middleton, N. Abson, and N. P. Brandon, "A new application for nickel foam in alkaline fuel cells," International Journal of Hydrogen Energy, vol. 34, pp. 6799-6808, 2009.

[52] F. Bidault, D. J. L. Brett, P. H. Middleton, N. Abson, and N. P. Brandon, "An improved cathode for alkaline fuel cells," vol. 35, pp. 1783-1788, 2010.

[53] E. Yeager, "Electrocatalysts for O2 reduction," Electrochimica Acta, vol. 29, pp. 1527-1537, 1984.

[54] H. S. Wroblowa, "Electroreduction of oxygen:: A new mechanistic criterion," Journal of electroanalytical chemistry and interfacial electrochemistry, vol. 69, p. 195, 1976.

[55] N. M. Marković and P. N. Ross Jr, "Surface science studies of model fuel cell electrocatalysts," Surface Science Reports, vol. 45, pp. 117-229, 2002.

[56] P. N. Ross, Handbook of Fuel Cells: Fundamentals, Technology and Applications, 2003.

[57] B. N. Grgur, N. M. Marković, and P. N. Ross, "Temperature-dependent oxygen electrochemistry on platinum low-index single crystal surfaces in acid solutions," Canadian Journal of Chemistry, vol. 75, pp. 1465-1471, 1997.

[58] N. M. Marković, H. A. Gasteiger, B. N. Grgur, and P. N. Ross, "Oxygen reduction reaction on Pt(111): effects of bromide," Journal of Electroanalytical Chemistry, vol. 467, pp. 157-163, 1999.

[59] V. Stamenkovic, N. M. Markovic, and P. N. Ross Jr, "Structure-relationships in electrocatalysis: oxygen reduction and hydrogen oxidation reactions on Pt(111) and Pt(100) in solutions containing chloride ions," Journal of Electroanalytical Chemistry, vol. 500, pp. 44-51, 2001.

[60] J.-S. Park, S.-H. Park, S.-D. Yim, Y.-G. Yoon, W.-Y. Lee, and C.-S. Kim, "Performance of solid alkaline fuel cells employing anion-exchange membranes," Journal of Power Sources, vol. 178, pp. 620-626, 2008.

[61] F. Bidault, D. J. L. Brett, P. H. Middleton, and N. P. Brandon, "Review of gas diffusion cathodes for alkaline fuel cells," Journal of Power Sources, vol. 187, pp. 39-48, 2009.

[62] Y. Ernest, "Dioxygen electrocatalysis: mechanisms in relation to catalyst structure," Journal of Molecular Catalysis, vol. 38, pp. 5-25, 1986.

[63] F. Alcaide, E. Brillas, and P. L. Cabot, "Hydrogen oxidation reaction in a Pt-catalyzed gas diffusion electrode in alkaline medium," Journal of The Electrochemical Society, vol. 152, pp. E319-E327, 2005.

[64] N. Markovic, H. Gasteiger, and P. N. Ross, "Kinetics of Oxygen Reduction on Pt(hkl) Electrodes: Implications for the Crystallite Size Effect with Supported Pt Electrocatalysts," Journal of The Electrochemical Society, vol. 144, pp. 1591-1597, 1997.

[65] A. Parthasarathy, S. Srinivasan, A. J. Appleby, and C. R. Martin, "Electrode kinetics of oxygen reduction at carbon-supported and unsupported platinum microcrystallite/Nafion® interfaces," Journal of Electroanalytical Chemistry, vol. 339, pp. 101-121, 1992.

[66] S. Srinivasan, D. J. Manko, H. Koch, M. A. Enayetullah, and A. J. Appleby, "Recent advances in solid polymer electrolyte fuel cell technology with low

platinum loading electrodes," Journal of Power Sources, vol. 29, pp. 367-387, 1990.

[67] C. Song, Y. Tang, J. L. Zhang, J. Zhang, H. Wang, J. Shen, et al., "PEM fuel cell reaction kinetics in the temperature range of 23–120°C," Electrochimica Acta, vol. 52, pp. 2552-2561, 2007.

[68] B. E. Hayden, D. Pletcher, J.-P. Suchsland, and L. J. Williams, "The influence of support and particle size on the platinum catalysed oxygen reduction reaction," Physical Chemistry Chemical Physics, vol. 11, 2009.

[69] B. E. Hayden and J.-P. Suchsland, "Support and Particle Size Effects in Electrocatalysis," in Fuel Cell Catalysis, ed: John Wiley & Sons, Inc., 2008, pp. 567-592.

[70] H. A. Gasteiger and P. N. Ross, "Oxygen Reduction on Platinum Low-Index Single-Crystal Surfaces in Alkaline Solution: Rotating Ring DiskPt(hkl) Studies," The Journal of Physical Chemistry, vol. 100, pp. 6715-6721, 1996/01/01 1996.

[71] K. Kinoshita, "Particle Size Effects for Oxygen Reduction on Highly Dispersed Platinum in Acid Electrolytes," Journal of The Electrochemical Society, vol. 137, pp. 845-848, 1990.

[72] H. A. Gasteiger, S. S. Kocha, B. Sompalli, and F. T. Wagner, "Activity benchmarks and requirements for Pt, Pt-alloy, and non-Pt oxygen reduction catalysts for PEMFCs," Applied Catalysis B: Environmental, vol. 56, pp. 9-35, 2005.

[73] W. Sheng, H. A. Gasteiger, and Y. Shao-Horn, "Hydrogen Oxidation and Evolution Reaction Kinetics on Platinum: Acid vs Alkaline Electrolytes," Journal of The Electrochemical Society, vol. 157, pp. B1529-B1536, 2010.

[74] F. H. B. Lima, J. Zhang, M. H. Shao, K. Sasaki, M. B. Vukmirovic, E. A. Ticianelli, et al., "Catalytic Activity−d-Band Center Correlation for the O2 Reduction Reaction on Platinum in Alkaline Solutions," The Journal of Physical Chemistry C, vol. 111, pp. 404-410, 2007/01/01 2006.

[75] R. Adzic, Recent advances in the kinetics of oxygen reduction, 1998.

[76] Y.-F. Yang, Y.-H. Zhou, and C.-S. Cha, "Electrochemical reduction of oxygen on small palladium particles supported on carbon in alkaline solution," Electrochimica Acta, vol. 40, pp. 2579-2586, 1995.

[77] R. J. Taylor and A. A. Humffray, "Electrochemical studies on glassy carbon electrodes: II. Oxygen reduction in solutions of high pH (pH>10)," Journal of electroanalytical chemistry and interfacial electrochemistry, vol. 64, pp. 63-84, 1975.

[78] M. Appel and A. J. Appleby, "A ring-disk electrode study of the reduction of oxygen on active carbon in alkaline solution," Electrochimica Acta, vol. 23, pp. 1243-1246, 1978.

[79] G. Jürmann and K. Tammeveski, "Electroreduction of oxygen on multiwalled carbon nanotubes modified highly oriented pyrolytic graphite electrodes in alkaline solution," Journal of Electroanalytical Chemistry, vol. 597, pp. 119-126, 2006.

[80] K. C. Neyerlin, W. Gu, J. Jorne, and H. A. Gasteiger, "Study of the Exchange Current Density for the Hydrogen Oxidation and Evolution Reactions," Journal of The Electrochemical Society, vol. 154, pp. B631-B635, 2007.

[81] H. A. Gasteiger, J. E. Panels, and S. G. Yan, "Dependence of PEM fuel cell performance on catalyst loading," Journal of Power Sources, vol. 127, pp. 162-171, 2004.

[82] V. S. Bagotzky and N. V. Osetrova, "Investigation of hydrogen ionization on platinum with the help of micro-electrodes," Journal of Electroanalytical Chemistry, vol. 43, pp. 233-249, 1973.

[83] P.-L. Cabot, F. Alcaide, and E. Brillas, "Hydrogen reaction at open circuit in alkaline media on Pt in a gas-diffusion electrode," Journal of Electroanalytical Chemistry, vol. 626, pp. 183-191, 2009.

[84] N. M. Markovica, S. T. Sarraf, H. A. Gasteiger, and P. N. Ross, "Hydrogen electrochemistry on platinum low-index single-crystal surfaces in alkaline solution," Journal of the Chemical Society, Faraday Transactions, vol. 92, 1996.

[85] T. J. Schmidt, P. N. Ross Jr, and N. M. Markovic, "Temperature dependent surface electrochemistry on Pt single crystals in alkaline electrolytes: Part 2.

The hydrogen evolution/oxidation reaction," Journal of Electroanalytical Chemistry, vol. 524–525, pp. 252-260, 2002.

[86] N. M. Marković, B. N. Grgur, and P. N. Ross, "Temperature-Dependent Hydrogen Electrochemistry on Platinum Low-Index Single-Crystal Surfaces in Acid Solutions," The Journal of Physical Chemistry B, vol. 101, pp. 5405-5413, 1997/07/01 1997.

[87] F. T. Bacon, "The High Pressure Hydrogen-Oxygen Fuel Cell," Industrial & Engineering Chemistry, vol. 52, pp. 301-303, 1960/04/01 1960.

[88] M. Cifrain and K. Kordesch, "Hydrogen/oxygen (air) fuel cells with alkaline electrolytes," in Handbook of Fuel Cells, ed: John Wiley & Sons, Ltd, 2010.

[89] R. P. O'Hayre, Fuel cell fundamentals, Chapter 8, 2006.

[90] F. R. Brushett, M. S. Naughton, J. W. D. Ng, L. Yin, and P. J. A. Kenis, "Analysis of Pt/C electrode performance in a flowing-electrolyte alkaline fuel cell," International Journal of Hydrogen Energy, vol. 37, pp. 2559-2570, 2012.

[91] T. Isomura, K. Fukuta, H. Yanagi, S. Ge, and C.-Y. Wang, "Impact of Low Cathode Humidification on Alkaline Membrane Fuel Cell Performance," ECS Meeting Abstracts, vol. 1101, pp. 221-221, 2011.

[92] Y. C. Cao, X. Wang, and K. Scott, "The synthesis and characteristic of an anion conductive polymer membrane for alkaline anion exchange fuel cells," Journal of Power Sources, vol. 201, pp. 226-230, 2012.

[93] G. Merle, M. Wessling, and K. Nijmeijer, "Anion exchange membranes for alkaline fuel cells: A review," Journal of Membrane Science, vol. 377, pp. 1-35, 2011.

[94] K. N. Grew and W. K. S. Chiu, "A Dusty Fluid Model for Predicting Hydroxyl Anion Conductivity in Alkaline Anion Exchange Membranes," Journal of The Electrochemical Society, vol. 157, pp. B327-B337, 2010.

[95] S. Gu, R. Cai, T. Luo, Z. Chen, M. Sun, Y. Liu, et al., "A Soluble and Highly Conductive Ionomer for High-Performance Hydroxide Exchange Membrane Fuel Cells," Angewandte Chemie International Edition, vol. 48, pp. 6499-6502, 2009.

[96] S. Chempath, J. M. Boncella, L. R. Pratt, N. Henson, and B. S. Pivovar, "Density Functional Theory Study of Degradation of Tetraalkylammonium Hydroxides," The Journal of Physical Chemistry C, vol. 114, pp. 11977-11983, 2010/07/15 2010.

[97] S. Watanabe, K. Fukuta, and H. Yanagi, "Determination of Carbonate Ion in MEA during the Alkaline Membrane Fuel Cell (AMFC) Operation," ECS Transactions, vol. 33, pp. 1837-1845, 2010.

[98] G. Couture, A. Alaaeddine, F. Boschet, and B. Ameduri, "Polymeric materials as anion-exchange membranes for alkaline fuel cells," Progress in Polymer Science, vol. 36, pp. 1521-1557, 2011.

[99] J. R. Varcoe and R. C. T. Slade, "An electron-beam-grafted ETFE alkaline anion-exchange membrane in metal-cation-free solid-state alkaline fuel cells," Electrochemistry Communications, vol. 8, pp. 839-843, 2006.

[100] M. B. JR Varcoe, DM Halepoto, JP Kizewski, SD Poynton and RCT Slade, "Membrane and electrode materials for alkaline membrane fuel cells," University of Surrey, Guilford, 2008.

[101] J. R. Varcoe, R. C. T. Slade, E. L. H. Yee, S. D. Poynton, and D. J. Driscoll, "Investigations into the ex situ methanol, ethanol and ethylene glycol permeabilities of alkaline polymer electrolyte membranes," Journal of Power Sources, vol. 173, pp. 194-199, 2007.

[102] J. R. Varcoe, J. P. Kizewski, D. M. Halepoto, S. D. Poynton, R. C. T. Slade, and F. Zhao, "FUEL CELLS – ALKALINE FUEL CELLS | Anion-Exchange Membranes," in Encyclopedia of Electrochemical Power Sources, G. Editor-in-Chief: Jürgen, Ed., ed Amsterdam: Elsevier, 2009, pp. 329-343.

[103] R. C. T. Slade and J. R. Varcoe, "Investigations of conductivity in FEP-based radiation-grafted alkaline anion-exchange membranes," 14th International Conference on Solid State Protonic Conductors, Kyoto, Japan, 7-11 September 2008, vol. 176, pp. 585-597, 2005.

[104] H. Herman, R. C. T. Slade, and J. R. Varcoe, "The radiation-grafting of vinylbenzyl chloride onto poly(hexafluoropropylene-co-tetrafluoroethylene) films with subsequent conversion to alkaline anion-exchange membranes: op-

timisation of the experimental conditions and characterisation," Journal of Membrane Science, vol. 218, pp. 147-163, 2003.
[105] H. Yanagi and K. Fukuta, "Anion Exchange Membrane and Ionomer for Alkaline Membrane Fuel Cells (AMFCs)," ECS Meeting Abstracts, vol. 802, pp. 783-783, 2008.
[106] J. R. Varcoe and R. C. T. Slade, "Prospects for alkaline anion-exchange membranes in low temperature fuel cells," Fuel Cells, vol. 5, pp. 187-200, 2005.
[107] T. N. Danks, R. C. T. Slade, and J. R. Varcoe, "Alkaline anion-exchange radiation-grafted membranes for possible electrochemical application in fuel cells," Journal of Materials Chemistry, vol. 13, 2003.
[108] J. R. Varcoe, R. C. T. Slade, and E. Lam How Yee, "An alkaline polymer electrochemical interface: a breakthrough in application of alkaline anion-exchange membranes in fuel cells," Chemical Communications, 2006.
[109] J.-H. Hong, D. Li, and H. Wang, "Weak-base anion exchange membranes by amination of chlorinated polypropylene with polyethyleneimine at low temperatures," Journal of Membrane Science, vol. 318, pp. 441-444, 2008.
[110] H. A. Kostalik, T. J. Clark, N. J. Robertson, P. F. Mutolo, J. M. Longo, H. c. D. Abruña, et al., "Solvent Processable Tetraalkylammonium-Functionalized Polyethylene for Use as an Alkaline Anion Exchange Membrane," Macromolecules, vol. 43, pp. 7147-7150, 2010/09/14 2010.
[111] T. J. Clark, N. J. Robertson, H. A. Kostalik Iv, E. B. Lobkovsky, P. F. Mutolo, H. c. D. Abruña, et al., "A Ring-Opening Metathesis Polymerization Route to Alkaline Anion Exchange Membranes: Development of Hydroxide-Conducting Thin Films from an Ammonium-Functionalized Monomer," Journal of the American Chemical Society, vol. 131, pp. 12888-12889, 2009/09/16 2009.
[112] Y. Wan, B. Peppley, K. A. M. Creber, and V. T. Bui, "Anion-exchange membranes composed of quaternized-chitosan derivatives for alkaline fuel cells," Journal of Power Sources, vol. 195, pp. 3785-3793, 2010.
[113] J. R. Varcoe, "Investigations of the ex situ ionic conductivities at 30 [degree]C of metal-cation-free quaternary ammonium alkaline anion-exchange membranes in static atmospheres of different relative humidities," Physical Chemistry Chemical Physics, vol. 9, 2007.

[114] Z. Ogumi, "Preliminary study on direct alcohol fuel cells employing anion exchange membrane," Electrochemistry, vol. 70, pp. 980-983, 2002.

[115] M. Tanaka, K. Fukasawa, E. Nishino, S. Yamaguchi, K. Yamada, H. Tanaka, et al., "Anion conductive block poly(arylene ether)s: Synthesis, properties, and application in alkaline fuel cells," Journal of the American Chemical Society, vol. 133, pp. 10646-10654, 2011.

[116] L. A. Adams, S. D. Poynton, C. Tamain, R. C. Slade, and J. R. Varcoe, "A carbon dioxide tolerant aqueous-electrolyte-free anion-exchange membrane alkaline fuel cell," ChemSusChem, vol. 1, pp. 79-81, 2008.

[117] R. Zeng, S. D. Poynton, J. P. Kizewski, R. C. T. Slade, and J. R. Varcoe, "A novel reference electrode for application in alkaline polymer electrolyte membrane fuel cells," vol. 12, pp. 823-825, 2010.

[118] R. Zeng, R. C. T. Slade, and J. R. Varcoe, "An experimental study on the placement of reference electrodes in alkaline polymer electrolyte membrane fuel cells," Electrochimica Acta, vol. 56, pp. 607-619, 2010.

[119] C. Tamain, S. D. Poynton, R. C. T. Slade, B. Carroll, and J. R. Varcoe, "Development of Cathode Architectures Customized for H2/O2 Metal-Cation-Free Alkaline Membrane Fuel Cells," The Journal of Physical Chemistry C, vol. 111, pp. 18423-18430, 2007/12/01 2007.

[120] J. Zhou, M. Unlu, J. A. Vega, and P. A. Kohl, "Anionic polysulfone ionomers and membranes containing fluorenyl groups for anionic fuel cells," Journal of Power Sources, vol. 190, pp. 285-292, 2009.

[121] S. Lu, J. Pan, A. Huang, L. Zhuang, and J. Lu, "Alkaline polymer electrolyte fuel cells completely free from noble metal catalysts," Proceedings of the National Academy of Sciences of the United States of America, vol. 105, pp. 20611-20614, 2008.

[122] M. Mamlouk, K. Scott, J. A. Horsfall, and C. Williams, "The effect of electrode parameters on the performance of anion exchange polymer membrane fuel cells," International Journal of Hydrogen Energy, vol. 36, pp. 7191-7198, 2011.

[123] M. Piana, M. Boccia, A. Filpi, E. Flammia, H. A. Miller, M. Orsini, et al., "H2/air alkaline membrane fuel cell performance and durability, using novel

ionomer and non-platinum group metal cathode catalyst," Journal of Power Sources, vol. 195, pp. 5875-5881, 2010.

[124] K. Fukuta, H. Inoue, Y. Chikashige, and H. Yanagi, "Improved Maximum Power Density of Alkaline Membrane Fuel Cells by the Optimization of Catalyst Layer Construction," ECS Meeting Abstracts, vol. 1001, pp. 275-275, 2010.

[125] T. Isomura, K. Fukuta, H. Yanagi, S. Ge, and C.-Y. Wang, "Alkaline Membrane Fuel Cell Operated at Elevated Temperatures," ECS Meeting Abstracts, vol. 1002, pp. 751-751, 2010.

[126] K. Oda, H. Kato, K. Fukuta, and H. Yanagi, "Optimization of RRDE Method for the Evaluation of Catalyst Activity in Alkaline Solution," ECS Meeting Abstracts, vol. 1001, pp. 192-192, 2010.

[127] H. I. Kenji Fukuta, Shin Watanabe, and Hiroyuki Yanagi, "In-situ Observation of CO2 through the Self-purging in Alkaline Membrane Fuel Cell (AMFC)," ECS Transactions, vol. 19, pp. 23-27, 2009.

[128] C. Gibbs, "Improvements in or relating to catalysts for fuel cells," United Kingdom Patent, 2011.

[129] R. R. Adzic, J. Zhang, K. Sasaki, M. B. Vukmirovic, M. Shao, J. X. Wang, et al., "Platinum monolayer fuel cell electrocatalysts," Topics in Catalysis, vol. 46, pp. 249-262, 2007.

[130] H. A. Gasteiger, S. S. Kocha, B. Sompalli, and F. T. Wagner, "Activity benchmarks and requirements for Pt, Pt-alloy, and non-Pt oxygen reduction catalysts for PEMFCs," Applied Catalysis B-Environmental, vol. 56, pp. 9-35, 2005.

[131] M. Shao, "Palladium-based electrocatalysts for hydrogen oxidation and oxygen reduction reactions," vol. 196, pp. 2433-2444, 2011.

[132] R. Pattabiraman, "Electrochemical investigations on carbon supported palladium catalysts," Applied Catalysis A: General, vol. 153, pp. 9-20, 1997.

[133] C. Bianchini and P. K. Shen, "Palladium-Based Electrocatalysts for Alcohol Oxidation in Half Cells and in Direct Alcohol Fuel Cells," Chemical Reviews, vol. 109, pp. 4183-4206, 2009/09/09 2009.

[134] E. Antolini, "Palladium in fuel cell catalysis," Energy & Environmental Science, vol. 2, pp. 915-931, 2009.

[135] A. E. Bolzán, M. E. Martins, and A. J. Arvía, "The electrodissolution of base palladium in relation to the oxygen electroadsorption and electrodesorption in sulphuric acid solution," Journal of electroanalytical chemistry and interfacial electrochemistry, vol. 172, pp. 221-233, 1984.
[136] J. Matthey. (2015). Platinum Group Metal Prices. Available: http://www.platinum.matthey.com/prices/
[137] T. Sergio, "Work function, electronegativity, and electrochemical behaviour of metals: III. Electrolytic hydrogen evolution in acid solutions," Journal of electroanalytical chemistry and interfacial electrochemistry, vol. 39, pp. 163-184, 1972.
[138] S. A. Grigoriev, E. K. Lyutikova, S. Martemianov, and V. N. Fateev, "On the possibility of replacement of Pt by Pd in a hydrogen electrode of PEM fuel cells," International Journal of Hydrogen Energy, vol. 32, pp. 4438-4442, 2007.
[139] S. N. Pronkin, A. Bonnefont, P. S. Ruvinskiy, and E. R. Savinova, "Hydrogen oxidation kinetics on model Pd/C electrodes: Electrochemical impedance spectroscopy and rotating disk electrode study," Electrochimica Acta, vol. 55, pp. 3312-3323, 2010.
[140] N. M. Marković, C. A. Lucas, V. Climent, V. Stamenković, and P. N. Ross, "Surface electrochemistry on an epitaxial palladium film on Pt(111): surface microstructure and hydrogen electrode kinetics," Surface Science, vol. 465, pp. 103-114, 2000.
[141] J. Greeley, J. K. Nørskov, L. A. Kibler, A. M. El-Aziz, and D. M. Kolb, "Hydrogen Evolution Over Bimetallic Systems: Understanding the Trends," Chemphyschem, vol. 7, pp. 1032-1035, 2006.
[142] Y.-H. Cho, B. Choi, Y.-H. Cho, H.-S. Park, and Y.-E. Sung, "Pd-based PdPt(19:1)/C electrocatalyst as an electrode in PEM fuel cell," Electrochemistry Communications, vol. 9, pp. 378-381, 2007.
[143] Y. Tang, H. Zhang, H. Zhong, and Z. Xu, "In-situ investigation on the CO tolerance of carbon supported Pd–Pt electrocatalysts with low Pt content by electrochemical impedance spectroscopy," International Journal of Hydrogen Energy, vol. 37, pp. 2129-2136, 2012.

[144] D. C. Papageorgopoulos, M. Keijzer, J. B. J. Veldhuis, and F. A. de Bruijn, "CO Tolerance of Pd-Rich Platinum Palladium Carbon-Supported Electrocatalysts," Journal of The Electrochemical Society, vol. 149, pp. A1400-A1404, 2002.

[145] A. C. Garcia, V. A. Paganin, and E. A. Ticianelli, "CO tolerance of PdPt/C and PdPtRu/C anodes for PEMFC," Electrochimica Acta, vol. 53, pp. 4309-4315, 2008.

[146] A. Damjanovic and V. Brusić, "Oxygen reduction at Pt-Au and Pd-Au alloy electrodes in acid solution," Electrochimica Acta, vol. 12, pp. 1171-1184, 1967.

[147] S. Kondo, M. Nakamura, N. Maki, and N. Hoshi, "Active Sites for the Oxygen Reduction Reaction on the Low and High Index Planes of Palladium," The Journal of Physical Chemistry C, vol. 113, pp. 12625-12628, 2009/07/23 2009.

[148] K. Jukk, N. Alexeyeva, C. Johans, K. Kontturi, and K. Tammeveski, "Oxygen reduction on Pd nanoparticle/multi-walled carbon nanotube composites," Journal of Electroanalytical Chemistry, vol. 666, pp. 67-75, 2012.

[149] R. Rego, M. C. Oliveira, F. Alcaide, and G. Álvarez, "Development of a carbon paper-supported Pd catalyst for PEMFC application," International Journal of Hydrogen Energy, 2012.

[150] C.-L. Lee, H.-P. Chiou, and C.-R. Liu, "Palladium nanocubes enclosed by (100) planes as electrocatalyst for alkaline oxygen electroreduction," International Journal of Hydrogen Energy, vol. 37, pp. 3993-3997, 2012.

[151] L. Jiang, A. Hsu, D. Chu, and R. Chen, "Size-Dependent Activity of Palladium Nanoparticles for Oxygen Electroreduction in Alkaline Solutions," Journal of The Electrochemical Society, vol. 156, pp. B643-B649, 2009.

[152] M. H. Shao, K. Sasaki, P. Liu, and R. R. Adzic, "Pd3Fe and Pt monolayer-modified Pd3Fe electrocatalysts for oxygen reduction," Zeitschrift für physikalische Chemie, vol. 221, pp. 1175-1190, 2007.

[153] J. Kim, J. E. Park, T. Momma, and T. Osaka, "Synthesis of Pd-Sn nanoparticles by ultrasonic irradiation and their electrocatalytic activity for oxygen reduction," Electrochimica Acta, vol. 54, pp. 3412-3418, 2009.

[154] X. Wang, Y. Tang, Y. Gao, and T. Lu, "Carbon-supported Pd–Ir catalyst as anodic catalyst in direct formic acid fuel cell," Journal of Power Sources, vol. 175, pp. 784-788, 2008.

[155] R. Larsen, S. Ha, J. Zakzeski, and R. I. Masel, "Unusually active palladium-based catalysts for the electrooxidation of formic acid," Journal of Power Sources, vol. 157, pp. 78-84, 2006.

[156] S. Y. Shen, T. S. Zhao, and J. B. Xu, "Carbon-supported bimetallic PdIr catalysts for ethanol oxidation in alkaline media," Electrochimica Acta, vol. 55, pp. 9179-9184, 2010.

[157] L. Zhang, K. Lee, and J. Zhang, "The effect of heat treatment on nanoparticle size and ORR activity for carbon-supported Pd–Co alloy electrocatalysts," Electrochimica Acta, vol. 52, pp. 3088-3094, 2007.

[158] A. Serov, T. Nedoseykina, O. Shvachko, and C. Kwak, "Effect of precursor nature on the performance of palladium–cobalt electrocatalysts for direct methanol fuel cells," Journal of Power Sources, vol. 195, pp. 175-180, 2010.

[159] T. Mimani and S. Mayanna, "Study of the role of sodium hypophosphite in electroless nickel bath solution," Journal of Chemical Sciences, vol. 109, pp. 203-209, 1997.

[160] AkzoNobel. (2012). Ketjen. Available: http://www.akzonobel.com/polymer/our_products/product_search/index.aspx?appid=0&pgid=30&cat=Electroconductive+Blacks

[161] H.-L. Chiang, C. P. Huang, and P. C. Chiang, "The surface characteristics of activated carbon as affected by ozone and alkaline treatment," Chemosphere, vol. 47, pp. 257-265, 4// 2002.

[162] X. Yu and S. Ye, "Recent advances in activity and durability enhancement of Pt/C catalytic cathode in PEMFC: Part I. Physico-chemical and electronic interaction between Pt and carbon support, and activity enhancement of Pt/C catalyst," Journal of Power Sources, vol. 172, pp. 133-144, 10/11/ 2007.

[163] S. Kim and S.-J. Park, "Effects of chemical treatment of carbon supports on electrochemical behaviors for platinum catalysts of fuel cells," Journal of Power Sources, vol. 159, pp. 42-45, 9/13/ 2006.

[164] S. J. Yoo and Y.-E. Sung, "Design of Palladium-Based Alloy Electrocatalysts for Hydrogen Oxidation Reaction in Fuel Cells," in Fuel Cell Science, ed: John Wiley & Sons, Inc., 2010, pp. 111-146.

[165] J. F. Watts and J. Wolstenholme, "Electron Spectroscopy: Some Basic Concepts," in An Introduction to Surface Analysis by XPS and AES, ed: John Wiley & Sons, Ltd, 2005, pp. 1-15.

[166] J. F. Watts and J. Wolstenholme, "Compositional Depth Profiling," in An Introduction to Surface Analysis by XPS and AES, ed: John Wiley & Sons, Ltd, 2005, pp. 79-111.

[167] J. B. Xu, T. S. Zhao, S. Y. Shen, and Y. S. Li, "Stabilization of the palladium electrocatalyst with alloyed gold for ethanol oxidation," International Journal of Hydrogen Energy, vol. 35, pp. 6490-6500, 2010.

[168] E. Desimoni, "XPS determination of oxygen-containing functional groups on carbon-fibre surfaces and the cleaning of these surfaces," Surface and interface analysis, vol. 15, pp. 627-634, 1990.

[169] M. J. Larsen and E. M. Skou, "ESR, XPS, and thin-film RRDE characterization of nano structured carbon materials for catalyst support in PEM fuel cells," Journal of Power Sources, vol. 202, pp. 35-46, 3/15/ 2012.

[170] J. Zhang, PEM Fuel Cell Electrocatalysts and Catalyst Layers: Fundamentals and Applications, Chapter 10: Springer, 2008.

[171] S. P. Thompson, J. E. Parker, J. Potter, T. P. Hill, A. Birt, T. M. Cobb, et al., "Beamline I11 at Diamond: A new instrument for high resolution powder diffraction," Review of Scientific Instruments, vol. 80, Jul 2009.

[172] R. W. Cheary and A. Coelho, "A fundamental parameters approach to X-ray line-profile fitting," Journal of Applied Crystallography, vol. 25, pp. 109-121, 1992.

[173] C. Roth, N. Martz, T. Buhrmester, J. Scherer, and H. Fuess, "In-situ XAFS fuel cell measurements of a carbon-supported Pt–Ru anode electrocatalyst in hydrogen and direct methanol operation," Physical Chemistry Chemical Physics, vol. 4, pp. 3555-3557, 2002.

[174] S. Maniguet, R. J. Mathew, and A. E. Russell, "EXAFS of carbon monoxide oxidation on supported Pt fuel cell electrocatalysts," The Journal of Physical Chemistry B, vol. 104, pp. 1998-2004, 2000.

[175] E. Principi, A. Witkowska, S. Dsoke, R. Marassi, and A. Di Cicco, "An XAS experimental approach to study low Pt content electrocatalysts operating in PEM fuel cells," Physical Chemistry Chemical Physics, vol. 11, pp. 9987-9995, 2009.

[176] M. Herron, S. Doyle, S. Pizzini, K. Roberts, J. Robinson, G. Hards, et al., "In situ studies of a dispersed platinum on carbon electrode using X-ray absorption spectroscopy," Journal of Electroanalytical Chemistry, vol. 324, pp. 243-258, 1992.

[177] B.-J. Hwang, L. S. Sarma, J.-M. Chen, C.-H. Chen, S.-C. Shih, G.-R. Wang, et al., "Structural models and atomic distribution of bimetallic nanoparticles as investigated by X-ray absorption spectroscopy," Journal of the American Chemical Society, vol. 127, pp. 11140-11145, 2005.

[178] A. E. Russell and A. Rose, "X-ray absorption spectroscopy of low temperature fuel cell catalysts," Chemical reviews, vol. 104, pp. 4613-4636, 2004.

[179] M. Newville. (2004, Fundamentals of XAFS.

[180] S. W. T. Price, J. M. Rhodes, L. Calvillo, and A. E. Russell, "Revealing the Details of the Surface Composition of Electrochemically Prepared Au@Pd Core@Shell Nanoparticles with in Situ EXAFS," The Journal of Physical Chemistry C, vol. 117, pp. 24858-24865, 2013/11/27 2013.

[181] S. M. H. E.A. Stern, "Chapter 10 Principles and Applications of EXAFS
" in Handbook on synchrotron radiation
vol. 2, G. V. E. D. E. Marr, Ed., ed Amsterdam [etc.]: North-Holland, 1987, pp. 995 - 1040.

[182] S. V. Myers, A. I. Frenkel, and R. M. Crooks, "X-ray Absorption Study of PdCu Bimetallic Alloy Nanoparticles Containing an Average of ~64 Atoms," Chemistry of Materials, vol. 21, pp. 4824-4829, 2009/10/27 2009.

[183] M. R. Knecht, M. G. Weir, A. I. Frenkel, and R. M. Crooks, "Structural Rearrangement of Bimetallic Alloy PdAu Nanoparticles within Dendrimer Tem-

plates to Yield Core/Shell Configurations†," Chemistry of Materials, vol. 20, pp. 1019-1028, 2008/02/01 2007.

[184] A. I. Frenkel, A. Yevick, C. Cooper, and R. Vasic, "Modeling the Structure and Composition of Nanoparticles by Extended X-Ray Absorption Fine-Structure Spectroscopy," Annual Review of Analytical Chemistry, vol. 4, pp. 23-39, 2011.

[185] B. Ravel and M. Newville, "ATHENA, ARTEMIS, HEPHAESTUS: data analysis for X-ray absorption spectroscopy using IFEFFIT," Journal of Synchrotron Radiation, vol. 12, pp. 537-541, 2005.

[186] J. J. Rehr, R. C. Albers, and S. I. Zabinsky, "High-order multiple-scattering calculations of x-ray-absorption fine structure," Physical Review Letters, vol. 69, pp. 3397-3400, 12/07/ 1992.

[187] M. Newville, "EXAFS analysis using FEFF and FEFFIT," Journal of Synchrotron Radiation, vol. 8, pp. 96-100, 2001.

[188] M. Newville, P. Līviņš, Y. Yacoby, J. J. Rehr, and E. A. Stern, "Near-edge x-ray-absorption fine structure of Pb: A comparison of theory and experiment," Physical Review B, vol. 47, pp. 14126-14131, 06/01/ 1993.

[189] M. S. Nashner, A. I. Frenkel, D. L. Adler, J. R. Shapley, and R. G. Nuzzo, "Structural Characterization of Carbon-Supported Platinum−Ruthenium Nanoparticles from the Molecular Cluster Precursor PtRu5C(CO)16," Journal of the American Chemical Society, vol. 119, pp. 7760-7771, 1997/08/01 1997.

[190] R. E. Benfield, "Mean coordination numbers and the non-metal-metal transition in clusters," Journal of the Chemical Society, Faraday Transactions, vol. 88, pp. 1107-1110, 1992.

[191] M. Ellner, "Zusammenhang zwischen strukturellen und thermodynamischen eigenschaften bei phasen der kupfer-familie in T10-B4-systemen," Journal of the Less Common Metals, vol. 78, pp. 21-32, 4// 1981.

[192] R. W. G. Wyckoff, Crystal structures. New York: Interscience Publishers, 1963.

[193] J. Waser, H. A. Levy, and S. W. Peterson, "The structure of PdO," Acta Crystallographica, vol. 6, pp. 661-663, 1953.

[194] A. A. Bolzan, C. Fong, B. J. Kennedy, and C. J. Howard, "Structural Studies of Rutile-Type Metal Dioxides," Acta Crystallographica Section B, vol. 53, pp. 373-380, 1997.

[195] H. Niehus, W. Heiland, and E. Taglauer, "Low-energy ion scattering at surfaces," Surface Science Reports, vol. 17, pp. 213-303, 1993.

[196] E. Taglauer, "Probing surfaces with ions," Surface Science, vol. 299-300, pp. 64-76, 1994.

[197] A. W. Denier van der Gon, R. Cortenraad, W. P. A. Jansen, M. A. Reijme, and H. H. Brongersma, "In situ surface analysis by low energy ion scattering," Nuclear Instruments and Methods in Physics Research Section B: Beam Interactions with Materials and Atoms, vol. 161–163, pp. 56-64, 3// 2000.

[198] H. H. Brongersma, T. Grehl, E. R. Schofield, R. A. P. Smith, and H. R. J. ter Veen, "Analysis of the Outer Surface of Platinum-Gold Catalysts by Low-Energy Ion Scattering," Platinum Metals Review, vol. 54, pp. 81-87, // 2010.

[199] J. Gustafson, A. R. Haire, and C. J. Baddeley, "Depth-profiling the composition of bimetallic nanoparticles using medium energy ion scattering," Surface Science, vol. 605, pp. 220-224, 1// 2011.

[200] H. H. Brongersma, M. Draxler, M. De Ridder, and P. Bauer, "Surface composition analysis by low-energy ion scattering," Surface Science Reports, vol. 62, pp. 63-109, 2007.

[201] D. R. Baer, D. J. Gaspar, P. Nachimuthu, S. D. Techane, and D. G. Castner, "Application of Surface Chemical Analysis Tools for Characterization of Nanoparticles," Analytical and bioanalytical chemistry, vol. 396, pp. 983-1002, 01/06 2010.

[202] J. Zhang, PEM Fuel Cell Electrocatalysts and Catalyst Layers: Fundamentals and Applications, Chapter 11: Springer, 2008.

[203] Y. Garsany, O. A. Baturina, K. E. Swider-Lyons, and S. S. Kocha, "Experimental Methods for Quantifying the Activity of Platinum Electrocatalysts for the Oxygen Reduction Reaction," Analytical Chemistry, vol. 82, pp. 6321-6328, 2010/08/01 2010.

[204] K. J. J. Mayrhofer, G. K. H. Wiberg, and M. Arenz, "Impact of Glass Corrosion on the Electrocatalysis on Pt Electrodes in Alkaline Electrolyte," Journal of The Electrochemical Society, vol. 155, pp. P1-P5, 2008.

[205] L. Demarconnay, C. Coutanceau, and J. M. Léger, "Electroreduction of dioxygen (ORR) in alkaline medium on Ag/C and Pt/C nanostructured catalysts—effect of the presence of methanol," Electrochimica Acta, vol. 49, pp. 4513-4521, 10/1/ 2004.

[206] L. Demarconnay, C. Coutanceau, and J. M. Léger, "Study of the oxygen electroreduction at nanostructured PtBi catalysts in alkaline medium," Electrochimica Acta, vol. 53, pp. 3232-3241, 3/10/ 2008.

[207] T. Maiyalagan and K. Scott, "Performance of carbon nanofiber supported Pd–Ni catalysts for electro-oxidation of ethanol in alkaline medium," Journal of Power Sources, vol. 195, pp. 5246-5251, 8/15/ 2010.

[208] "Impedance and its Corresponding Electrochemical Processes," in Electrochemical Impedance Spectroscopy in PEM Fuel Cells, ed: Springer London, 2010, pp. 95-138.

[209] N. Fouquet, C. Doulet, C. Nouillant, G. Dauphin-Tanguy, and B. Ould-Bouamama, "Model based PEM fuel cell state-of-health monitoring via ac impedance measurements," Journal of Power Sources, vol. 159, pp. 905-913, 9/22/ 2006.

[210] P. Corradini, F. Pires, V. Paganin, J. Perez, and E. Antolini, "Effect of the relationship between particle size, inter-particle distance, and metal loading of carbon supported fuel cell catalysts on their catalytic activity," Journal of Nanoparticle Research, vol. 14, pp. 1-9, 2012/08/03 2012.

[211] Y. Liang, H. Zhang, H. Zhong, X. Zhu, Z. Tian, D. Xu, et al., "Preparation and characterization of carbon-supported PtRuIr catalyst with excellent CO-tolerant performance for proton-exchange membrane fuel cells," Journal of Catalysis, vol. 238, pp. 468-476, 2006.

[212] V. Penmatsa, H. Kawarada, Y. Song, and C. Wang, "Comparison of different oxidation techniques for biofunctionalization of pyrolyzed carbon," Material Science Research India, vol. 11, pp. 01-08, 2014.

[213] E. Raub, "Metals and alloys of the platinum group," Journal of the Less Common Metals, vol. 1, pp. 3-18, 1959.
[214] G. S. Fonseca, G. Machado, S. R. Teixeira, G. H. Fecher, J. Morais, M. C. M. Alves, et al., "Synthesis and characterization of catalytic iridium nanoparticles in imidazolium ionic liquids," Journal of Colloid and Interface Science, vol. 301, pp. 193-204, 2006.
[215] R. Mathew and A. Russell, "XAS of carbon supported platinum fuel cell electrocatalysts: advances towards real time investigations," Topics in Catalysis, vol. 10, pp. 231-239, 2000/05/01 2000.
[216] A. Jentys, "Estimation of mean size and shape of small metal particles by EXAFS," Physical Chemistry Chemical Physics, vol. 1, pp. 4059-4063, 1999.
[217] H.-G. Fritsche and R. Benfield, "Exact analytical formulae for mean coordination numbers in clusters," Zeitschrift für Physik D Atoms, Molecules and Clusters, vol. 26, pp. 15-17, 1993/03/01 1993.
[218] A. M. Beale and B. M. Weckhuysen, "EXAFS as a tool to interrogate the size and shape of mono and bimetallic catalyst nanoparticles," Physical Chemistry Chemical Physics, vol. 12, pp. 5562-5574, 2010.
[219] M. S. Nashner, A. I. Frenkel, D. Somerville, C. W. Hills, J. R. Shapley, and R. G. Nuzzo, "Core Shell Inversion during Nucleation and Growth of Bimetallic Pt/Ru Nanoparticles," Journal of the American Chemical Society, vol. 120, pp. 8093-8101, 1998/08/01 1998.
[220] M. R. Knecht, M. G. Weir, A. I. Frenkel, and R. M. Crooks, "Structural Rearrangement of Bimetallic Alloy PdAu Nanoparticles within Dendrimer Templates to Yield Core/Shell Configurations†," Chemistry of Materials, vol. 20, pp. 1019-1028, 2008/02/01 2008.
[221] A. Pozio, M. De Francesco, A. Cemmi, F. Cardellini, and L. Giorgi, "Comparison of high surface Pt/C catalysts by cyclic voltammetry," Journal of Power Sources, vol. 105, pp. 13-19, 2002.
[222] J. Zhang, PEM Fuel Cell Electrocatalysts and Catalyst Layers: Fundamentals and Applications, Chapter 16: Springer, 2008.
[223] J. Kaiser, L. Colmenares, Z. Jusys, R. Mörtel, H. Bönnemann, G. Köhl, et al., "On the Role of Reactant Transport and (Surface) Alloy Formation for the

CO Tolerance of Carbon Supported PtRu Polymer Electrolyte Fuel Cell Catalysts," Fuel Cells, vol. 6, pp. 190-202, 2006.

[224] O. Yépez and B. R. Scharifker, "Oxidation of CO on hydrogen-loaded palladium," Journal of Applied Electrochemistry, vol. 29, pp. 1185-1190, 1999.

[225] T. J. Schmidt, H. A. Gasteiger, G. D. Stab, P. M. Urban, D. M. Kolb, and R. J. Behm, "Characterization of High-Surface-Area Electrocatalysts Using a Rotating Disk Electrode Configuration," Journal of The Electrochemical Society, vol. 145, pp. 2354-2358, 1998.

[226] J. Koutecky and V. Levich, "The use of a rotating disk electrode in the studies of electrochemical kinetics and electrolytic processes," Zh. Fiz. Khim, vol. 32, pp. 1565-1575, 1958.

[227] A. J. Bard and L. R. Faulkner, "Method Involving Forced Convention--Hydrodynamic Methods," in Electrochemical Methods: Fundamentals and Applications, ed: Wiley, 2000, pp. 331-367.

[228] H. A. Gasteiger, N. M. Markovic, and P. N. Ross, "H2 and CO Electrooxidation on Well-Characterized Pt, Ru, and Pt-Ru. 1. Rotating Disk Electrode Studies of the Pure Gases Including Temperature Effects," The Journal of Physical Chemistry, vol. 99, pp. 8290-8301, 1995/05/01 1995.

[229] N. A. Maiorova, A. A. Mikhailova, O. A. Khazova, and V. A. Grinberg, "Thin-film rotating disk electrode as a tool for comparing the activity of catalysts in the hydrogen oxidation reaction," Russian Journal of Electrochemistry, vol. 42, pp. 331-338, 2006/04/01 2006.

[230] F. J. Vidal-Iglesias, J. Solla-Gullón, V. Montiel, and A. Aldaz, "Errors in the use of the Koutecky–Levich plots," Electrochemistry Communications, vol. 15, pp. 42-45, 2// 2012.

[231] J. Masa, C. Batchelor-McAuley, W. Schuhmann, and R. Compton, "Koutecky-Levich analysis applied to nanoparticle modified rotating disk electrodes: Electrocatalysis or misinterpretation," Nano Research, vol. 7, pp. 71-78, 2014/01/01 2014.

[232] V. S. Molchanov and N. E. Prikhidko, "Corrosion of silicate glasses by alkaline solutions," Bulletin of the Academy of Sciences of the USSR, Division of chemical science, vol. 6, pp. 1179-1184, 1957/10/01 1957.

[233] J. Durst, A. Siebel, C. Simon, F. Hasche, J. Herranz, and H. A. Gasteiger, "New insights into the electrochemical hydrogen oxidation and evolution reaction mechanism," Energy & Environmental Science, vol. 7, pp. 2255-2260, 2014.

[234] N. K. Nag, "A Study on the Formation of Palladium Hydride in a Carbon-Supported Palladium Catalyst," The Journal of Physical Chemistry B, vol. 105, pp. 5945-5949, 2001/06/01 2001.

[235] K. J. J. Mayrhofer, A. S. Crampton, G. K. H. Wiberg, and M. Arenz, "Analysis of the Impact of Individual Glass Constituents on Electrocatalysis on Pt Electrodes in Alkaline Solution," Journal of The Electrochemical Society, vol. 155, pp. P78-P81, June 1, 2008 2008.

[236] L. Zeng, T. S. Zhao, L. An, G. Zhao, X. H. Yan, and C. Y. Jung, "Graphene-supported platinum catalyst prepared with ionomer as surfactant for anion exchange membrane fuel cells," Journal of Power Sources, vol. 275, pp. 506-515, 2/1/ 2015.

[237] P. J. Ferreira, G. J. la O, Y. Shao-Horn, D. Morgan, R. Makharia, S. Kocha, et al., "Instability of Pt/C electrocatalysts in proton exchange membrane fuel cells - A mechanistic investigation," Journal of the Electrochemical Society, vol. 152, pp. A2256-A2271, 2005.

[238] Y. Shao-Horn, W. C. Sheng, S. Chen, P. J. Ferreira, E. F. Holby, and D. Morgan, "Instability of Supported Platinum Nanoparticles in Low-Temperature Fuel Cells," Topics in Catalysis, vol. 46, pp. 285-305, 2007/12/01 2007.

[239] R. Perry, "Analysis of durability of MEAs in automotive PEMFC applications," DOE 2012 Annual Progress Report, 2012.

[240] Vijay Ramani and J. Prakash, "Synthesis and Characterization of Mixed-Conducting Corrosion Resistant Oxide Supports," DOE Hydrogen and Fuel Cells Program, 2013 Annual Progress Report, 2013.

[241] J. Jiang and T. Aulich, "High activity and durability of Pt catalyst toward methanol electrooxidation in intermediate temperature alkaline media," Journal of Power Sources, vol. 209, pp. 189-194, 7/1/ 2012.

[242] H. An, L. Pan, H. Cui, B. Li, D. Zhou, J. Zhai, et al., "Synthesis and performance of palladium-based catalysts for methanol and ethanol oxidation in alkaline fuel cells," Electrochimica Acta, vol. 102, pp. 79-87, 7/15/ 2013.

[243] H. Zarrin, J. Wu, M. Fowler, and Z. Chen, "High durable PEK-based anion exchange membrane for elevated temperature alkaline fuel cells," Journal of Membrane Science, vol. 394–395, pp. 193-201, 3/15/ 2012.

[244] M. A. Hossain, Y. Lim, S. Lee, H. Jang, S. Choi, Y. Jeon, et al., "Comparison of alkaline fuel cell membranes of random and block poly(arylene ether sulfone) copolymers containing tetra quaternary ammonium hydroxides," International Journal of Hydrogen Energy, vol. 39, pp. 2731-2739, 2/14/ 2014.

[245] H. Tang, Z. Qi, M. Ramani, and J. F. Elter, "PEM fuel cell cathode carbon corrosion due to the formation of air/fuel boundary at the anode," Journal of Power Sources, vol. 158, pp. 1306-1312, 8/25/ 2006.

[246] I. Roche, E. Chaînet, M. Chatenet, and J. Vondrák, "Durability of carbon-supported manganese oxide nanoparticles for the oxygen reduction reaction (ORR) in alkaline medium," Journal of Applied Electrochemistry, vol. 38, pp. 1195-1201, 2008/09/01 2008.

[247] D. Wang, H. L. Xin, Y. Yu, H. Wang, E. Rus, D. A. Muller, et al., "Pt-Decorated PdCo@Pd/C Core–Shell Nanoparticles with Enhanced Stability and Electrocatalytic Activity for the Oxygen Reduction Reaction," Journal of the American Chemical Society, vol. 132, pp. 17664-17666, 2010/12/22 2010.

[248] L. Gu, N. Luo, and G. H. Miley, "Cathode electrocatalyst selection and deposition for a direct borohydride/hydrogen peroxide fuel cell," Journal of Power Sources, vol. 173, pp. 77-85, 11/8/ 2007.

[249] F. C. T. Team, "Cell component accelerated stress test protocols for PEM fuel cells," USCAR Fuel Cell Tech Team, 2010.

[250] B. Pollet, "The use of ultrasound for the fabrication of fuel cell materials," International Journal of Hydrogen Energy, vol. 35, pp. 11986-12004, 2010.

[251] F. H. B. Lima and E. A. Ticianelli, "Oxygen electrocatalysis on ultra-thin porous coating rotating ring/disk platinum and platinum–cobalt electrodes in alkaline media," Electrochimica Acta, vol. 49, pp. 4091-4099, 2004.

[252] A. B. J. Sobrido, N. Mansor, R. Jervis, F. Corà, C. Gibbs, P. F. McMillan, et al., "Carbon Nitrides: New Electroactive Materials for Energy Conversion and Storage Applications," Meeting Abstracts, pp. 1566-1566, 2014.
[253] A. B. J. Sobrido, I. Dedigama, N. Mansor, R. Jervis, T. Miller, F. Corà, et al., "Graphitic Carbon Nitride Materials for Energy Applications," ECS Transactions, vol. 64, pp. 13-30, 2015.
[254] N. Mansor, A. Belen Jorge, F. Corà, C. Gibbs, R. Jervis, P. F. McMillan, et al., "Development of Graphitic-Carbon Nitride Materials as Catalyst Supports for Polymer Electrolyte Fuel Cells," ECS Transactions, vol. 58, pp. 1767-1778, August 31, 2013 2013.
[255] N. Mansor, A. B. Jorge, F. Corà, C. Gibbs, R. Jervis, P. F. McMillan, et al., "Graphitic Carbon Nitride Supported Catalysts for Polymer Electrolyte Fuel Cells," The Journal of Physical Chemistry C, vol. 118, pp. 6831-6838, 2014/04/03 2014.

9 Appendix

9.1 HOR Curves

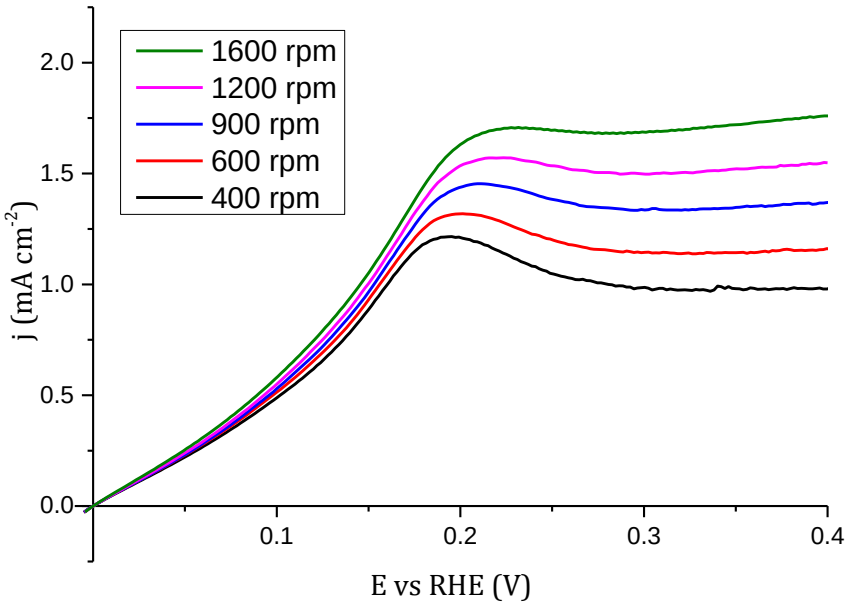

Figure 9.1 HOR curves for the Pd/C catalyst at various rotation rates in 0.1M KOH at 5 mVs^{-1} in the PTFE cell. The data highlights the hydrogen storage properties of the Pd, with the effect being more pronounced at lower rotation rates.

9.2 Koutecky-Levich Plots

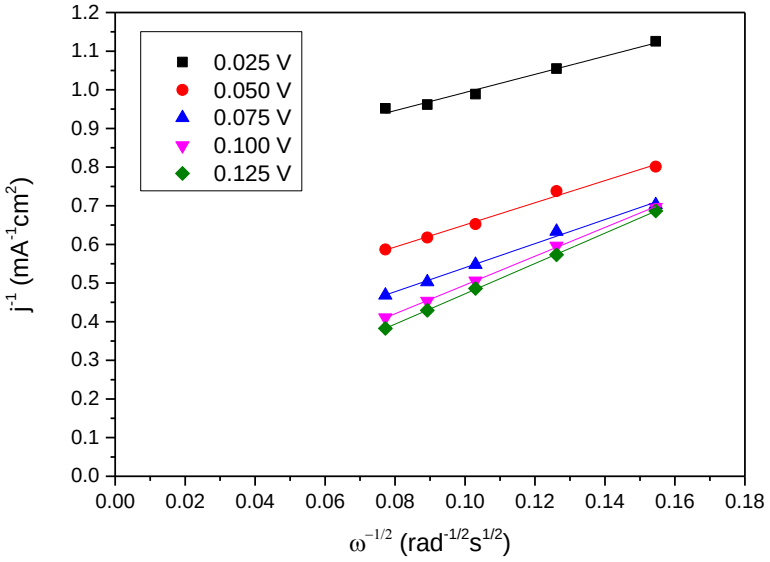

Figure 9.2 Pt/C in glass cell K-L plots

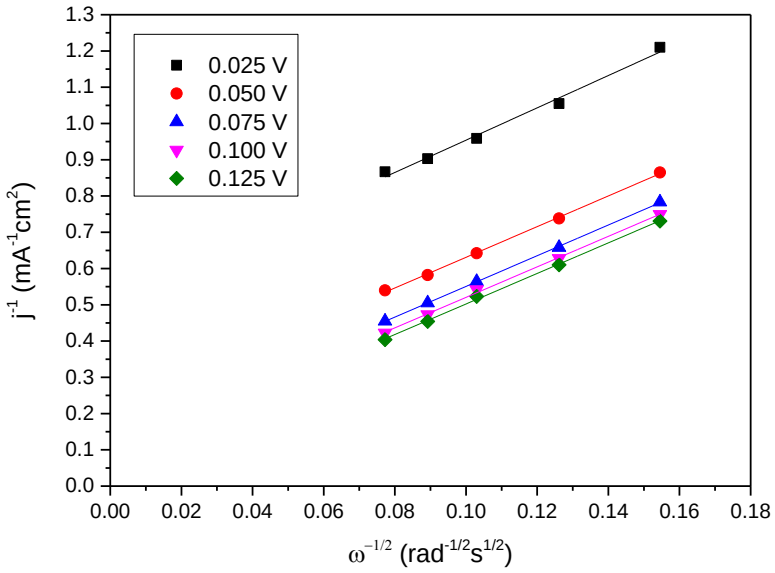

Figure 9.3 PdIr/C in glass cell K-L plots

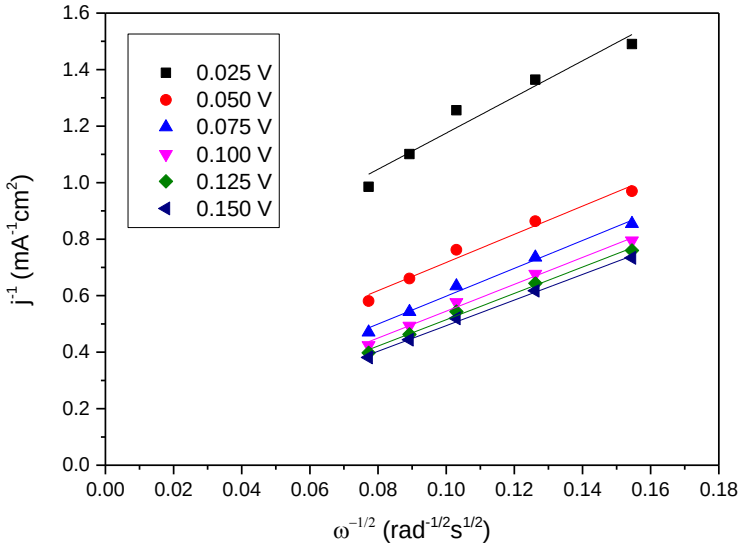

Figure 9.4 PdIr/C in PTFE cell K-L plot

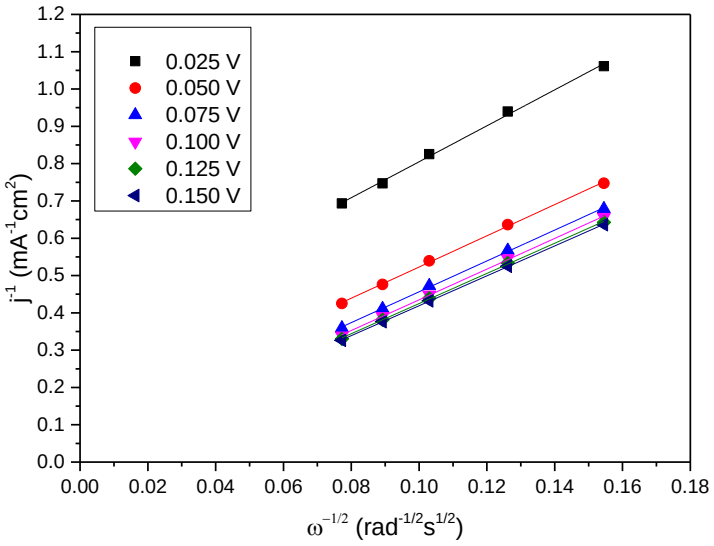

Figure 9.5 PdIr/C_{HSA} PTFE cell K-L plot

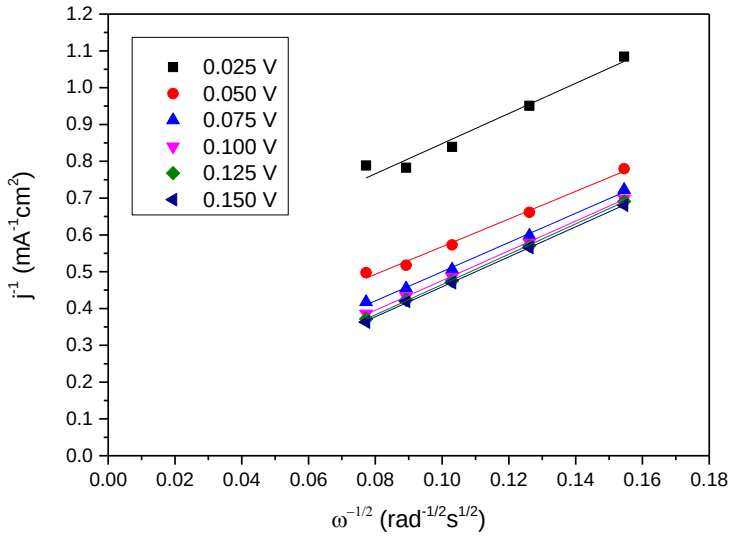

Figure 9.6 Pt/C in PTFE cell K-L plot

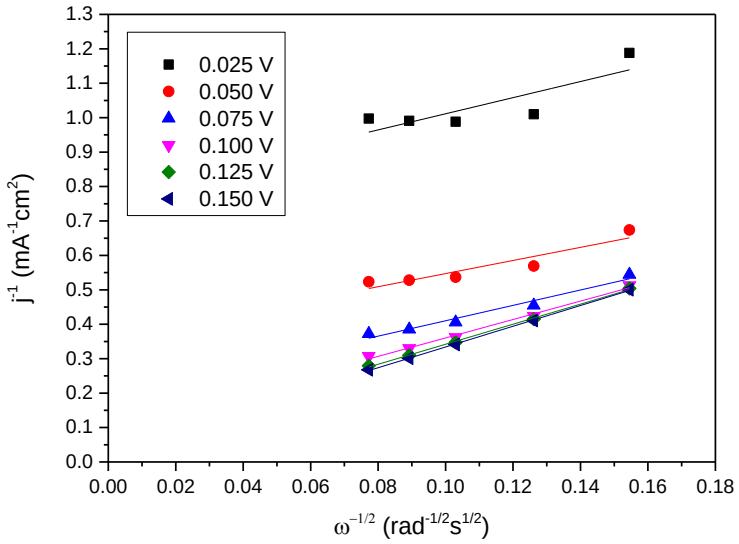

Figure 9.7 PdIr/C-Naf in PTFE cell K-L plot

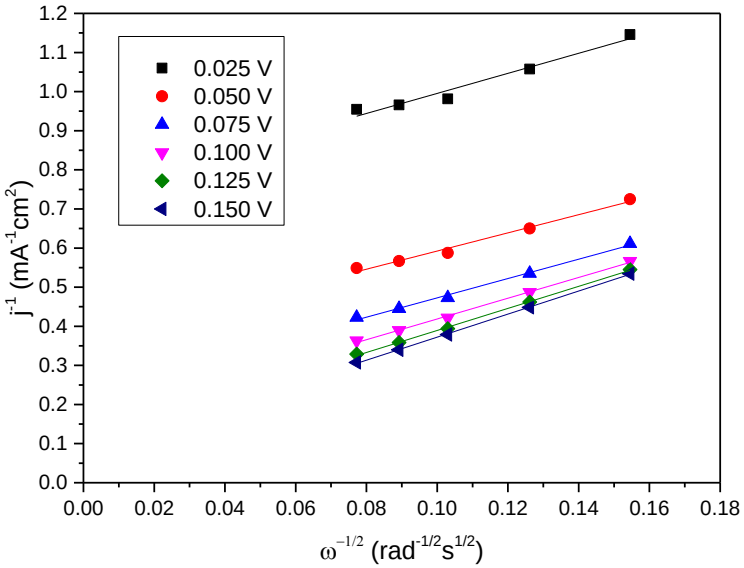

Figure 9.8 Pt/C-Naf in PTFE cell K-L plot